USE OF FINITE-ELEMENT ANALYSIS TO IMPROVE WELL CEMENTING IN HTHP CONDITIONS

A Dissertation

by

HENRY ARIAS

Submitted to the Office of Graduate Studies of
Texas A&M University
in partial fulfillment of the requirements for the degree of

DOCTOR OF PHILOSOPHY

Chair of Committee,	Jerome J. Schubert
Committee Members,	Hans Juvkam-Wold
	Catalin Teodoriu
	Giovanna Biscontin
Head of Department,	A. Daniel Hill

August 2013

Major Subject: Petroleum Engineering

ABSTRACT

Oil companies need to evaluate the risk of annular fluid or gas migration if cement fails during the life of the well. Sustained casing pressure can lead to shutting in the wells to avoid health, safety, and environment (HSE) risks and government fines. To understand the long-term integrity of cement in high temperature and high pressure (HTHP) conditions and the mechanical properties that affect the ability of cements to seal fluids, this project used finite-element models (FEMs) to study the stress-causing phenomena. FEM analyses in ABAQUS version 6.11 were used to determine the potential of cement failure in oil wells. The model uses a 3D section of a well that can be used for different casing and formation types under different loading conditions.

The model built in ABAQUS version 6.11 allows incorporating materials with nonlinear mechanical properties; it also uses FEM analysis to forecast fractures inside the cement under different loading scenarios like hydraulic fracture jobs or casing tests. The finite-element model included cases for cement cracking, cement debonding, and plastic deformation of the cement and rock that can generate loss of zonal isolation.

Linear manner: set cements behave elastically until a failure criterion is reached, and then they can behave plastically. The FEM approach can reproduce stresses, strains, and volume changes in the material under different environmental HTHP conditions.

Cemented wells have both tensile and compressive stresses that make some parts of the cement sheath experience fracture initiation, plastic deformation, or debonding.

This dissertation provides a model that will help drillers design the set cement for long-term integrity in HPHT well conditions. The FEM predicts if the cement sheath can develop debonding, cracks or plastic deformations during the life of the well. The cement sheath needs to be designed for long-term zonal isolation to avoid interzonal communications, remedial costs and environmental problems related to cement seal.

A CMS™-300 Automated Permeameter, a mechanical properties analyzer, HPHT cement consistometer, annular expansion molds, and tri-axial test equipment were used in this study to test cements for specific applications in three Colombian oil fields, including an oil field with in-situ combustion project.

DEDICATION

To my parents (in memory) and all my family

To my wife Delvi and my son Leonardo for their love and understanding during the long period of time to complete this research.

ACKNOWLEDGEMENTS

I wish to express my sincere thanks and appreciation to the chairman of my graduate advisory committee, Dr. Jerome J. Schubert, for his continuous guidance, enthusiasm and support throughout my graduate studies and research. I extend my appreciation to the other members of the Dissertation Committee, Dr. Hans Juvkam-Wold, Dr. Catalin Teodoriu, and Dr. Giovanna Biscontin for their suggestions to complete this work.

I would like to express to my sincere gratitude (in memory) to Dr. James E. Russell, who encouraged me to pursue this Ph.D. at Texas A& M University. His knowledge and kindness have been continuous reasons for admiration.

I would like to acknowledge the invaluable help and knowledge provided by all to the faculty and staff at the Department of Petroleum Engineering at Texas A&M University, especially to Dr. Christine Ehlig-Economides, Dr. A. Daniel Hill, Dr. Stephen A. Holditch, Dr. Hans Juvkam-Wold, Dr. Peter P. Valkó, Dr. Darla-Jean Weatherford, and Dr. Ding Zhu, for providing me the opportunity to pursue my studies for the Master's Degree and Ph.D. at Texas A&M University.

Finally, I express my sincere indebtedness to all engineers at Ecopetrol S.A., Halliburton Colombia, and Kimeca de México, especially to Jenny Carvajal, Sergio Acosta, Gino Nucci, Luis Ignacio Valderrama, Javier Urdaneta, Juan R. Garzón, Jose Luis Garcia Lozano, and all my coworkers who believed in this project and gave me the support necessary to carry it out successfully.

NOMENCLATURE

A	Area, in^2
BWOC	By weight of cement
CAE	Complete Abaqus environment
CAP	Calcium aluminate phosphate
CBL-VDL	Cement bond log-variable density log
CCS	Confining compressive strength, psi
CHP	Critical hydration period
C_b	Bulk compressibility, psi^{-1}
Co	Cohesive strength of cement, psi
c_p	Specific heat, Btu/(lbm×°F)
C_r	Rock matrix compressibility, psi^{-1}
D	Diameter, in
DST	Drill stem test
D^e	Fourth-order elasticity tensor
E	Young's modulus, psi
E_c	Young's modulus of cement, psi
E_f	Young's modulus of formation, psi
ECD	Equivalent circulating density, ppg
E_D	Dynamic Young's modulus, 10^6 psi
E_S	Static Young's modulus, 10^6 psi

F	Force, psi
FEA	Finite-element analysis
FEM	Finite-element model
FMA	Fluid migration analyzer cell
G	Shear modulus, psi
Gps	Gallons per sack
H (x)	Heaviside function
HPHT	High-pressure and high-temperature
ICP	Colombian Petroleum Institute
M	Hardening parameter
MDT	Modular dynamic tester
K	Bulk modulus, psi
K_C	Fracture toughness, psi×in$^{0.5}$
K_I	Stress intensity factor, psi×in$^{0.5}$
k, k_x, k_y, k_z	Thermal conductivity, Btu/(hr×in×°F)
K_r	Bulk modulus of the skeleton material, psi
L	Length, in
lbs/sx	Pounds per sack
MPRO	Mechanical properties analyzer
P	Load at failure, lbf
PEEQ	Equivalent plastic strain
p_p	Pore pressure, psi

Q	Generated heat, BTU
q_x, q_y, q_z	Energy conducted in x,y, and z axis
ppg	Pounds per gallon
S	Overburden pressure, psi
So	Cohesive strength of rock, psi
S_{11}	Radial stress
S_{22}	Tangential stress
SAGD	Steam-assisted gravity drainage
SCP	Sustained casing pressure
SCVF	Surface casing vent flow
S/Z	overburden gradient, psi/ft
T	Temperature, °F
T_o	Tensile strength, psi
t_c	Compressional wave transit time, μs/ft
t_{ma}	Compressional wave transit time of the matrix rock, μs/ft
t_{sma}	Shear-wave transit time of the matrix rock, μs/ft
t_s	Shear-wave transit time, μs/ft
UCA	Ultrasonic cement analyzer
UCS	Unconfined compressive strength, psi
UGS	Underground gas storage
VM	Von Mises stresses
Vp	Compressional wave sonic velocity, km/s

V_s	Shear-wave sonic velocity, km/s
V_{sh}	Nonlinear volume of shale
WOC	Water/oil contact
Woc	Waiting-on-cement time
XFEM	Extended finite-elment model
Z	Depth, ft
α	Linear thermal expansion coefficient, 1/°F
α_b	Biot's constant
α_V	Volumetric thermal expansion coefficient, 1/°F
$\in_{ij}$	Tensorial shear strain
$\in_{vol}$	Volumetric strain
ε	Total strain
ε^{cp}	Creep strain
ε^{e}	Elastic strain
ε^{p}	Plastic strain
γ_{ij}	Engineering strain
δ	Shear bond strength, psi
δ_r	Radial expansion, in
δ_{ij}	Kronecker delta
ϕ	Porosity
ϕ_c	Angle of internal friction of cement
ϕ_f	Angle of internal friction of formation

Ψ_d	Dilation angle, deg.
μ_f	Coefficient of internal friction
ρ_b	Bulk density, g/cm^3
σ_1	Maximum normal stress, psi
σ_2	Intermediate normal stress, psi
σ_3	Minimum normal stress or confining pressure, psi
σ'_{ij}	Effective stress, psi
σ_{ij}	Total stress, psi
σ_{oct}	Octahedral stress, psi
σ_v	Vertical stress, psi
σ_h	Minimum horizontal stress, psi
σ_H	Maximum horizontal stress, psi
σ_{xx}, σ_{yy}	Normal stress in x, y directions, psi
σ_r	Radial stress, psi
σ_θ	Tangential stress, psi
ν	Poisson's ratio
ν_c	Poisson's ratio of cement
ν_f	Poisson's ratio of formation
ν_s	Static Poisson's ratio
τ	Shear stress in the Mohr-Coulomb criterion, psi
τ_{ij}	Shear stress acting in the i, j plane; psi

τ_{max}	Maximum shear stress in the Mohr-Coulomb criterion, psi
$\tau_{xy,}$ τ_{yz}	Shear stress acting in the x, y or y, z plane; psi

TABLE OF CONTENTS

LIST OF FIGURES

LIST OF TABLES

CHAPTER I

INTRODUCTION

This dissertation describes a 3D finite-element model to investigate the effect of mechanical and thermal properties of the cement sheath to help the user design better cement slurries. This research uses the commercial software Abaqus version 6.11 to study the mechanical and thermal interaction among formation, cement sheath, and casing while applying different loads and temperature during the life of the well. Inner and outer microannuli and radial cracks in the cement sheath can create sustained casing pressure and interzonal communication due to loss of long-term cement seal during post-cementing operations.

In this research the finite element analyses use the Mohr-Coulomb plasticity model to describe failure of the cement and rock under compression/shear stresses and temperature changes. Abaqus software version 6.11 was used to build this 3D finite-element analysis to overcome the limitations of linear elasticity models, including anisotropic in-situ stresses in the model. The model involves mechanical and thermal properties of the rock, cement, and casing to determine cement cracking, debonding of cement, and plastic deformation of the cement and rock.

The 3D finite-element model considers mechanical and thermal properties of the cement and rock such as Young's modulus, Poisson's ratio, cohesion, confined compressive strength, tensile strength, thermal conductivity, specific heat, and thermal expansion coefficients. Uniaxial and triaxial tests were done for set cements to determine their mechanical properties. Also, mechanical properties of the formations of the oil fields were included to accomplish the analyses.

Polymers, glass fibers, carbon fibers, and other cementing additives were used to improve the mechanical properties of set cements for HTHP and in-situ combustion projects in Colombia. Assessment of 3D finite-element analyses built in Abaqus and

Halliburton's software was done. Fig. 1.1 illustrates the location of the area of study showing Cupiagua, Apiay and Chichimene fields.

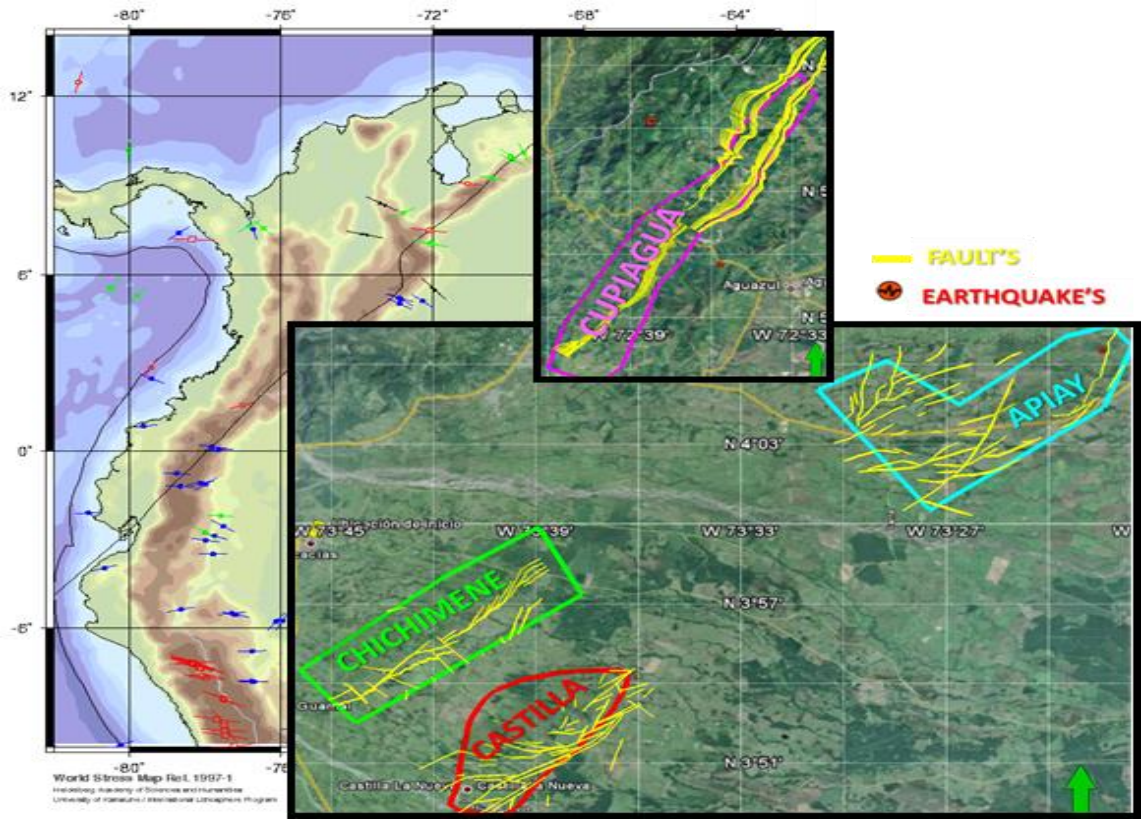

Fig. 1.1—Location of Apiay, Chichimene and Cupiagua fields

1.1 Organization of the Dissertation

The first part of the dissertation describes the problem and the objectives and gives an outline of the methodology followed in this research. Chapter II presents a literature review of mechanical and thermal properties of rock and well cements, and Chapter III discuses the use of finite-element analysis and cement failure in oil wells. Chapter IV gives an explanation of the FEM and shows a sensitivity analysis of mechanical and thermal properties of cements in HPHT conditions. Chapter V shows the results of uniaxial, triaxial and permeability tests of set cements from three cementing

service companies. Also, non-Portland cement for in-situ combustion wells (Calcium Phosphate Cement) was modified to improve its mechanical properties for in-situ combustion project in Colombia.

Chapter VI presents the analyses of the results obtained by simulation using an FEM built with Abaqus version 6.11 and Halliburton's software for Apiay, Chichimene and Cupiagua wells. Finally, the conclusions and recommendations for future work are presented in Chapter VII.

1.2 Well Cement Failure for HPHT Conditions

About of 50% of casing strings exhibit sustained casing pressures caused by cement failure, and HTHP conditions of oil wells can increase this statistic. Cement sheath failure can be associated with sustained casing pressure, early water production, and interzonal communication. FEM was developed to predict cement failures like plasticity and radial cracking based on their mechanical and thermal properties.

Unconfined compressive strength of the set cement is not the only mechanical property used to evaluate the quality of the cement sheath. Mechanical and thermal properties of set cement, formation and casing, in-situ stress data, well configuration, and operational loads are required to do an assessment of the cement seal for long-term zonal isolation. Cement sheaths for oil wells have to be designed to withstand the different pressure tests, completion, hydraulic fracturing jobs, and bottomhole pressure changes during depletion of the reservoir.

1.3 Objectives and Methodology

The main objectives of this research were to

- Develop a finite-element model in Abaqus 6.11 version to understand how the cement sheath fails in HTHP wells.
- Evaluate the mechanical and thermal properties of specific well cements in laboratory.

- Design well cements for long-term isolation for specific oil fields in Colombia using FEM analysis.
- Evaluate the use of some additives to improve mechanical properties of well cements.
- Understand the state of the art in well cements and their limitations.

The research methodology of this work consists of four parts: reviewing literature, developing FEM in Abaqus version 6.11, performing laboratory tests of set cements to determine their mechanical and thermal properties, applying an FEM to predict cement failure for specific fields in Colombia.

- For the literature review in Chapter II, I examined the short- and long-term properties of well cements, mechanical and thermal properties of rocks and cements, failure criteria in set cements, and fracture mechanics. In Chapter III, I researched the state of the art of cement fatigue in oil wells, flexible cements, self-healing cements, and cement placement evaluation. Also, I show an introduction to FEM and XFEM applied for cement-sheath failure.
- To understand the behavior of the cement sheath for HPHT wells, I built a FEM in Abaqus to determine whether plasticity behavior of the cement and formation is responsible for inner and outer microannuli. Sensitivity analyses of the mechanical and thermal properties of the well cements were done to see the effect on plasticity and cracks of the set cement.
- Numerous lab tests were done to evaluate the elasticity of the cement and mechanical properties such as Young's modulus, Poisson's ratio, friction angle, cohesion, tensile strength, porosity, permeability, and expansion of cements. Latex, glass fibers, and carbon fibers were tested to improve elasticity and tensile strength of the set cement. Also, mechanical properties of rocks were calculated with electrical logs and calibrated with triaxial tests. Theoretical and empirical equations to estimate mechanical properties for set cements are identical to those used for rock mechanics.

- FEMs in Abaqus version 6.11 and Halliburotn’s software were applied to evaluate new cement designs for long-term isolation in Cupiagua, Apiay and Chichimene oil fields.

CHAPTER II

MECHANICAL AND THERMAL PROPERTIES OF ROCKS AND WELL CEMENTS

Chapter II gives a theoretical background of short and long-term properties requirements of set cements. This is followed by reviewing concepts of rock mechanics and thermodynamics to understand zonal isolation problems during the life of the well. Mechanical and thermal properties of rocks and set cements were used in the simulation of cement behavior in Chapter IV and VI.

2.1 Short- and Long-Term Properties of Set Cements

In the past, the well cement was designed to fulfill short-term requirements, and any isolation problem was attributed to a bad cementing job without considering the mechanical and thermal properties of the cement and formation. The main objectives for well cementing are[1]:

- Support the casing.
- Protect the casing from shock loads.
- Provide a seal between zones with different pressure levels or fluid content during the well life.
- Protect casing from corrosion.
- Seal off zones of lost circulation.

The cement slurry and the cement sheath need to meet the following requirements:

- The cement slurry must have no free water and no setting.
- The cement slurry needs to be easily mixed and pumped.
- The cement slurry must have the appropriate thickening time, fluid loss, and gel strength and optimal rheological properties for mud removal.

- The cement slurry needs to develop strength quickly after placement in the annulus. This property avoids migration of fluids from the formations to the well, which could lead to a well control incident.
- The set cement has to be impermeable and must develop mechanical properties to ensure the well life with different downhole conditions of temperature, pressure, and chemical exposure. Set cements should have water permeability less than 0.1 md.
- The cement sheath requires a good bonding to casing and formation.

The well cementing industry has realized that well cement can lose the ability to provide zonal isolation during the lifetime of the well. It is common to see a good hydraulic seal after the cementing job, but a gas migration problem can come out after a hydraulic fracturing treatment. Long-term properties such as resistance to downhole chemical attack have occasionally been taken into account. In the United States, 15% of primary cementing jobs fail, and one third of these cement failures are related to gas or fluid migration. [2]

If cement slurries have the right additives, the cement can fulfill both the short-term and long-term requirements to provide zonal isolation of the well. The short-term requirements are related to the cement slurry properties, and long-term requirements deal with mechanical and thermal properties of cement and formation to withstand the well loads including in-situ stresses. Typical short- and long-term properties of the cement are shown in Table 2.1.

Cement tensile strength, Young's modulus, Poisson's ratio, cohesion, and friction angle are the principal mechanical properties of the well cements to determine if the cement sheath can withstand the loads of the well during its life. Besides the mechanical properties of the cement, its thermal cement properties must also be known. Chapter IV will show results of different uniaxial, triaxial, thermal, and permeability tests done on the designed set cements.

TABLE 2.1—SHORT- AND LONG-TERM PROPERTY REQUIREMENTS OF CEMENTS (FROM REF. 3)

Short Term: Cement Slurry	Long Term: Cement Sheath
Environmentally acceptable	Thermally stable under downhole conditions of pressure and temperature
Desired density	Resists downhole chemicals
Mixable at the surface	Mechanical properties to withstand stresses from various downhole operations and provides zonal isolation for the life of the well
Non-settling under static and dynamic conditions	
Zero free water	
Desired thickening time, fluid loss and strength development	
100% placement in the annulus	
Resists fluid influx	

2.2 Rock Mechanics Concepts

2.2.1 Stress

Fig. 2.1a considers a randomly oriented plane of area δA, containing a point O, and on which acts an elementary force $\delta\vec{F}$, the result of all forces acting on δA. The stress vector at point O, on the plane δA whose normal is in the direction OP, is then defined as follows[4]:

$$\bar{\sigma}_{OP} = \lim_{\delta A \to 0}\left(\frac{\overline{\delta F}}{\delta A}\right). \quad \text{.....} \quad (2.1)$$

In rock mechanics, the convention is that compressive stresses are positive, as most underground situations are under compressive loading conditions.

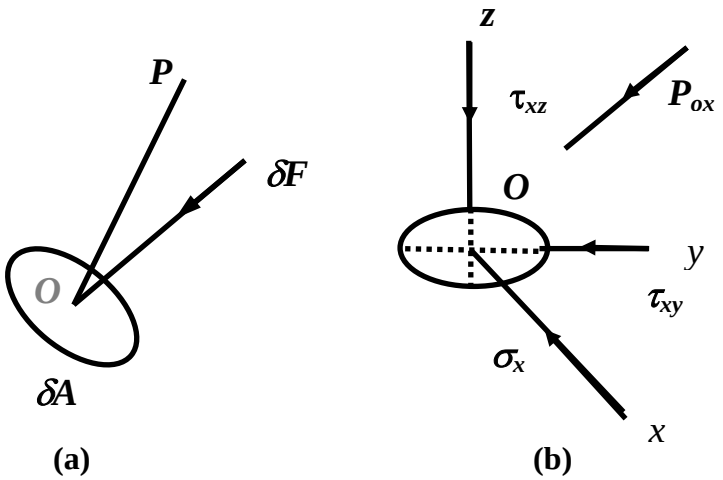

Fig. 2.1—Stress decomposition (after Ref. 4)

Stresses have the same units as pressure (psi, kPa, and so forth). The difference is that pressures related to fluids at rest are hydrostatic (same value in every direction) while stresses that relate to solids are generally not hydrostatic. At one point *O* in a solid, stresses can vary depending on the orientation of the plane δA on which they act. For instance, in most formations, the vertical in-situ stress can be quite different from the horizontal in-situ stresses.

Fig. 2.1b illustrates a right-handed system of orthogonal axes O_x, O_y, and O_z at *O*. If we take *OP* in the O_x-direction, the vector $\vec{P}_{ox}$ will have the components σ_x, τ_{xy}, and τ_{xz} acting into the O_x-, O_y-, and O_z-directions, respectively.

The stress σ_x is called a normal component of stress because it is perpendicular to the elementary area δA. The stress components τ_{xy} and τ_{xz} are in the plane of the elementary area and are called shear stresses because they tend to shear the material in the plane δA.

Similarly, if *OP* is taken in the O_y-direction, the components would be σ_y, τ_{yx}, and τ_{yz}. Similar notations exist for the O_z-direction. The nine quantities[4]

$$\begin{pmatrix} \sigma_x & \tau_{xy} & \tau_{xz} \\ \tau_{yx} & \sigma_y & \tau_{yz} \\ \tau_{zx} & \tau_{zy} & \sigma_z \end{pmatrix} \quad \text{.....} \quad (2.2)$$

are called the stress components at point *O*. In solids, the forces on three orthogonal faces at one point are generally different.

However, using the principle of conservation of angular momentum, it can be shown that $\tau_{ij} = \tau_{ji}$, where $i \neq j$ and the indices *i* and *j* represent any one of *x*, *y*, and *z*. Therefore, only six stress components are sufficient to define the symmetrical matrix.

2.2.2 Strain

When a body is subjected to a stress field, it will deform; the relative positions of its points will be altered. If the relative positions of the particles of a body are changed so that their initial and final positions cannot be made to correspond by translation or rotation (rigid body motion), the body is strained.

If the displacements are *u*, *v*, and *w* in the *x*, *y*, and *z* directions, respectively, the components of strain are[5]

$$\in_{xx} = \frac{\partial u}{\partial x}, \quad \text{.....} \quad (2.3)$$

$$\in_{yy} = \frac{\partial v}{\partial y}, \quad \text{.....} \quad (2.4)$$

$$\in_{zz} = \frac{\partial w}{\partial z}, \quad \text{.....} \quad (2.5)$$

$$\gamma_{xy} = \frac{\partial u}{\partial y} + \frac{\partial v}{\partial x}, \quad \text{.....} \quad (2.6)$$

$$\gamma_{xz} = \frac{\partial u}{\partial z} + \frac{\partial w}{\partial x}, \text{ and} \quad \text{.....} \quad (2.7)$$

$$\gamma_{yz} = \frac{\partial v}{\partial z} + \frac{\partial w}{\partial y}. \quad \text{.....} \quad (2.8)$$

In subscript notation, the strain tensor is defined by

$$\in_{ij} = \frac{1}{2}\left(\frac{\partial u_i}{\partial x_j} + \frac{\partial u_j}{\partial x_i} \right); \text{ i, j=1,2,3.} \quad \text{..... (2.9)}$$

Note that

$$\gamma_{ij} = 2 \in_{ij} . \quad \text{..... (2.10)}$$

Eqs. 2.3 to 2.5 represent normal strains and Eqs. 2.6 to 2.8 are shear strains. Engineering strains, γ_{ij}, include some rotation, and this definition is used frequently for experimental work and numerical applications. Tensorial shear strains, $\in_{ij}$, describe a pure deformation, and this concept is useful for theoretical derivations.[5]

2.2.3 Linear Elasticity

Using the stress/strain relationships, elastic constants may be determined from a specimen of the cement or rock under load in a testing machine; these are usually referred to the static or quasistatic elastic constants. Using wave-propagation relationships, elastic constants may be also determined from measured elastic-wave velocities. Elastic constants determined from wave velocity are usually referred to as dynamic elastic constants. For an ideally elastic material, the static and dynamic constants are the same, and the material exhibits a perfectly linear stress/strain relationship over the load range. For rocks, particularly friable sands, and set cements this is not the case. At high confining pressure the stress/strain relation becomes more linear, and there is better agreement between the dynamic and static constants. In general, the values of the elastic constants obtained by static techniques are lower than those obtained by dynamic methods. [6]

2.2.3.1 Static Elastic Properties

2.2.3.1.1 Young's Modulus *(E)*

For isotropic materials that are linearly elastic, Young's modulus relates axial strain to axial stress when performing a simple tension or compression test (all other σ*'s* = 0)[5]:

$$\sigma_{xx} = E \in_{xx} . \quad \text{.....} \quad (2.11)$$

Young's modulus is proportional to the stiffness of the material sample under uniaxial loading. The higher the Young's modulus, the harder it is to deform the material. Oil well cements have a Young's modulus from 0.14 E+6 to 1.4 E+6 psi. Neat 15.6-ppg cement has Young's modulus above 2.5 E+6 psi. Young's modulus is extensively used in hydraulic fracturing, borehole stability, compaction/subsidence analysis, and well cementing.

2.2.3.1.2 Poisson's Ratio *(ν)*

Poisson's ratio relates axial strain to transverse normal strain in a simple tension or compression test (all other σ*'s* except σ_{xx}=0)[5]:

$$\in_{yy} = \in_{zz} = -\nu \in_{xx} . \quad \text{.....} \quad (2.12)$$

Poisson's ratio, ν, normally takes values from 0 to 0.5. Set cements have usually a Poisson's ratio of 0.05 to 0.25. For rocks, Poisson's ratio is typically 0.15 to 0.25.[6] For weak, highly porous rocks, Poisson's ratio may approach zero or even appear to become negative. Values of Poisson's ratio outside the theoretical limits imply experimental problems or that the material is not behaving elastically.

Knowledge of Poisson's ratio has applications in hydraulic fracturing, borehole stability, in-situ stress, subsidence, depletion-induced stresses, cement failure analysis, among others.

2.2.3.1.3 Shear Modulus *(G)*

Shear modulus relates shear stress to shear strain as follows[5]:

$$\tau_{xy} = 2G \in_{xy} = G\gamma_{xy} . \quad \text{.....} \quad (2.13)$$

The shear modulus, *G*, can be expressed in terms of *E* and ν as follows:

$$G = E / 2(1+\nu) . \quad \text{.....} \quad (2.14)$$

Shear modulus are worthwhile to determine the mechanical properties of set cements and rock.

2.2.3.1.4 Bulk Modulus *(K)*

Bulk modulus relates volumetric strain, $\in_{\text{vol}}$, to the mean normal or octahedral stress, σ_{oct}, *by*[5]

$$\sigma_{\text{oct}} = K \in_{\text{vol}} . \quad \text{.....} \quad (2.15)$$

where σ_{oct} and $\in_{\text{vol}}$ are defined by[5]

$$\sigma_{\text{oct}} = \frac{\sigma_{xx} + \sigma_{yy} + \sigma_{zz}}{3} \text{ and } \quad \text{.....} \quad (2.16)$$

$$\in_{\text{vol}} = \in_{xx} + \in_{yy} + \in_{zz} . \quad \text{.....} \quad (2.17)$$

The inverse of the bulk modulus is called compressibility, $1/K=C_b$. Table 2.2 shows the most common relation between isotropic elastic constants, and sets of two linearly independent parameters are required to describe the stress in function of strain, i.e. $\sigma=f(\in)$.[7]

TABLE 2.2—RELATIONS BETWEEN ISOTROPIC ELASTIC CONSTANTS (FROM REF. 7)

	E, ν	E, G	K, ν	K, G
E=	E	E	$3(1-2\nu)K$	$\dfrac{9K}{1+3K/G}$
ν=	ν	$-1+\dfrac{E}{2G}$	ν	$\dfrac{1-2G/3K}{2+2G/3K}$
G=	$\dfrac{E}{2(1+\nu)}$	G	$\dfrac{3(1-2\nu)K}{2(1+\nu)}$	G
K=	$\dfrac{E}{3(1-2\nu)}$	$\dfrac{E}{9-3E/G}$	K	K

A linear elastic material model is valid for small elastic strains (less than 5%), and the linear elastic behavior can be isotropic, orthotropic, or anisotropic. The total stress is defined from the total elastic strain as

$$\sigma = D^e \varepsilon^e . \quad \text{.....} \quad (2.17)$$

where σ is the total stress or Cauchy stress, D^e is the fourth-order elasticity tensor, and ε^e is the total elastic strain (log strain in finite-strain problems).

The number of independent components of the elasticity tensor D^e depends on symmetry properties. For large elastic strain (larger than 5%), the hyperelastic model is better to use in finite-element software.

A material can be classified as either isotropic, where an infinite number of symmetry planes pass through every point, or anisotropic, which has no symmetry planes. A material can be classified as orthotropic when it has two orthogonal symmetry planes for the elastic properties. The stress-strain relationship for isotropic material is given by:

$$\begin{pmatrix}\varepsilon_{11}\\ \varepsilon_{22}\\ \varepsilon_{33}\\ \gamma_{12}\\ \gamma_{13}\\ \gamma_{23}\end{pmatrix}=\begin{Bmatrix} 1/E & -\nu/E & -\nu/E & 0 & 0 & 0\\ -\nu/E & 1/E & -\nu/E & 0 & 0 & 0\\ -\nu/E & -\nu/E & 1/E & 0 & 0 & 0\\ 0 & 0 & 0 & 1/G & 0 & 0\\ 0 & 0 & 0 & 0 & 1/G & 0\\ 0 & 0 & 0 & 0 & 0 & 1/G \end{Bmatrix}\begin{Bmatrix}\sigma_{11}\\ \sigma_{22}\\ \sigma_{33}\\ \sigma_{12}\\ \sigma_{13}\\ \sigma_{23}\end{Bmatrix} \quad \text{.....} \qquad (2.18)$$

The stress-strain relationship for an orthotropic material is defined by three Young's moduli, E_1, E_2, E_3; three Poisson's ratios v_{12}, v_{13}, v_{23}; and three shear moduli G_{12}, G_{13}, and G_{23} associated with the material's principal directions. The relationship stress and strain for orthotropic material is given by the following expression:

$$\begin{pmatrix}\varepsilon_{11}\\ \varepsilon_{22}\\ \varepsilon_{33}\\ \gamma_{12}\\ \gamma_{13}\\ \gamma_{23}\end{pmatrix}=\begin{Bmatrix} 1/E_1 & -\nu_{21}/E_2 & -\nu_{31}/E_3 & 0 & 0 & 0\\ -\nu_{12}/E_1 & 1/E_2 & -\nu_{32}/E_3 & 0 & 0 & 0\\ -\nu_{13}/E_1 & -\nu_{23}/E_2 & 1/E_3 & 0 & 0 & 0\\ 0 & 0 & 0 & 1/G_{12} & 0 & 0\\ 0 & 0 & 0 & 0 & 1/G_{13} & 0\\ 0 & 0 & 0 & 0 & 0 & 1/G_{23} \end{Bmatrix}\begin{Bmatrix}\sigma_{11}\\ \sigma_{22}\\ \sigma_{33}\\ \sigma_{12}\\ \sigma_{13}\\ \sigma_{23}\end{Bmatrix} \quad \text{.....} \qquad (2.19)$$

The Possion's ratios v_{ij} characterize the transverse strain in the *j*-direction, when the material is stressed in the *i*-direction. Poisson's ratio v_{ij} is not equal to v_{ji}, but they are related by:

$$\nu_{ij}/E_i = \nu_{ji}/E_j \,. \quad \text{.....} \qquad (2.20)$$

Transverse isotropy is characterized by a plane of isotropy at every point in the material. Assuming the 1–2 plane to be the plane of isotropy at every point, transverse isotropy requires that $E_1=E_2=E_p$, $v_{31}=v_{32}=v_{tp}$, $v_{13}=v_{23}=v_{pt}$, and $G_{13}=G_{23}=G_t$, where *p* and *t* stand for "in-plane" and "transverse," respectively. In general, the quantities v_{tp} and v_{pt}

are not equal and are related by $\nu_{tp} / E_t = \nu_{pt} / E_p$. The stress/strain relationship for material with transverse isotropy is given by:

$$\begin{pmatrix} \varepsilon_{11} \\ \varepsilon_{22} \\ \varepsilon_{33} \\ \gamma_{12} \\ \gamma_{13} \\ \gamma_{23} \end{pmatrix} = \begin{Bmatrix} 1/E_p & -\nu_p/E_p & -\nu_{tp}/E_t & 0 & 0 & 0 \\ -\nu_p/E_p & 1/E_p & -\nu_{tp}/E_t & 0 & 0 & 0 \\ -\nu_{pt}/E_p & -\nu_{pt}/E_p & 1/E_t & 0 & 0 & 0 \\ 0 & 0 & 0 & 1/G_p & 0 & 0 \\ 0 & 0 & 0 & 0 & 1/G_t & 0 \\ 0 & 0 & 0 & 0 & 0 & 1/G_t \end{Bmatrix} \begin{Bmatrix} \sigma_{11} \\ \sigma_{22} \\ \sigma_{33} \\ \sigma_{12} \\ \sigma_{13} \\ \sigma_{23} \end{Bmatrix} \quad \ldots\ldots\ldots\ldots \quad (2.21)$$

where $G_p = E_p / 2\left(1+\nu_p\right)$ and the total number of independent constants is only five.

2.2.3.2 Dynamic Elastic Constants

The mechanical behavior of a cement specimen or rock under dynamic conditions can be obtained only if one knows its dynamic elastic constants. These can be obtained by initiating and propagating elastic waves through a core of given length or from sonic logs. Two types of elastic body waves can be generated: compressional and shear. The elastic wave theory shows that the velocity of *P* and *S* waves are related to the "dynamic" elastic constants through the following relationships[8]:

$$V_p = \left[\frac{E_D(1-\nu)}{\rho_b(1+\nu)(1-2\nu)}\right]^{\frac{1}{2}} \text{ and } \quad \ldots\ldots\ldots\ldots \quad (2.22)$$

$$V_s = \left[\frac{E_D}{2\rho_b(1+\nu)}\right]^{\frac{1}{2}}. \quad \ldots\ldots\ldots\ldots \quad (2.23)$$

Eqs. 2.22 and 2.23 relate as a system of two equations and two unknowns that can be solved for the dynamic Young's modulus, E_D, and Poisson's ratio, ν:

$$E_D = \rho_b V_p^2 \frac{(1+\nu)(1-2\nu)}{1-\nu} = \rho_b V_s^2 \frac{3V_p^2 - 4V_s^2}{V_p^2 - V_s^2} \text{ and } \quad \text{.....} \quad (2.24)$$

$$\nu = \frac{V_p^2 - 2V_s^2}{2\left(V_p^2 - V_s^2\right)}. \quad \text{.....} \quad (2.25)$$

A list of dynamic elastic constants in terms of transit times ($t_s=1/V_s$ and $t_c=1/V_p$) and bulk density is shown in Table 2.3.[9]

TABLE 2.3—DYNAMIC ELASTIC PROPERTIES (FROM REF. 9)

	Mechanical Property	Value
ν	Poisson's ratio	$\frac{\frac{1}{2}\left(t_s/t_c\right)^2 - 1}{\left(t_s/t_c\right)^2 - 1}$
G	Shear modulus	$1.347\times10^{10}\frac{\rho_b}{t_s^2}$
E	Young's modulus	$2G(1+\nu)$
K	Bulk modulus	$1.347\times10^{10}\rho_b\left(\frac{1}{t_c^2} - \frac{4}{3t_s^2}\right)$
C_b	Bulk compressibility (with porosity)	$\frac{1}{K_b}$
C_r	Bulk compressibility (zero porosity)	$1.347\times10^{10}\left(\frac{1}{t_{ma}^2} - \frac{4}{3t_{sma}^2}\right)\times g$
α_b	Biot elastic constant	$1-\frac{C_r}{C_b}$

In Table 2.2 t_s is the shear transit time in μs/ft, t_c is the compressional wave transit time in μs/ft, ρ_b is the bulk density in g/cm^3, g is the acceleration due to gravity in ft/s^2, t_{ma} is the compressional wave transit time of the matrix rock in μs/ft, t_{sma} is the shear wave transit time of the matrix rock in μs/ft. Moreover, ν and α are dimensionless,

G, E, K in psi, and C_b and C_r in psi^{-1}. The equations of Table 2.2 provide an efficient way to calculate elastic properties from log data.

2.2.4 Poroelasticity

The pore pressure in the cement sheath can change during the life of the cement during its hydration, and the cement pore pressure can drop to a very low value. Fluids from formations can migrate to the set cement to equilibrate the pressure. Also, the cement pore pressure can increase due to wellbore temperature.

Poroelasticity, as related to borehole proximity, will be looked at herein in terms of the effective stress concept that was introduced by Terzaghi[10] and modified by Biot.[11] This concept is based on the role pore pressure, p_p, plays in counteracting the mechanical stress carried through grain-to-grain contact. The efficiency of the pore-pressure effect is measured by a factor called the Biot constant, α_b, as given below:

$$\sigma_{ij}^{'} = \sigma_{ij} - \alpha_b p_p \delta_{ij} \text{ , and} \quad \text{..... (2.26)}$$

$$\alpha_b = 1 - \frac{C_r}{C_b}, \quad \text{..... (2.27)}$$

where σ'_{ij} is the effective stress, σ_{ij} is the total stress, α_b is the Biot constant, p_p is the pore pressure, δ_{ij} is the Kronecker delta, C_r is the cement or rock matrix compressibility, and C_b is the bulk compressibility.

If the cement or rock has no porosity (the rock matrix compressibility, C_r, is equal to the bulk compressibility, C_b), then the Biot constant, α_b, becomes zero. On the other hand, with high porosity the matrix compressibility is small compared to the bulk compressibility, which causes the Biot constant to approach unity. The Biot constant or poroelastic constant, α_b, describe the capacity of the fluid pressure to withstand the total applied pressure. Terzaghi[10] worked with soils, and he did not use a multiplier preceding the pore pressure term, p_p, i.e., α=1.

Fluids from the formation can move to the set cement. Assuming that the set cement is incompressible and the pore fluid is slightly compressible, the diffusion equation can be written[12]:

$$\frac{\partial^2 p_p}{\partial x^2} + \frac{\partial^2 p_p}{\partial y^2} + \frac{\partial^2 p_p}{\partial z^2} = \frac{\phi \mu c}{k} x \frac{\partial p_p}{\partial t^2}, \quad \text{.....} \qquad (2.28)$$

where p_p is the pore pressure, ϕ is the porosity, μ is the viscosity of the fluid, k is the permeability, and c is the fluid compressibility.

Permeability measurements use this diffusion equation to determine the permeability of the cement sheath. An operational procedure for determining the relative permeability of set cement to liquid or gas is contained in API RP 10B. The procedure compares permeability of cement samples rather than absolute permeability values.[12]

2.2.5 Plastic Deformation

The deformation of any material beyond the elastic limit is known as plasticity. Constitutive equations for plasticity are not well established. Several different idealizations have been proposed, taking into account the phenomena observed, but some are not quite useful. Set cement and rocks behave like elastic materials at low stress levels and plastic materials at high stress levels.

The main concepts supporting the plasticity theory are plastic strains and the yield criterion, flow rule, and hardening rule. In plastic strains, the total strain, $\delta\varepsilon$, can be expressed as the summation of the following vectors:

$$\delta\varepsilon = \delta\varepsilon^e + \delta\varepsilon^p + \delta\varepsilon^{cr} \quad \text{.....} \qquad (2.29)$$

where $\delta\varepsilon$ is the total strain, $\delta\varepsilon^e$ is the elastic strain, $\delta\varepsilon^p$ is the inelastic (plastic) time-independent strain rate, and $\delta\varepsilon^{cr}$ is the inelastic (creep) time-dependent strain. All set cements have some creep behavior, but it has been poorly studied in oil well cements.[12]

The elastic strain is reversible and the plastic strain is irreversible. *Yield criterion* is the point where irreversible changes occur in the rock. It separates states of stress that cause only elastic strains from those that cause plastic and elastic strains. *Flow rule* describes how the plastic strains develop from a given loading situation. The *hardening rule* describes how rocks under certain conditions might sustain an increasing load after the initial failure. The hardening or softening might be interpreted as a change of the yield surface in the principal stress space. In three dimensions, this can be described by a yield function that is a function of the state of stress and a hardening parameter[6]:

$$f(\partial_1 + \partial_2 + \partial_3 + M) = 0 \quad \text{.....} \quad (2.30)$$

The hardening parameter, *M*, determines the evolution of the yield curve with the amount of plastic deformation of the material.

The theory of elastoplasticity is the most-used theory to model set cement failure. Fig. 2.2 shows the stress-strain relationship of elasto-plastic deformation. From A to B, the relation between stress and strain is linear, and the slope of the curve is the Young's modulus, *E*. In this region (A to B), the theory of elasticity applies. Beyond Point B the slope of the curve decreases. From Point B to C the strain hardens, and beyond Point C the strain softens. An elastic, perfectly plastic material that has elastic behavior with no strain hardening or softening would move only through Points A, B, and D.

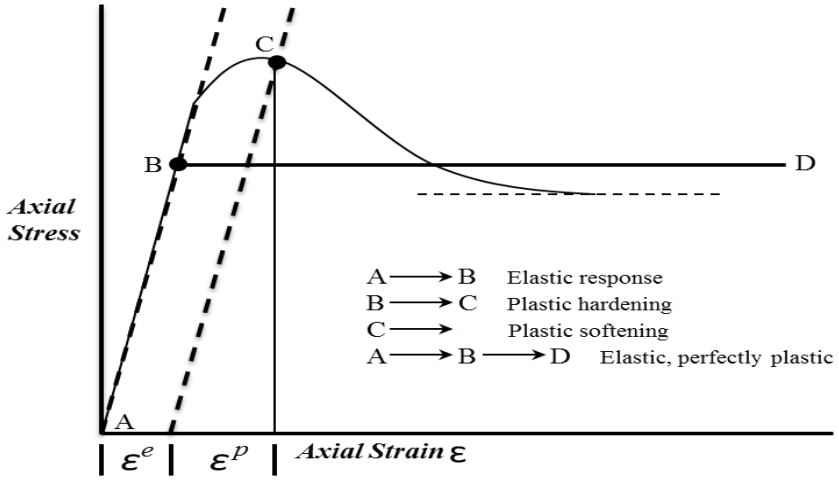

Fig. 2.2—Graphical representation of elasto-plastic deformation (after Ref. 12)

2.2.6 Thermoelasticity

Cement hydration, circulation of drilling and completion fluids, well stimulation, steam injection, and production lead to changes in the mechanical properties as temperature changes. Casing, cement, and rock expand with temperature increments at different rates, according to their thermal properties. The nonuniform heating of the casing, cement, and rock can produce nonuniform expansion of the materials, leading to failure of the cement or debonding.

2.2.6.1 Heat Transfer

Heat flow can happen when there is a difference in temperature within a body or between the body and its surrounding medium. Heat transfer problems have the following considerations[13]:

- The heat-transfer problem can have uncoupled, sequentially coupled, or full temperature-displacement heat-transfer solutions.
- There are three methods of heat transfer (conduction, convection, and radiation). Heat transfer in casing, cement, and formation is mainly by conduction.
- Heat-transfer problems can incorporate transient or steady-state analysis.

- Heat-transfer analyses can be nonlinear because the material properties are temperature dependent or because the boundary conditions are nonlinear.
- Finite-element analyses require elements that support heat transfer.

In uncoupled temperature-displacement analyses, the temperature fields are calculated without knowledge of the stress/deformation state in the bodies. Sequentially coupled thermal-stress analysis is performed by first solving the heat-transfer problem, then using the temperature solution into a stress analysis as a predefined field. A coupled temperature-displacement procedure is used to solve simultaneously for the stress/displacement and the temperature fields. A coupled analysis is used when the thermal and mechanical solutions affect each other strongly.

Transference of heat can be done by three distinct methods: conduction, convection, and radiation. In conduction, the heat passes through the material of the body itself. In convection, the heat is transferred by relative motion of portions of the heated body. In radiation, the heat passes between distant portions of the body by electromagnetic ratio. The heat is transferred in solids essentially by conduction, but in liquids and gases the heat is transferred by convection and radiation.

In steady-state thermal analysis (a system that is not changing with time), the internal energy term (the specific heat term) in the heat-transfer equation is not considered in the analysis. Transient time in thermal analysis is used to determine the heat flow in the materials with time. It is possible to have the same results for steady-state and transient time for a very long transient time response.

The energy balance for conduction in an infinitesimal volume of dimensions d_x, dy and dz the energy equation will be of the form[14]:

$$q_x + q_y + q_z - \rho_b c_p dxdydz \frac{\partial T}{\partial t} + Qdxdydz = q_{x+dx} + q_{y+dy} + q_{z+dz} \quad \text{.....} \qquad (2.31)$$

where q_x, q_y and q_z are energy conducted into the x, y, and z axes.

$$q_x = -k_x dydz \frac{\partial T}{\partial x} \quad \text{……...……} \quad (2.32)$$

$$q_y = -k_y dxdz \frac{\partial T}{\partial y} \quad \text{……...……} \quad (2.33)$$

$$q_z = -k_z dxdy \frac{\partial T}{\partial z} \quad \text{……...……} \quad (2.34)$$

$$\text{Change in internal energy} = \rho_b c_p dxdydz \frac{\partial T}{\partial t} \quad \text{…….……} \quad (2.35)$$

$$\text{Energy generated within the volume} = Qdxdydz \quad \text{……..……} \quad (2.36)$$

where q is the heat flow, T is the temperature; k is the thermal conductivity (which must be positive), ρ_b is the density, c_p is the specific heat, and Q is the generated heat (BTU or J). A negative sign appears in Eq. 2.32, 2.33, and 2.34 because the heat flows from high to low temperature, or opposite to the direction of the temperature field.

Taylor's theorem says that if *f(x)* and its derivatives are continuous on an interval containing $x=a$, then there are numbers x_o and x_o^* between a and x such that[15]

$$f(x) = f(a) + \frac{f'(a)}{1!}(x-a) + \frac{f''(a)}{2!}(x-a)^2 + ... \quad \text{…..…..……} \quad (2.37)$$

Using only the first two terms of Taylor's theorem to calculate qx+d_x, q_y+d_y and q_z+d_z, we have:

$$q_{x+dx} = -\left[k_x \frac{\partial T}{\partial x} + \frac{\partial}{\partial x}\left(k_x \frac{\partial T}{\partial x} \right) dx \right] dydz \quad \text{……..…..……} \quad (2.38)$$

$$q_{y+dy} = -\left[k_y \frac{\partial T}{\partial y} + \frac{\partial}{\partial y}\left(k_y \frac{\partial T}{\partial y} \right) dy \right] dxdz \quad \text{……..……..} \quad (2.39)$$

$$q_{z+dz} = -\left[k_z \frac{\partial T}{\partial z} + \frac{\partial}{\partial z}\left(k_z \frac{\partial T}{\partial z} \right) dz \right] dxdy \quad \text{……..……} \quad (2.40)$$

Replacing and reorganizing the terms in Eq. 2.31, we obtain:

$$\frac{\partial}{\partial x}\left(k_x \frac{\partial T}{\partial x}\right)+\frac{\partial}{\partial y}\left(k_y \frac{\partial T}{\partial y}\right)+\frac{\partial}{\partial z}\left(k_z \frac{\partial T}{\partial z}\right)+Q=\rho_b c_p \frac{\partial T}{\partial t} \quad \text{……..……} \quad (2.41)$$

Eq. 2.41 is a general form of heat conduction for the transient case. For an isotropic material, the thermal conductivity, k is the same in the x, y, and z directions, $k=k_x=k_y=k_z$. Replacing k_x, k_y and k_z for k, Eq. 2.41 becomes Eq. 2.42, which represents the heat conduction for the transient case for an isotropic material:

$$\frac{\partial^2 T}{\partial x^2}+\frac{\partial^2 T}{\partial y^2}+\frac{\partial^2 T}{\partial z^2}+Q=\frac{\rho_b c_p}{k}\frac{\partial T}{\partial t} \quad \text{……..…..……} \quad (2.42)$$

Steady state for heat transfer means that the temperature does not change with time, and there is no net change in the internal energy of the body $\left(\partial T/\partial t=0\right)$. This represents a time when the body has achieved thermal equilibrium. Eq. 2.43 denotes for heat conduction for the steady-state case for an anisotropic material:

$$\frac{\partial}{\partial x}\left(k_x \frac{\partial T}{\partial x}\right)+\frac{\partial}{\partial y}\left(k_y \frac{\partial T}{\partial y}\right)+\frac{\partial}{\partial z}\left(k_z \frac{\partial T}{\partial z}\right)+Q=0 \quad \text{……...……} \quad (2.43)$$

Eq. 2.44 refers to heat conduction in the steady-state case for an isotropic material:

$$\frac{\partial^2 T}{\partial x^2}+\frac{\partial^2 T}{\partial y^2}+\frac{\partial^2 T}{\partial y^2}+Q=0 \quad \text{……..……..……} \quad (2.44)$$

2.2.6.2 Thermal Conductivity

Thermal conductivity is the quantity of heat transmitted through a unit thickness in a direction normal to a surface of unit area, due to a unit temperature gradient under

steady-state conditions. Conduction take place when a temperature gradient exists in a solid (or stationary fluid) medium. The equation used to express heat transfer by conduction is known as Fourier's law and is expressed as[14]:

$$q_x = -k_x dydz \frac{\partial T}{\partial x} \quad \text{……..……..…….……} \quad (2.45)$$

From Eq. 2.45, the thermal conductivity in the *x* direction is given by:

$$k_x = -\frac{q_x}{dydz \frac{\partial T}{\partial x}} \quad \text{……..……..…….……} \quad (2.46)$$

where q_x is the heat transferred in the *x* direction per unit time (W or Btu/hr), $d_y d_z$ is the heat transfer area (m^2 or ft^2), *k* is the thermal conductivity of the material [W/m.K or Btu/(hr °F ft)], ∂T is the temperature difference across the material (K or °F), and ∂x is the material thickness (m or ft).

The thermal conductivity, *k*, is not constant for the same material; it depends on the temperature. This finite-element analysis assumes that the thermal conductivity does not change with the temperature; instead, it is a tensor, and it can be fully anisotropic, orthotropic, or isotropic. Typical units in the International System and English units are W/(m·K) and Btu/(hr °F ft), respectively. To convert between the two unit systems, we could use the relation 1 W/(m.K) = 0.5779 Btu/(hr.°F ft). To be consistent with the units in Abaqus software, the thermal conductivity in this study will use units in Btu/(hr °F in.).

2.2.6.3 Specific Heat

The specific heat of a material is defined by the following equation[14]:

$$c_p = \frac{\partial Q}{\partial T} \quad \text{……..……..……..…….……} \quad (2.47)$$

The specific heat, c_p of a material at temperature (T) is defined as $\partial Q/\partial T$ where ∂Q is quantity of heat necessary to raise the temperature of 1 unit mass of the material through the small temperature range ∂T. The specific heat per unit mass is given as a function of temperature and field variables. The specific heat of a material must be defined in heat conduction for transient analyses. Large changes in internal energy during a phase change should be modeled using "latent heat," not specific heat.

The International System and English units of specific heat are J/(Kg.K) and Btu/(lbm.°F), respectively. The equivalence of specific heat in the two systems can be given by 1 J/(Kg.K) = 0.000238846 Btu/(lbm.°F).

2.2.6.4 Thermal Expansion Coefficients

The coefficient of thermal expansion describes how the size of an object changes with a change in temperature. It measures the fractional change in volume per degree change in temperature at a constant pressure.

The volumetric thermal expansion coefficient is the most basic thermal expansion coefficient. All substances expand or contract when their temperature changes, and the expansion or contraction always occurs in all directions. Substances that expand at the same rate in any direction are called *isotropic*. In *anisotropic* materials, the total volumetric expansion is distributed unequally among the three axes.

2.2.6.5 The Volumetric Thermal Expansion Coefficient for Solids

If we ignore the effects of pressure on the material, the volumetric thermal expansion coefficient can be written by[14]:

$$\alpha_V = \frac{1}{V}\frac{dV}{dT}, \quad \text{……..……..……..…….……} \quad (2.48)$$

where V is the volume of the material, and dV/dT is the rate of change of that volume with temperature.

The coefficient of thermal expansion is a rock property. The volumetric thermal expansion coefficients are normally in the range 2.8-6.7 E-6/˚F (5-12 E-6/˚C), regardless of whether the rock is sand, shale, carbonate, granite, or basalt. Thermal expansion values are temperature dependent, and they increase slightly as temperature increases. Table 2.4 shows typical values of rock volumetric thermal expansions.

TABLE 2.4—TYPICAL VALUES OF ROCK VOLUMETRIC THERMAL EXPANSION

Rock	Thermal Expansion Coefficient, (1/˚C)	Thermal Expansion Coefficient, (1/˚F)
Granite	7-9 E-6	4-5 E-6
Basalt	6-8 E-6	3.3-4.4 E-6
Limestone	6 E-6	3.3 E-6
Dolomite	7-10 E-6	4-5.5 E-6
Sandstone	11-12 E-6	6.1-6.7 E-6
Quartzite	11-13 E-6	6.1-7.2 E-6
Marble	4-7 E-6	2.2-4 E-6

2.2.6.6 The General Volumetric Thermal Expansion Coefficient

In the general case of a gas, liquid, or solid, the coefficient of thermal expansion is given by[14]:

$$\alpha = \frac{1}{V}\left(\frac{\partial V}{\partial T}\right)_p \quad \text{……..……..……..……..……..……} \qquad (2.49)$$

The subscript p indicates that the pressure is constant during the expansion. In the case of a gas, the fact that the pressure is held constant is important, because the volume of a gas changes with changes in pressure.

2.3 Failure Criteria in Set - Cements

Cement slurries need to be able to withstand the wellbore stresses during the life of well. Set cement failure occurs when cracks or discontinuities come out in the matrix. Fig. 2.3 shows that a sample can have a brittle or ductile failure. A brittle failure means that the cement fails in the elastic section of the stress-strain deformation curve, and cracks initiate and propagate quickly. Set cements are brittle in tension under impact loading, and triaxial tests are brittle under low confining pressure. Ductile failure occurs in the plastic zone, and permanent deformation is created. Ductile failure is common in flexible cements at high confining pressure.[12]

When a true triaxial state of stress $(\sigma_1 \geq \sigma_2 \geq \sigma_3)$ is considered in the principal coordinate system, the major principal stress (σ_1) leading to compressive failure is a function of the two other principal stresses: intermediate stress (σ_2) and minimum horizontal stress (σ_3). This condition takes the form[4]:

$$\sigma_1 = f(\sigma_2, \sigma_3) \quad \text{.....(2.50)}$$

This relation is called a *failure criterion*, and the function f represents the strength characteristic of the material.

Many empirical criteria have been developed to predict failure in rocks, and they have been applied to set cements. The physical interpretation of these criteria must be known to apply them for specific problems associated with rock mechanics. In general, failure criteria are used to generate a failure envelope that usually separates the stable and unstable zones.

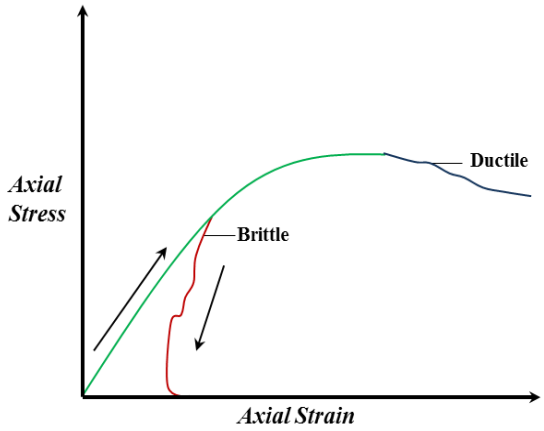

Fig. 2.3—Brittle versus ductile failure (from Ref. 12)

2.3.1 Mohr-Coulomb Failure Criterion

The Mohr-Coulomb failure criterion is the most popular failure criterion used in rocks and set cements, and it is based on the assumption that the yield phenomenon is frictional in nature; that is, the shear stress tending to cause shear yield on a plane in the rock is resisted by cohesion plus the product of a friction coefficient and the normal stress acting on the yield plane. The Mohr-Coulomb criterion ignores the influence of the intermediate principal stress, σ_2, and this criterion can be expressed in two different forms: the shear stress τ as a function of the normal stress σ_1, and maximum normal stress σ_1 as a function of the confining pressure σ_3.[4]

$$\tau = S_O + \mu_f \sigma \text{, or} \quad \text{.....} \quad (2.51)$$

$$\sigma_1 = UCS + \sigma_3 \tan^2\left(45° + \frac{\phi_f}{2}\right), \quad \text{.....} \quad (2.52)$$

where S_o is a constant which may be regarded as the inherent shear strength cohesion of the material at zero confining pressure. By analogy with ordinary sliding, the constant μ_f is called the coefficient of internal friction of the material. The angle of internal friction,

ϕ_f, is related to μ_f by the equation $\mu_f = \tan\phi_f$. UCS is the unconfined compressive strength. The relations between S_o, μ_f, ϕ_f, and *UCS* are:

$$\tan\left(45° + \frac{\phi_f}{2}\right) = \sqrt{1+\mu_f{}^2} + \mu_f = \frac{1+\sin\phi_f}{1-\sin\phi_f}. \quad \text{.....} \quad (2.53)$$

$$UCS = 2S_o \tan\left(45° + \frac{\phi_f}{2}\right). \quad \text{.....} \quad (2.54)$$

$$\mu_f = \tan\phi_f. \quad \text{.....} \quad (2.55)$$

In Fig. 2.4, σ-τ coordinates below the Mohr-Coulomb straight line represent stable conditions, σ-τ coordinates on the Mohr-Coulomb straight line represent limiting equilibrium, and σ-τ coordinates above the Mohr-Coulomb straight line represent unstable conditions.[16]

The hypothesis of this criterion is that the intermediate principal stress, σ_2, has no influence on rock or set cement failure; that is, the maximum shear stress $\tau_{max}=(\sigma_1-\sigma_3)/2$ is a dominant factor in the failure. Mohr-Coulomb parameters can be gotten from triaxial tests.

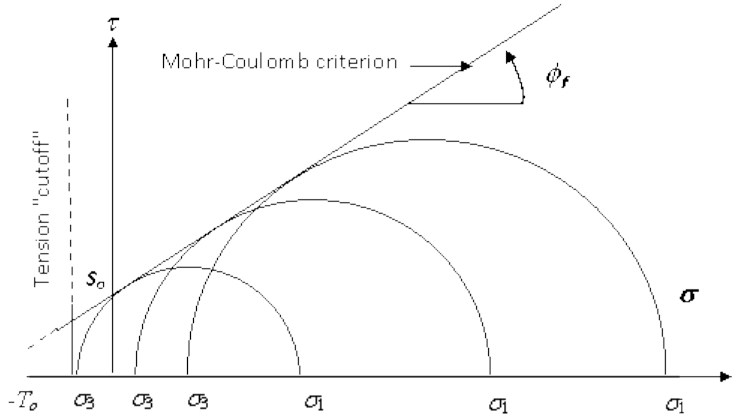

Fig. 2.4—The Mohr-Coulomb failure criterion with a tension cutoff (after Ref. 16)

A uniaxial core test is an unconfined test in which a force is applied parallel to the axis of the core sample. No lateral forces are applied and therefore the sample is unconfined. The magnitude of applied stress is increased until the sample reaches failure. The stress at failure is the unconfined compressive strength (UCS), which is a measure of a sample's strength expressed as the amount of stress it can withstand (when unconfined laterally) without failing. This test also yields data for Young's modulus and Poisson's ratio.

The triaxial core test is a confined test that measures strength at different levels of confining pressure. Axial and confining pressures are applied to the sample and are increased simultaneously until the desired test pressure is reached. The confining pressure is then held constant while the axial pressure is increased until the sample fails. This test yields confining compressive strength (CCS). Multiple confining core tests are used to determine cohesion and the angle of friction of the sample. Fig. 2.5 shows a typical tri-axial test result.

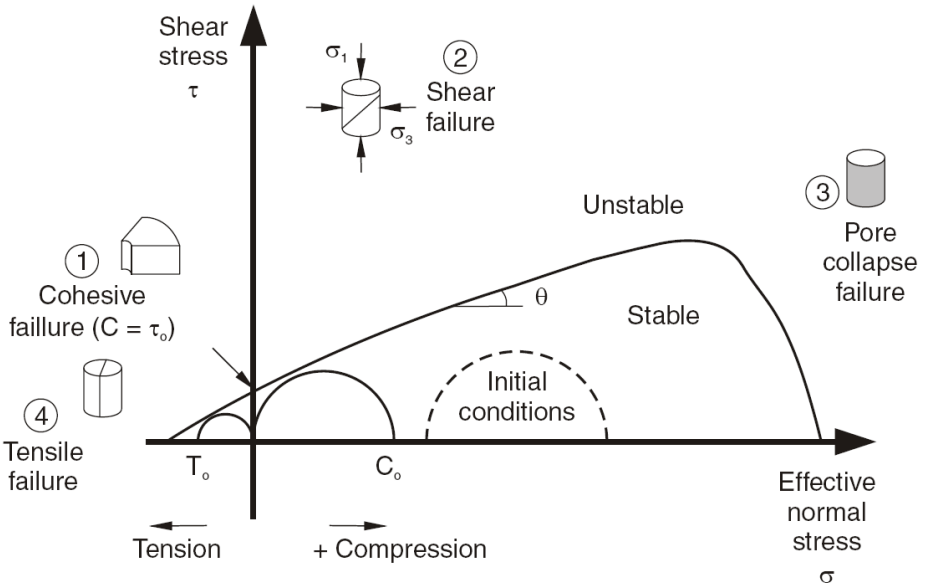

Fig. 2.5—A typical triaxial test result (from Ref. 17)

2.3.2 Mohr-Coulomb Plasticity

The Mohr–Coulomb yield surface is often used to model the plastic flow of geomaterials. Many such materials show dilatational behavior under triaxial states of stress, which the Mohr–Coulomb model does not include. Also, since the yield surface has corners, it may be inconvenient to use the original Mohr–Coulomb model to determine the direction of plastic flow as defined in the flow theory of plasticity.

A common approach used is a nonassociated plastic flow. An example of such a potential is the function given by[18]:

$$g = \sqrt{\left(\alpha c_y \tan\psi_d\right)^2 + G^2\left(\phi,\theta\right)q^2} - p\tan\phi\,, \quad \text{.....} \qquad (2.56)$$

where α is a parameter, c_y is the value of c when the plastic strain is zero (also called the initial cohesion yield stress), ψ_d is the angle made by the yield surface in the Rendulic plane at high values of p (this angle is also called the dilation angle), and G (φ, θ) is an appropriate function that is also smooth in the deviatoric stress plane.

The Mohr-Coulomb plasticity model[13]:

- is used to model materials with the classical Mohr-Coloumb yield criterion
- allows the material to harden and/or soften isotropically
- uses a smooth flow potential that has a hyperbolic shape in the meridional stress plane and a piecewise elliptic shape in the deviatoric stress plane
- is used with the linear elastic material model
- can be used for design applications in the geotechnical engineering area to simulate material response under essentially monotonic loading

2.3.3 Tensile Failure Criterion

The criterion for tensile failure initiation is simply determined by whether the minimum effective principal stress, σ_3, equals the negative of the uniaxial tensile strength, T_o[4]:

$$\sigma_3 = -T_o \quad \text{.....} \quad (2.57)$$

In this criterion the material is assumed to fail by brittle fracture. The Griffith criterion predicts that tensile strength is equal to the unconfined compressive strength divided by a factor from 8 to 12, but some measurements indicate ratios are greater than 100.[4]

2.4 Fracture Mechanics

Fracture mechanics is the discipline of solid mechanics that studies the behavior of cracked bodies subjected to stresses and strains. There are two primary modes of fracture: brittle and ductile.

The characteristics of brittle fracture are that cracks spread very rapidly with little or no plastic deformation, and cracks that initiate in a brittle material tend to continue to increase in size provided the loading will cause crack growth.

Ductile fractures go through three stages: void nucleation, growth, and coalescence. Also, the crack moves slowly and is accompanied by a large amount of plastic deformation. Furthermore, the crack typically will not grow unless the applied load is increased. A ductile fracture has a dimpled, cup-and-cone fracture appearance, and ductile fracture surfaces have larger necking regions and an overall rougher appearance than a brittle fracture surface.

The most common theories to predict the fractures are linear element fracture mechanics, cohesive zone models and elastic plastic fracture mechanics. Linear elastic fracture mechanics (LEFM) considers three distinct fracture modes: Modes I, II, and III. In the fracture Mode I of linear elastic fracture mechanics, the forces are perpendicular to the crack, pulling the crack open. In fracture Mode II, the forces are parallel to the crack: one force pushes the top half of the crack back and the other pulls the bottom half of the crack forward, both along the same line. This creates a shear crack, and the forces do not cause out-of-plane deformation. In fracture Mode III, the forces are transverse to

the crack, and this causes the material to separate and slide along itself, moving out of its original plane. Fig. 2.6 shows fracture Modes I, II II.

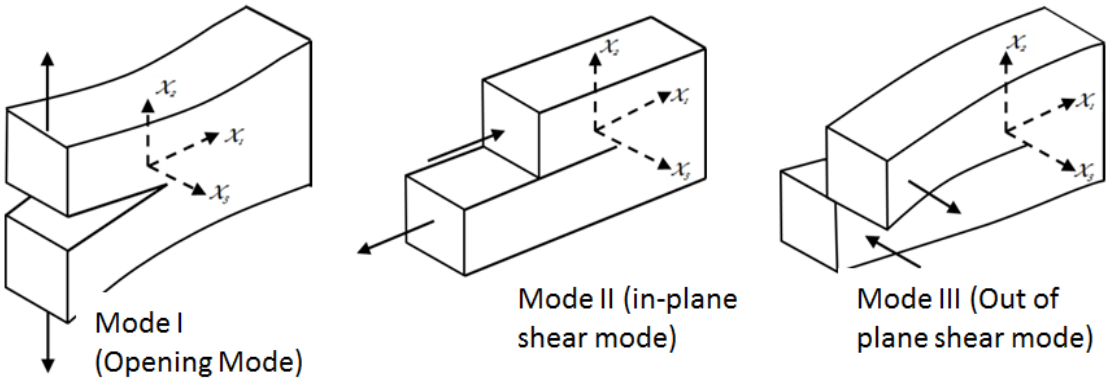

Fig. 2.6—Fracture modes (from Ref. 19)

The stress intensity factor (K_I) is a parameter that characterizes the local crack-tip stress field in the isotropic and linear elastic (brittle) materials. K_I characterizes the influence of load or deformation on the magnitude of the crack-tip stress and strain fields and measures the propensity for crack propagation or the crack driving forces. The stress intensity factor is used to predict the stress state ("stress intensity") near the tip of a crack, and when this value becomes critical, a small crack grows and the material fails.

This critical value is denoted K_C and is known as the fracture toughness, a material property. The stress-intensity factor relates the local crack-tip fields with the global aspects of the problem. Fracture toughness is strongly dependent on temperature, specimen thickness and crack extension. Fig. 2.7 shows fracture toughness as a function of crack extension, called the *resistance curve*. The variation in fracture toughness with crack growth is $K_R(\Delta a)$, and $K_R(0) = K_C$, where Δa is the crack length and K_C is the fracture toughness, psi×in$^{0.5}$ [Pa×m$^{0.5}$].

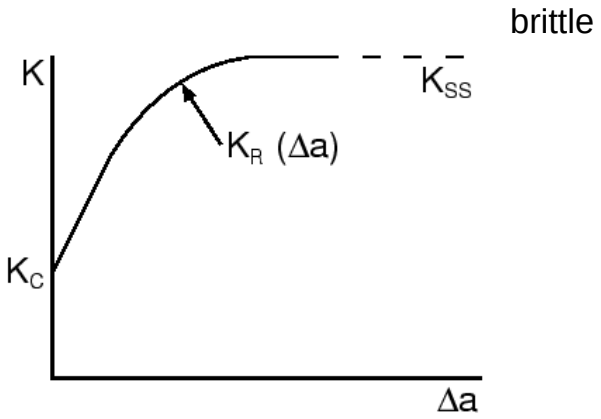

Fig. 2.7—Intensity factor vs. crack length (from Ref. 19)

2.5 Evaluation of Rock Mechanical Properties

The material properties include strength parameters such as effective angle of internal friction, effective cohesion, and tensile strength, and physical properties such as Young's modulus and Poison ratio.

Normally it is very difficult to have lab tests of rock mechanical properties for the whole well, so dynamic elastic properties of rock can be calculated from wireline log data and then compared with static elastic properties determined in the laboratory. This is particularly useful because the dynamic Young's modulus, which is a measure of the stiffness of rock under dynamic loading conditions, is correlated with rock strength. This mathematical correlation allows computing a continuous profile of mechanical properties over any interval for which the appropriate data are available.

The dynamic Young's modulus (E_D) can be calculated from the sonic log data and bulk density (ρ_b) log data using the following expression (included in Table 2.2):

$$\nu = \frac{0.5\left(t_s/t_c\right)^2 - 1}{\left(t_s/t_c\right)^2 - 1}, \quad \text{.....} \quad (2.58)$$

$$G = 1.347 \times 10^{10} \frac{\rho_b}{t_s^2}, \text{ and} \quad \text{.....} \quad (2.59)$$

$$E_D = 2G(1+\nu), \quad \text{.....} \quad (2.60)$$

where ν is Poisson's ratio, E_D is the dynamic Young's modulus with units of psi, G is the shear modulus with units of psi, ρ_b is the bulk density with units of g/cm^3, and t_s is the shear-wave transit time with units of μs/ft .

Determining the dynamic Young's modulus from sonic waves usually requires accurate measurements of the compressional wave transit time, shear-wave transit time, and bulk density.

If the compressional wave velocity and the formation bulk density are known from density logs, but the shear wave velocity is unknown, an estimate for the dynamic Young's modulus can be made by using[20]

$$E_D = \frac{1.13 \times 10^4 \rho_b}{t_c^2}, \quad \text{.....} \quad (2.61)$$

where E_D is the dynamic Young's modulus expressed in units of E+6 psi, ρ_b is the formation bulk density with units of g/cm^3, and t_c is the compressional wave transit time with units of μs/ft. Eq. 2.61 implies that E_D is little dependent on Poisson's ratio, ν.

The compressional wave velocity alone can be used in sonic logs to estimate the dynamic Young's modulus[20]:

$$E_D = 0.265 V_P^{2.04}, \quad \text{.....} \quad (2.62)$$

where E_D is the dynamic modulus with units of E+6 psi and V_P is the compressional wave velocity with units of km/s. Eq. 2.62 implies that E_D depends basically on V_p.

Once the dynamic Young's modulus *(E_D)* is known, the static Young's modulus *(E_S)* for sandstones can be estimated by[20, 21]

$$E_S = 0.0293E_D^2 + 0.4533E_D \text{ or} \quad \text{.....} \quad (2.63)$$

$$E_S = 10(A_o + A_1 \log E_D). \quad \text{.....} \quad (2.64)$$

In Eq. 2.63 E_D and E_S are expressed in units of E+6 psi. In Eq. 2.64 E_D and E_S are in units of psi and the values of A_o and A_1 (listed on Table 2.5) depend on the porosity of the sandstone.

A similar correlation exists for shales[20]:

$$E_S = 0.0428E_D^2 + 0.2334E_D, \quad \text{.....} \quad (2.65)$$

where E_D and E_S are expressed in units of E+6 psi.

TABLE 2.5. A_O AND A_1 VALUES IN EQ. 2.61 (FROM REF. 21)

Porosity	Ao	A_1
10% to 15%	2.137	0.6612
15% to 25%	1.829	0.6920
>25%	-0.4575	0.9402

Correlations of unconfined compressive strength, *UCS*, are given by[20, 6]

$$UCS = 0.2787E_S^2 + 2.458E_S \text{ and} \quad \text{.....} \quad (2.66)$$

$$UCS = 3.3\times10^{-20}\rho_b^2 V_P^4 \left(\frac{1+\nu}{1-\nu}\right)^2 (1-2\nu)(1+0.78V_{sh}). \quad \text{.....} \quad (2.67)$$

In Eq. 2.66 *UCS* is the unconfined compressive strength expressed in units of kpsi and E_S is the static Young's modulus with units of E+6 psi. In Eq. 2.67 *UCS* is in

units of Mpa, ρ_b is bulk density in units of kg/m^3, V_p is the compressional wave velocity expressed in units of m/s, ν is Poisson's ratio, and V_{sh} is the fraction of shale in the sandstone.

Eq. 2.67 implies that the unconfined compressive strength *(UCS)* is relatively little dependent on ν, and the important factor is $\rho_b^2 V_p^4$, and in particular the compressional wave velocity.

2.6 Brazilian Tests

The Brazilian (indirect tension) test is the most widely used method to obtain the tensile strength of rocks. Hydraulic fracture of a rock or set cement is related to in-situ stresses and tensile strength of the materials. The Brazilian tension test applies a compressional load to a circular disc shape specimen placed between two platens, producing a nearly uniform tensile stress distribution normal to the load, leading to the failure of the disk by splitting. Tensile strength, *To*, is determined from the maximum load recorded before the first load drop in the test, *P*, and the specimen length and diameter, *L* and *D*, by the elastic theory[12]:

$$T_O = \frac{2P}{\pi LD} \quad \text{.....} \quad (2.68)$$

where *P* is the load at failure with units of lbf, *L* is the length of the specimen with units of inches, *D* is the diameter of the test specimen with units of inches, *To* is the tensile strength with units of psi.

The International Society of Rock Mechanics suggests that samples for the Brazilian tests have a length-to-diameter ratio of at least 0.5, and the difference can be 12%. According to the standard Brazilian test, the arc in degree of the contact area is approximately 10˚. In addition, the rock cylinder is assumed to be homogeneous, linear elastic, and isotropic. It is important to stop the test as soon as possible after the fracture happens to examine the form of the break. If the test is not stopped immediately after the

break, then additional failure may be observed if the sample remains between the platens.

The tensile strength can increase slightly with the temperature, and it is attributed to the ductile behavior of the set cement or rock at high temperature due to an increase in resistance against deformation.[4] Brazilian tests are performed to determine tensile strength and the triaxial compression tests are performed to determine elastic modulus and compressive strength of set cement or rock. Tensile strength frequently has values from 1/8 to 1/12 the unconfined compressive strength, UCS.[4]

2.7 Cement-Formation Bonding

Cementing recommendations are frequently based on the compressive or tensile strength of set cement. The assumption is that a material satisfying certain strength requirements will provide an adequate bond to the casing and formation. Field and laboratory experience has shown that this assumption is not always valid.[12]

In a wellbore, shear bond and hydraulic bond are two criteria often considered for effective zonal isolation along the cement/casing and cement/formation interfaces. Shear bonding mechanically supports the pipe in the hole and is determined by measuring the force required to initiate pipe movement in a cement sheath. Shear bond strength is given by:

$$\delta = \frac{P}{A} \quad \text{.....} \quad (2.69)$$

where δ is shear bond strength (psi), P is load at failure (pounds), and A is contact area (square inches).

Hydraulic bonding blocks the migration of fluids in a cemented annulus. It is usually measured by applying pressure at the pipe/cement or pipe/formation interface until leakage occurs. For zonal isolation, hydraulic bonding is more important than shear bonding. Fig. 2.8 shows hydraulic bonding to pipe and formation.

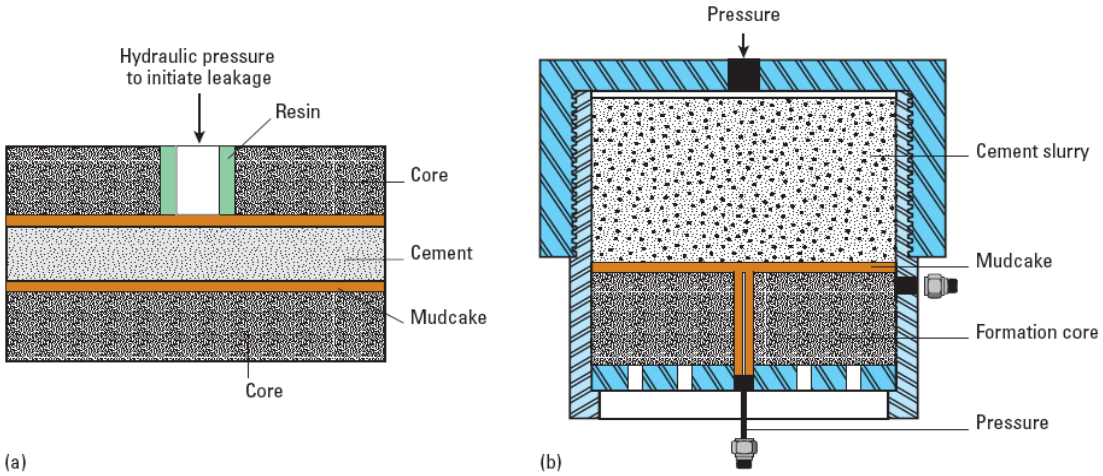

Fig. 2.8—Hydraulic bonding to pipe (a) and formation (b) (from Ref. 12)

CHAPTER III

FINITE AND EXTENDED FINITE-ELEMENT ANALYSIS AND CEMENT FAILURE IN OIL WELLS

This chapter gives a theoretical background for finite-element analysis (FEA), extended finite-element analysis (XFEA), and an explanation of how set cement can fail in oil wells, especially in HPHT wells. It also describes some of how the Abaqus model was built to simulate cement sheath behavior.

3.1 Finite-Element Method

Physical phenomena can be described in terms of partial-differential equations, but solving these equations by classical analytical methods for arbitrary shapes is very complex. The finite-element method (FEM), which was developed in the 1950s for the aerospace industry, is a numerical approach by which these partial differential equations can be solved approximately. FEA can solve petroleum engineering problems that involve stress and strain analysis, heat transfer, electric and magnetic fields, lubrication, fluid flow, and many other problems.

The methodology of FEA is to divide the body into finite elements, often just called *elements*, connected by nodes to get an approximate solution with great value from an engineering standpoint. The FEM consists of the following steps:

- Preprocessing. The arbitrary shape is divided into finite elements.
- Element formulation. In this step the equations for the elements are developed according to the properties of the element.
- Assembly. The equations for the entire system are obtained from the equations of the individual elements.
- Solving the equations.
- Post processing: The results of finite-element analysis are shown as strains, stresses, temperatures, cracks, etc.

Finite-element analysis allows predicting the impact of diverse loads and temperatures of the well in the cement sheath during the life of the well. This approach is valuable to optimize the mechanical and expansion characteristics of set cements, and the information is used to investigate and select the slurry additives.

Abaqus, finite-element software, was used in this study to understand and predict the cement sheath behavior. Abaqus is a highly sophisticated, general purpose FEA code developed to solve nonlinear stress problems like plasticity or contact conditions. The plasticity of the rock or cement can be a cause of lack of inner or outer microannuli. (A microannulus is a gap less than 200 microns; a wider gap is called a cement channel. Gas can migrate out of the designed flow zone in a gap of 70 microns and oil in a gap of 200 microns).

The FEM was built in the reservoir section to understand the long-term effect on the cement sheath of all load conditions during the life of the well, including thermal and pressure changes during drilling, completion, hydraulic fracturing, and production. The FEA in this study includes the following steps:

- Drilling. Removal of rock for the drill bit generates stresses around the borehole. The formation is under a three-dimensional state of stress: overburden and minimum and maximum horizontal stresses. The drilling fluid causes a hydrostatic pressure in the deformed borehole. Borehole stability analysis was used model the final shape and size of the borehole.
- Cementing. The casing is run in the borehole; the casing should be centralized with a minimum 70% standoff. Prefluxes and spacers were pumped before the cement slurry to remove the filter cake and the drilling fluid. Pipe movement, right centralization, and fluid density hierarchy were required to improve mud removal during cementing operations.
- Hardening. During this step the cement slurry become solid cement. The pressure inside the casing is equal to the drilling fluid pressure or completion fluid pressure. The casing contracts because of the pressure difference inside and outside of the casing. The inner microannulus, between the casing and

cement, can result from variations in wellbore pressure during the hardening process.

- Shrinkage. During cement setting, the cement can reduce its volume as it hydrates. The cement shrinkage or expansion depends on the chemical composition and temperature of the cement slurry, and conventional cements shrink from 0.5% to 7%.[22, 23] If water is freely available during the cement hydration phase, the cement won't shrink or it will shrink partially. In the case of foam cements, the shrinkage can also be compensated for by an internal source such as well-dispersed gas bubbles inside the cement so that the gas will expand to occupy the reduced volume.[3] Most of the total bulk shrinkage takes place 8 to 24 hrs from time the cement slurry is mixed.[24]
- Completion. The drilling fluid located inside the casing is replaced by the completion fluid. The hydrostatic pressure inside the casing depends on the completion fluid density. There is a chance that an inner microannulus could be created as a result of contraction of the casing when heavier drilling fluid is changed by a lighter completion fluid after cement setting.
- Hydraulic fracturing. After drilling the well, it is necessary to evaluate the necessity to fracture the well to increase its production. Not all wells require hydraulic fracturing to have the expected production. During a hydraulic job, a high pressure builds inside the casing to fracture the formation, and the casing tends to expand, pushing on the cement and formation. The fracture pressure of the formation depends mainly on total in-situ stresses and tensile strength of the rock. Fracture pressure could cause plastic deformation, shear deterioration, or cracking of the cement or rock due to pressure loading, which may come from well sections different from perforated zones.
- Production. The amount of pressure inside the casing will depend essentially on the formation pressure. The formation pressure and pressure inside the casing change with production time and behavior of reservoir. The casing tends to contract, causing an inner microannulus.

3.2 Extended Finite-Element Method (XFEM)

The extended finite-element was introduced by Belytschko and Black based on the partition of unity method of Babuska and Melenk.[25] XFEM can be used where conventional FEM fails or it is computationally expensive, like in wells with cracks and debonding of the cement sheath.

A numerical XFEM is constructed by dividing the model into two parts. The first part generates a mesh for the domain geometry (neglecting the existence of any cracks or other discontinuities) and the other part reaches the finite-element approximation by "enrichment functions." Local enrichment functions are added to the finite-element shape functions, which allow the approximated field and its derivates to be discontinuous within an element. So a domain can be modeled by finite-elements without explicitly meshing discontinuities.

The crack definition is trouble-free because the mesh of the part is independent of the crack; it is not necessary to specify the crack initiation and the propagation path. Furthermore, the convergence rate is improved for the finite-element solution, and it can be used for nonlinear material and nonlinear geometric analysis.

The enrichment functions for fracture modeling use the Heaviside and branch functions. The Heaviside function represents the displacement jump across the crack-face and crack-tip asymptotic function to model singularity. The Heaviside function is applied to elements entirely cut by a fracture and is given by Eq. 3.1[13]:

$$H(x) = \begin{cases} 1 & \text{if } (\boldsymbol{x} - \boldsymbol{x}^*) \cdot \boldsymbol{n} \geq 0 \\ -1 & \text{otherwise} \end{cases} \quad \text{……..……...…..……..} \qquad (3.1)$$

where $\boldsymbol{x}$ is an integration point, $\boldsymbol{x}^*$ is the closest point to $\boldsymbol{x}$ on the crack face and $\boldsymbol{n}$ is the unit normal at $\boldsymbol{x}^*$. Fig. 3.1 explains the Heaviside function.

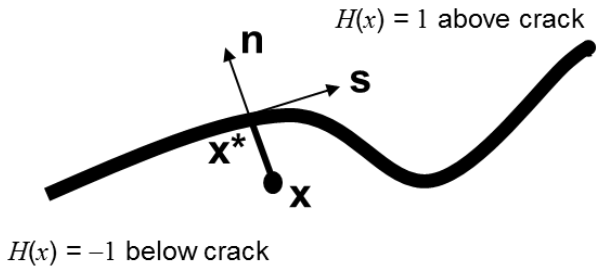

Fig. 3.1—Heaviside function (from Ref. 13)

The branch functions are used to enrich elements that contain fracture tips and are given by Eq. 3.2. The branch functions account for crack-tip singularity, and they use displacement field basis functions for sharp cracks in an isotropic, linear-elastic material.

$$\left(F_\alpha(x)\right)_{\alpha=1}^{4} = \left(\sqrt{\mathrm{r}}\sin\frac{\theta}{2},\ \sqrt{\mathrm{r}}\cos\frac{\theta}{2},\ \sqrt{\mathrm{r}}\sin\theta\sin\frac{\theta}{2},\ \sqrt{\mathrm{r}}\sin\theta\cos\frac{\theta}{2}\right) \quad \text{……..…....} \qquad (3.2)$$

where (r, θ) denote coordinate values from a polar coordinate system located at the crack tip, and θ=0 is tangent to the crack at the tip.

These functions span the asymptotic crack-tip function of elastostatics, and the term $\sqrt{r}\sin\frac{\theta}{2}$ takes into account the discontinuity across the crack face. The use of asymptotic crack-tip functions is not restricted to crack modeling in an isotropic elastic material. The same approach can be used to represent a crack along a two-material interface, affecting the interface, or in an elastic/plastic power law hardening material.[13] Fig. 3.2 shows the coordinate configuration front enrichment functions in two dimensions.

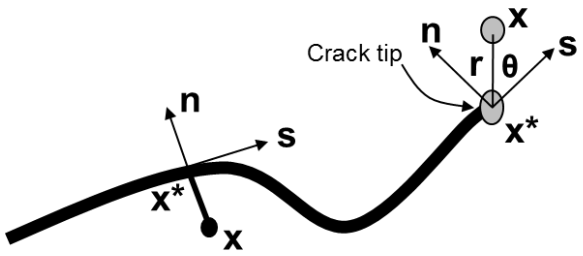

Fig. 3.2—Normal and tangential coordinates for a smooth crack (from Ref.13)

The addition of these enrichments results in the following displacement field within a fracture domain as described in Eq. 3.3.[13]

$$u^h(x) = \sum_{I \in N} N_I(x) \left[u_I + \underbrace{H(x) a_I}_{I \in N_\Gamma} + \underbrace{\sum_{\alpha=1}^{4} F_\alpha(x) b_I^\alpha}_{I \in N_\Lambda} \right] \quad \text{.....} \qquad (3.3)$$

where N is the set of nodes, $H(x)$ is the Heaviside function, and combinations of α, b, and I provide degrees of freedom.

3.2.1 Modeling Cracks with the Phantom Node Approach (Crack Propagation Implementation) in Extended Finite Elements

This approach was introduced by Belytschko and et al. [25]This method does not include the asymptotic crack-tip enrichment functions and the discontinuous element with Heaviside enrichment is treated as a superposition of two continuous elements with phantom nodes.

The cracked element splits into two parts when the element is cut by the crack. Each part is formed by a combination of some real and phantom nodes depending on the orientation of the crack. Each phantom node and its corresponding real node are no longer tied together and can move apart. Fig. 3.3 shows the phantom node method.

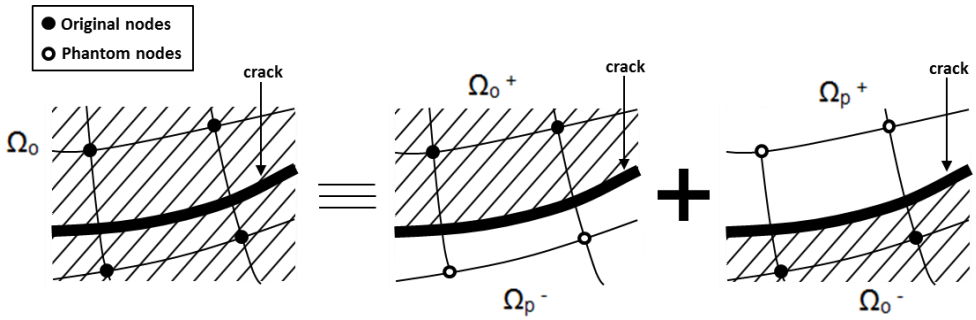

Fig. 3.3—The principle of the phantom node method (from Ref. 13)

The magnitude of the separation is governed by the cohesive law until the cohesive strength of the cracked element is zero, after which the phantom and the real nodes move independently. To have a set of full interpolation bases, the part of the cracked element that belongs in the real domain, Ω_0, is extended to the phantom domain, Ω_p. Then the displacement in the real domain, Ω_0, can be interpolated by using the degrees of freedom for the nodes in the phantom domain, Ω_p. The jump in the displacement field is realized by simply integrating only over the area from the side of the real nodes up to the crack; i.e., Ω_0^+ and Ω_0^-.[13]

3.2.2 Level Set Method for Locating a Crack in Extended Finite Elements

The level set method is useful for the description of crack geometry, because it fits naturally with the XFEM and makes it possible to model arbitrary crack growth without remeshing. A level set (also called level surface or isosurface) of a real-valued function is the set of all points at which the function attains a specified value.

Two functions, Φ and Ψ, are used to completely describe the crack. The level set $\Phi = 0$ represents the crack face, and the intersection of level sets $\Phi = 0$ and $\Psi = 0$ denotes the crack front. The function values need to be specified only at nodes belonging to elements cut by the crack. No explicit representation of the boundaries or interfaces is needed because they are entirely described by the nodal data. Two signed distance functions per node are generally required to describe the crack geometry.

The nodal value of the function Φ is the signed distance of the node from the crack face, and is positive on one side of the crack face, negative on the other. The nodal value of the function Ψ is the signed distance of the node from an almost-orthogonal surface passing through the crack front. The function Ψ has zero value on this surface and is negative on the side towards the crack. Fig. 3.4 represents a crack in two dimensions by the two sig ned distance functions, Ψ and Φ.

Node	Φ	Ψ
1	+0.25	−1.5
2	+0.25	−1.0
3	−0.25	−1.5
4	−0.25	−1.0

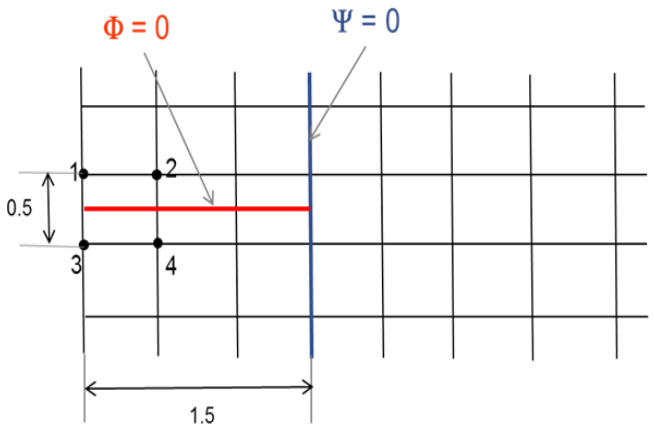

Fig. 3.4—Representation of a crack in two dimensions by two signed distance functions Ψ and Φ (from Ref. 19)

3.2.3 Damage Modeling

Damage modeling allows the degradation and failure of an enriched element. The failure mechanism consists of a damage initiation criterion and a damage evolution law. The initial response is assumed to be linear, but it is possible to define the damage evolution law. Damage modeling is achieved through the use of a traction-separation law across the fracture surface.

Fig. 3.5 describes a typical linear and a typical nonlinear traction-separation response with a failure mechanism. The enriched elements do not undergo damage under pure compression.

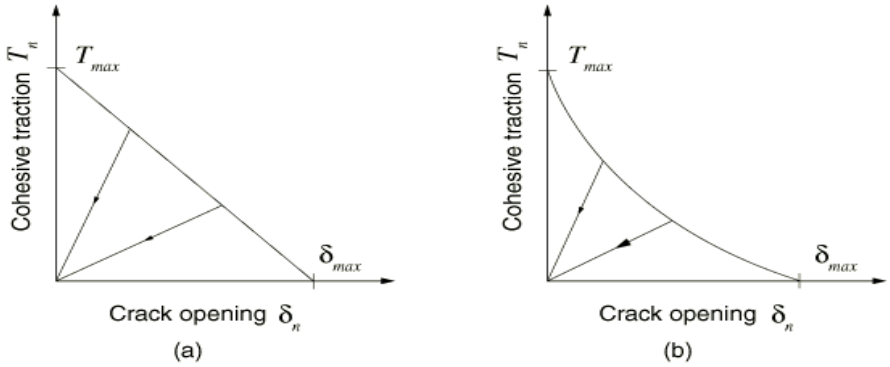

Fig. 3.5—Typical linear (a) and nonlinear (b) traction-separation response (from Ref. 13)

3.2.4 Crack Initiation and Direction of Crack Extension in Extended Finite Elements

XFEM uses two damage initiation criteria: the maximum principal stress criterion (MAXPS) and the maximum principal strain criterion (MAXPE). The crack initiation happens when the maximum principal stress or the maximum principal strain reaches its critical value. The crack plane is perpendicular to the direction of the maximum principal stress or strain. The damage initiation criterion is satisfied when $1.0 \leq f \leq 1.0 + f_{tol}$ where f is the selected damage criterion and f_{tol} is a user-specified tolerance value.

The maximum principal stress criterion is represented by Eq. 3.4:

$$f = \left\{ \frac{\langle \sigma_{max} \rangle}{\sigma^0_{max}} \right\} \quad \text{.....} \qquad (3.4)$$

σ^0_{max} represents the maximum principal stress. The symbol $\langle\ \rangle$ represents the Macaulay bracket. The Macaulay brackets, which are used to show that a purely compressive stress state does not initiate damage. Damage is assumed to initiate when the maximum principal stress ratio (as defined in the expression above) reaches a value of one.

The maximum principal strain criterion can be represented by Eq. 3.5:

$$f = \left[\frac{\langle \varepsilon_{\max} \rangle}{\varepsilon_{\max}^{0}} \right] \quad \text{.....} \qquad (3.5)$$

where, $\varepsilon_{\max}^{0}$ represents the maximum principal strain, and the Macaulay brackets signify that a purely compressive strain does not initiate damage. Damage is assumed to initiate when the maximum principal strain ratio reaches a value of one.

3.3 Cement Fatigue in Oil Wells

Mechanical properties of cement behind the casing are important for the success of a well during its productive life and abandonment, especially when wells are drilled in high pressure and high temperature (HPHT) conditions. HPHT conditions are formally defined as an undisturbed bottomhole temperature greater than 300°F (149°C) and the maximum anticipated pore pressure of any porous formation to be drilled through exceeds 0.8 psi/ft (~15.3 ppg) or requiring a BOP with a rating in excess of 10,000 psi (68.95 MPa).

Zonal isolation must continue not only during the full life of the well but also after its abandonment. The consequences of cement sheath failure include production and safety loss, environmental damage, additional remedial jobs, well shutdown to comply with government regulations, and even loss of the well.

During the lifetime of a well, operational events can damage cement sheath or cause cement debonding. Hydraulic fracturing, thermal cycling, pressure testing, or high drawdown for production can lead to radial fractures or debonding of the cement by plastic deformations of the cement and/or rock. The cement must be designed to withstand the changing conditions during the life of the well, including its abandonment.

The data required for the FEA includes the elastic, plastic, and thermal properties of the cement and formation. The common cement sheath and rock properties are Young's modulus, Poisson's ratio, compressive strength, cohesion, friction angle, tensile strength, dilatancy angle, the effective volume change from cement hydration, porosity,

and permeability. Also, it is important to be acquainted with casing properties like the thickness and elastic and thermal properties of the steel.

Designing the cement slurry or determining the main cause of the cement sheath failure requires knowledge of the operational details of drilling, casing centralization, completion, stimulation, production, and formation in-situ stresses. Cement shrinkage, plastic deformations, debonding, and cement fractures are the main failures of set cements.

An effective design of the slurry and well geometry can help to mitigate inner or outer microannulus and cement fractures. Debonding, cement sheath cracks, or plastic (permanent) deformation of the cement or formation could initiate the failure of the cement seal.

Underground gas storage (UGS) wells need cement to provide a long-term isolation that can guarantee safe operations during injection or production cycles. Underground gas storage wells can be drilled in salt formations, porous rock with depleted hydrocarbons reservoirs, or abandoned mines.

High temperature wells or SAGD fields or steam-injection wells need a particular analysis because the wells heat up and cool down during steam cycling. When the borehole heats up, the casing expands, and it could crack the cement. Borehole cooling could originate inner or outer microannuli due to debonding of the cement.

The cement and formation could deform plastically (permanently) during high-pressure tests or hydraulic-fracturing jobs. This plastic deformation could also create inner or outer microannuli. The elastic and plastic properties of the cement could be different, and these differences weaken the cement so that it cannot withstand the loads that generate cracks in the cement, plastic deformations, or debonding.

Cracking of the cement sheath and plastic deformations could cause radial and vertical fluid migration, especially in gas reservoirs with their high-mobility conditions. Cement shrinkage is caused by external volume reduction, which occurs during the cement hydration process. Cement shrinkage and plastic deformation are normally the main cause of debonding the cement/casing or cement/formation. This cement shrinkage

or plastic debonding may originate with vertical fluid migration, which depends on the width of the gap, viscosity of the fluid, and drawdown.

A good design of the cement will avoid remedial cement jobs and reduce the cost of well abandonment. It is sometimes not possible to have successful cement squeezes, because of the difficulty of injecting cement slurry inside the inner and outer microannuli.

3.4 Shrinkage and Cement Expansion

Portland cements experience hydration reactions in the presence of water. The volume of the hydrating components such as water and cement powder is larger than the volume of the hydrated cement. This volume contraction is called *total chemical shrinkage.* The amount of water absorbed by the cement during the hydration is related to the total chemical shrinkage. The total chemical shrinkage resulting in external volume changes of a cement specimen is called *bulk shrinkage*.[22]

The main constituents of Portland cement are C_3S (tri-calcium silicate), C_2S (di-calcium silicate), C_3A (tri-calcium aluminates), and C_4AF (tetra-calcium aluminum-ferrite), of which C_3S is the major component, followed by C_2S. The major hydration products are the rigid calcium-silicate hydrate gel, C-S-H, and calcium hydroxide, $Ca(OH)_2$, which are lower-density (higher-volume) products in relation to C_3S or C_2S. Eqs 3.6 and 3.7 shows the hydration of Portland cement:

$$2(CaO)_3(SiO_2)+7H_2O=(CaO)_3(SiO_2)_2\,4(H_2O)+3Ca(OH)_2 \quad \text{…...……..} \qquad (3.6)$$

$$2(CaO)_2(SiO_2)+5H_2O=(CaO)_3(SiO_2)_2\,4(H_2O)+Ca(OH)_2 \quad \text{…...……....} \qquad (3.7)$$

Portland cement has chemical shrinkage during hydration. Free access to additional water can reduce the bulk shrinkage, and lack of free water may lead to high bulk shrinkage. If the cement contains expanding agents, the shrinkage effect will be superposed by the expansion. The cement expansion can be towards the casing or towards the formation. Expanding cement has the risk of creating an inner microannulus

in the case of unconsolidated formations and cement cracking in hard formations. A cement expansion up to 0.2% can be acceptable to avoid cement cracking.

An inner microannulus can be created by radial displacement of the casing under pressure or temperatures variations. The outer microannulus can be generated by chemical shrinkage of the cement.[26] Expanding cements can only prevent outer microannuli in soft or unconsolidated formations, but the risk of creating an inner microannulus remains. Also, controlled expanding cements are a solution to get a good hydraulic seal in hard rock formations.[22]

Cement expansion can be achieved by the addition of cement-expanding agents like calcium sulfate or sodium sulfate to form ettringite, $(CaO)_6(Al_2O_3)(SO_3)_3 32H_2O$.[27] Other expanding cements contain calcium and magnesium oxide (MgO) [0.25 – 1% BWOC]. The expanding cements do not compensate for microannuli formed once the expansion is completed. The expansion of the cement lasts for days and sometimes weeks, which allows the cement to compensate for changes of mud density during drilling of the next section.

Total chemical shrinkage of the cement is the reduction in volume that occurs during cement hydration, and it has potential detrimental effects in the long-term zonal isolation. Once the cement begins to develop compressive strength, the total chemical shrinkage can happen as bulk shrinkage. Bulk shrinkage is the external volume reduction that can occur during the hydration of Portland cement, and it leads to debonding and microannuli between cement and casing or cement and formation. Also, bulk shrinkage may cause tensile cracks and subsequent increased permeability and reduce tensile strength. This phenomenon leads to annular pressure behind the casing or communication between formations.

Cement slurries have to be designed with enough elasticity and tensile strength to resist internal crack development during hydration. Laboratory results demonstrate the dependence of shrinkage on the shear history of the cement slurry. The cement shrinkage is lower when the slurry has been sheared for a longer time, indicating that part of the shrinkage occurs when the slurry is still in the liquid state.

There are several shrinkage measurement methods, like the flask method, balloon method, ring-mold method, sleeve method, cement hydration analyzer (CHA) and fluid migration analyzer cell (FMA). The CHA is a precision instrument that measures four key aspects of oil-well cement:

- Its susceptibility to gas migration.
- Its degree of hydration.
- Its bulk shrinkage during curing.
- The gas permeability of the cement.

The CHA is a closed system in which nitrogen gas is injected into the bottom of the cement slurry at any time during its hydration or setting. The cement's susceptibility to gas migration is determined if nitrogen gas injection pressure is transmitted up through the column of cement to the top side of the cement sample where the pore pressure is measured. The amount of gas that enters the cell gives an indication of the cement shrinkage.

The flask method, balloon method, and ring-mold methods provide good measurements of shrinkage under ambient conditions. A fluid migration analyzer cell (FMA) is good alternative to measure cement shrinkage under downhole conditions. The balloon method measures the bulk shrinkage of cement, and the flask method measures the chemical shrinkage. A large difference between the two types of shrinkage is related to the cement's internal stresses.[24]

Chemical shrinkage leads to pore pressure reduction and eventual pore collapse when cement has no free access to water, for example, in front of impermeable layers like shale, granite or clay stones. Pore pressure reduction can be so high that it can cause negative pore pressure and pore collapse.

Water is used for the cement hydration, and the cement permeability must be high enough to allow the external fluid to invade the cement's pore structure. The bulk shrinkage can be avoided by maintaining constant pore pressure during the hydration process. During the hardening process, the pressure applied to the formation and casing decreases because the cement turns into a solid. The shrinkage effect can be

compensated by gas bubbles like nitrogen inside the cement, and this is the principle of foam cement.

It is very common to have cement bulk shrinkage between 0.5 and 5%, depending on the temperature and pressure conditions and access to free water. The total volume shrinkage can be a combination of internal and external shrinkage that can result in damage to the cement sheath in the form of tensile cracks (internal shrinkage) or the creation of an inner or outer microannulus (external shrinkage). The top of the cement column can move downwards to compensate for the bulk cement shrinkage, but once the cement has developed enough strength, the volume variation cannot be matched by the same displacement.[23,26,28,29] Results from a sensitivity analysis concluded that the optimum cement design should have no bulk shrinkage and post-set expansion limited to less than1%.[29]

The mechanical and thermo-elastic properties of the cement can be modified to fulfill the borehole conditions to have a good cement sheath. Reinforcement of tensile strength and modifying the thermal properties can reduce the risk of a bad cementing job. A finite-element analysis can determine how stresses can change with time and location at the bottom borehole conditions.

Cement failure occurs when tangential forces exceed bonding forces, tensile strength, and plastic limits. Some of the principal events that could damage the cement sheath include[30]:

- Cement hydration could be a source of cement shrinkage leading to tensile cracking and formation of outer and inner microannuli.
- Pressure and temperature changes during hydrocarbon production, fluid injection, pressure testing, and hydraulic fracturing can cause debonding and cement radial cracking.
- Perforation shock waves and subsequent drilling shock waves can create cement radial cracking.
- Far-field stresses can modify after changing the pressure and temperature of the reservoir.

Failure of the sealing capacity due to radial cracking can create radial and vertical fluid migration. Debonding at the cement/casing interface or cement/formation interface can cause vertical migration depending of the gap, draw down pressure, and viscosity of the migrating fluid. Shear deterioration may allow fluid migration depending on the level of strain failure, drawdown pressure, and migrating fluid viscosity. The cementing companies can develop a cement sheath with lower Young's modulus, higher tensile strength, and higher bounding strength and shrinkage compensation.

The clearance between the casing and the cement is related to the casing movement during the cementing job and the temperature change that the cement can withstand. More cement thickness can withstand the different movement patterns of the casing. This property cannot affect the integrity of the cement, but it could affect the cost to heat up the well in a steam injection process.[30] It is very common in the oil industry to accept a cement thickness of ¾ in. or higher.

Formation and cement mechanical properties can affect the debonding of cement/formation or develop plastic deformations of the cement or rock. This phenomenon may allow some leakage. Foam cements have different elastic mechanical properties than nonfoamed cements, and it is necessary to ensure that the nitrogen quality remains as it was designed. Nitrogen bubbles improve the tensile strength of the foam cement, and this helps the cement to absorb the temperature and pressure cycling caused by different loads in the well life, like perforating and hydraulic fracturing.[31]

Tensile strength of the cement can be improved by including organic or inorganic additives like latex, glass and carbon fibers. Mechanical properties have to be measured in the laboratory, and this information is used in the FEA model to reduce the risk of cement failure during the well life.

The microannulus can be filled with expanding agents in the cement. When the expanding cement is surrounded by a rock with a lower Young's modulus, it is easier for the cement to expand outward, pushing the rock and creating an inner microannulus. If the Young's modulus of the cement is lower than the Young's modulus of the rock, it will be easier for the cement to expand inward, closing the microannulus. Consequently,

an expanding agent has to be added to cement with a lower Young's modulus than the surrounding rock to ensure that the expansion is inwards.[32]

3.5 Flexible Cements

Conventional cements could fail during the well life in three modes: debonding from the casing or formation, radial cracks, or plastic deformation. Cement sheath failure during well testing, hydraulic fracturing, tectonic movement, fluid production, or perforating can cause early water production, sustained casing pressures, and interzonal communication. Cement failure can lead to remedial cement jobs, reduced production, and casing collapse.

The oil industry requires highly resilient and flexible well cements that can withstand shear and compressional stresses. The required mechanical set cement properties call for low Young's modulus and tensile strength ratio. Elastic cements normally have Young's moduli around 1 E+6 psi and tensile strength values higher than 400 psi, Poisson's ratio around 0.15, among others. Flexible cements require high Poisson's ratio, high cement cohesion, low permeability, and no shrinkage to avoid microannuli. The relationship between deformation of the cement and the stresses generated is governed by the Young's modulus of the cement. The lower the Young's modulus, the easier it is to stretch or squeeze the cement. An elastic cement sheath can withstand stress and temperature changes better than a stiffer cement sheath. I will show in Chapter V that cement failure happens first under tensile loading than under compression.

Fig. 3.6 shows an example of a stress/strain plot of elastic and conventional cement sheath. The area under the elastic region gives the resiliency of the cement sheath. The resiliency is a representation of the amount of energy that the cement can withstand and still remain elastic. The resiliency of an elastic cement sheath is higher than the resiliency of a conventional cement sheath.[34]

The conventional cement sheath fails in brittle behavior at a stress of σ_c and strain of ε_c. The elastic cement sheath starts plastic deformation at a stress of σ_e, but the

cement can withstand stresses in the plastic region. The cement sheath has to be designed to be in the elastic region to recover to its original dimension when the stress is removed.

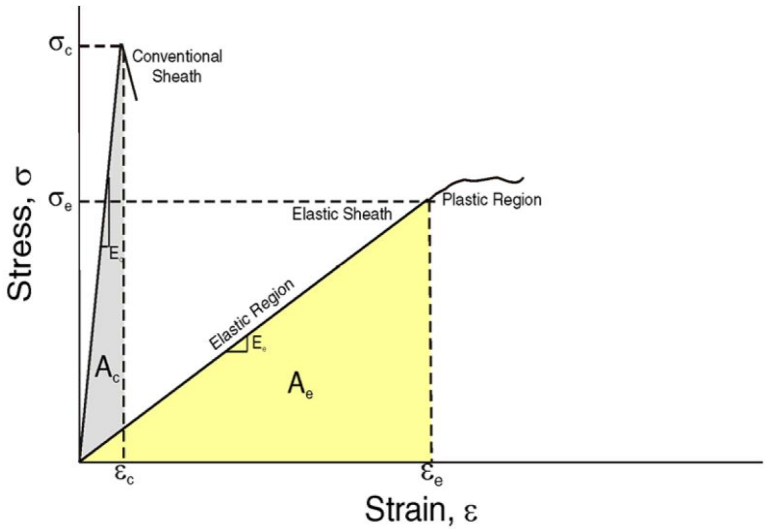

Fig. 3.6—Stress—strain behavior of elastic and conventional set cements (from Ref. 34)

Conventional slurry reduction using extenders (e.g., sodium silicate or bentonite) can increase the flexibility but decrease the permeability, compressive strength and tensile strength too much. Several cement additives can increase the elasticity like vulcanized rubber and elastomeric materials. Tensile strength of the cement can be increased by latex, silica fumes, and glass and carbon fibers.

Latex is general term describing an emulsion polymer. A wide variety of monomers like vinyl acetate, vinyl chloride, acrylics, acrylonitrile, ethylene, styrene, and butadiene are used to prepare commercial latexes. Latex provides the following benefits to the cement:

- Improves pumpability of the cement slurry because latex reduces the ECD.
- Decreases cement permeability.
- Increases elasticity of the cement.
- Reduces the shrinkage.

- Improves bonding between cement/steel and cement/formation interfaces.
- Reduces cement shattering when perforated.
- Increases resistance to corrosive fluids.
- Reduces fluid loss rate.

In latex-modified systems, the latex particles form a plastic film that surrounds and coats the C-S-H phase. Latex bridges the microcracks in the set cement and limits their propagation. Latex increases the tensile strength of the set cement and reduces cement permeability. Styrene butadiene latex is also an effective additive for the prevention of annular gas migration and can withstand temperatures as high as 350ºF (176 ºC). Latex or elastomeric products help increase the cement sheath stability to resist cumulative stress and cyclic loading by lowering the Young's modulus and rising Poisson's ratio.

Glass, carbon, and nylon fibers have been used to increase the tensile strength of the set cement without decreasing the compressive strength. Glass fibers can also be used as a lost-circulation fiber for cement and drilling fluids. Glass fibers can withstand maximum temperatures of 600ºF, and carbon fibers do not have an upper temperature limit. Fiber concentration varies from 0.5 to 2.5% BWOC.

This shrinkage can be a combination of internal and external shrinkage that can result in damage to the cement sheath in the form of tensile cracks or microannuli due to debonding. An optimum cement design should have no bulk shrinkage and post-set expansion limited to less than 1%.[35] High cement- permeability could be related to inner shrinkage of the set cement or high porosity due to poor slurry design.

Foamed cement has been used as flexible cement for its improved mechanical properties and minimum cement shrinkage. Foamed cement's tensile strength, ductility, and displacement properties have made it especially useful in several zonal-isolation scenarios.[36] Also, foamed cements have improved drilling fluid displacement and fluid loss.

The compressive strength of foamed cement varies according to the nitrogen content and the strength of the base slurry. As the nitrogen content increases, the density

and compressive strength decrease. The permeability of foamed cement varies with the quality of the cement, base slurries, N_2 ratio, foamer concentration, bubble texture, and depth of the well.[37]

How many times and how readily the cement will recover its original size after loading is limited. A cement sheath has to be designed to withstand cyclic loads because the cement sheath could have fatigue and fail rapidly. Fig. 3.7 shows a plot of stress vs. number of cycles that a material can resist. Below the endurance limit, S_{EL}, the material can withstand an infinite number of cycles.

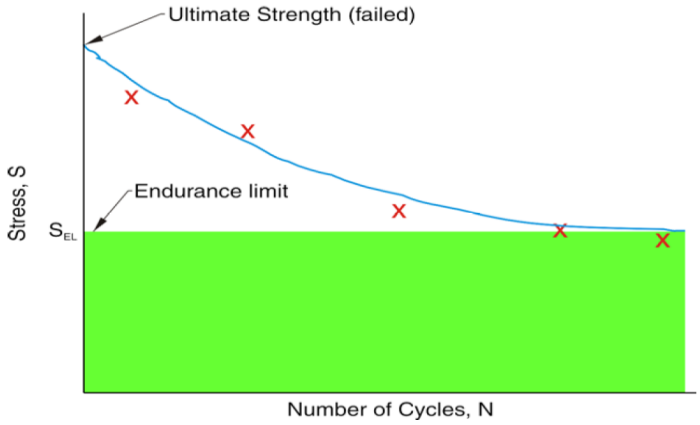

Fig. 3.7—Stress vs. number of cycles behavior plot (from Ref. 34)

3.6 Self-Healing Cement

One of the key properties of self-healing cement is the ability to self-heal in the presence of hydrocarbons, repairing the microannulus or internal cement cracks. The cement system can react to hydrocarbons, and it expands and fills the flow path to prevent additional fluid flow. Self-healing cement can be placed along any section of the annulus to create a long-term seal above the reservoir. The cement sheath can have both elastic and self-healing properties. Self-healing cements can seal a microannulus of 100-250 microns, but not a mud channel.

Self-healing cements do not have special requirements for pumping equipment or spacers. Self-healing cement can be designed at densities from 11.7 to 16 ppg and temperature application ranges from 68 (20˚C) to 280˚F (138˚C). UCA (Ultrasonic Cement Analyzer) measurements must be used to calculate the acoustic impedance of the cement under pressure and temperature, which in turn allow calibrating the sonic and ultrasonic logging tools.[38]

Sustained casing pressure (SCP) is defined as development of annular pressure at the wellhead that can be bled to zero, but then the pressure at the wellhead builds up again, and the cycle is repeated with time. The annulus cannot be shut in, and the gas is allowed to escape to the atmosphere through a surface casing vent. This flow is known as surface casing vent flow (SCVF). The presence of SCP or SCVF indicates inadequate zonal isolation has allowed communication to the annulus from a sustainable pressure source. Changing stresses in the wellbore may cause microannuli, cracks, or both, leading to sustained annular pressure problems.

Self-healing cements contain self-healing additives and conventional additives like dispersants, antifoams, retarders, fluid-loss-control agents, and gas migration additives, if necessary. The self-healing cement needs standard tests like measurement of rheological properties, free fluid, free water, fluid loss, thickening time, and UCS.

3.7 Cement Placement Evaluation

Acoustic logging is the most widely used and efficient method to evaluate cementing jobs. Acoustic log interpretation requires quality control of the log, cement, and formation properties, and knowledge of the cementing job.

A CBL-VDL (cement bond log-variable density log) is a conventional logging tool to evaluate the quality of the cement after setting in the well. The log measures the amplitude or attenuation of a wave (20- to 30-kHz frequency) traveling along the casing. The CBL gives a quantitative indication of the quality of the bonding between the cement and casing, while the VDL gives a qualitative indication of the bonding between the formation and cement. Good cement bonding is identified by a low CBL value

(average CBL value of 5 mV in 7–in. casing), weak casing arrivals, and strong formation arrivals on VDL.

CBL-VDL gives an average measurement, which may obscure channels around the casing, and ultrasonic measurements can complement the CBL-VDL results. Ultrasonic tools, introduced in the 1990s, operate at frequencies between 200 and 700 kHz. The ultrasonic technique makes a small area of the casing resonate through its thickness. Fluids behind the casing tend to resonate, and solid cement behind the casing tends to damp the resonance. The resonance signal is analyzed to calculate the thickness of the casing and the acoustic impedance of the material behind the casing.

Ultrasonic tools have less sensitivity to a liquid-filled microannulus between the pipe and cement, but they have good spatial resolution. Gas behaves as a barrier that reflects the ultrasound. The measured impedance of neat cement is more sensitive to a microannulus than lower-density cements. However, ultrasonic tools are affected by pipe rugosity or roughness. Also, ultrasonic tools are limited in heavy solid-weighted mud, especially in oil-base mud. Ultrasonic tools can work in water-base mud up to 16 ppg and in oil-base mud up to 13 ppg.[12]

Foamed cements have low impedance that causes interpretation problems. Neat cement has an impedance of about 6 MRayl (10^6×1 kg·s−1·m−2), liquids 1 to 3 MRayl, and gas below 0.1 MRayl. Foam cements and light cements have an impedance of about 2.5 MRayl. Flexural wave imaging logs can evaluate any type of cement, from traditional slurries and heavy cements to the latest lightweight and foam cements.

Sonic and ultrasonic tools determine the bonding between the casing and cement, and they give qualitative information of the bonding between the formation and casing. Ultrasonic tools are affected by high mud densities, but sonic tools are affected by liquid-filled microannuli. Ultrasonic logs are generally easier to interpret and less ambiguous than sonic logs, but the combination of sonic and ultrasonic cement logs is better. Fig. 3.8 shows ultrasonic cement sheath evaluation. The proper interpretation of cement logs requires information about the well and the cement properties.

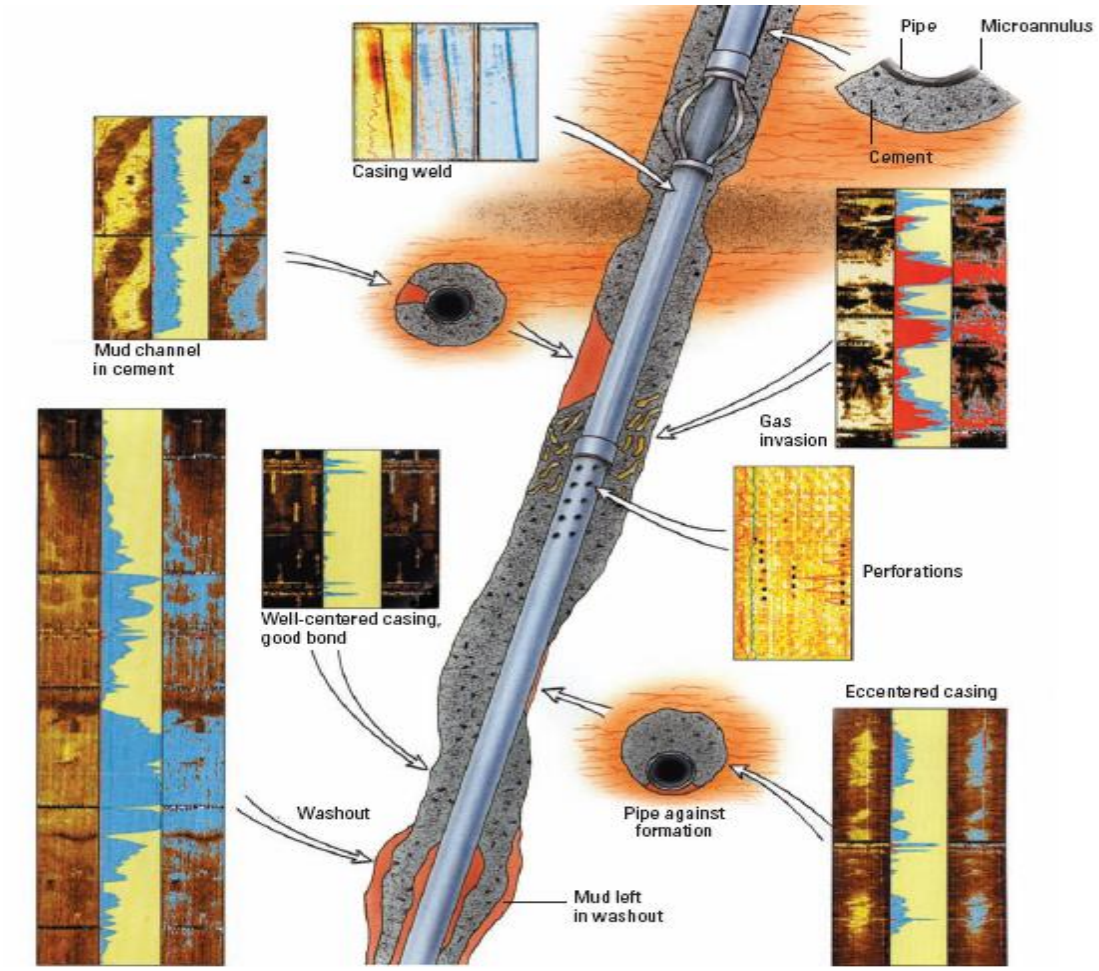

Fig. 3.7—Ultrasonic cement sheath evaluation (from Ref. 12)

CHAPTER IV

CEMENT FAILURE IN HPHT WELLS

Mechanical properties of cement behind the casing are important for the success of the well during its productive life and abandonment, especially when wells are drilled in high pressure and high temperature (HPHT) conditions. Zonal isolation must continue not only during the full life of the well but also after its abandonment. The consequences of cement sheath failure include production loss, safety reduction, environmental damage, additional remedial jobs, well shutdown to comply with government regulations, and even the loss of the well.

Events during the lifetime of a well can damage the cement sheath or cause cement debonding. Hydraulic fracturing, thermal cycling, pressure testing, or high drawdown pressure for production can lead to radial fractures or debonding of the cement due to plastic deformations of the cement and/or rock. The cement must be designed to withstand changing conditions during the life of the well, including its abandonment.

The data required for finite-element analysis includes the elastic, plastic, and thermal properties of the cement and formation. Engineers must know the operational details of drilling, casing centralization, completion, stimulation and production to design the cement slurry and avoid cement sheath failure. I studied the risk of plastic deformation of set cements and rocks, cement debonding, and cracks of the cement using finite-element analysis (FEA). These factors lead to vertical fluid migration that depends on the width of the gap, viscosity of the fluid, and drawdown.

High-temperature wells, in-situ combustion wells, or steam injection wells need particular analysis because the wells heat up and cool down during their life. When the borehole heats up, the casing expands, and it could crack the cement. Borehole cooling leads to inner or outer microannuli if the cement debonds. Oil and gas wells could have

more than 30 years of lifetime, and drilling engineers must ensure long-term seal of the cement.

The cement and formation could deform plastically (permanently) during high pressure tests or hydraulic fracturing jobs. This plastic deformation also creates inner or outer microannuli. The elastic and plastic properties of set cements are different, and with these differences, some set cements can't withstand well-loading conditions, resulting in cracks, plastic deformations, or debonding of the cement.

The oil industry normally takes into consideration the following recommendations for a primary cementing job to reduce short-term problems[30]:

- Run compatibility tests between spacers, mud, and cement slurry.
- Run lab tests to check for free water in the cement slurry. If the slurry has excessive free water, channels will be created, leading to loss of zonal isolation. Free water will also lead to a slurry volume reduction. As water is removed from the slurry, a pressure drop in the cement column can lead to an influx of water or reservoir fluids. The slurry sedimentation test is documented in API RP 10B.
- Run fluid-loss control tests, both dynamic and static. When excessive amounts of fluid are lost from the slurry during placement, the increase in slurry density may result in lost circulation. Also, if a significant percentage of water is lost dynamically from the slurry, rheology and thickening time may be negatively affected. High static fluid loss will lead to a slurry volume reduction, reducing the hydrostatic pressure and causing premature setting of the cement. Fluid loss of the cement slurry in the reservoir should be less 50 ml/30 min. A filter-press cell is used to measure the fluid loss in cement slurry.
- Allow unconfined compressive strength (UCS) of the set cement to develop adequate mechanical properties to support the casing for the life of the well. Ultrasonic cement analyzer (UCA) tests of the cement should have more than 500 psi in 24 hours at borehole static temperature.
- Make sure in the laboratory that the cement slurry has a critical hydration period (CHP) less than 45 minutes. A good value of CHP is less than 20 minutes. The

CHP time begins when the slurry no longer transmits hydrostatic pressure that overbalances the pore pressure of the formation and ends when the slurry has developed enough cohesive strength to prevent the entry and flow of reservoir fluids into the annulus.

- Centralize the casing with a minimum 70% standoff. When an annulus is concentric, its eccentricity is zero and the pipe standoff is 100%. Conversely, when the casing is touching the wall of the borehole, the eccentricity is 1 while the pipe standoff ratio is 0%. A good casing centralization ensures that the density and rheology of the washers, spacers, and cement slurries maximize mud removal.
- Make sure that the hole is clean of caving or cuttings before starting to pump pre-fluxes, spacers, and cement slurry.
- Lower the yield point of the mud to 9 to 14 lb/ft^2 at bottomhole conditions. The use of Fann 70 equipment to determine the yield point of the mud in the bottom of the hole on the basis of its pressure and temperature has been useful in Ecopetrol's operations. This methodology can reduce the possibility of hole packoff or stuck liner hanger tools during well cementing, which can happen if the mud yield point decreases excessively in the well.
- Lower the 30-minute mud gel to less than 30 lb/ft^2 or flat gels between 10 and 30 minutes.
- Reciprocate and rotate the casing to break the gel strength of the mud. Casing movement (reciprocation and rotation) improves the quality of primary cementing jobs. Casing movement breaks up zones of immobile mud, which can cause cement channeling. Casing rotation is complex in deviated wells, and casing thread connections, cementing head, and other necessary equipment must be checked before starting rotation.
- Monitor flowline properties of mud (plastic viscosity, yield point, mud density, and gas cut) while circulating casing volume. These mud properties can tell us the mud conditions at bottomhole.

- Maintain rheology and density of spacers higher than mud. Spacers should occupy 300 m or 1,000 ft of the annular volume or 10 minutes of pumping time. The rheology and density of the cement slurry must be higher than those of the spacers. Studies have shown that a minimum increase of 10% in density or minimum 1 ppg density difference for each successive fluid is ideal for effective displacement of one fluid by another.
- Maximize the displacement rate and use software for borehole cleaning and cement placement simulation. When the cement slurry is in the hole/casing annular space, pumping rates should be 7 to 9 BPM to increase the chances to have good mud removal. The key forces taken into account are buoyancy forces, friction forces, yield and gel stresses, and initial forces. During borehole cleaning, equivalent circulating density (ECD) should not reach the fracture gradient of the formations. Avoid cementing operations when the well has lost circulation, and cure mud losses before cementing. If circulation has been lost, reduce the pumping rates to reduce ECD of the fluids during cementing operations.
- Maintain correct mud density to avoid excessive borehole washouts that could cause cement channels. Unconsolidated formations and high-tectonic-stressed formations are prone to have excessive washouts. Mud is left in the washouts, because the cement slurry could not displace the drilling fluid.

Oil companies have traditionally focused on solving short-term cement failures like poor casing centralization, poor borehole cleaning, cement coverage of oil-bearing zones, and cement compressibility. They have recently begun to dedicate special attention to long-term failure of the cement because loss of well integrity cannot always be related to short-term cement failure. The cement sheath can be damaged over the lifetime of the well, and it must be repaired or the well must be abandoned. The likelihood that cement squeezes will be successful is low because of the difficulty of injecting cement slurry inside the inner and outer microannuli or in the cement cracks.

Abaqus finite-element analysis software is used to understand and predict the cement sheath behavior. Abaqus is a highly sophisticated, general-purpose finite-element code developed to solve nonlinear stress analysis like plasticity, contact conditions, or cracking simulation. The plasticity of the rock or cement can be a cause of lack of inner or outer microannuli.

The finite-element model (FEM) in this project was built in the reservoir section to understand the long-term effects of thermal and pressure changes on the cement sheath during the life of the well, including completion, hydraulic fracturing, and production. The FEM takes into consideration the history of previous and current temperatures, well-loading conditions, and deformations of rock, cement, and casing to do the analysis. This finite-element analysis (FEA) involves the following steps:

- Drilling. Removal of rock by the drill bit generates stresses around the borehole. The formation is under a 3D state of stress: overburden and minimum and maximum horizontal stresses. The drilling fluid causes a hydrostatic pressure in the deformed borehole. A borehole stability analysis could model the final shape and size of the borehole, but that study was beyond the scope of this research.
- Cement Pumping. The casing is run in the borehole; the casing should be centralized with a minimum 70% standoff. Prefluxes and spacers are pumped before the cement slurry to remove the filter cake and the drilling fluid. Pipe movement, centralization, and fluid density hierarchies are required to improve mud removal during cementing operations. This study also analyzed the effect of casing decentralization.
- Cement Hardening. During this step, the cement slurry becomes solid cement. The pressure inside the casing is equal to the drilling- or completion-fluid pressure. The casing contracts because of the different pressures inside and outside of it. Inner microannuli (casing/cement) can result from wellbore pressure variation during the hardening process.
- Cement shrinkage. During cement setting, the cement can reduce its volume by hydration volume reduction. The cement shrinkage or expansion depends on the

chemical composition and temperature of the cement slurry, and conventional cements shrink from 0.5% to 7%.[22, 23] If water is freely available from the formation during the cement-hydration phase, the cement won't shrink or it will shrink partially. In the case of foam cements, cement shrinkage can also be offset by an internal source such as well-dispersed gas bubbles inside the cement so that the gas will expand to occupy the reduced volume.[3] Most of the total bulk shrinkage takes place from 8 to 24 hours after the cement slurry is mixed.[24] This FEA did not study shrinkage or expanding effects of the set cement. Newer set cements have been designed to avoid shrinkage, and some set cements are designed to have a controlled expansion.

- Well completion. The drilling fluid placed inside the casing is replaced by the completion fluid. The hydrostatic pressure inside the casing depends on the completion fluid density. Inner microannuli could be created as a result of contraction of the casing when heavier drilling fluid is changed by a lighter completion fluid.
- Hydraulic fracturing of the well. After drilling, the well must be evaluated to determine the necessity to fracture it to increase its production. Not all wells require hydraulic fracturing to reach the expected production. During a hydraulic job, high pressure inside the casing fractures the formation, and the casing tends to expand, pushing on the cement and formation. The fracture pressure depends mainly on total in-situ stresses and tensile strength of the rock. Fracture pressure could cause plastic deformation, shear deterioration, or cracking of the cement under pressure loading.
- Well production. The amount of pressure inside the casing depends essentially on the formation pressure and drawdown. Depletion of the reservoir decreases the pressure inside the well, and the casing tends to contract, causing inner microannuli.

Because of computing time restriction, I only used transient analysis for the hydraulic fracturing step. However, the FEM was not restricted to having transient analysis in all the steps.

4.1 Approach to the Cement Failure Using Abaqus

Abaqus is a commercial finite-element program which was designed as a flexible tool for linear and nonlinear element modeling. Abaqus was used to approach the solution of cement failure in HPHT conditions. The model in Abaqus considers the following assumptions:

- All the materials were homogeneous and continuous (casing, cement, and formation).
- The system was axisymmetric due to the boundary conditions, and only a quadrant of the annular structure was modeled.
- The cement sheath was perfectly bonded to the formation and casing. However, an assessment of tensile stresses and debonding strength of the set cement can determine if debonding exists or not.
- The wall thickness of the casing was uniform.
- There was no shrinkage or expansion of the cement.
- Following Abaqus software convention, negative and positive stresses mean compression and tension, in that order.

The Abaqus/Complete Abaqus Environment (CAE) user was responsible for unit consistency throughout the model. The system of units used for the cement failure analysis during this study was US units for stress and heat transfer analyses. This FEM shows the effect of the cement Young's modulus, cement Poisson’s ratio, and cement cohesion strength, Co, for different rock mechanical and thermal properties.

4.1.1 Data for Cement and Formation Failure Analysis

Abaqus version 6.11 was used to study the behavior of the cement at high pressures and high temperatures with different mechanical and thermal formation

properties. Table 4.1 shows the geometry of the borehole and well-loading conditions used in the FEM.

TABLE 4.1—WELL DATA FOR FEA OF CEMENT AND FORMATION FAILURE

	Wells			
Well Data	**Case 1**	**Case 2**	**Case 3**	**Case 4**
Borehole depth, ft	15,000	8,500	15,000	15,000
Bit size, in.	8.50	8.50	8.50	8.50
Borehole, in.	9.50	9.50	9.50	9.50
Casing OD, in.	7.63	7.63	7.63	7.63
Casing ID, in.	6.63	6.63	6.63	6.63
Overburden pressure, psi	15,000	8,500	15,000	15,000
Maximum horizontal stress pressure, psi	18,000	10,115	18,000	18,000
Minimum horizontal stress pressure, psi	10,500	6,630	10,500	10,500
Mud pressure, psi	7,800	3,978	7,800	7,800
Mud temperature, °F	100	135	100	100
Cement slurry pressure, psi	8,252	4,244	8,252	8,252
Pressure of completion fluid, psi	4,500	3,713	6,552	6,552
Hydraulic fracturing pressure, psi	13,500	7,886	16,000	14,772
Hydraulic fracturing fluid temperature, °F	150	135	150	150
Bottomhole production pressure, psi	3,500	1,500	4,000	4,000
Formation temperature, °F	350	192	350	350

Mechanical and thermal properties of set cements of Tables 4.2 and 4.4 were determined in the rock mechanics labs, and they will be explained in detail in Chapter V. Mechanical properties of C7, Cuervos, and Barco formations of Cupiagua wells were calculated with Eqs. 2.58, 2.61, 2.63, 2.65 and 2.66, and the results were calibrated with triaxial tests (Table 4.3). Mechanical properties of A, B, and C rocks of Table 4.3 were taken to study the effect of set cements at soft, medium, and hard formations.

Table 4.4 shows thermal properties of the formation, cement, and casing. Also, Young's modulus and the Poisson's ratio of the casing were 30 E+6 psi and 0.3, respectively. Formation and casing thermal properties were taken from WellLife

Software of Halliburton. The FEA used Mohr-Coulomb plasticity model with an absolute plastic strain of zero.

TABLE 4.2—CEMENT MECHANICAL PROPERTIES

Cement Name	Slurry Density, lb/gal	Young's Modulus, (Ec), psi	Poisson's ratio (υ_c)	Friction Angle (ϕ_c), deg	Dilation Angle (Ψ_d), deg	Cohesive Strength (Co), psi	UCS, psi	To, psi
LifeCem	15.8	1.28E+6	0.160	19	19	1,770	4,937	449
Design 6	15.6	7.39E+5	0.072	21	21	1,600	4,692	542

TABLE 4.3—FORMATION MECHANICAL PROPERTIES

Formation Name	Young's Modulus (Ef), psi	Poisson's Ratio (υ_f)	Friction Angle, (ϕ_f), deg	Dilation Angle (Ψ_d), deg	Cohesive Strength (So), psi	UCS, psi
A Rock	4.0E+6	0.20	30	27	1,500	14,290
B Rock	1.7E6	0.20	25	20	1,200	4,980
C Rock	7.0E+6	0.25	45	27	6,390	30,860
C7 (sandstones)	1.03E+6	0.24	36	36	2,939	11,511
Cuervos (shale)	3.0E+6	0.25	25	25	4,000	13,318
Barco (sandstones)	8.3E+6	0.25	45	27	5,700	31,000

TABLE 4.4—THERMAL PROPERTIES OF CEMENT, CASING AND FORMATION

Material	Density, ppg	Thermal Expansion Coefficient (α), 1/°F	Thermal Conductivity (k), Btu/(hr×in×°F)	Specific Heat Capacity (c_p), Btu/(lbm×°F)
LifeCem cement	15.8	5.556E-06	0.01983	0.50158
Design 6 and conventional cements	15.6	5.556E-06	0.04817	0.50158
All formations	15.0	5.556E-06	0.04815	0.23885
Casing	65.7	7.222E-06	0.72224	0.11942

4.1.2 Meshing and Initial and Boundary Conditions

This study focused on investigating the behavior of different cements and different rocks in an HPHT environment. The formation geometry for the model considered a block of 50 in. x 50 in. x 10 in. The vertical dimension was 10 in. The

horizontal dimensions of the parallelogram were more than five times the borehole radius to achieve correct simulations of boundary conditions at infinity.[39]

The mesh model considered element types that can handle a couple of temperature-displacement models. The element types of the parallelogram were hexahedron elements with an 8-node, thermally coupled brick with trilinear displacement and temperature (C3D8RT). The elements considered reduced integration and hourglass control. The advantage of reduced integration elements was that the strains and stresses were calculated at the locations that provide optimal accuracy. A second advantage was that the reduced number of integration points decreased computing time and storage requirements. The disadvantage was that the reduced integration procedure could admit deformation modes that caused no straining at the integration points. To prevent these excessive deformations, an additional artificial stiffness was added to the element. In this so-called hourglass control procedure, a small artificial stiffness was associated with the zero-energy deformation modes.[13]

Fig. 4.1 shows the mesh model of the formation showing C3D8RT elements. The mesh model of the formation requires a finer mesh at the casing/formation annulus to have a better understanding of the stress behavior and deformations of the cement sheath and cement/formation contact throughout the FEA. The FEM demands that casing and cement sheath have the same mesh size of formation. The dark gray area in the plot is due to minute mesh size close to the borehole. A finer mesh in the FEM avoids problems of convergence and erroneous results.

The FEM represents only one quarter of the total borehole or domain because the other part of the borehole can be generated using the “mirror” feature of Abaqus. This feature was used to reduce computation time with greater density of elements in the analysis.

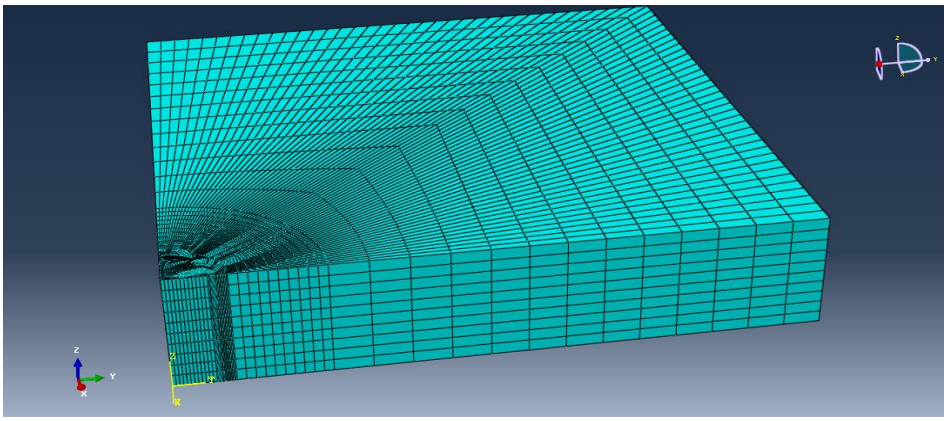

Fig. 4.1—Mesh model of the formation with C3D8RT elements

The von Mises failure criterion was used in FEA to evaluate the failure in the cement and formation. This criterion states that failure occurs if the combination of the three principal stresses exceeds the yield strength of the material. Mathematically, the von Mises criterion is expressed as[40]

$$\sigma_{VM} = \sqrt{\frac{(\sigma_1 - \sigma_2)^2 + (\sigma_2 - \sigma_3)^2 + (\sigma_3 - \sigma_1)^2}{2}} \quad \ldots\ldots\ldots\ldots\ldots\ldots\ldots\ldots\ldots\ldots \quad (4.1)$$

where σ_1 is the maximum principal stress magnitude, σ_2 is the intermediate principal stress magnitude, and σ_3 is the minimum principal stress magnitude.

Tangential and radial stresses in a homogeneous and isotropic material are defined by[41]:

$$\sigma_\theta = \frac{1}{(1-v^2)}[\varepsilon_\theta E + (v + v^2)\sigma_r - (1 + v)\alpha E \Delta T] \quad \ldots\ldots\ldots\ldots\ldots\ldots\ldots\ldots\ldots\ldots \quad (4.2)$$

$$\sigma_r = \frac{\sigma_\theta(1-v^2)+(1+v)\alpha E \Delta T - \frac{E\delta_r}{r}}{(v+v^2)} \quad \ldots\ldots\ldots\ldots\ldots\ldots\ldots\ldots\ldots\ldots \quad (4.3)$$

where σ_θ is the tangential, ε_θ is the tangential strain, E is the Young's modulus, υ is the Poisson's ratio, α is the linear thermal expansion, ΔT is temperature change, σ_r is the

radial stress, and δ_r is the radial expansion. Analytical solutions of tangential and radial stresses of casing, cement and rock can be found in open literature.[41]

This FEM was run for drilling, cementing, completion, hydraulic fracturing, and production steps. The main objective of this FEA was to show the phenomenon of plastic deformation of the set cement and formation after well completion, hydraulic fracturing jobs, and well production. Plasticity of the rock and cement was measured in this FEA model as equivalent plastic strain, PEEQ—the maximum total plastic strain.

$$PEEQ = \int_0^t \sqrt{\frac{2}{3} \sum_{i,j=1,2,3} \left(\dot{\varepsilon}_{ij}^{p} \dot{\varepsilon}_{ij}^{p} \right)} \, dt \qquad \text{(4.4)}$$

where $\dot{\varepsilon}_{ij}^{p}$ is plastic strain rate tensor and *t* is time.

The FEM developed in this study had additional considerations:

- There was impermeable borehole wall or perfect mud cake, and there was no mud or cement filtrate into the formation.
- The cement sheath was perfectly bonded to the formation and casing in the completion, hydraulic fracturing, and production steps.
- Pore pressure was not included in the FEM.
- Each step considers the previous results. Plastic deformations were cumulative.
- The FEA model includes in-situ rock temperature and fluid temperatures of the fluids in the well during drilling, completion, hydraulic fracturing, and production.

4.1.3 Cement Behavior in Front of Hard and Soft Formations of Deep Wells

In the first case scenario, the FEM disclosed the effect on a specific set cement in front of Barco (sandstone) and Cuervos (shale) formations, preserving the same load conditions of a deep well. Borehole data of the Case 1 well, and mechanical and thermal properties of Barco and Cuervos formations and LifeCem cement were taken from Tables 4.1, 4.2, 4.3, and 4.4 to build the FEM. LifeCem cement has lower Young's

modulus than the Barco and Cuervos formations. The FEM shows tangential/radial stresses and plastic deformation (PEEQ) of the model to determine the chances of debonding and cracks of the set cement after well completion, hydraulic fracturing, and production.

Fig. 4.2 clearly illustrates that after drilling the well, von Mises stresses can reach higher values in soft formations than in hard formations. Case 1 well in Table 4.1 considered a well drilled in a strike-slip stress regime where the maximum horizontal stress was higher than the vertical stress, and the minimum horizontal stress was lower than the vertical stress. Von Mises stresses generated around the borehole were higher in the minimum horizontal (x-axis) in-situ stress direction than in the maximum horizontal (y-axis) in-situ stress direction. The behavior of the rock during drilling and life of the well can help us to understand the behavior of set cements.

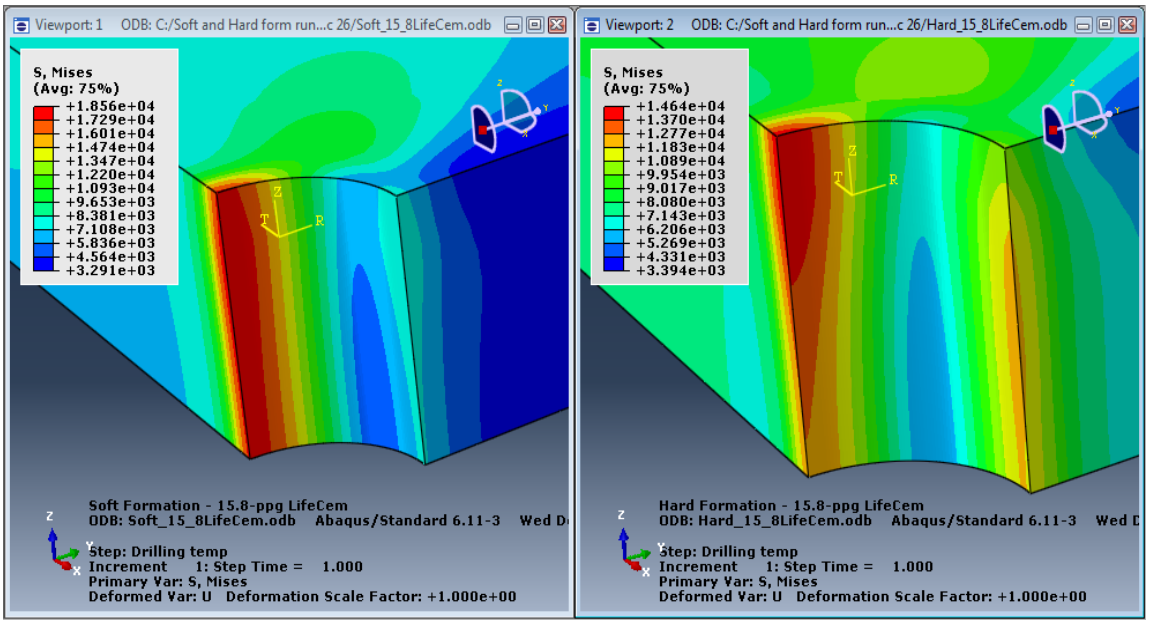

Fig. 4.2—Von Mises stresses at soft (left) and hard formations (right) of Case 1 well after drillling

Fig. 4.3 points out that after drilling the well, tangential stresses, S22 (CSYS-1), were in compression in the Cuervos (shale) formation and in tension and compression in

the Barco (sandstone) formation of Case 1wells. The maximum compressive stresses in the borehole were in the direction of the minimum horizontal in-situ stress direction (x-axis), and minimum compressive or tensile stresses were in the maximum horizontal in-situ stress direction (y-axis). This explains in geomechanics why breakouts are created in the minimum horizontal in-situ stress direction, and fractures are made in the maximum horizontal in-situ stress direction.

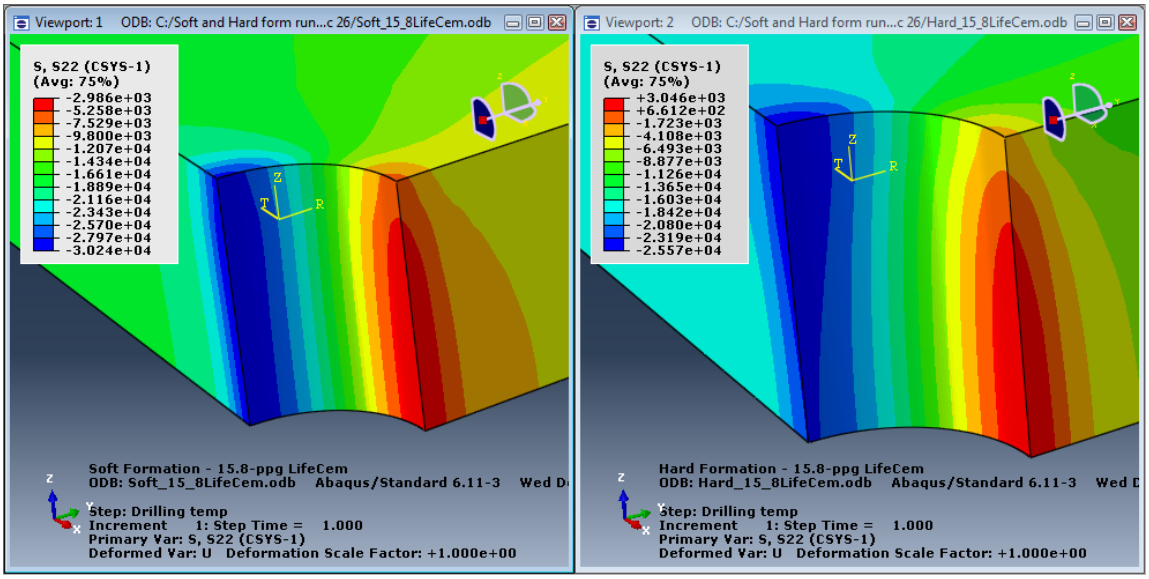

Fig. 4.3—Tangential stresses at soft (left) and hard formations (right) of Case 1 wells after drilling

Radial stresses, S11 (CSYS-1), need to be considered after well completion to determine the risk of cement debonding from casing and formation or plastic deformation. In this phase of the well life, the hydrostatic pressure of the fluid completion acts on the inner surface of the casing. Because this completion fluid pressure is lower than cement slurry pressure, the casing stretches, leading to cement debonding.

Fig. 4.4 undoubtedly shows that tensile radial stresses of LifeCem cement were lower in the Barco formation than in the Cuervos formation after well completion with

the loads of the Case 1 well. Partial debonding of LifeCem cement is clear in Cuervos formation because tensile radial stresses were greater than its debonding strength. A lab test in Chapter V shows where cement debonding strength was 0.83 of its tensile strength, and this relationship was used during this dissertation.

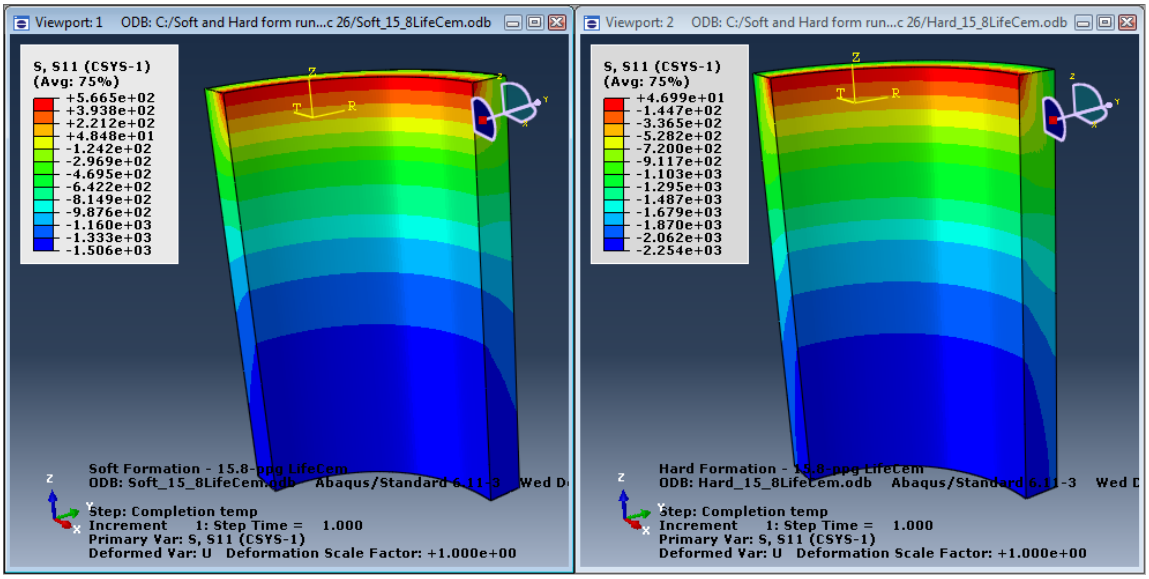

Fig. 4.4—Radial stresses of LifeCem cement at soft (left) and hard formations (right) of Case 1 wells after well completion

During the hydraulic fracturing process, the casing expands, pushing on the cement and formation. Hydraulic fracturing jobs could be the main cause of cement cracks and plastic deformation in the cement and rock throughout the well life. The hydraulic fracturing pressure used in this FEA analysis was 13,500 psi (Table 4.1). A temperature steady-state response was done with a hydraulic fracturing fluid with a temperature of 150°F. The formation had an original temperature of 350°F, and it was cooled down by the hydraulic fracturing fluid. This temperature changes created change of stresses at the casing, cement, and formation.

Fig. 4.5 clearly shows that tangential stresses of LifeCem cement were higher in front of the Barco formation than in front of the Cuervos formation after hydraulic

fracturing jobs at Case 1 wells of Table 4.1. It is obvious that LifeCem cement had initial radial cracks, because tangential stresses at the casing/cement contact were greater than 449 psi, the tensile strength of the cement. Tangential stresses in the set cement close to the formation were lower than the tensile strength of the LifeCem cement, and therefore the cement cracks did not fracture the set cement completely.

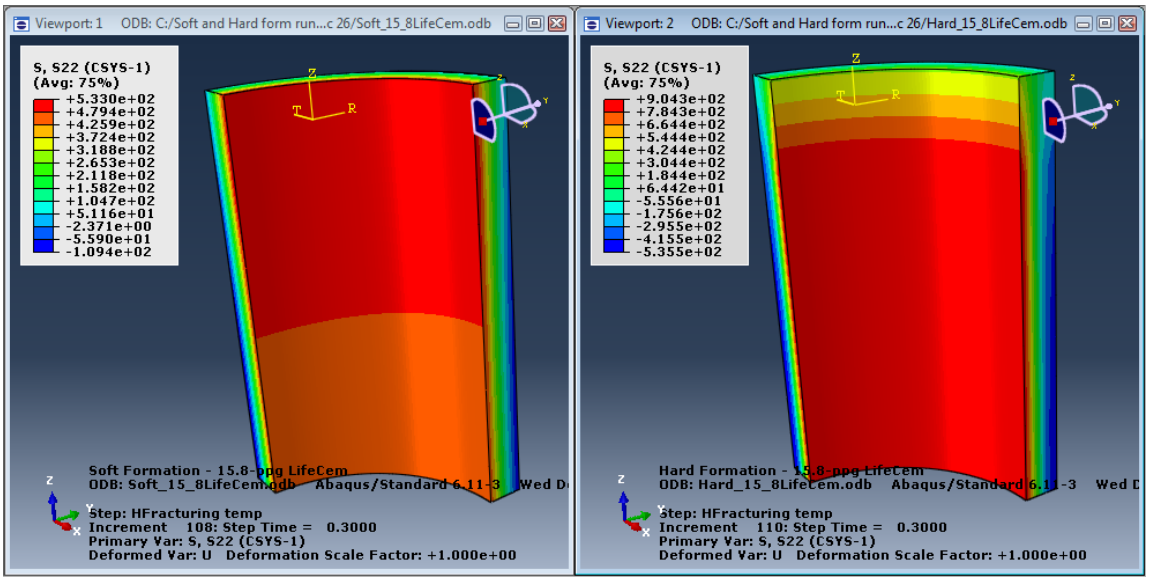

Fig. 4.5—Tangential stresses of set cement in front of soft (left) and hard formation (right) of Case 1 wells after hydraulic fracturing job

Fig. 4.6 shows radial stresses of LifeCem cement during well production with a bottomhole production pressure of 3,500 psi at Barco and Cuervos formations and loads of Case 1 well in Table 4.1. LifeCem cement clearly had partial debonding in front of the Cuervos formation, because the tensile radial stresses were greater than its debonding strength and tensile strength.

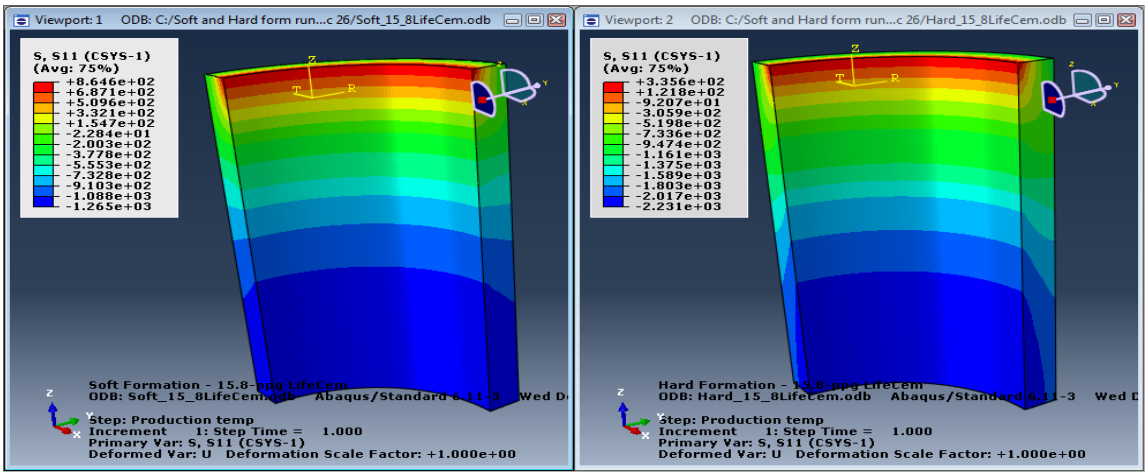

Fig. 4.6—Radial stresses of set cement in front of soft (left) and hard formation (right) during production of Case 1 wells

Fig. 4.7 visibly shows that LifeCem cement had plastic deformations (PEEQ) in front of the Barco formation. Also, Barco formation had plastic deformation in the maximum horizontal in-situ stress direction. There was no PEEQ of set cement in front of the Cuervos formation. In this scenario, LifeCem was more likely to have debonding at the Cuervos formation, and it was more prone to cement cracks and plastic deformation at Barco formation. Also, the Barco formation had plastic deformation with LifeCem cement.

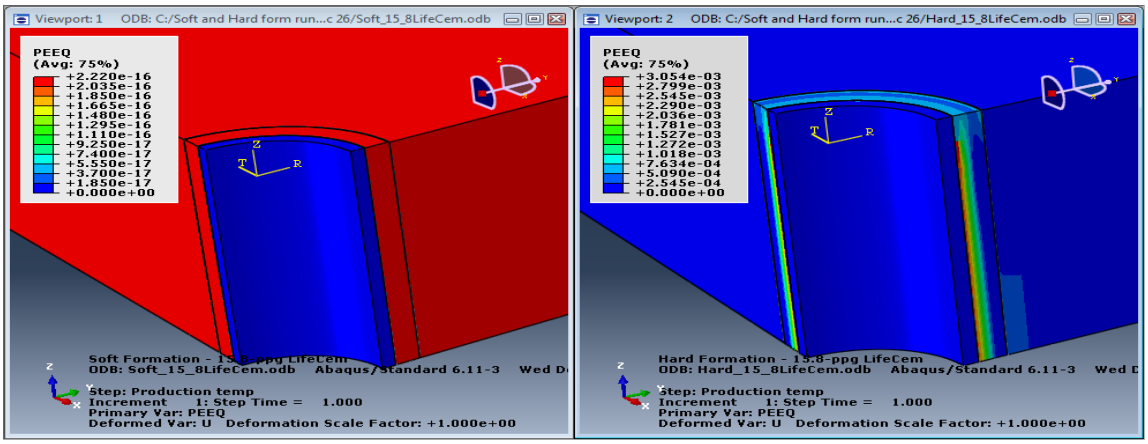

Fig. 4.7—PEEQ in front of soft (left) and hard formation (right) during production of Case 1 wells

4.1.4 Cement Behavior of Two Different Set Cements in Front of Soft Formation

Two types of set cements with different mechanical properties were analyzed to have general guidelines of Young's modulus of set cements for zonal isolation of formations. Tables 4.1, 4.2, 4.3, and 4.4 show borehole data of the Case 2 well, mechanical and thermal properties of LifeCem and Design 6 cements and C7 formation worked in the FEM. Cement Design 6 has lower Young's modulus than C7 formation, but LifeCem cement has higher Young's modulus than C7 formation.

Fig. 4.8 illustrates clearly that Cement Design 6 led to lower cement tensile radial stresses after well completion than LifeCem cement. Tensile radial stresses are responsible for cement debonding, leading to inner and outer microannuli. Cement Design 6 and LifeCem require 331 psi and 368 psi of cement debonding strength to avoid inner microannuli, in that order.

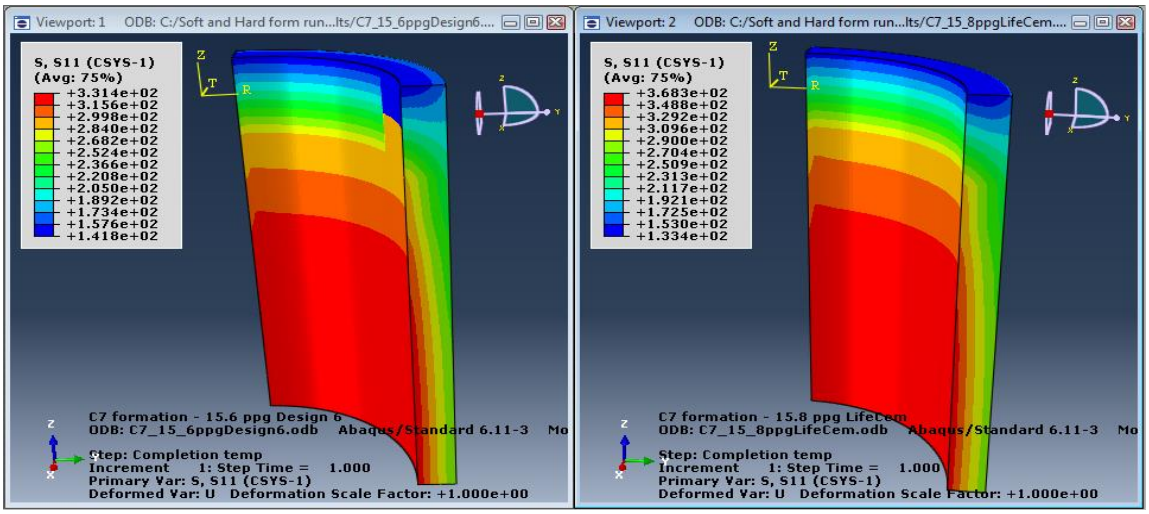

Fig. 4.8—Radial stresses at cement Design 6 (left), and cement 15.8-ppg LifeCem (right) in front of C7 formation after well completion

Fig. 4.9 illustrates openly that in hydraulic fracturing jobs of the C7 formation, cement Design 6 requires lower tensile strength to avoid radial cracks than LifeCem cement. The higher the cement's Young's modulus, the higher tangential stresses

generated in set cement. The tensile strength requirement to avoid cracks of cement Design 6 and LifeCem were 372 psi and 611 psi, in that order.

Fig. 4.10 shows visibly how the rock was cooled down due to the hydraulic fracturing fluid in both scenarios, and the effects of stress changes were included in the analysis. Thermal properties of the cement have influence on stresses and plastic deformations.

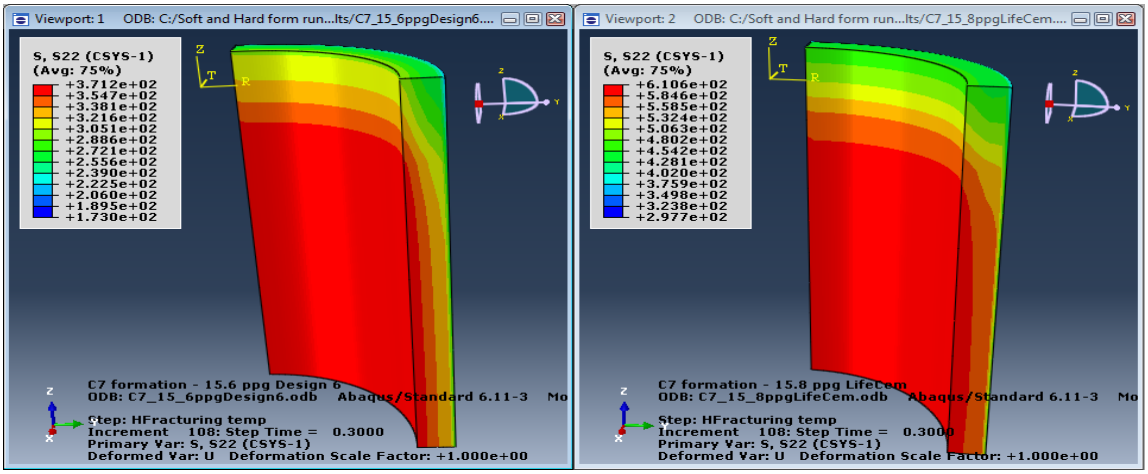

Fig. 4.9—Tangential stresses at cement Design 6 (left), and cement 15.8-ppg LifeCem (right) in front of C7 formation at the end of hydraulic fracturing job

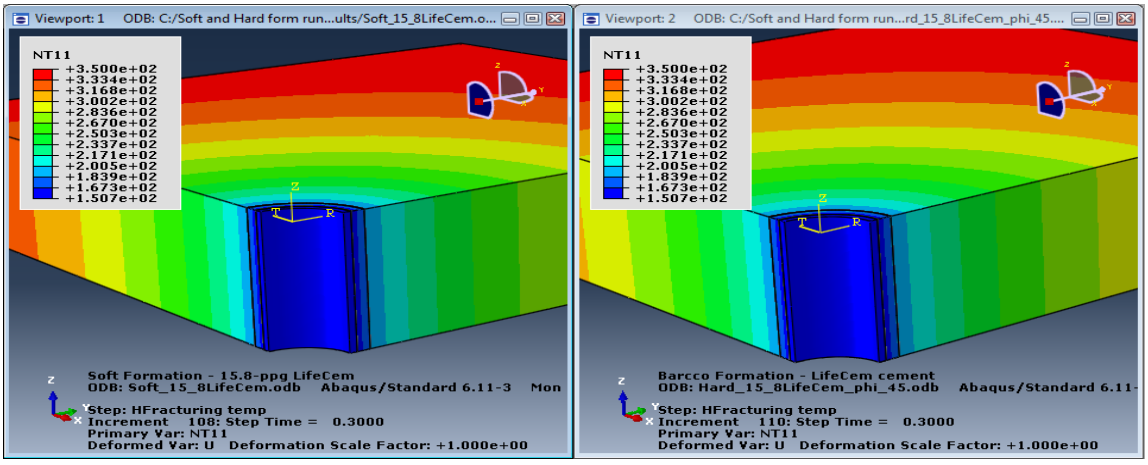

Fig. 4.10—Temperature changes of casing, cement and formation after hydraulic fracturing of C7 formation

Bottomhole casing pressure changes during well production and its pressure can be measured in real time by installing a pressure gauge at the bottomhole or estimated by reservoir simulation. Set cements have particularly high effects of changes of temperature and loading/unloading pressure, mainly during hydraulic fracturing and production.

Fig. 4.11 clearly shows that cement Design 6 requires lower debonding strength than LifeCem cement during well production with bottomhole production pressure of 1,500 psi. The lower the cement Young's modulus is, the lower the debonding strength requirement of the set cement during well production. The debonding strength requirement of cement Design 6 and LifeCem were 829 psi and 980 psi, in that order to avoid cement debonding. The tensile radial stresses were obviously higher than cement debonding strengths of both set cements, and cement partial debonding was inevitable in this specific condition.

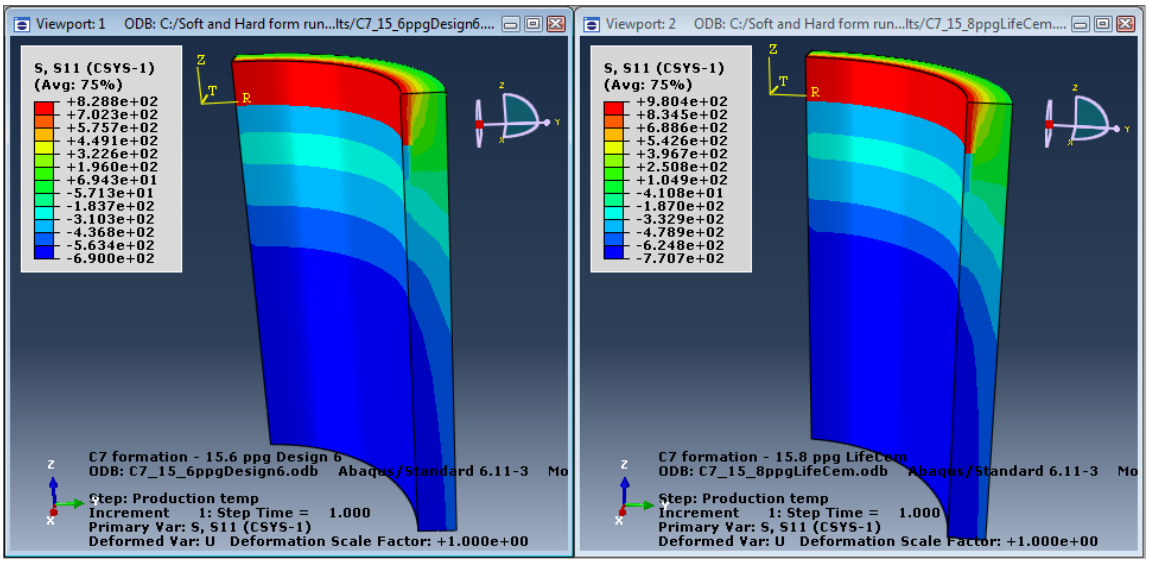

Fig. 4.11—Radial stresses at cement Design 6 (left), and cement 15.8-ppg LifeCem (right) in front of C7 formation during well production with bottomhole production pressure of 1,500 psi

Plastic deformation of the formation and cement were cumulative after each step of the well life. Plastic deformation of the cement and rock can lead to inner and outer

microannuli, and they can increase their size if cement grains erode. Also, grain size of the cement could affect the erosion of the set cement.

Fig. 4.12 clearly shows that Design 6 and LifeCem cements did not have plastic deformation during well production with bottomhole production pressure of 1,500 psi. The Young's moduli of the set cements have conveniently lower values than rocks to reduce the risk of debonding, radial crack, and PEEQ of the set cement. Finally, Design 6 cement with lower Young's modulus than C7 formation was clearly less likely to debonding and radial cracks than LifeCem cement.

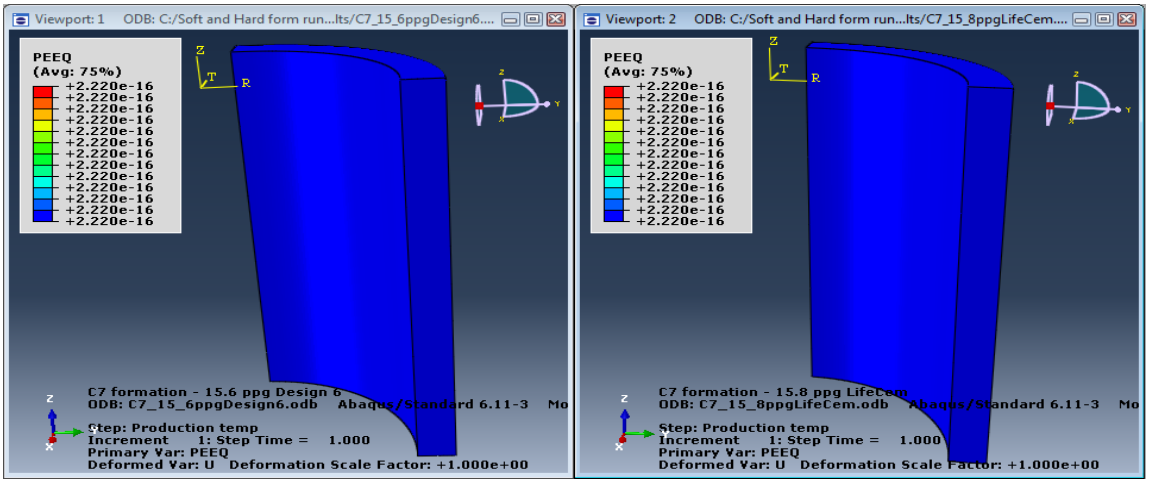

Fig. 4.12— PEEQ at cement Design 6 (left), and cement 15.8-ppg LifeCem (right) in front of C7 formation during well production with bottomhole production pressure of 1,500 psi

4.2 PEEQ Sensitivity Analysis with Different Set Cements and Constant Formation Mechanical Properties

The FEA model built in Abaqus in this research was used to study the effect of Young's modulus, Poisson's ratio, and cohesion of the cement on the equivalent plastic strain, PEEQ, of the cement and formation during the life of the well.

Borehole data of Case 3 well given in Table 4.1, mechanical properties of "A" rock formation in Table 4.3, and thermal properties of casing, conventional cement, and formation in Table 4.4 were used in the FEM. "A" rock had an estimated UCS of 14,000

psi. The mechanical properties of set cements were changed during this sensitivity analysis, except friction and dilation angles that remained constant at 17° and 16°, in that order. Young's modulus of the formation was always higher than the Young's moduli of the set cements.

4.2.1 Sensitivity Analysis of PEEQ after Well Completion

Fig. 4.13 unmistakably illustrates that cement PEEQ increases for set cements with high Young's modulus and low cement cohesion, Co. When Co increases, cement PEEQ decreases for different cement Young's moduli, Ec. Cements with Young's modulus lower than 1.0 E+6 psi clearly had low cement PEEQ. Cement PEEQ was null for cement cohesion of 2,600 psi and higher.

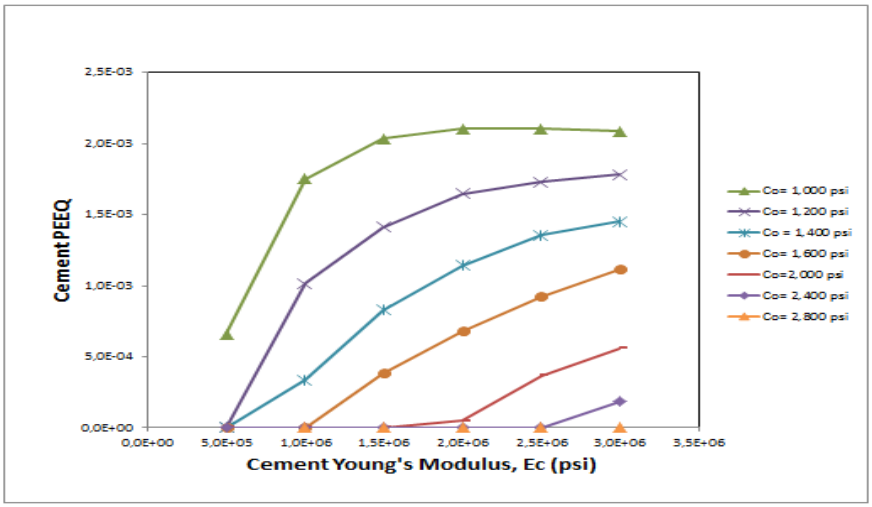

Fig. 4.13—Cement Young's Modulus, Ec (psi) vs. Cement PEEQ after well completion for cement Poisson's ratio of 0.15

Fig. 4.14 clearly shows that set cements with a Young's modulus of 1 E+6 psi had higher plastic deformation for set cements with low Poisson's ratio and low Co. In set cements with Young's modulus of 1.0 E+6 psi, cement PEEQ was negligible for Co of 2,000 psi and higher.

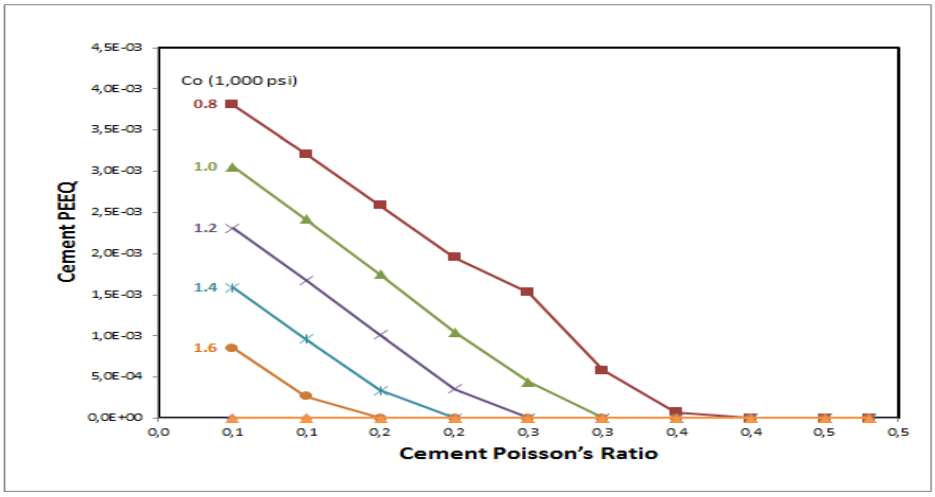

Fig. 4.14—Cement Poisson's Ratio vs. Cement PEEQ after well completion for cement Young's modulus of 1.0 E+6 psi

Figs. 4.15 and 4.16 show no change in formation PEEQ for different scenarios of Ec, Co, and, cement Poisson's ratio after well completion. This means that regardless of mechanical properties, the set cements had the same formation PEEQ after well completion.

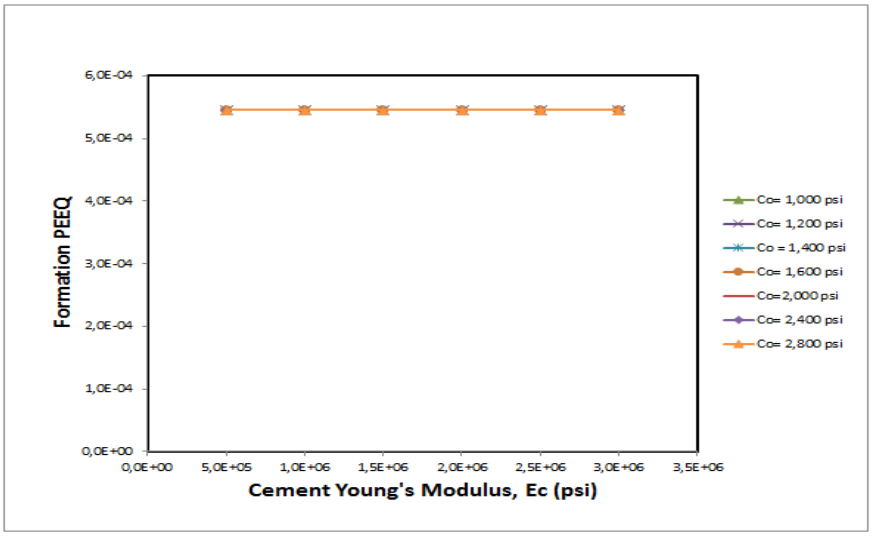

Fig. 4.15—Cement Young's Modulus, Ec (psi) vs. Formation PEEQ after well completion for cement Poisson's ratio of 0.15

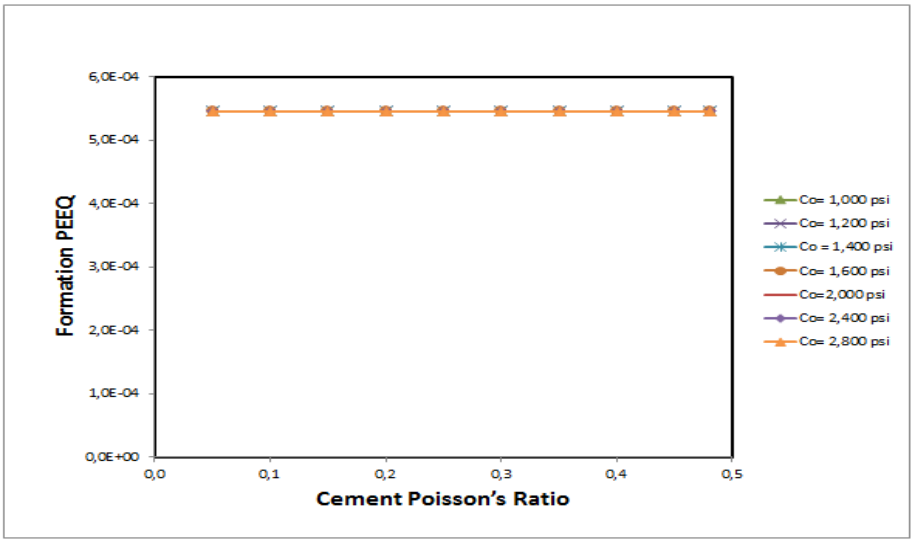

Fig. 4.16—Cement Poisson's Ratio vs. Formation PEEQ after well completion for cement Young's modulus of 1.0 E+6 psi

Fig. 4.17 shows an example of the FEA where cement PEEQ was mainly created at the casing/cement contact. The maximum formation PEEQ was in the y-axis that coincides with the maximum horizontal in-situ stress direction. Plastic deformation of cement and formation could instigate inner and outer microannuli, in that order.

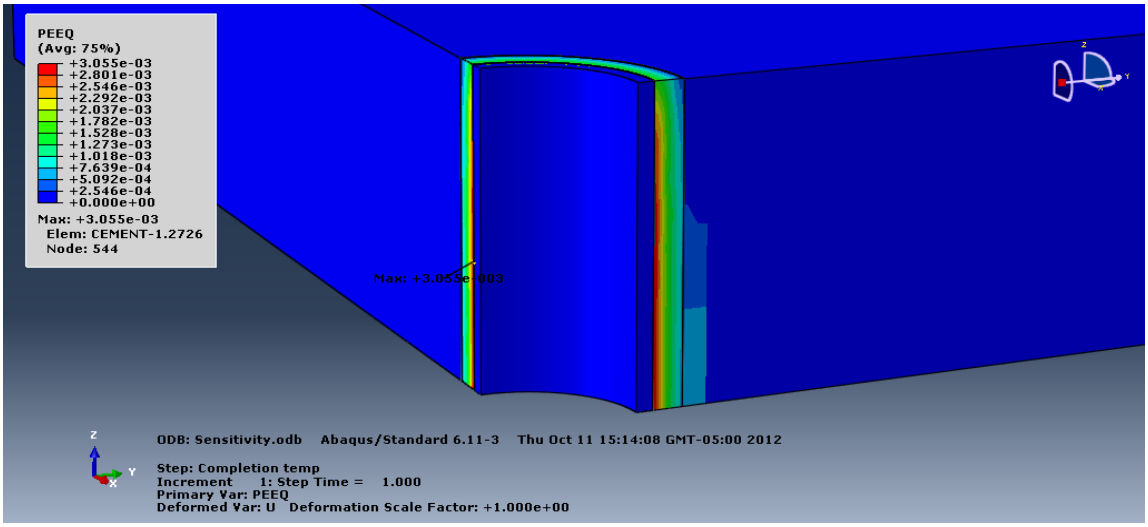

Fig. 4.17—FEA for cement Young's modulus of 1.0 E+6 psi, cement cohesion of 1,000 psi, and cement Poisson's ratio of 0.05 after well completion

Consistent with the previous sensitivity analysis, set cements can be easily designed with low Young's modulus, especially lower than 1.0 E+6 psi, and high cement cohesion and high Poisson's ratio to reduce cement PEEQ during well completion. Chapter V of this dissertation includes lab tests where Co decreases when cement Young's modulus decreases, and therefore a correct balance of both properties is necessary for a good cement design.

4.2.2 Sensitivity Analysis of PEEQ After Hydraulic Fracturing

During hydraulic fracturing jobs, the casing expands, pushing the cement against the formation. Figs. 4.18 and 4.19 clearly show that cement PEEQ decreases for low Ec, especially below 1.0 E+6 psi, high values of Co, and high cement Poisson's ratios.

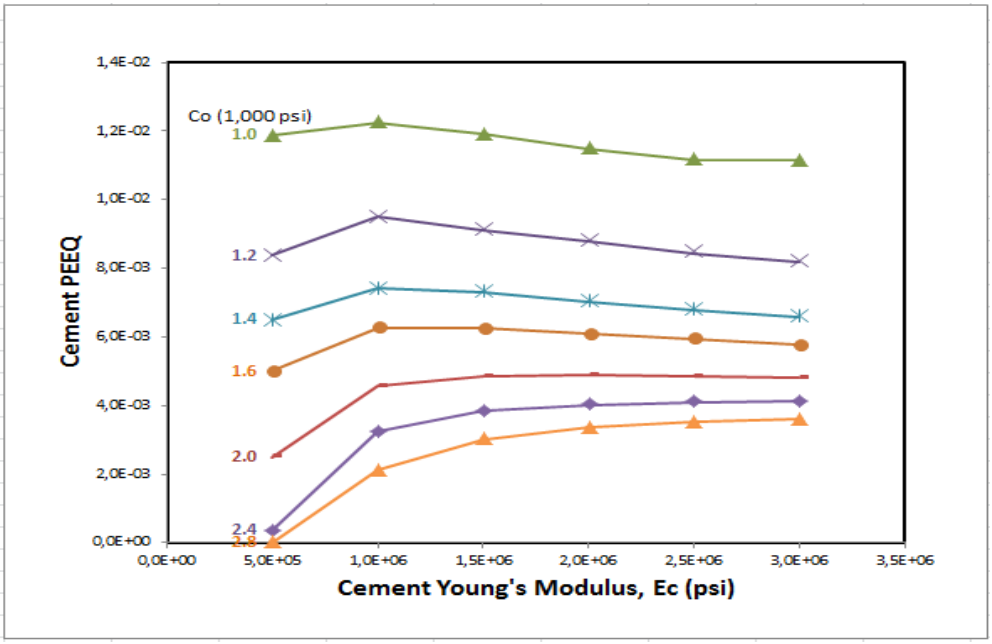

Fig. 4.18—Cement Young's Modulus, Ec (psi) vs. Cement PEEQ after hydraulic fracturing for cement Poisson's ratio of 0.15

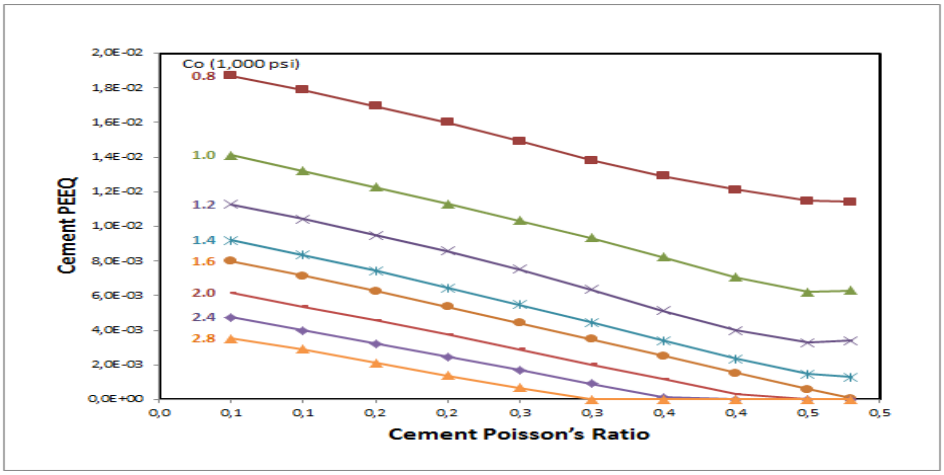

Fig. 4.19—Cement Poisson's Ratio vs. Cement PEEQ after hydraulic fracturing for cement Young's modulus of 1.0 E+6 psi

Fig. 4.20 illustrates that formation PEEQ depends directly on E_c. Consequently, when E_c increases, formation PEEQ increases, too. Formation PEEQ increased sharply when Ec went up from 0.5 E+6 psi to 1.0 E+6. Therefore, a cement set with a Young's modulus lower than 1.0 E+6 psi and high had low cement and formation PEEQ.

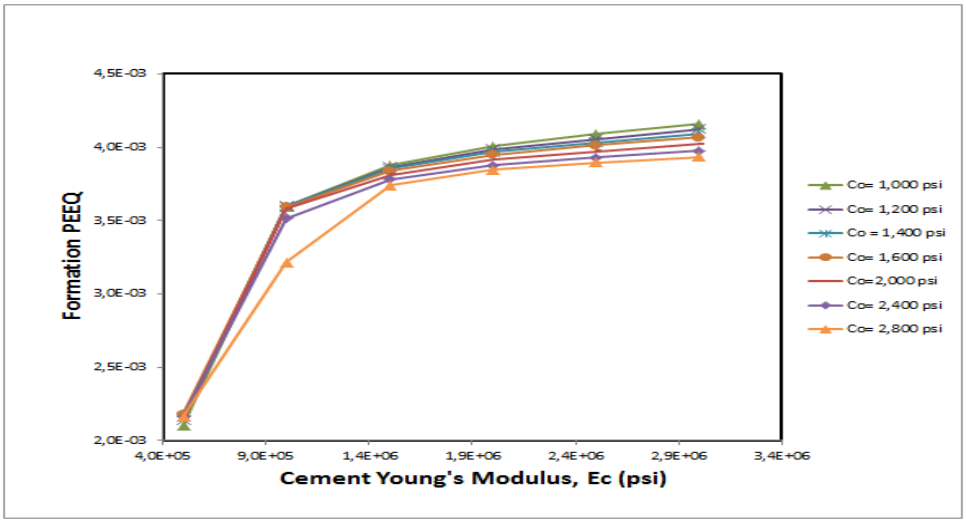

Fig. 4.20—Cement Young's Modulus, Ec (psi) vs. Formation PEEQ after hydraulic fracturing for cement Poisson's ratio of 0.15

Formation PEEQ did not behave linearly with cement Poisson's ratio and Co after hydraulic fracturing (Fig. 4.21). Formation PEEQ results depend on the specific value of cement Poisson's ratio and Co.

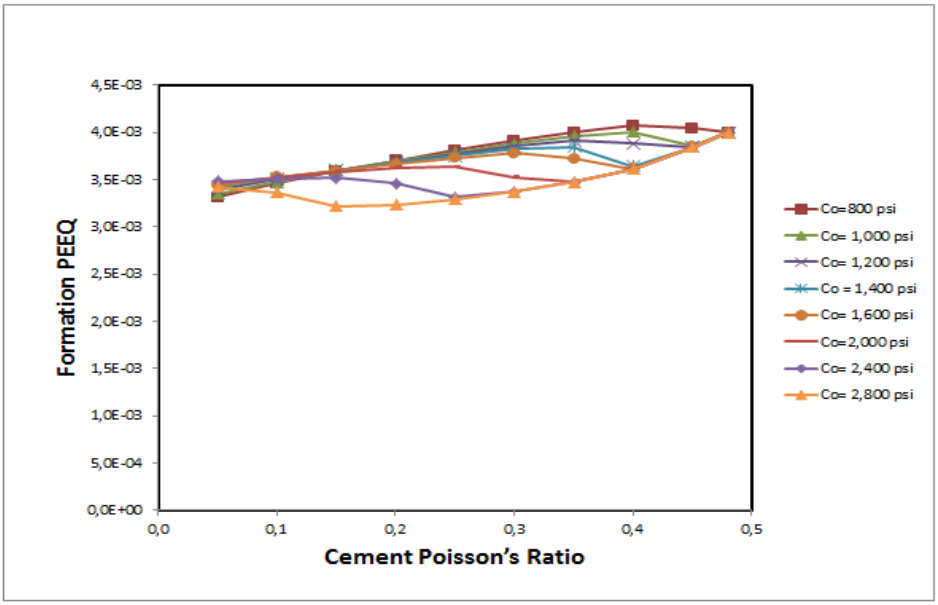

Fig. 4.21—Cement Poisson's Ratio vs. Formation PEEQ after hydraulic fracturing for cement Young's modulus of 1.0 E+6 psi

Fig. 4.22 shows an example of the FEM after hydraulic fracturing done during the sensitivity analysis. PEEQ appeared in the whole cement sheath, and it can initiate cracks in the set cement. Formation PEEQ took place in the maximum horizontal stress direction y-axis.

Cement and formation PEEQ increased several times from well completion to the hydraulic fracturing step. This is because the pressure required during hydraulic fracturing jobs acts on the inner surface of the casing, stretching the set cement and leading to plastic deformation. Moreover, cement PEEQ increased drastically when the Young's modulus went from 0.5 E+6 psi to 1.0 E+6 psi for different cement cohesions. Finally, cement PEEQ was low for set cements with high Co and low Ec for hydraulic fracturing jobs.

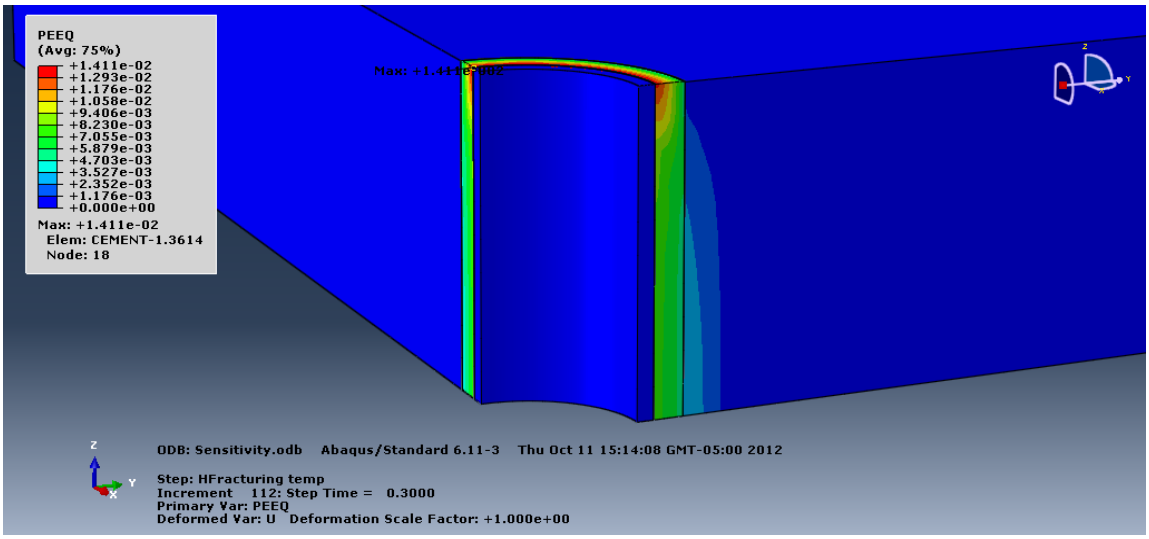

Fig. 4.22—FEA for cement Young's modulus of 1.0 E+6 psi, cement cohesion of 1,000 psi, and cement Poisson's ratio of 0.05, after hydraulic fracturing

4.2.3 Sensitivity Analysis of PEEQ During Well Production

During well production, the hydrostatic pressure inside the casing decreases and contracts it, reducing compressive stresses of cement and formation. This FEA considered a bottomhole production pressure of 4,000 psi (Table 4.1).

Fig. 4.23 shows that during well production, set cements with Young's modulus less than 1.0 E+6 psi and Co higher than 1,600 psi were less prone to high PEEQ. Also during well production, set cements with high Poisson's ratio and high Co were less likely to have cement PEEQ (Fig. 4.24). Cement cohesion, Co, was clearly an important mechanical property to avoid cement plastic deformation.

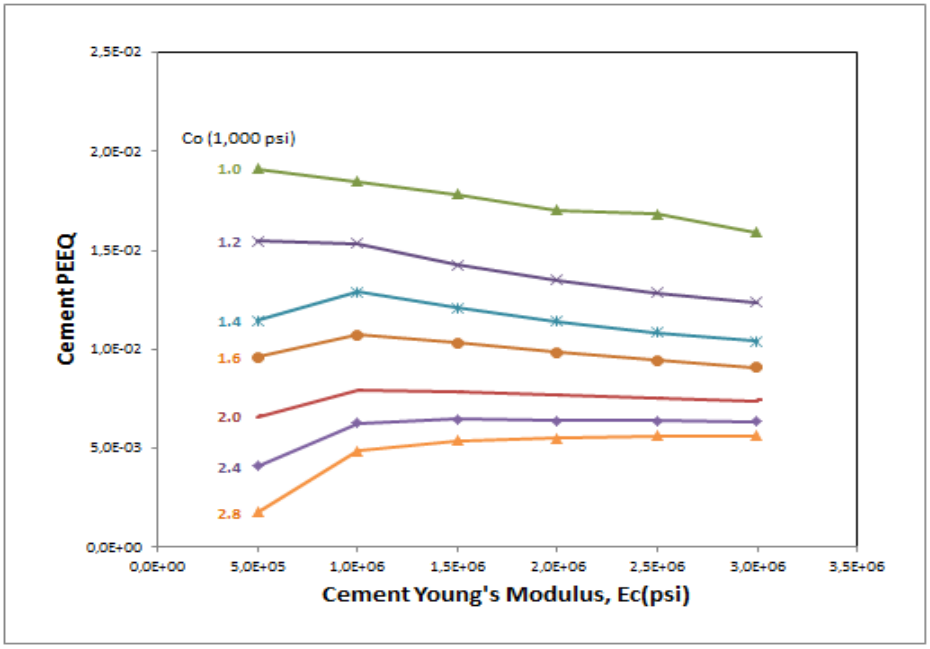

Fig. 4.23—Cement Young's Modulus, Ec (psi) vs. Cement PEEQ during production for cement Poisson's ratio of 0.15

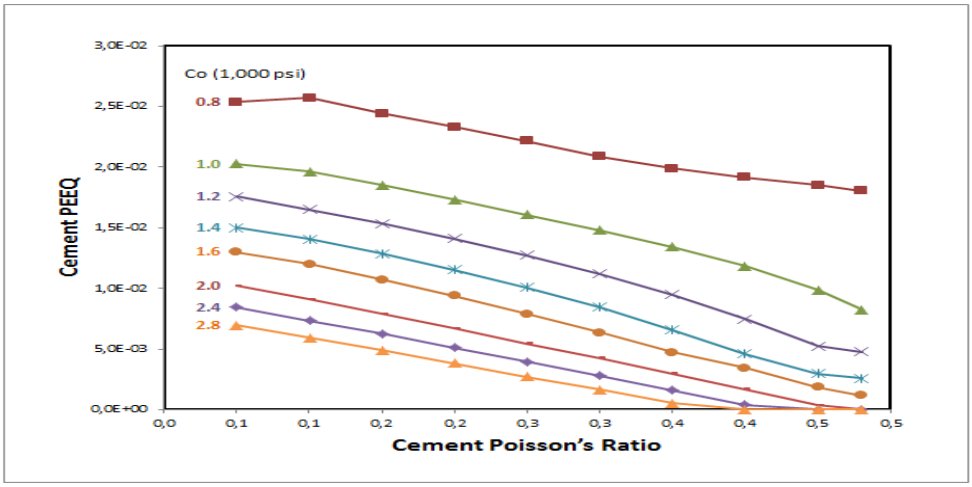

Fig. 4.24—Cement Poisson's ratio vs. cement plastic deformation during well production for cement Young's modulus of 1.0 E+6 psi

Fig. 4.25 shows that formation PEEQ increased when cement Young's modulus also increased during well production. Clearly, formation PEEQ does not depend on Co. Also, formation PEEQ increases abruptly in the set cements with Young's modulus

between 0.5 E+6 psi and 1.0 E+6 psi. I will show in Chapter V that most of the set cements tested in the rock mechanics lab had a Young's modulus between 0.5 E+6 and 1.5 E+6 psi. Also, Fig. 4.26 does not show a linear proportion of formation PEEQ and cement Poisson's ratio or cement Co during well production.

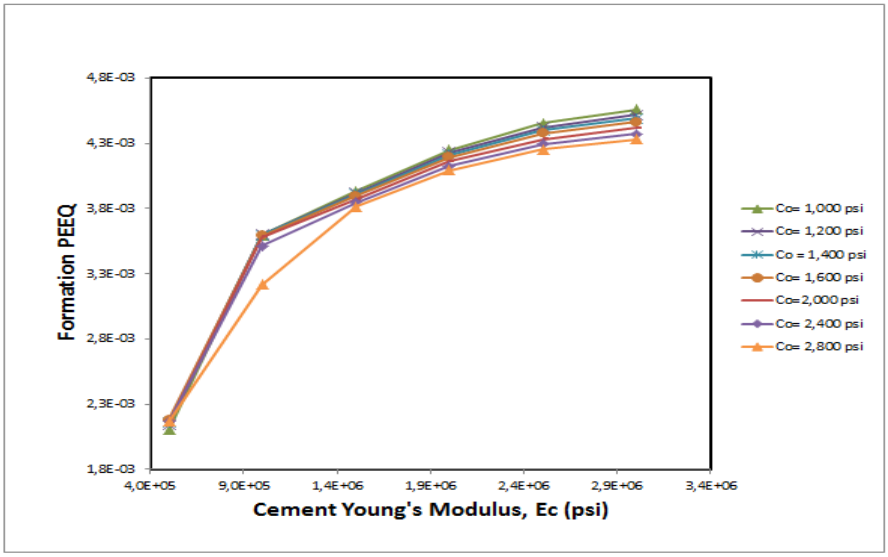

Fig. 4.25—Cement Young's Modulus, Ec (psi) vs. Formation PEEQ during well production for cement Poisson's ratio of 0.15

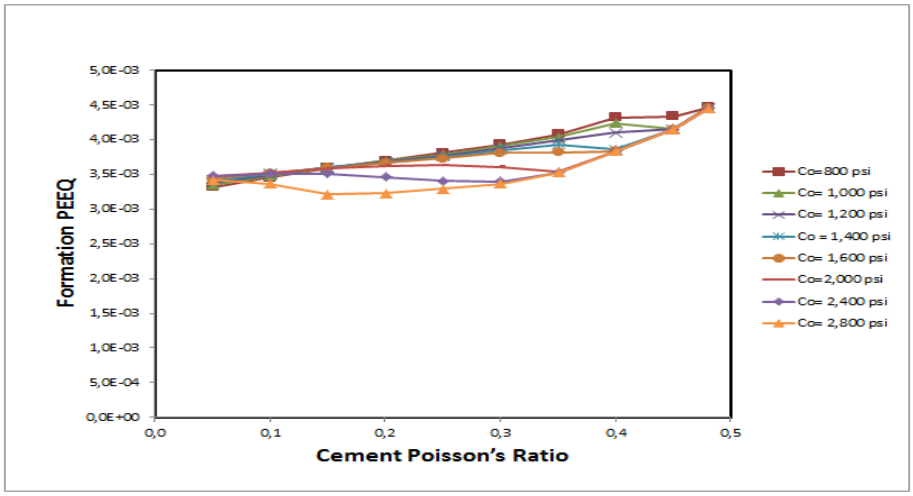

Fig. 4.26—Cement Poisson's Ratio vs. Formation PEEQ during well production for cement Young's modulus of 1.0 E+6 psi

Fig. 4.27 shows the FEM where PEEQ was higher in the cement than in the formation, leading to inner and outer microannuli. Formation PEEQ was evident in the maximum horizontal stress direction y-axis. The FEA model showed that during the life of the well, PEEQ or total plastic strain of cement and formation were low for well completion, but they increased after hydraulic fracturing jobs and well production. Hydraulic fracturing jobs were the main source of cement and formation PEEQ.

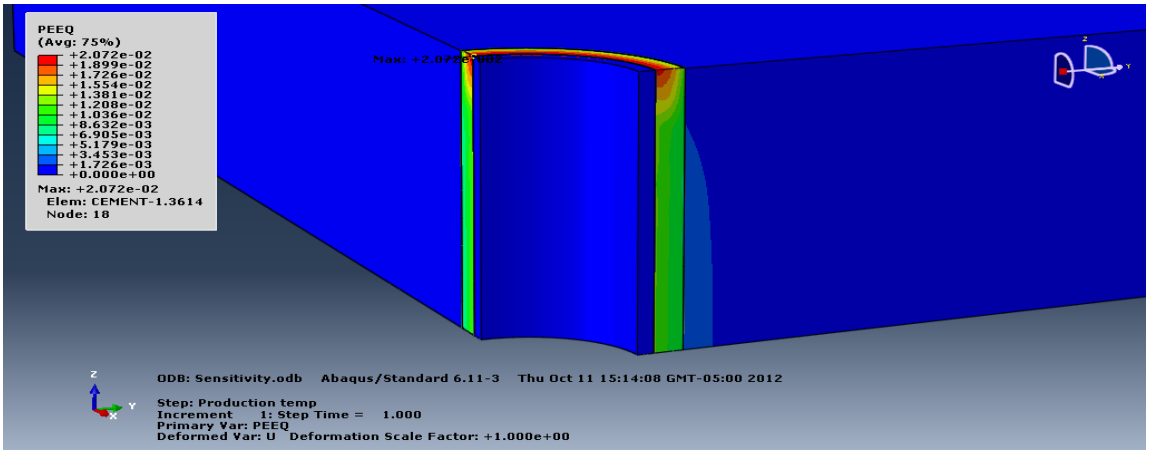

Fig. 4.27— FEA for cement Young's modulus of 1.0 E+6 psi, cement cohesion of 1,000 psi, and cement Poisson's ratio of 0.05 after production (casing, cement, and formation are shown)

Appendix A shows comprehensive results of cement and formation PEEQ as functions of cement Young's modulus, Poisson's ratio, and cement Co. A set cement with a high Young's modulus and therefore high UCS were not the solution to have a good cement sheath. The FEM developed in this project indicates that set cements with low Young's modulus (lower than 1.0 E+6 psi), high cohesion (greater than 1,200 psi), and high Poisson's ratio (greater than 0.2) could reduce cement plastic deformation of "A" rock. Risks of radial cracks of set cements were not included, but it was shown previously that low cement Young's modulus had lower risk of cracks. Numerous cement additives can be added to cement slurries to improve their mechanical properties of set cements, and they will be shown in Chapter V.

4.3 Cement Failure in Front of Soft and Hard Rocks using Abaqus Software

In this section, I studied the cement failure of set cements in soft and hard rocks to determine the risks of plastic deformations, cement debonding, and cracks of the set cements during the life of the well. Tables 4.1, 4.3, and 4.4 show Case 3 well data, mechanical properties of "B" and "C" rocks, and thermal properties of casing, conventional cement, and formation. Cohesion, friction and dilation angles of set cements remained constant at 1,000 psi, 17°, and 16°, in that order.

"B" and "C" rocks had an estimated UCS of 4,980 and 30,860 psi, one-to-one. According to their UCS, "B" rock matches up with a soft rock and "C" rock with a hard rock for a well at 15,000 ft. The other mechanical properties were in concordance with the Young's modulus of the rock.

Figs. 4.27, 4.28, and 4.29 illustrate that cement PEEQ increased when Ec increased and cement Poisson's ratio decreased in front of "B" and "C" rocks after well completion, hydraulic fracturing, and well production. Also, cement PEEQ increased from well completion to well production in each scenario.

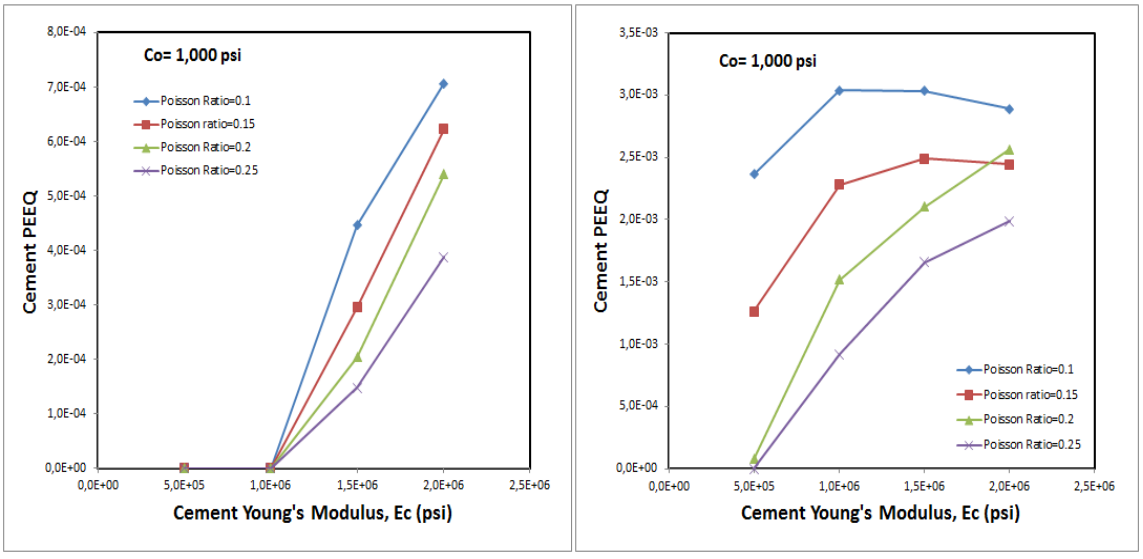

Fig. 4.28—PEEQ of set cement after well completion for "B" rock (left) and "C" rock (right)

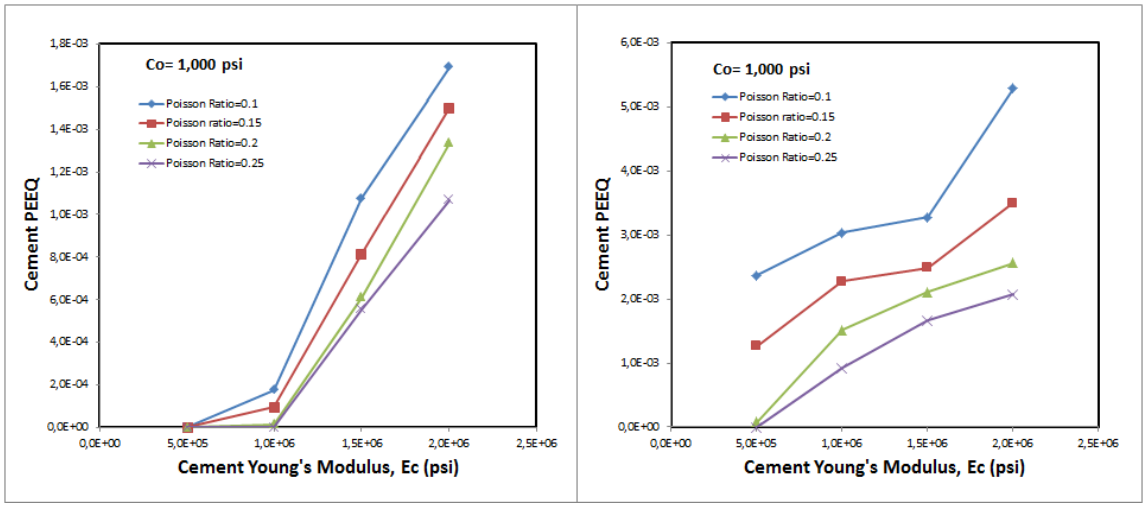

Fig. 4.29—PEEQ of set cements after hydraulic fracturing job for "B" rock (left) and "C"rock (right)

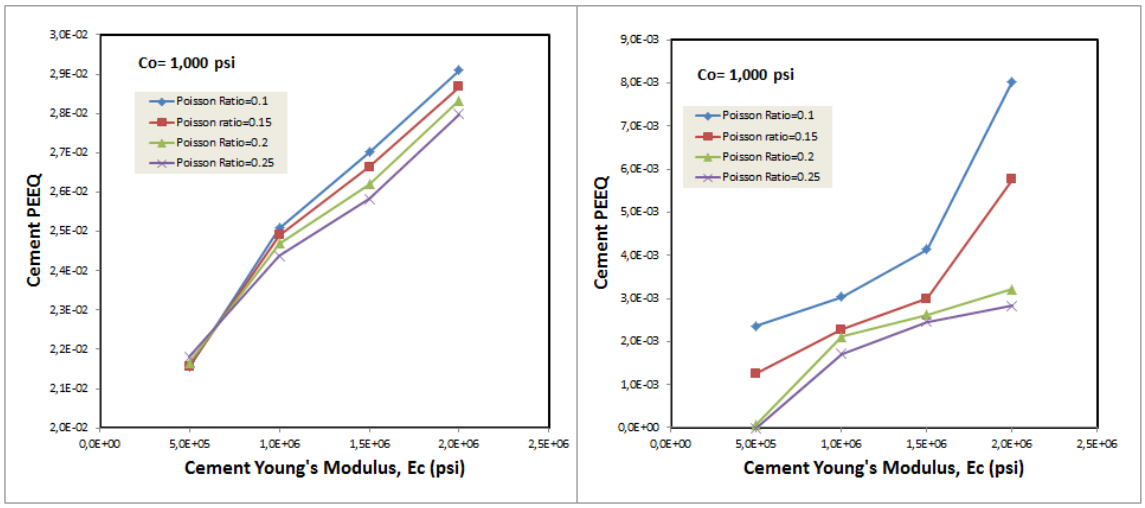

Fig. 4.30—PEEQ of set cement during well production for "B" rock (left) and "C" rock (right)

"B" rock had lower cement PEEQ after well completion and hydraulic fracturing, but during well production "B" rock had higher cement PEEQ than "C." The FEM showed plastic deformation of "B" rock in the direction of the minimum horizontal stress x axis during drilling, and this value continued constant during well life.

Formation PEEQ increased when cement Young's modulus increased and cement Poisson's ratio decreased (Fig. 4.31). Formation PEEQ was created during hydraulic fracturing, and it did not increase during well production.

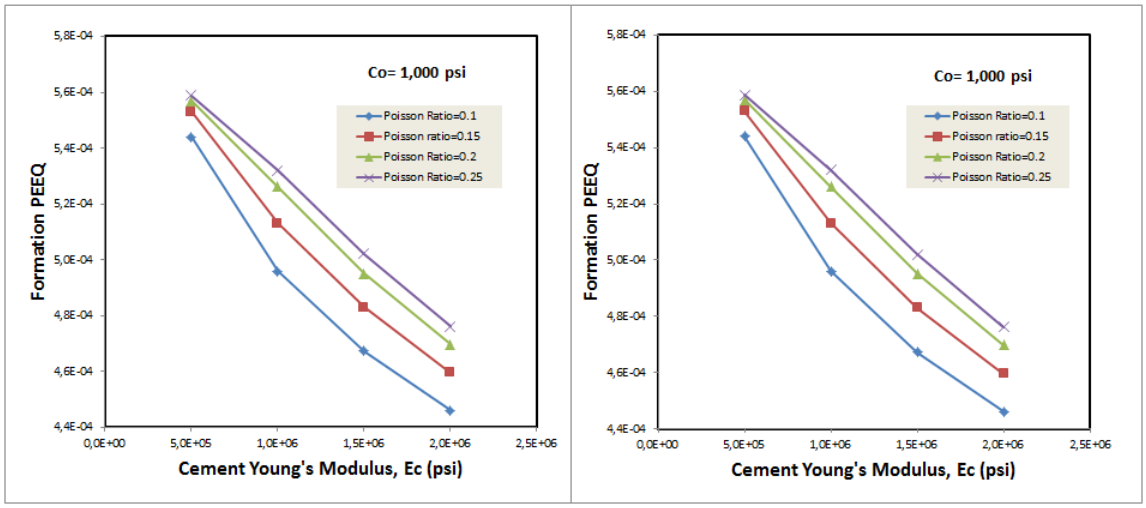

Fig. 4.31—Formation PEEQ after hydraulic fracturing (left) and well production for "C" Rock (right)

Fig 4.32 clearly shows that set cements were more likely to have debonding in front of "B" rock than in "C" rock during well completion. Set cements were always in compression in front of "C" rock during well completion. If tensile radial stresses of set cements are higher than their debonding strength, the cement debonds from the casing.

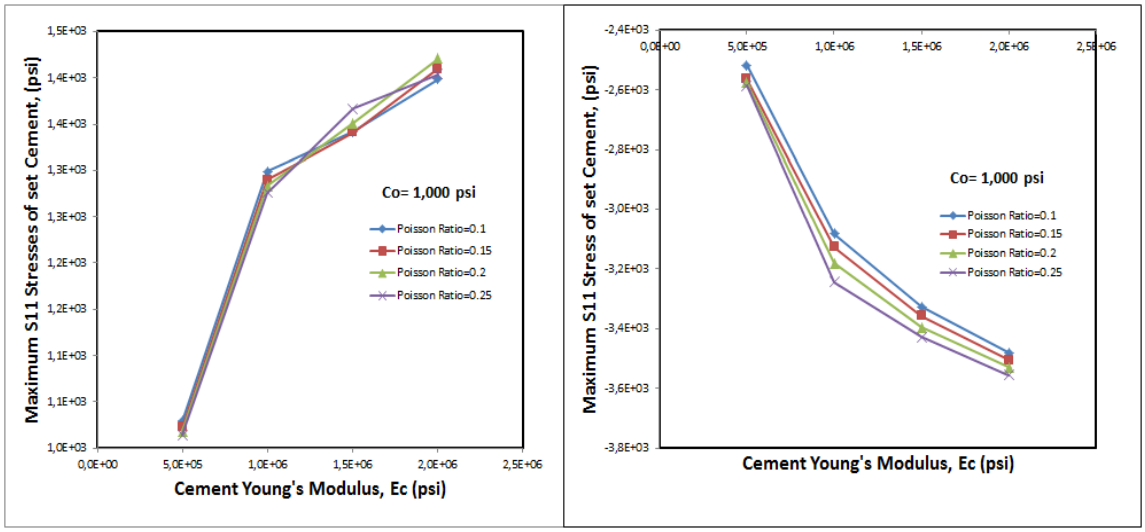

Fig. 4.32—Maximum radial stress of set cements after well completion in front of "B" rock (left) and "C" rock (right)

Fig. 4.33 illustrates that set cements had higher tensile tangential stresses in front of “B” rock than in front of “C” rock. Tensile tangential stresses of set cements in front of “C” rock were less than 150 psi, or in compression. If tensile radial stresses of set cements are higher than their tensile strength, cracks are created in the set cements.

Fig. 4.34 shows that set cements in front of “B” rock were more likely to have debonding than in front of “C” rock, because tensile radial stresses of set cements were higher with “B” rock than with “C” rock. Also, set cements with the lowest Young’s modulus and highest Poisson’s ratio were less prone to debonding in front of “C” rock.

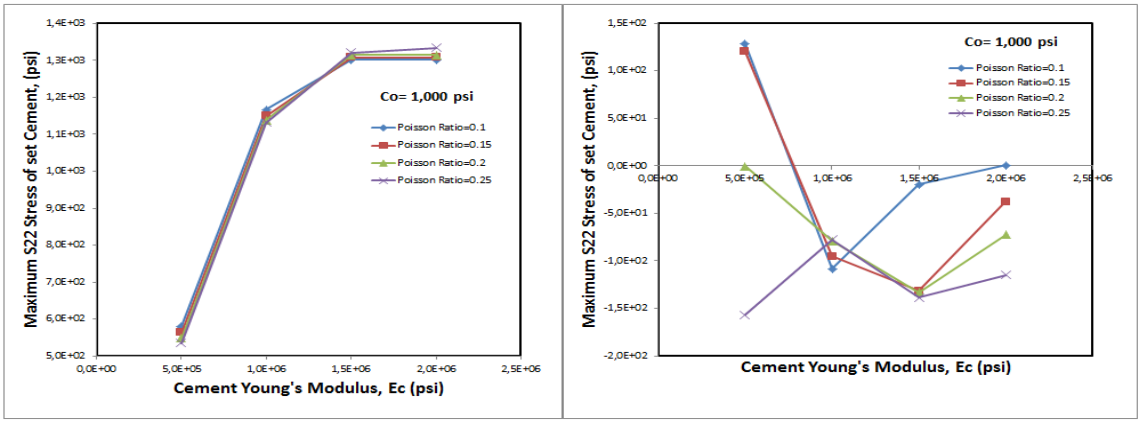

Fig. 4.33—Maximum tangential stress of set cements after hydraulic fracturing in front of “B” rock (left) and “C” rock (right)

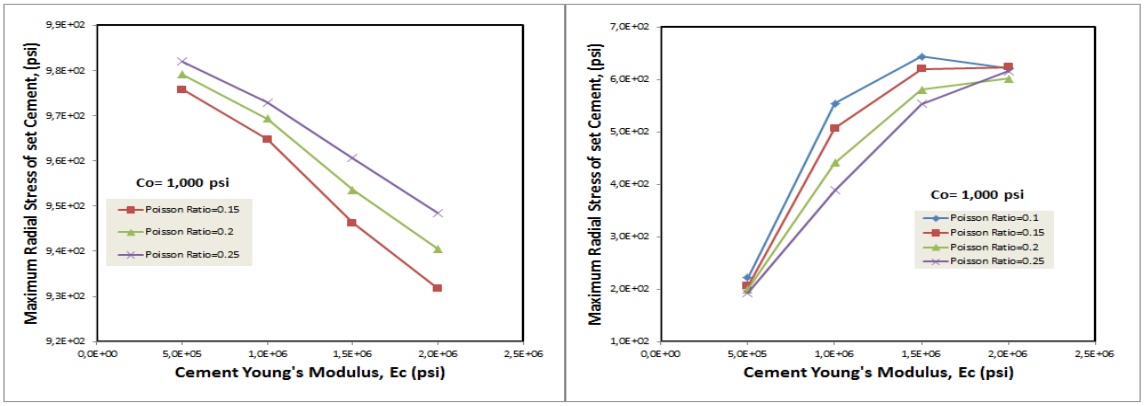

Fig. 4.34—Maximum radial stress of set cements during well production in front of “B” rock (left) and “C” rock (right)

Wrapping up the previous results, set cements in front of soft rocks were more likely to have debonding and radial cracks than in front of hard rocks. Also, set cements in front of soft formations were less prone to plastic deformation than hard rocks during hydraulic fracturing jobs.

4.4 Cement Failure with Different Rock Strengths and Cement Types using Abaqus Software

Several rock mechanical properties of the rocks and set cements were analyzed to validate the common assumption that the set cement with the lowest Young's modulus/ tensile strength ratio has the best zonal isolation. The FEM involves a thermoelastoplastic analysis during drilling, cementing, well completion, hydraulic fracturing, and well production to investigate the effect of PEEQ, radial cracking, and debonding on different mechanical properties of rocks and set cements. Well data used for this sensitivity analysis was included in Case 4 of Table 4.1. Mechanical properties of set cements and rocks were given in Tables 4.5 and 4.6, in that order. Thermal properties of casing, set cements and formations were defined in Table 4.4. Cement bonding strength was assumed as 0.83 times its tensile strength, according to lab tests of ThermaLock cement discussed in Chapter V.

Mechanical properties of set cements and rocks were determined during this research, and they were carefully selected to investigate the effect of set cements with different Young's moduli, UCS, and Poisson's ratio on diverse rock properties. C7 and Guadalupe formations match with soft and medium-hard formations for a 15,000-ft well. Likewise, Mirador and Barco formation correspond to hard formations for a 15,000-ft well. Rock mechanical properties were determined from formations of Cupiagua wells in Colombia.

TABLE 4.5—CEMENT MECHANICAL PROPERTIES OF SELECTED CEMENTS

Cement Name	UCS, psi	Young's Modulus, (Ec) psi	Poisson's Ratio(υ_c)	Tensile Strength, (To), psi	Friction Angle (ϕ_c), deg	Cohesion, (Co), psi	Young's Modulus / Tensile Strength Ratio
Design 2TL (14.5-ppg)	3,416	1.14+06	0.14	513	13	1,359	2,222
Design 7 (15.6-ppg)	3,999	6.92E+05	0.053	449.8	28	1,300	1,538
San Antonio (14.5-ppg)	6,868	1.41E+06	0.19	675	25	2,200	2,090

TABLE 4.6—FORMATION MECHANICAL PROPERTIES OF SELECTED FORMATIONS

Formation Name	Young's Modulus (Ef), psi	UCS, psi	Poisson's Ratio (υ_f)	Friction Angle (ϕ_f), deg	Dilation Angle , (Ψ_d) deg	Cohesion, psi
C7	1.03E+6	11,511	0.24	36	36	2,939
Guadalupe	2.05E+06	14,588	0.25	42	42	4,873
Mirador	6.29E+06	36,200	0.13	50	50	5,776
Barco	8.30E+06	31,000	0.25	45	25	5,700

The difference between the mechanical properties of set cements and rocks make engineering decisions difficult. Therefore, running the FEM was necessary to determine the chances of radial cracks, debonding and PEEQ of the set cements and rocks during the well life.

Tables 4.7 and 4.8 clearly show that cement Design 7 had the lowest von Mises stresses (VM), tangential stresses (S22), and radial stresses (S11) in front of C7 and Guadalupe formations after hydraulic fracturing and well production. However, this set cement developed incipient radial cracks in the casing/cement contact during hydraulic fracturing, and partial debonding of casing/cement during well production. The FEM did not show PEEQ of the three set cements of C7 and Guadalupe formations. Cement Design 7 had the lowest Young's/tensile strength ratio of the set cements shown in Table 4.5, and it could have the best zonal isolation of the three assessed set cements for C7 and Guadalupe formations.

TABLE 4.7—FEA WITH DIFFERENT SET CEMENTS AT C7 FORMATION

	Hydraulic Fracturing					Well Production				
Cement Name	Max. VM, psi	Max. S22, psi	Radial cracks	Cem. PEEQ, %	Form. PEEQ, %	Max. VM, psi	Max. S11 Stress, psi	Debond	Cement PEEQ, %	Form. PEEQ, %
Design 2TL	1,845	864	Initial cracks	0	0	1,608	818	Partial	0	0
Design 7	**1,530**	**588**	**Initial cracks**	**0**	**0**	**1,309**	**664**	**Partial**	**0**	**0**
San Antonio	2,010	1,026	Initial cracks	0	0	1,786	877	Partial	0	0

TABLE 4.8—FEA WITH DIFFERENT SET CEMENTS AT GUADALUPE (SHALE) FORMATION

	Hydraulic Fracturing					Well Production				
Cement Name	Max. VM, psi	Max. S22, psi	Radial cracks	Cem. PEEQ, %	Form. PEEQ, %	Max. VM, psi	Max. S11 Stress, psi	Debond	Cement PEEQ, %	Form. PEEQ, %
Design 2TL	1,964	758	Initial cracks	0	0	1,795	792	Partial	0	0
Design 7	**1,670**	**542**	**Initial cracks**	**0**	**0**	**1,461**	**629**	**Partial**	**0**	**0**
San Antonio	2,106	881	Initial cracks	0	0	1,967	857	Partial	0	0

Tables 4.9 and 4.10 clearly illustrate that San Antonio cement had the best zonal isolation of the three evaluated set cements of Table 4.5. However, Barco formation had some PEEQ that could initiate an outer microannulus. Set cements with the lowest Young's modulus/tensile strength ratio was not the solution, especially for hard formations like Mirador and Barco formations, and the integrity of the set cement had to be checked with the FEM.

TABLE 4.9—FEA WITH DIFFERENT SET CEMENTS AT MIRADOR FORMATION

Cement Design	Hydraulic Fracturing					Well Production				
	Max. VM, psi	Max. S22, psi	Radial cracks	Cem. PEEQ, %	Form. PEEQ, %	Max. VM, psi	Max. S11 Stress, psi	Debond	Cement PEEQ, %	Form. PEEQ, %
2TL	2,611	368	No	0.083	0	2,506	323	No	0.12	0
Design 7	2,787	721	Initial Cracks	0.310	0	2,229	314	No	0.31	0
San Antonio	**2,674**	**365**	**No**	**0**	**0**	**2,861**	**361**	**No**	**0**	**0**

TABLE 4.10— FEA WITH DIFFERENT SET CEMENTS AT BARCO FORMATION

Cement Design	Hydraulic Fracturing					Well Production				
	Max. VM, psi	Max. S22, psi	Radial cracks	Cem. PEEQ, %	Form. PEEQ, %	Max. VM, psi	Max. S11 Stress, psi	Debond	Cement PEEQ, %	Form. PEEQ, %
Design 2TL	2,824	359	No	0.054	0.045	2,486	236	No	0.073	0.045
Design 7	2,925	727	Radial cracks	0.406	0.052	2,215	240	No	0.406	0.052
San Antonio	**2,768**	**299**	**No**	**0**	**0.043**	**2,899**	**254**	**No**	**0**	**0.043**

Fig. 4.35 clearly shows that tangential stresses of cement Design 7 in front of Barco formation were higher than the tensile strength of the cement during the planned hydraulic fracturing job. Therefore, initial radial cracks of cement Design 7 were evident. Also, PEEQ of cement Design 7 and Barco formation were obvious after the hydraulic fracture job.

Fig. 4.36 illustrates that tangential stresses of San Antonio cement in front of Barco formation did not reach tensile strength during hydraulic fracturing. Consequently, San Antonio cement did not have radial cracks during the hydraulic fracturing job. Nevertheless, PEEQ was developed in Barco formation in the maximum horizontal in-situ stress direction y-axis.

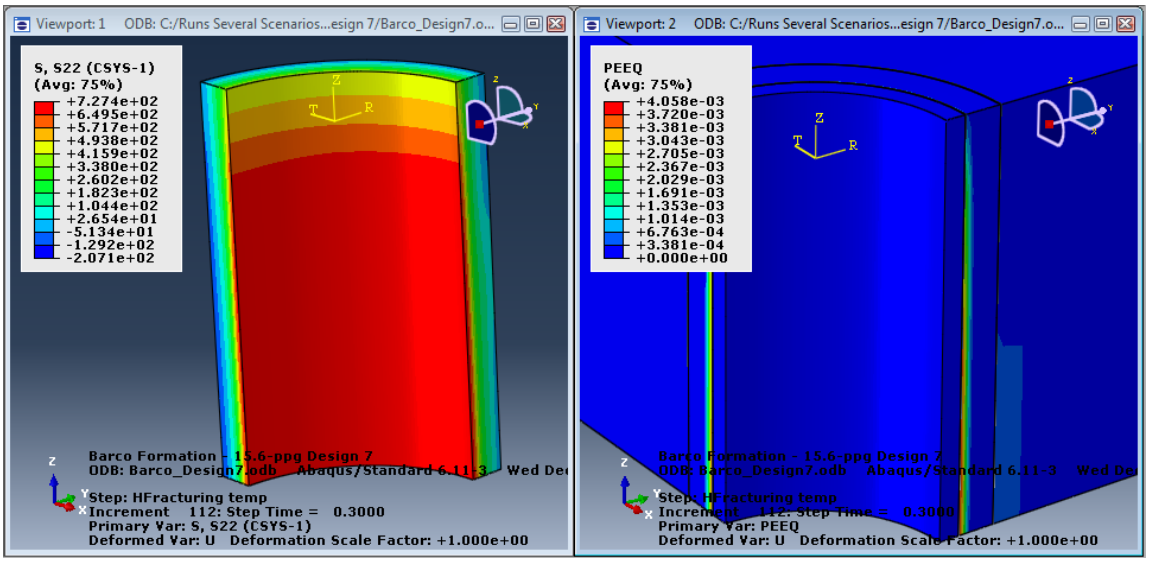

Fig. 4.35—Tangential stresses of Design 7 cement (left) and PEEQ of cement Design 7 and Barco formation (right) after hydraulic fracturing

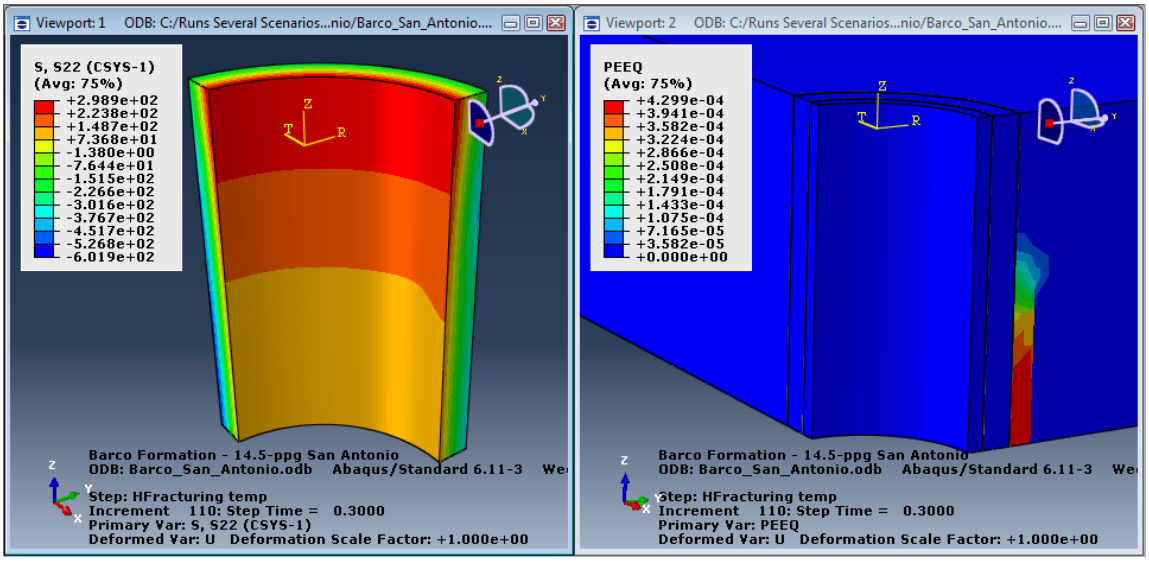

Fig. 4.36—Tangential stresses of San Antonio cement (left) and PEEQ of cement San Antonio and Barco formation (right) after hydraulic fracturing

This chapter showed that set cements with the lowest Young's moduli, the highest Poisson's ratios, and cement Cos experienced the lowest formation and cement PEEQ. Furthermore, set cements with lower Young's moduli than the rock were less

likely to have debonding and radial cracks. Moreover, set cements in front of soft rocks were more prone to debonding and radial cracks than in front of hard rocks. Likewise, set cements in front of soft formations had lower plastic deformations than in hard rocks during hydraulic fracturing jobs. Also, if hard rocks had plastic deformations during hydraulic fracturing jobs, they were created in the maximum horizontal stress direction y-axis.

Finally, this work showed that set cements with the lowest Young's modulus/tensile strength ratio were not the solution for zonal isolation of hard formations, and FEA was essential to select the appropriate set cement. Chapter V of this dissertation includes lab tests with different products to improve elasticity of set cements to avoid or reduce the plasticity of set cements and rocks around the borehole.

CHAPTER V

LABORATORY TESTS IN ELASTIC- PLASTIC CEMENTS

This chapter shows laboratory tests done for assorted Portland and non-Portland cements designed during this research. Set cements from different cementing companies were analyzed to measure their mechanical and thermal properties to be used at Apiay, Chichimene, and Cupiagua fields for Ecopetrol, Colombia. These laboratory tests were used in the finite-element analyses built during this study to determine whether these cements can withstand the different loads during the life of the wells. Also, well cements should have water permeability lower than 0.1 md to prevent interzonal communication.[12]

The goal of the slurry designs was finding elastic set cements from different cementing companies to reduce their failure in three different oil fields of Ecopetrol. Also, I assessed Portland and non-Portland cements for an in-situ combustion project in Chichimene field.

Uniaxial, triaxial, and Brazilian tests of different set cements were done with an MTS 815 rock mechanics system at the Colombian Petroleum Institute (ICP) of Ecopetrol in Colombia. Also, uniaxial and triaxial tests were done by Schlumberger and Halliburton in Houston and Duncan, Oklahoma, respectively. Set cements with densities of 14.2 ppg, 14.5 ppg, 15.6 ppg, and 15.8 ppg were tested to meet field requirements.

Cement samples for uniaxial and triaxial tests had an average of 2.97-in. lengths and 1.5-in. diameters, and length-to-diameter ratios of 1.98. Samples for the Brazilian tests had an average length-to-diameter ratio of 0.5. The lengths of the samples for the Brazilian tests averaged 0.75 in., and the diameter averaged 1.5 in. Core dimensions of set cements evaluated during this dissertation were in agreement with the International Society of Rock Mechanics.

Cement slurry designs were done in agreement with the three cementing companies during this study to incorporate flexible particles or additives to improve

elasticity and resiliency of the set cements. Flexible cements can withstand cyclic changes that occur over the life of HTHP wells and in-situ combustion projects. Appendixes B and C show cement slurry designs and laboratory tests result for the Halliburton, Schlumberger, and Baker cements; the designs were tested following API Specification 10A and API Recommended Practice (RP) 10B.

Portland cement is primarily a mixture of tricalcium silicate (C_3S) and dicalcium silicate (C_2S). Addition of water to Portland cement forms a gelatinous calcium silicate hydrate called the "C-S-H phase," which is responsible for the strength and stability of the set cement. At temperatures above 230°F (110°C), the C-S-H phase becomes alpha dicalcium silicate hydrate (α-C_2SH). Alpha dicalcium silicate is much denser and more permeable than the C-S-H phase. Also, the compressive strength of the set cement decreases at temperatures above 230°F. [12]

The strength retrogression problem was solved by reducing the bulk lime-to-silica ratio (C/S ratio) in the cement. The conversion to α-C_2SH was prevented by the addition of 35% to 40% by weight of cement (BWOC) of silica flour or silica sand, reducing the CaO/SiO_2 ratio to about 1.0. The molar CaO/SiO_2 ratio for neat cement is approximately 3. Silica-stabilized Portland cements can withstand temperatures up to 480°F (250°C). The low tensile strength and low resiliency of Portland cement in high temperatures cause it to crack and buckle under high stress, instead of deforming.[12]

Thermal cements are required in deep oil and gas wells, geothermal wells, and thermal recovery conditions such as steamflooding and in-situ combustion. A typical slurry composition for HTHP wells would consist of Class H or Class G cement, 35% to 40% BWOC silica, weighting agent, dispersants, fluid-loss additives, and retarders for high-temperature conditions. Silica-stabilized Portland cement compositions are used commonly to cement geothermal wells.

The principle of thermal recovery is based on reducing the viscosity of oil by heating it within the reservoir. The reservoir temperature of the in-situ combustion process may normally fluctuate in the range of 572°F to 842°F (300°C to 450°C) and the fire front may reach from 1,202°F to 1,472°F (650°C to 800°C). [42] Portland cement

undergoes strength retrogression when static temperatures exceed 230°F (110°C), and 35% to 40% BWOC silica sand or silica flour must be added. Laboratory studies of Portland cement with silica flour cured at 158°F (70°C) and thermal cycled about 662°F (350°C) confirmed visible large cracks in the set cement.[42]

Some studies support that Portland cement with carbon fibers and metakaolin can be used for in-situ combustion at temperatures lower than 842°F (450°C). Carbon fibers, 10% to 15% BWOC, improve ductility of the Portland cement sheath when it is subjected to thermal cycling. Also, the addition of metakaolin (10% to 15% BWOC) to Portland cement minimizes the release of calcium hydroxide from set, hardened cement and hence retains the compressive strength and low permeability at temperatures lower than 842°F (450°C). [42]

Portland cement has been modified recently to withstand contact with temperatures above 1,472°F (800°C). The approach is adding 35% silica flour, 27.5% graphite/metakaolin, fluid-loss additive, cement dispersant, and the lowest water content possible to minimize the permeability of the set cement.[43] The weakness of these laboratory tests is that CO_2 generated from the in-situ combustion process can deteriorate Portland cement. Latex additive has been used to reduce the CO_2 effect.

If oil wells with in-situ combustion recovery are exposed to temperatures between 700°F and 1,700°F (371°C and 926°C), high-aluminum cements are suitable.[12] Calcium aluminate phosphate (CAP) cements can withstand all temperatures generated at the combustion front, but common cementing additives used for Portland cement-based systems don't work for CAP cements.[42] CAP cement is not affected by CO_2.

5.1 Laboratory Tests done for Halliburton Cements

5.1.1 Uniaxial, Tensile Strength and Petrophysical Tests of Halliburton Portland Cements

It is important to have several set cements with the desired mechanical properties at different temperatures and confining pressures to be applied under several constraints like slurry density, mechanical rock properties, in-situ temperatures, and costs. The

Model 6265 Mechanical Properties Analyzer (MPRO) was used during this study to measure dynamic Young's modulus and Poisson's ratio properties of cement slurries to pick the samples with low Young's modulus before testing them at the rock mechanics lab. Set cements with low Young's modulus create less tangential stresses around the cement sheath and lower tensile strengths are needed to withstand compressive loads. However, I will show once more in Chapter VI that set cements with the lowest Young's modulus/ tensile strength ratios are not enough to guarantee zonal isolation for different oil fields.

The ElastiCem additive includes elastomers and fibers designed by Halliburton to decrease brittleness while enhancing the elasticity and resilience of a cement sheath. The LifeCem additive is an elastomer that gives elasticity and self-healing properties to the set cement, and it can seal microfissures when set cements are in contact with hydrocarbons.[44]

ElastiCem and non-ElastiCem cements were cured at 122◦F for 24 hours and atmospheric pressure, and dry samples were tested in the rock mechanics lab. Plugs of Portland cements categorized by Designs 1 to 9 were cured at 122°F and atmospheric pressure for 72 hours, and wet samples were tested in the rock mechanics lab.

Once 15.8-ppg LifeCem cement slurry was set, cylindrical samples were cured at 201°F and 4,000 psi in a cement autoclave for 10 days to determine expansion, thermal conductivity, and mechanical properties before and after the curing process to get a comparison and analysis of the cement sheath. 15.8-ppg LifeCem cement tests were done in Duncan by Halliburton.

Appendixes B and C show slurry designs and lab tests of Halliburton Portland cements. Cement plugs were tested to determine elasticity and permeability of the set cements for this study at ICP, Duncan and Houston. Appendix B also describes the function of each cement additive. The ability of the set cement to prevent annular fluid flow has economic and environmental implications for the operator company.

Table 5.1 clearly shows that 15.6-ppg cement designs can have lower Young's modulus/tensile strength ratio than 14.5-ppg set cements. Also, cement slurry density

was not the only way to have low Young's modulus of set cement. Cement Design 3 included the ElastiCem additive, which gives self-healing properties when it is in contact with hydrocarbons. These set cements were designed for three oil fields of Ecopetrol.

TABLE 5.1—AVERAGE MECHANICAL PROPERTIES OF HALLIBURTON PORTLAND CEMENTS

Cement Name	UCS, psi	Young's Modulus (Ec), psi	Poisson's Ratio (ν_c)	Tensile Strength (To), psi	Friction Angle (ϕ_c), deg	Cohesion (Co), psi	Young's Modulus/ Tensile Strength Ratio
14.5-ppg ElastiCem	3,126	1.16E+06	0.218	363,7	---	---	3,189
14.5-ppg non-ElastiCem	5,250	1.18E+06	0.217	347.5	---	---	3,390
15.6-ppg ElastiCem	---	---	---	362.3	---	---	---
15.8-ppg ElastiCem	4,430	1.14E+06	0.209	369.5	---	---	3,093
15.8-ppg LifeCem	4,937	1.28E+06	0.158	449	19	1,769	2,851
Design 3 (15.8-ppg)	5,028	6.43E+05	0.089	473.3	24	1,600	1,357
Design 6 (15.6-ppg)	4,692	7.39E+05	0.072	541.6	21	1,600	1,365
Design 7 (15.6-ppg)	3,999	6.92E+05	0.053	449.8	28	1,300	1,538
Design 9 (14.5-ppg)	2,885	5.47E+05	0.113	369.7	---	---	1,480
Design 10 (15.8-ppg)	3,438	9.25E+05	0.2	417	26	1,050	2,218

Fig. 5.1 shows that cement Design 9 had the lowest UCS and Young's modulus of the samples, and this result was related to FDP-C987 elastomer. Chapter VI will show the need of running the FEM to determine the best set cement for different oil fields.

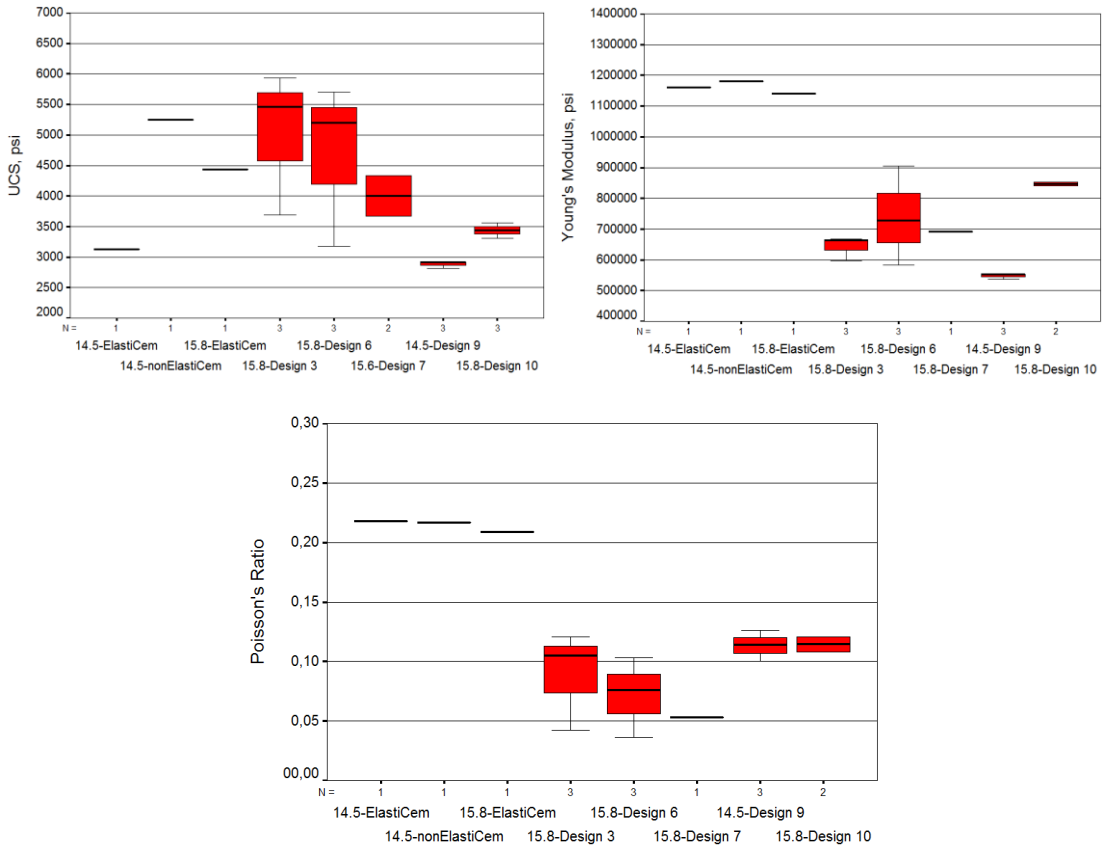

Fig. 5.1—UCS (top left), Young's modulus (top right), and Poisson's ratio (bottom) for Halliburton Portland cements

Fig. 5.2 shows that cement Designs 3, 6 and 7 had higher tensile strength values than the others, and those were associated with glass fibers in the cement designs. Cement Designs 9 and 10 included carbon fibers. Elastomers decreased Young's modulus of Portland set cements, and tensile strength results had better outcomes with glass fibers than carbon fibers.

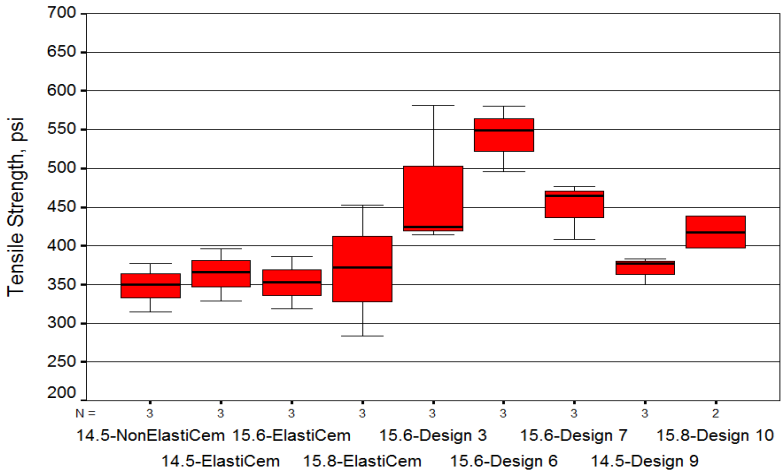

Fig. 5.2—Tensile strength for Halliburton Portland cements

Fig. 5.3 shows stress strain-curves during the compression tests. UCS and Young's modulus were computed from the axial strain curve, and Poisson's ratio was calculated from circumferential and axial strain curves. The Young's modulus was calculated from the slope of the linear part of the axial strain curve. The uniaxial compression photos of set cements showed a failure plane parallel to the axial load. Analogous behavior has been observed in rocks.[45]

The Brazilian test is an indirect method to determine uniaxial tensile strength. Fig. 5.4 shows the loading curve of the disk-shaped specimen required exceeding the tensile stress of set cement, and Eq. 2.68 was used to calculate its tensile strength.

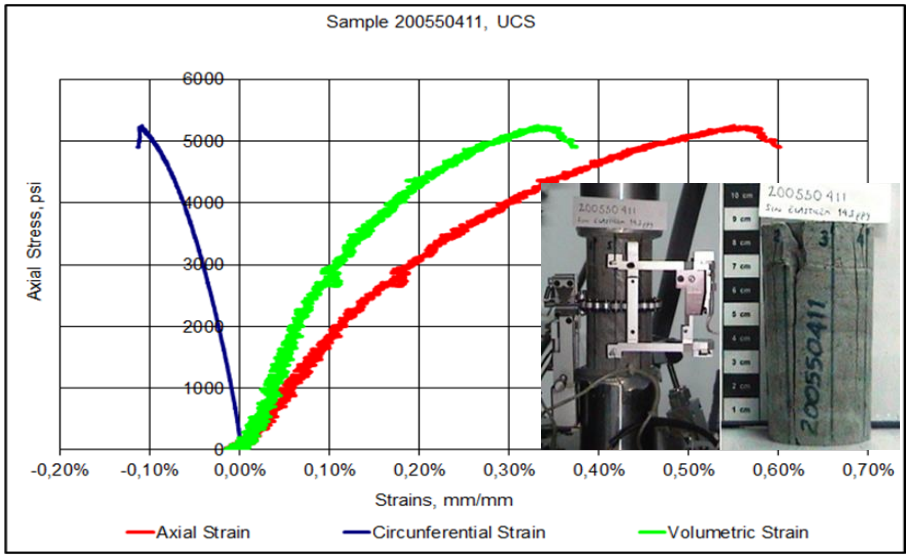

Fig. 5.3—Stress strain-curve and photo of uniaxial test for Halliburton Portland cement

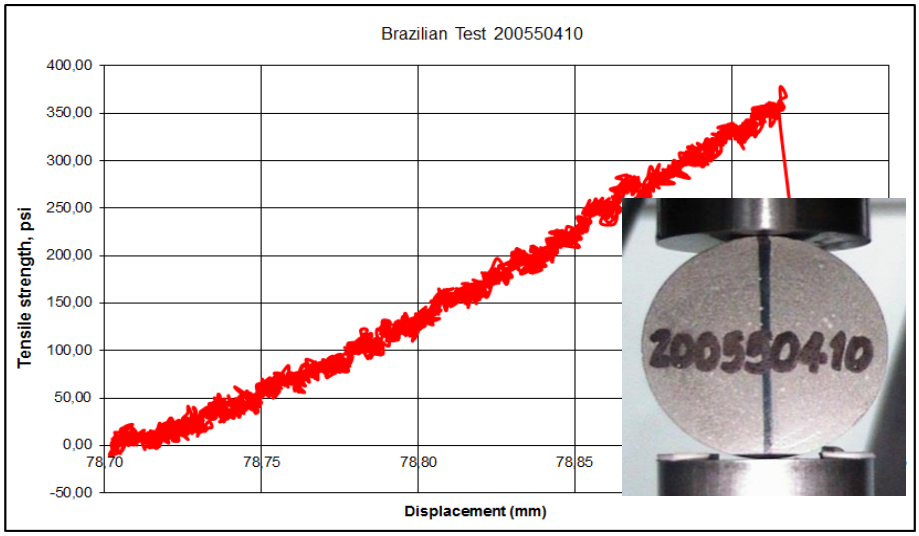

Fig. 5.4—Brazilian test result and photo for Halliburton Portland cement

Triaxial tests were done to determine the friction angle and cohesion of set cements to be used in the FEA. Fig. 5.5 includes one uniaxial and two confined pressure tests used to determine the friction angle and cement cohesion of Design 3 cement. Friction angles of set cement were lower than shale and sandstone, which have average values 30° and 45°.[45]

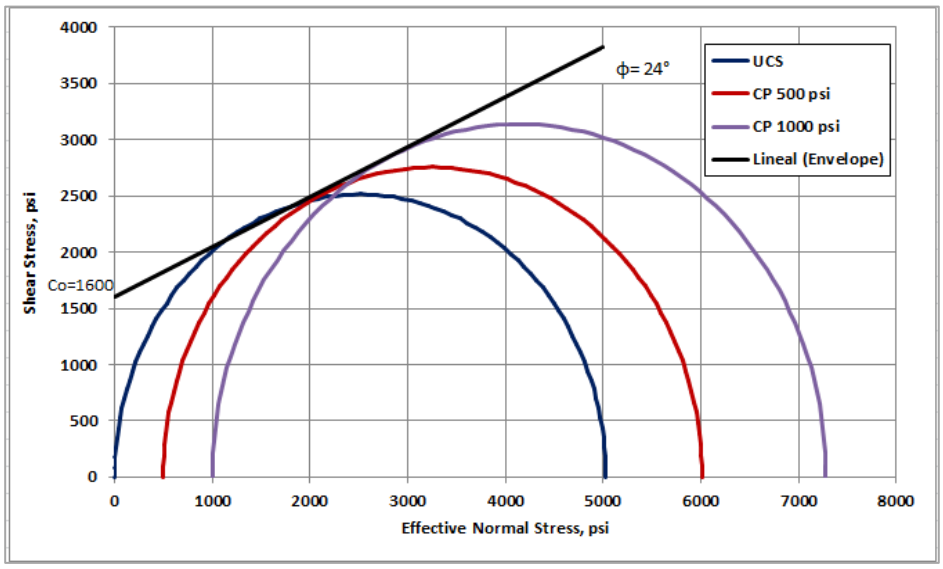

Fig. 5.5—Mohr failure envelope of Portland cement Design 3

Ring molds of 15.8-ppg LifeCem cement were placed in a chamber filled with oil and kept at bottomhole conditions for a month while cement expansion was measured. Table 5.2 shows that 15.8-ppg LifeCem Cement can expand up to 0.47% in 28 days, and this gives the ability to seal microannuli or heal small cracks.

TABLE 5.2—CEMENT EXPANSION OF 15.8-PPG LIFECEM SLURRY, HALLIBURTON - DUNCAN

Time, days	Expansion,%
3	0.39874
7	0.42012
14	0.42876
28	0.46983

Thermal conductivity *k* is the quantity of heat transmitted through a unit thickness in a direction normal to a surface of unit area in response to a unit temperature gradient under steady-state conditions. Eq. 2.46 describes thermal conductivity. Thermal conductivity was not constant; it depended on the temperature and cement density.

Table 5.3 shows that 15.8-ppg LifeCem cement had lower thermal conductivity than conventional set cements, and it provides better insulating capability and lower heat transfer during production. Thermal conductivity of 15.8-ppg conventional set cement has 0.71 BTU /hr-ft°F at 70°F. [12]

TABLE 5.3—THERMAL CONDUCTIVITY OF 15.8-PPG LIFECEM CEMENT, HALLIBURTON - DUNCAN

Temperature, °F	Thermal Conductivity, BTU /hr ft °F
101	0.3166
127	0.3195
154	0.3056
180	0.2883
225	0.23804

Table 5.4 shows that 14.5-ppg ElastiCem and 15.6-ppg untreated Portland cements had permeability greater than 0.1 md, which can affect the cement seal. Cracks may have been created during the cement shrinkage stage. Latex can reduce permeability and shrinkage of set cements. [12]

TABLE 5.4—POROSITY AND PERMEABILITY OF HALLIBURTON PORTLAND CEMENTS

Sample Name	Porosity, %	Klinkenberg Permeability, md
14.5-ppg ElastiCem cement	0.850	0.218
15.6-ppg ElastiCem cement	0.003	0.013
15.8-ppg ElastiCem cement	0.004	0.016
15.6-ppg Design 3	23.8	0.019
15.6-ppg Design 6	22.9	0.070
15.6-ppg Design 7	21.9	0.0035
15.6-ppg Design 10	5.5	0.0005
15.6-ppg Portland cement (water and Portland cement)	27.4	1.4

5.1.2 Halliburton Thermal Cement

Halliburton's ThermaLock cement is designed from recycled fly ash, calcium phosphate hydrates, calcium aluminate hydrates, sodium polyphosphates, and mica-like calcium alumino-silicates so that it is both CO_2 and acid resistant. ThermaLock is a solution for high-temperature or geothermal wells. It has been laboratory tested and proven at temperatures as low as 140°F and as high as 700°F.[46] ThermaLock cement cannot be in contact with Portland cement because their combination causes early cement set of ThermaLock cement. Therefore, a cementing truck must be available for pumping only the ThermaLock cement slurry.

Chichimene field, an oilfield in Colombia, will have in-situ combustion, so the well cement must be designed to withstand bottomhole temperatures of at least 500°F. Several uniaxial, triaxial, and Brazilian tests were done to determine the mechanical cement properties of ThermaLock cement.

Appendixes B and C show slurry designs and uniaxial and triaxial tests carried out for ThermaLock cement designs. Laboratory tests of Designs 1TL/2TL and 6TL were done at Halliburton Technology Center in Duncan and Houston.

Design 1TL was an alternative for cementing $9^5/_8$–in, casing. Design 2TL was planned for 7-in. production liner. Spherelite and Latex 3000 were used to reduce cement slurry density and provide elasticity to ThermaLock cement. Cylindrical samples of ThermaLock cement Designs 1TL (15.5-ppg) and 2TL (14.5-ppg) were cured for 14 days at 600°F and bottomhole pressure of 4,461 psi and 4,730 psi, respectively.

Table 5.5 shows that ThermaLock Designs 1TL and 2TL had Young's modulus higher than 1.0 E+6 psi, and they have more chances to have fissures or cracks during a hydraulic fracturing job. ThermaLock cement design 2TL had lower Young's modulus/tensile strength ratio than Design 1TL. Some samples of ThermaLock Design 1TL had some microfissures before testing, leading to dispersion of tensile strength values as shown in Appendix C.

TABLE 5.5—MECHANICAL PROPERTIES OF 1TL AND 2TL THERMALOCK CEMENT DESIGNS, HALLIBURTON - DUNCAN

Design	UCS, psi	Young's Modulus (Ec), psi	Poisson's Ratio(ν_c)	Tensile Strength (To), psi	Cohesion (Co), psi	Friction Angle (ϕ_c), deg	Young's modulus/ tensile strength ratio
Design 1TL (15.5-ppg)	3,323	1.34E6	0.12	405	1,271	17.1	3,309
Design 2TL (14.5-ppg)	3,416	1.14E6	0.14	513	1,359	13.0	2,222

Flexible cements have high tensile strength, low Young's modulus values, high Poisson's ratio and high cohesion to reduce chances of microfissures or debonding under various download conditions. Set cements with high Young's modulus create higher tangential stresses than cements with low Young's modulus. This phenomenon increases the chances of microfissures when the well is submitted to high internal pressures or temperatures.

Table 5.6 summarizes three permeability tests of ThermaLock cements where the set cements did not show strength retrogression after being cured at 600°F. All three ThermaLock cements had permeability values lower than 0.1 md.

TABLE 5.6—WATER AND KLINKENBERG PERMEABILITY OF THERMALOCK CEMENTS

Design	Water Permeability, md	Klinkenberg Permeability, md
Design 1TL (15.5-ppg)	0.013	----
Design 2TL (14.5-ppg)	0.01	0.014
Design 4TL (14.5-ppg)	---	0.0081

Numerous uniaxial, triaxial, and Brazilian tests for ThermaLock cements were carried out to improve elasticity of ThermaLock cement design 2TL. The curing temperature of ThermaLock cement was 200°F, matching with the reservoir temperature.

Tables 5.7 and 5.8 illustrate numerically the different mechanical properties of ThermaLock Designs 3TL, 4TL and 5TL under different confining pressures. It is clear that mechanical properties depend on confining pressure. Design 3TL showed lower Young's modulus and lower tensile strength than Designs 4TL and 5TL. Stress strain-curves of ThermaLock cement with carbon and glass fibers had better linear elastic behavior than the others. Curing time of ThermaLock cement showed an important role in the development of its mechanical properties: curing for 7 days tripled the tensile strength of ThermaLock cement that was cured for only 1 day at 200°F.

TABLE 5.7—UNIAXIAL AND TRIAXIAL TESTS OF THERMALOCK CEMENTS

Sample Name	Confining Pressure, psi	Number of Samples	UCS/CCS, psi	Young's Modulus (Ec), psi	Poisson's Ratio (ν_c)
ThermaLock Cement, 14.5-ppg (Design 3TL cured for 1 day).	0	4	2,412.9	3.91E+05	0.16
	500	1	2,127.9	1.91E+05	0.08
	1,500	1	4,335.0	3.95E+05	0.04
ThermaLock, 14.5-ppg with 2% BWOC glass fibers (Design 4TL cured for 7 days).	0	1	1,973.2	7.97E+05	0.09
ThermaLock, 14.5-ppg with 2% BWOC carbon fibers (Design 5TL cured for 7 days).	0	1	3,284.7	8.42E+05	0.15
	500	1	4,036.9	7.03E+05	0.15

TABLE 5.8—TENSILE STRENGTH RESULTS OF THERMALOCK CEMENTS

Sample Name	Number of Samples	Tensile Strength (To), psi	Standard Deviation, psi	Young's Modulus/ Tensile Strength
ThermaLock, 14.5-ppg (Design 3TL cured for 1 day).	3	102.1	23.5	3,830
ThermaLock, 14.5-ppg (Design 3TL cured for 7 days).	7	377	54.8	---
ThermaLock, 14.5-ppg, 2% BWOC glass fibers (Design 4TL cured for 7 days).	10	381.4	32,8	2,090
ThermaLock, 14.5-ppg, 2% BWOC carbon fibers (Design 5TL cured for 7 days).	5	490.6	55.6	1,716

During the curing period, there is a chemical reaction between cement and water called the hydration period. Hydration occurs only if water is available and if the cement's temperature stays within a suitable range. Through the curing period, the cement has a hydration process, which commonly requires 5 to 7 days of curing. If the set cement does not have available water, it can develop microfractures that affect the mechanical properties, especially tensile strength. ThermaLock Design 5TL showed the lowest Young's modulus/tensile strength value, but it was necessary to run the FEM to understand the cement behavior during the in-situ combustion project at Chichimene field, Colombia.

Tensile strength of the set cements plays an important role in withstanding hydraulic fracturing jobs. The set cement fails in tension when its tangential stresses exceed the tensile strength value. Fig. 5.6 schematically illustrates the profound effect of curing period and glass and carbon fibers on tensile strength of ThermaLock cements. In this case, Design 5TL cured for 7 days increased its tensile strength property by 28.8% in comparison with Design 3TL. Carbon fibers have the advantage that they can resist temperatures similar to those that occur in in-situ combustion. Also, ThermaLock cement Designs 5TL and 6TL showed low data dispersion.

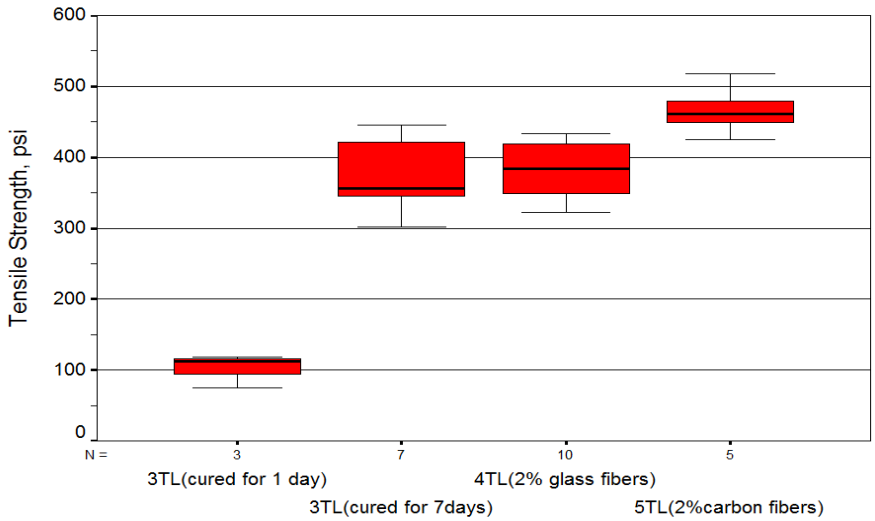

Fig. 5.6—Tensile strength results of ThermaLock cements

The Mohr-Coulomb criterion states that, for compressive failure, the shear stress tending to cause failure is opposed by the cohesion of the material and by a factor analogous to the coefficient of friction multiplied by the effective normal stress acting across the failure plane.[4] In the Mohr failure envelope of ThermaLock Design 5TL, the sample had cohesion of 1,327 psi and friction angle of 12.1° (Fig. 5.7). The Mohr failure envelope was built with uniaxial and triaxial tests with a confining pressure of 0 and 500 psi, in that order. I used FEM in Chapter IV to demonstrate that cement cohesion was related to plasticity of cement and rock, especially in HTHP wells. The higher the cement cohesion, the lower the cement and rock plasticity observed in the FEM.

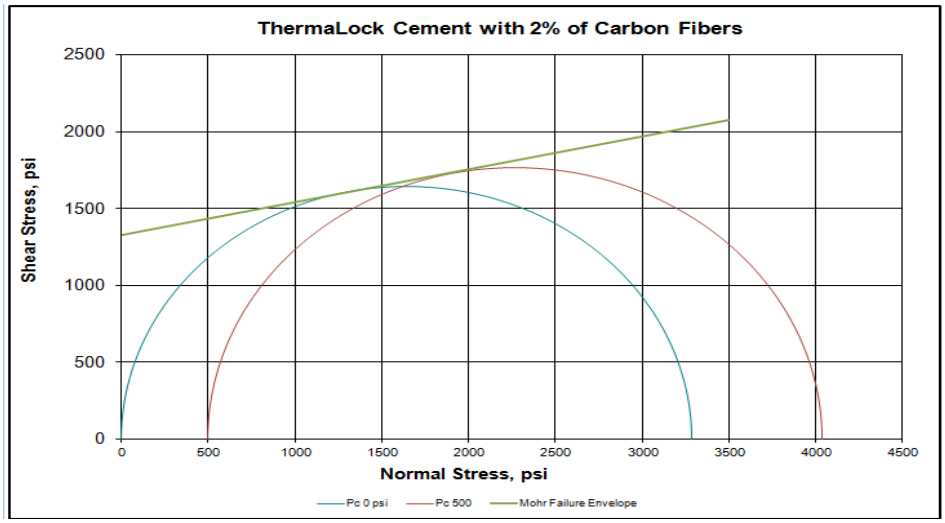

Fig. 5.7—Mohr failure envelope of ThermaLock cement with 2% of carbon fibers (Design 5TL)

ThermaLock cement of 14.5-ppg density with 2.5% BWOC carbon fibers (Design 6TL) was also tested at Halliburton Labs in Houston to determine additional properties like shear bond strength, thermal conductivity, and water permeability. Appendix B shows the additives of ThermaLock cement Design 6TL. Mechanical properties for the ThermaLock cement slurry were conducted under two separate curing conditions:

- The first set was cured in a water bath at 170°F for 2 weeks and atmospheric pressure (ATM).
- The second set was cured at 4,000 psi and 170°F for 1 week and then cured at 550°F and 4,000 psi for an additional week (HTHP).

Table 5.9 illustrates clearly the effect of curing temperature and pressure on mechanical properties and permeability of ThermaLock Design 6TL. The slurry included spherelite beads that were potentially compressed when the samples were taken to 4,000 psi pressure during curing and testing. After checking the specific gravity of the set samples, the density measured to be 15.5 ± 0.1 ppg. Tensile and compressive strength increased their values because the samples were compacted by the pressure. Appendix C shows the results of every test done for ThermaLock cement Design 6TL.

TABLE 5.9—MECHANICAL, THERMAL AND PERMEABILITY TESTS DONE FOR THERMALOCK CEMENT OF 14.5-PPG WITH 2.5% BWOC CARBON FIBERS (DESIGN 6TL)

Name of the Test	Cured Samples at 170 °F and atmospheric pressure (ATM)		Cured Samples at 550 °F and 4,000 psi (HTHP)	
	Number of Samples	Value	Number of Samples	Value
Average Shear Bond Strength, psi	3	488		
Average Brazilian Tensile Strength, psi	4	586	2	830
Average Cube Compressive Strength, psi	3	2958		
Average Cylinder Compressive Strength, psi	2	2127	3	3456
Average Thermal Conductivity, BTU/hr/ft/ °F at 70°F	2	0.439		
Average Water Permeability, md	1	0.002	2	0.007

A water permeability Tester with “Modified Hassler" cell was used to determine water permeability of ThermaLock cement of Design 6TL. Lab results showed that

ThermaLock cement permeability does not substantially change its permeability after being cured at 550°F and 4,000 psi.

Thermal conductivity and casing/cement shear bond strength of 15.8-ppg Portland cement reported in literature are 0.71 BTU/hr/ft/°F and 403 psi. [12] ThermaLock Design 6TL at 70°F had lower thermal conductivity than 15.8-ppg Portland cement (Table 5.9). This condition was favorable for in-situ combustion projects because less heat is transmitted to the casing and cement sheath.

ThermaLock Design 6TL had higher Casing/cement shear bond strength than 15.8-ppg Portland cement. This property reduces the risk of casing/cement debonding. It is important to highlight that shear bond strength/tensile strength ratio was 0.83, and this value was used for all set cements during this study. However, this ratio can be increased by sandblasting the pipe or otherwise giving a rougher edge. Chapter VI will use measured mechanical and thermal properties of ThermaLock Designs 5TL and 6TL to simulate the cement behavior at in-situ combustion conditions in Chichimene field.

5.2 Laboratory Tests for Schlumberger Cements

Flexstone cements were tested in uniaxial and triaxial cells to find their mechanical properties and evaluate their application for Ecopetrol's fields. FlexStone cements are flexible cements designed by Schlumberger to give mechanical properties that enable set cements to conform to stress changes that occur during drilling, production, hydraulic fracturing, and abandonment of the wells. The mechanical properties of FlexStone cements were customized by using trimodal particle-size distribution.

Schlumberger set cements were designed for Chichimene and Apiay fields, which have formation temperatures of 185°F and 240°F at their respective pay zones. FlexStone cements were not taken into account for the in-situ combustion project in Chichimene field, because they do not withstand temperatures above 450°F.

Cement plug samples were cured at 185°F and 3,500 psi for 72 hours, except 15.6-ppg FlexStone plugs that were cured at 240°F and 3,500 psi for 72 hours. Curing temperature and pressure match with reservoir conditions.

Table 5.10 illustrates that the Young's moduli of Schlumberger cements were equal to or lower than 1.0 E+6 psi, and most of them had Poisson's ratios close to 0.2. However, the only two FlexStone cements tested in the rock mechanics lab had low Co, an important mechanical property to have low plastic deformation of set cements. The lowest Young's modulus/tensile strength ratio matches with 14.55-ppg FlexStone cement cured at 180°F, and it was used in Chapter VI for the FEM of Chichimene field. Cement slurry designs and uniaxial/triaxial tests are shown in Appendixes B and C.

TABLE 5.10—UNIAXIAL AND TRIAXIAL TESTS OF SCHLUMBERGER CEMENTS

Cement Name	UCS, psi	Young's Modulus (Ec), psi	Poisson's Ratio (ν_c)	Tensile Strength (To), psi	Friction Angle (ϕ_c), deg	Cohesion (Co), psi	Young's Modulus/ Tensile Strength Ratio
14.2-ppg FlexStone cement.	4,645	9.78E+05	0.21	233	---	---	4,197
14.2-ppg cement - high UCS.	4,907	1.0E+06	0.21	---	---	---	---
14.5-ppg cement class GD 907.	3,044	8.32 E+05	0.18	309	---	---	2,692
15.6-ppg FlexStone cement.	3,751	8.09 E+05	0.21	370	---	---	2,186
14.55-ppg FlexStone Cured at 180°F and 3,000 psi.	3,308	7.54+05	0.19	383	25	1,070	1,968
14.55-ppg FlexStone Cured at 240°F and 3,000 psi.	3,008	7.50E+05	0.16	326	28	900	2,300
14.55-ppg FlexStone Cured at 180°F and 3,000 psi. Tests done by SLB	1,740	4.54E+05	0.21	336	---	---	1,351
14.55-ppg FlexStone Cured at 240°F and 3,000 psi, Tests done by SLB	2,870	6.35E+5	0.23	324	---	---	1,960

Fig. 5.8 clearly shows that 14.55-ppg FlexStone cement decreased its tensile strength when it was cured at 240°F, instead of 180°F. 14.55-ppg Flexstone cement increased its tensile strength by changing their particle-size distribution, and carbon or glass fibers were not added. 14.55-ppg Flexstone design was done to improve tensile strength values of 14.2-ppg FlexStone cement.

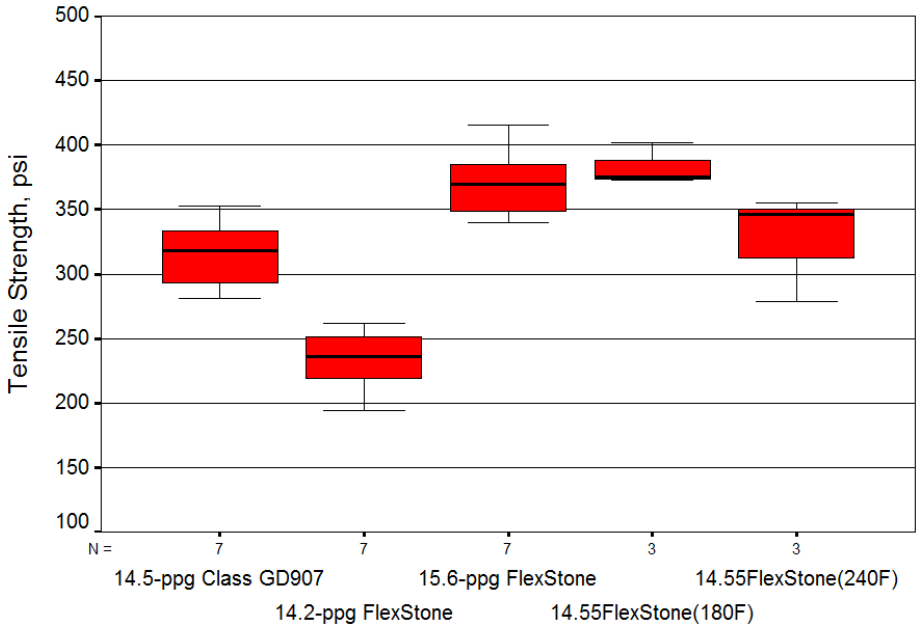

Fig. 5.8—Tensile strength for Schlumberger cements

Fig. 5.9 schematically illustrates that 14.55-ppg Flextone cement had slight strength retrogression when it was cured at 240°F. Also, the higher the UCS, the higher the Young's modulus of cement plugs was. 14.2-ppg cement high- compressive strength showed the highest value of UCS, which is in concordance with that cement slurry. Furthermore, all the cement samples showed high Poisson's ratios, with value higher than 0.16, which makes them flexible.

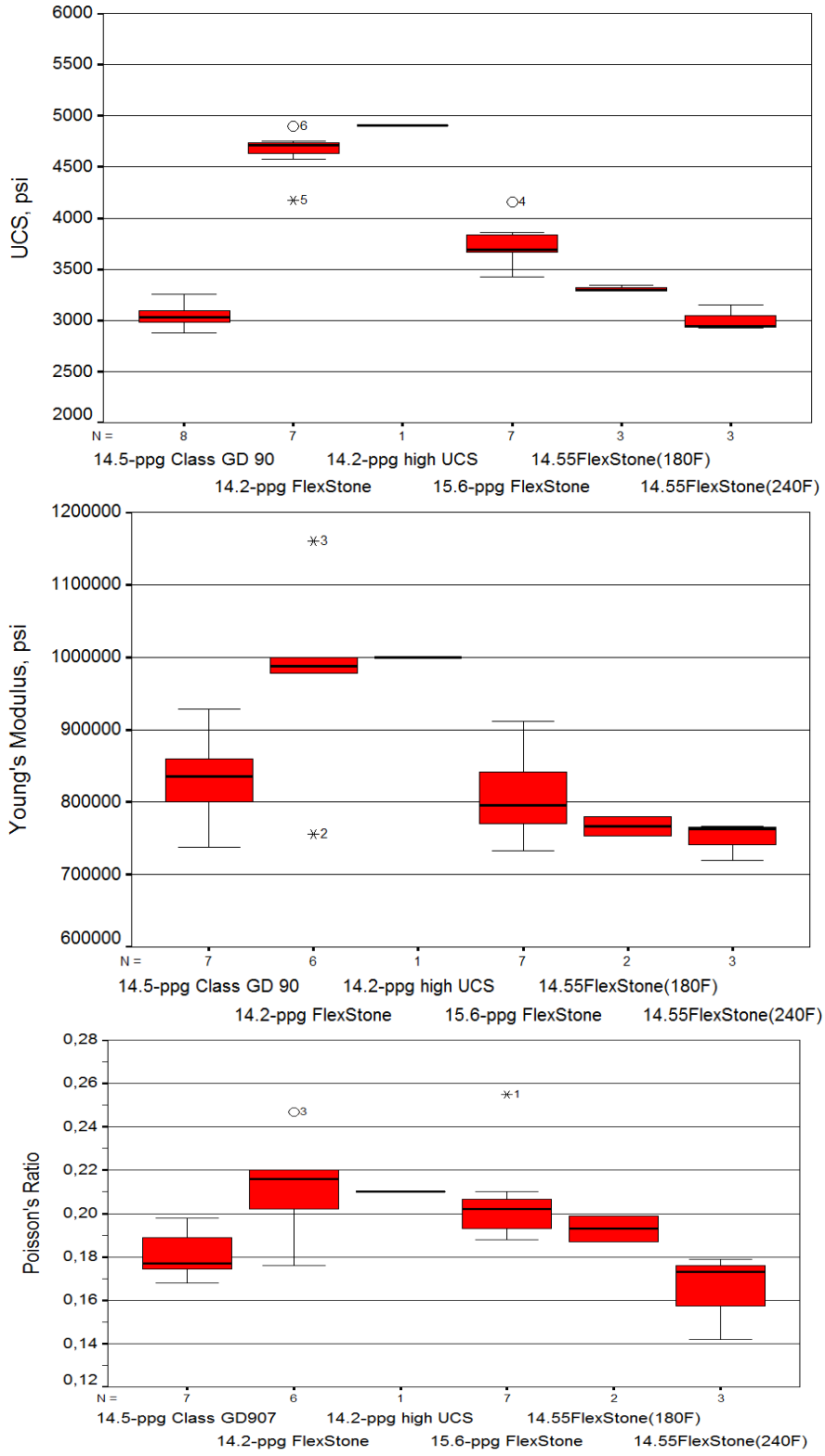

Fig. 5.9— UCS (above), Young's modulus (middle), Poisson's ratio (below) of Schlumberger cements

Fig. 5.10 shows clearly that FlexStone cements failed or cracked almost parallel to the axial load during axial tests. This fail behavior is also typical of rock failure. Tensile strength had some bifurcations, but they were considered acceptable according to the International Society of Rock Mechanics.

Fig. 5.10—Photos of uniaxial and tensile strength tests for 15.6-ppg FlexStone cements

Table 5.11 shows clearly that the permeability of FlexStone cements tested during this research had extraordinarily low values of permeability that give good cement seal properties without loads. The low values of set cement porosity did not increase its Young's modulus. Lab tests carried out with three cement companies during this research showed set cement porosities between 0.004 and 16.5%.

TABLE 5.11—PETROPHYSICAL PROPERTIES OF SCHLUMBERGER CEMENTS

Sample Name	Porosity, %	Klinkenberg Permeability, md
14.2-ppg FlexStone cement	3.2	0.0003
14.5-ppg FlexStone cured at 180°F	10.7	0.0005
14.5-ppg FlexStone cured at 240°F	6.4	0.0006
15.6 FlexStone cement	4.3	0.0008

Tables 5.12 and 5.13 show that in two curing conditions, 14.5-ppg Flexstone cement had a percentage of expansion lower than 0.2%, the minimum recommended to avoid cement cracking. Expansion of the set cements can result in cracking and failure in an unrestrained environment. Expansive cements must have lower Young's modulus than the formation; otherwise, the cement will not expand toward the casing, and this creates an inner microannulus.[12]

TABLE 5.12—14.55-PPG FLEXSTONE CEMENT EXPANSION TESTS, CURED AT 180°F AND 3,000 PSI, SCHLUMBERGER - HOUSTON

Time, days	Measurements, in	Linear Expansion, %
Initial	0.7461	0.00
1	0.7512	0.06
2	0.7585	0.14

TABLE 5.13—14.55-PPG FLEXSTONE CEMENT EXPANSION TESTS, CURED AT 240°F AND 3,000 PSI, SCHLUMBERGER - HOUSTON

Time, days	Measurements, mm	Linear Expansion, %
Initial	0.7445	0,00
1	0.7475	0,03
2	0.7535	0,10

5.3 Laboratory Tests for Set Cements of Baker Company

Four cement slurries of Baker Company were designed for Chichimene and Cupiagua fields. Fire Set cement is Portland cement that was designed for the in-situ

combustion project of Chichimene field, and it was planned as an alternative of ThermaLock cement.

Sample plugs of Baker cements were cured at 211°F and 3,000 psi for 24 hrs. Furthermore, Fire Set cement was cured at 500°F for 1 month in a muffle oven, and then it was tested in a triaxial cell to determine its mechanical properties and contrast them with Fire Set cement that was cured at 211°F.

Calcium aluminate (with or without silica) and Pozzolanic cements are recommended for high-temperature environments like in-situ combustion projects, because Portland cements normally have strength retrogression.[12] Baker Company designed Fire Set cement to withstand temperatures above 500°F in CO_2 environments.[43]

Table 5.14 clearly shows that 14.5-ppg Cupiagua cement had the lowest Young's modulus/tensile strength ratio and the highest cohesion value, important parameters to design a flexible and mechanically improved cement system. The high values of tensile strength of the San Antonio and Yopal set cements were appropriate for the high values of their UCS. The higher the Young's modulus of set cements, the higher the UCS and Co of the analyzed set cements. Appendixes B and C show the cement slurry designs and results of all the uniaxial and triaxial tests done for Baker Hughes cements.

TABLE 5.14—AVERAGE MECHANICAL PROPERTIES OF BAKER PORTLAND CEMENTS

Cement Name	UCS, psi	Young's Modulus (Ec), psi	Poisson's Ratio (ν_c)	Tensile Strength (To), psi	Friction Angle (ϕ_c), deg	Cohesion (Co), psi	Young's Modulus/ Tensile Strength Ratio
14.5-ppg San Antonio	6,868	1.41E+06	0,19	675	25	2,200	2,089
14.5-ppg Yopal	5,541	1.46E+06	0,23	536	38	1,200	2,728
14.5-ppg Reservoir	5,713	1.02E+06	0,19	597	13	2,270	1,708
14.5-ppg Fire Set cured at 211°F	3,984	5.57E+05	0.17	321	---	---	1,735
14.5-ppg Fire Set cured at 500°F	1,692	5.70E+05	0,14	145	33	470	3,931

Fig. 5.11 schematically illustrates that Baker set cements, except Fire Set cement, had extraordinarily high values of tensile strength. Fire Set cement cured at 500°F had much lower tensile strength than Fire Set cement cured at 211°F. However, it is necessary to verify that Fire Set resists corrosion caused by CO_2.

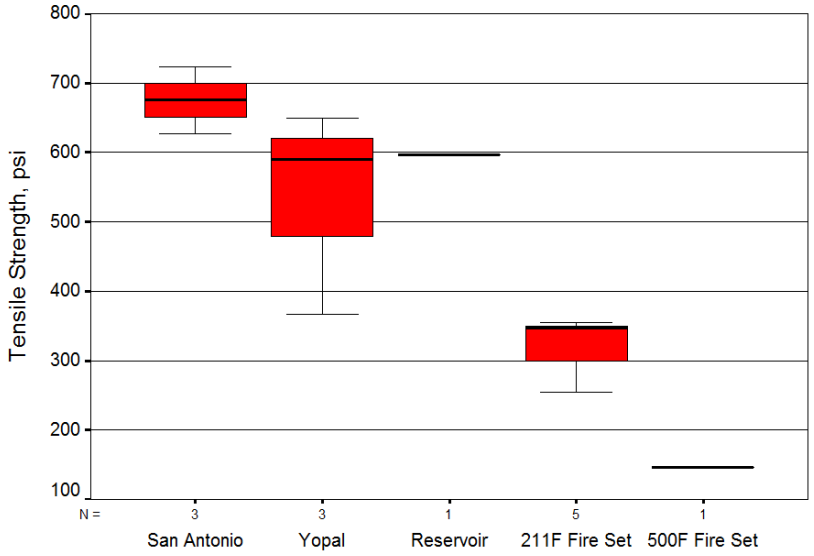

Fig. 5.11—BoxPlot of tensile strength of Baker cements

Fig. 5.12 exhibits Boxplots of UCS, Young's modulus, and Poisson's ratio for Baker set cements. It is clear that San Antonio and Yopal cements had extraordinarily high values of Young's modulus, and these values are not acceptable for flexible cements. Fire Set cement cured at 500°F had strength retrogression due to its low values of UCS and tensile strength. Reservoir set cement showed good mechanical properties, especially for deep wells, and the FEM will be presented in Chapter VI.

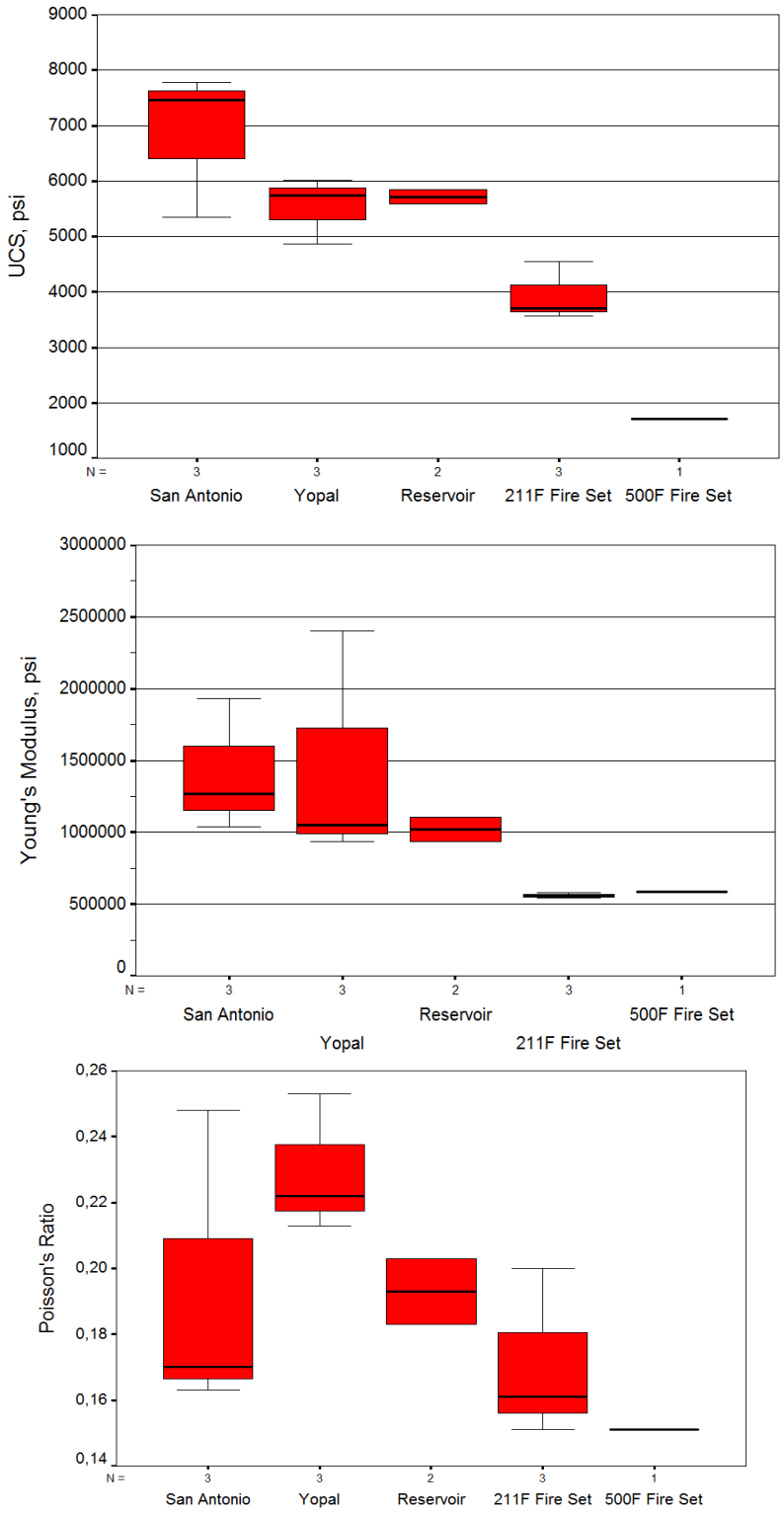

Fig. 5.12— UCS (above), Young's modulus (middle), Poisson's ratio (below) of Baker cements (uniaxial tests)

Figs. 5.13 and 5.14 clearly show that the Young's modulus of San Antonio cement was lower in the uniaxial test than in the triaxial test with confining pressure of 1,000 psi. The Young's modulus of the set cement is the slope of the axial strain vs. axial compression curve during uniaxial and triaxial tests. Also, the cement plug subjected to triaxial tests had an inclined failure plane with the axial load; a similar failure pattern is observed in rocks.

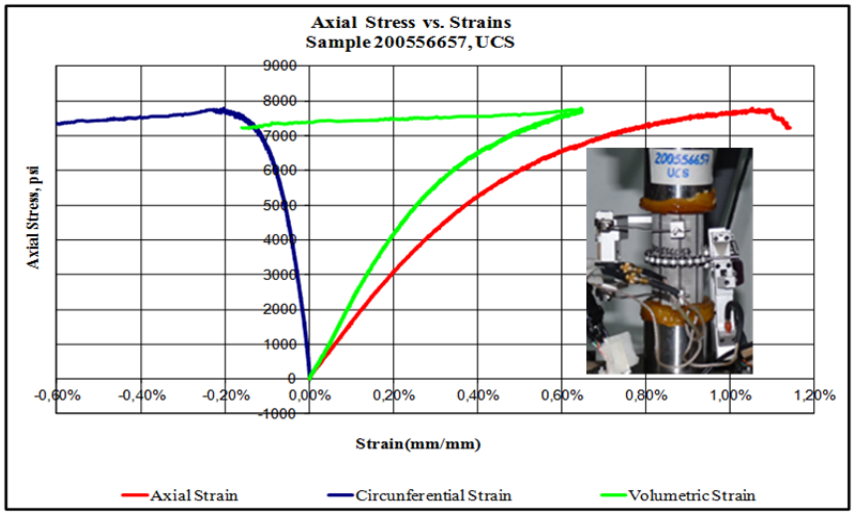

Fig. 5.13—Stress/strain curve and photo of uniaxial test for San Antonio cement

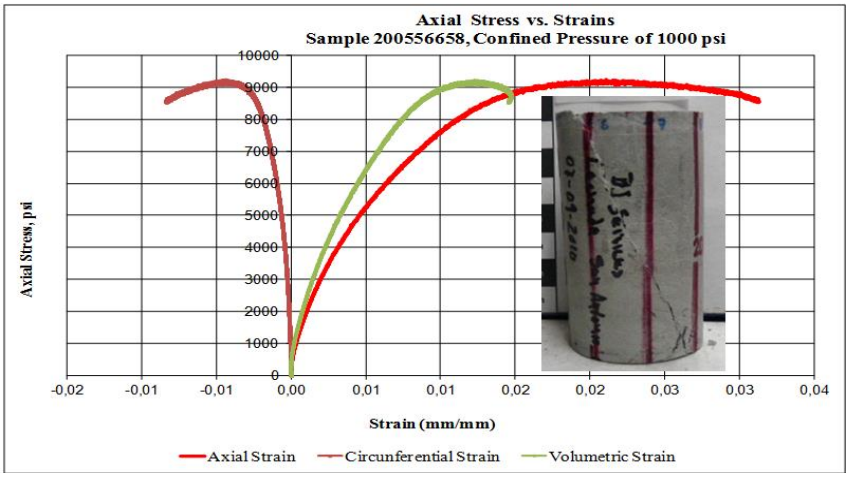

Fig. 5.14—Stress/strain curve and photo of triaxial test of San Antonio cement

Conducting a series of uniaxial and triaxial tests defines an empirical Mohr-Coulomb failure envelope that describes failure of the set cement at different confining pressures. The Mohr-Coulomb failure envelope can also be linearized; the angle of the line is called the friction angle and its intercept with the shear stress, the cohesive strength or cohesion. [4]

The Mohr envelope for San Antonio cement was built from the average of three UCS tests and one triaxial test with a confining pressure of 1,000 psi. I showed in Chapter IV that high cement cohesion reduced the chances of cement plastic deformation in the well, and other mechanical properties like tensile strength, Young's modulus and Poisson's ratio must be taken into account.

Fig. 5.15 schematically illustrates the cohesion and friction angle in the Mohr envelope of San Antonio cement. The cohesion, intersection of the Mohr envelope with the shear stress axis, was 2,200 psi and the slope of the Mohr envelope was 22°. Baker set cements had extraordinarily high cohesion values measured during this study.

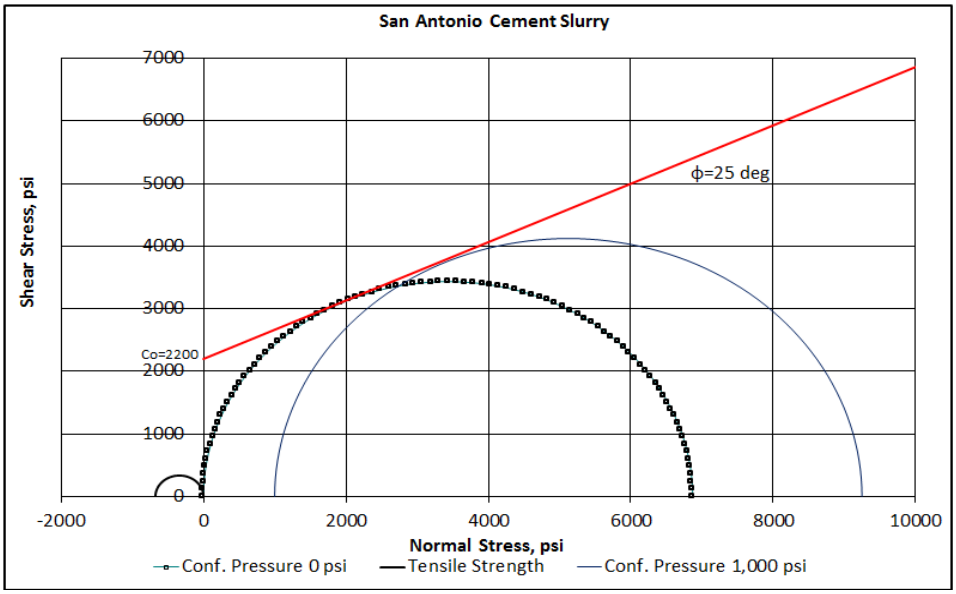

Fig. 5.15—Mohr envelope for San Antonio cement

A triaxial test of San Antonio set cement was run with a confining pressure of 12,000 psi, but the sample did not fail with an axial load of 18,300 psi. Fig. 5.16 shows photos of San Antonio set cement after calling off the triaxial test. The sample had axial and circumferential plastic deformations without apparent cracks. This phenomenon can be related to the high porosity of San Antonio set cement as shown in Table 5.15. Cements with high porosity and/or high elasticity should not display a maximum peak stress at high confining pressure, but can exhibit hardening because of compaction.[12] San Antonio and Fire Set cements showed permeability higher than 0.1 md that could affect the cement seal even without well loads.

Fig. 5.16—San Antonio cement sample, after a triaxial test with confining pressure of 12,000 psi

TABLE 5.15—PETROPHYSICAL PROPERTIES OF BAKER SET CEMENT

Sample Name	Porosity, %	Klinkenberg Permeability, md
San Antonio	16.54	0.8693
Reservoir	2.8	0.0001
Fire Set	42.6	0.176

Mechanical and thermal properties of the set cements of the three cementing service companies were included in the FEM developed during this dissertation and shown in Chapter VI to evaluate the zonal isolation capacity. Some of these set cements were included in the operation of Ecopetrol Company.

CHAPTER VI

SIMULATION OF CEMENT BEHAVIOR WITH FEA MODEL AND COMMERCIAL SOFTWARE

Simulation of cement behavior requires determining the mechanical and thermal properties of the formation and cement as well as the different loads that the cement sheath will need to withstand during the life of the well. Commercial software uses analytical or finite-element models (FEMs) to simulate cement failure, but knowing the limitations of the software is essential. Analytical models usually assume only elastic behavior; they do not take into account the plastic behavior of rock and set cement, whereas FEMs can simulate the thermo-elastic and plastic behavior of set cements and rocks. Finally, the software must takes into account cumulative stresses and plastic deformations in the set cement and formation during the life of the wells.

Failure of set cement is generally due to debonding, plastic deformation, and radial cracking. I determined risk of these with 3D finite-element stress analysis (FEA). Cement sheath fatigue was not included during these analyses.

Inner and outer microannuli can be related to plastic deformations or debonding of the cement from the casing or formation, which could lead to vertical migration of fluids. Set cement in the well can have inner (casing/cement) and outer (cement/formation) debonding.

As I discussed in Chapter V the shear strength/tensile strength (To) ratio observed for ThermaLock cements was 0.83. During this research, the shear bonding strength of set cements was constrained in the flowing range:

$$0.83 \times To \leq \delta \leq To, \quad \text{(6.1)}$$

where To is the tensile stress of set cement and δ is the shear bonding strength of set cement. The shear bonding strength of set cement cannot be higher than To. Formation-

to-cement bonding is normally lower than cement-to-casing bonding. Shear bonding strength tests data are available in open literature or they can be carried out according to ASTM C952 specifications. [12]

Radial compressive stresses can be created during the expansion of the casing against the cement sheath throughout hydraulic fracturing or steam injection. Radial cracks in the set cement are failures in tension as a result of shrinkage of the cement due to reduction in hydration volume, hydraulic fracturing, a rise in temperature inside the casing, or combinations of factors.

Mechanical properties of the rocks were calculated with equations given in Chapter 2 of this dissertation, and they were calibrated with uniaxial, triaxial, and Brazilian core tests done at ICP, Colombia. This mechanical properties and in-situ stresses of the formations of the Apiay, Chichimene, and Cupiagua fields were used to simulate cement behavior in the reservoirs in the three oil fields. Ecopetrol, the Colombian National Petroleum Company, is the operator of these fields.

Mechanical properties, azimuth, and magnitude of the in-situ stresses of the Apiay, Chicimene, and Cupiagua fields are shown in Appendix D; they were calculated using data from fracture-gradient jobs, borehole breakouts, and fracture-induced tensile fractures. [45] Appendixes B and C show cement slurries and the mechanical properties of elastic cements designed during this research with Halliburton, Schlumberger, and Baker Companies for the Apiay, Chichimene, and Cupiagua fields.

Chapter VI shows simulation of the cement behavior for three fields with Halliburton WellLife software and FEMs developed during this study. This FEM that was built in Abaqus is more comprehensive than WellLife software, but FEMs require some background knowledge of rock mechanics. Finally, the FEMs treated tensile stresses as positive and compressive stresses as negative.

6.1 Simulation of Cement Behavior at Apiay Field, Colombia

Apiay field has three pay-zone formations: T2, K1, and K2. These three formations are sandstone with intercalations of shale. This field produces heavy crude oil

in the T2 formation and medium crude oil in the K1 and K2 formations. Apiay wells have an average true vertical depth of 11,000 ft. Recent wells have been drilled with an inclination between 50 and 90° degrees to meet geological and reservoir requirements.

Table 6.1 illustrates borehole data and loads that the cement sheath needs to withstand during the life of Apiay wells. All data was taken from drilling history of the wells, temperature logs, and hydraulic fracturing jobs of the field.

TABLE 6.1—BOREHOLE DATA AND LOADS AT APIAY WELLS

Well Data	Reservoirs		
	T2	K1	K2
Formation top, ft	**10,050**	**10,250**	**10,750**
Borehole, in.	8.50	8.50	8.50
Casing OD, in.	7	7	7
Casing ID, in.	6.276	6.276	6.276
Overburden pressure, psi/ft	1.0	1.0	1.0
Maximum horizontal stress pressure, psi/ft	1.21	1.21	1.21
Minimum horizontal stress pressure, psi/ft	0.8	0.8	0.8
Azimuth of maximum horizontal stress direction, deg	115	115	115
Formation pore pressure, psi	**3,431**	**4,477**	**3,798**
Mud gradient, psi/ft	0.468	0.468	0.468
Mud temperature, °F	**168**	**169**	**170**
Cement slurry density, ppg	15.8	15.8	15.8
Completion fluid density, ppg	8.4	8.4	8.4
Hydraulic fracturing pressure, psi	**10,556**	**10,920**	**11,336**
Hydraulic fracturing fluid temperature, °F	**168**	**169**	**170**
Bottomhole production pressure, psi	1,500	1,500	1,500
Tubular fluid temperature during production, °F	**220**	**221**	**223**
Surface temperature, °F	90	90	90
Formation temperature, °F/100 ft	1.21	1.21	1.21

Table 6.2 shows the mechanical and thermal rock properties estimated for pay zones in the field. The mechanical rock properties were estimated by electrical logs and calibrated with triaxial tests. Specific heat capacity and thermal expansion of set cements were taken from the library of Halliburton's WellLife software.

TABLE 6.2—MECHANICAL AND THERMAL ROCK PROPERTIES AT APIAY FIELD

Mechanical and Thermal Properties	Formation Names		
	T2	K1	K2
Formation density, ppg	21.11	20.61	20.78
UCS, psi	8,721	7,885	10,057
Young's modulus, psi	2.9 E+06	3.5 E+06	3.8 E+06
Poisson ratio	0.25	0.23	0.21
Friction angle, deg	49	48	50
Cohesion, psi	2,152	2,343	2,505
Volumetric specific heat, BTU/ (ft^3.°F)	14.76	14.76	14.76
Specific heat capacity, Btu/(lbm×°F)	0.0935	0.0958	0.0950
Thermal conductivity, BTU/ (hr.in.°F)	0.0475	0.0475	0.0475
Thermal expansion, 1/°F	5.56E-6	5.56E-6	5.56E-6

Table 6.3 illustrates the mechanical and thermal properties of Portlant cement Design 3 of Halliburton used to simulate cement behavior of Apiay wells. Chapter V and Appendix C describe in detail all the mechanical properties of designed set cements.

TABLE 6.3—MECHANICAL AND THERMAL PROPERTIES OF PORTLAND CEMENTS FOR APIAY FIELD

Mechanical and Thermal Property	15.8-ppg LifeCem	15.8-ppg Design 3	15.6-ppg Design 7
Cement slurry density, ppg	15.8	15.8	15.6
UCS, psi	4,937	5,028	3,999
Young's modulus, psi	1.28 E+6	6.43E+5	6.29E+05
Poisson's ratio	0.158	0.089	0.053
Cohesion, psi	1,769	1,600	1300
Friction angle, deg	19	24	28
Tensile strength, psi	449	473.3	449.8
Expected debonding strength (0.83*To), psi	372	392	373
Young's modulus/tensile strength	**3,093**	**1,357**	**1,538**
Volumetric specific heat, BTU/(ft^3°F)	59.4	59.4	59.4
Specific heat capacity (Btu/(lbm.°F)	0,509	0,509	0,508
Thermal conductivity, BTU/ (hr.in.°F) @ 225°F	0.0198	0.0198	0.0198
Thermal expansion, 1/°F	6.11E-6	6.11E-6	6.11E-6
Tensile fracture energy, BTU/ft^2	0.00607545	0.00607545	0.00607545
Hydration volume change, %	0	0	0
Hydration heat, BTU/ft3	2656.8	2656.8	2656.8

Design 3 with 15.8-ppg Portland cement included LifeCem, expansive cement additive, glass fibers and latex to decrease Young's modulus, incorporate self-healing properties, increase the tensile strength, and mitigate the effects of reduction of

hydration volume of the set cement. Change in negative hydration volume can cause bulk shrinkage of the set cement. Appendix B shows the cement slurry designs done during this dissertation with Halliburton, Schlumberger, and Baker Hughes Companies.

The WellLife software of Halliburton is also based on finite-element analysis (FEA) that includes wellbore conditions and operational loads that exert stresses on the cement sheath and predict cement failure. Simulations allow designing the required cement sheath properties to withstand the different loads during the life of the well.

Figs. 6.1, 6.2, and 6.3 show the results of WellLife software for 15.8-ppg Portland cement Design 3 for the T2, K1, and K2 formations in Apiay field. These three formations were in the same borehole section. Cement Design 3 had the lowest modulus/tensile strength ratio of the three set cements in Table 6.3.

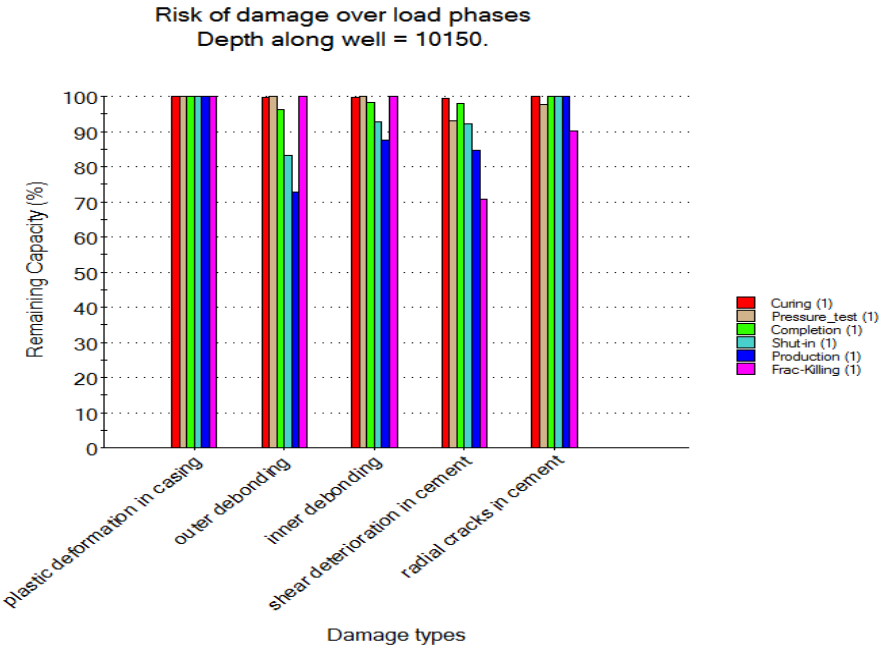

Fig. 6.1—Risk of damage of cement Design 3 at T2 formation in Apiay wells with WellLife software

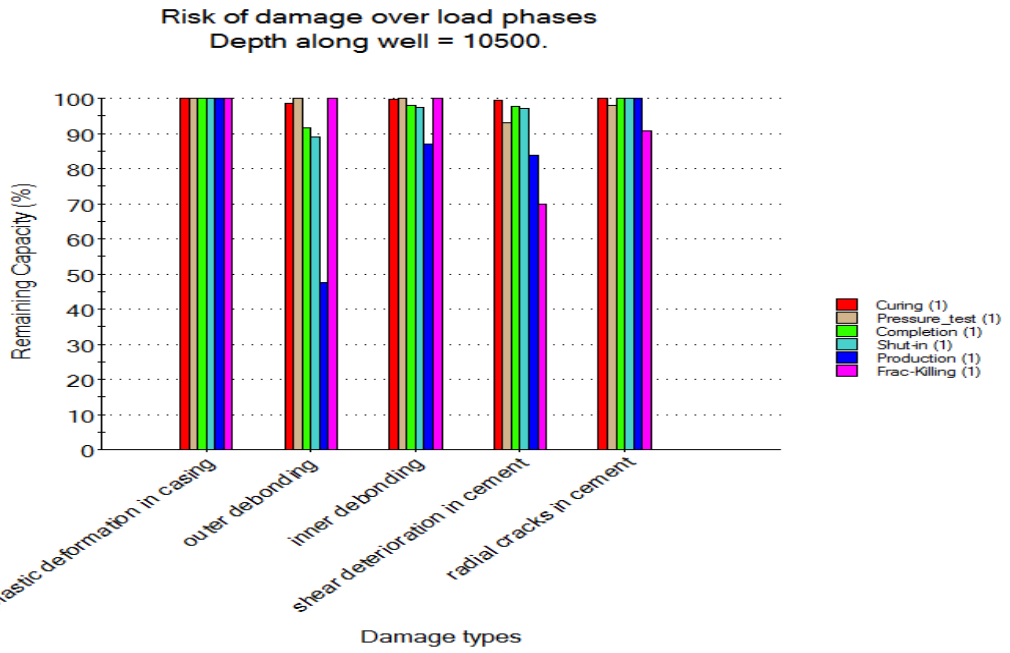

Fig. 6.2—Risk of damage of cement Design 3 at K1 formation of Apiay wells with WellLife software

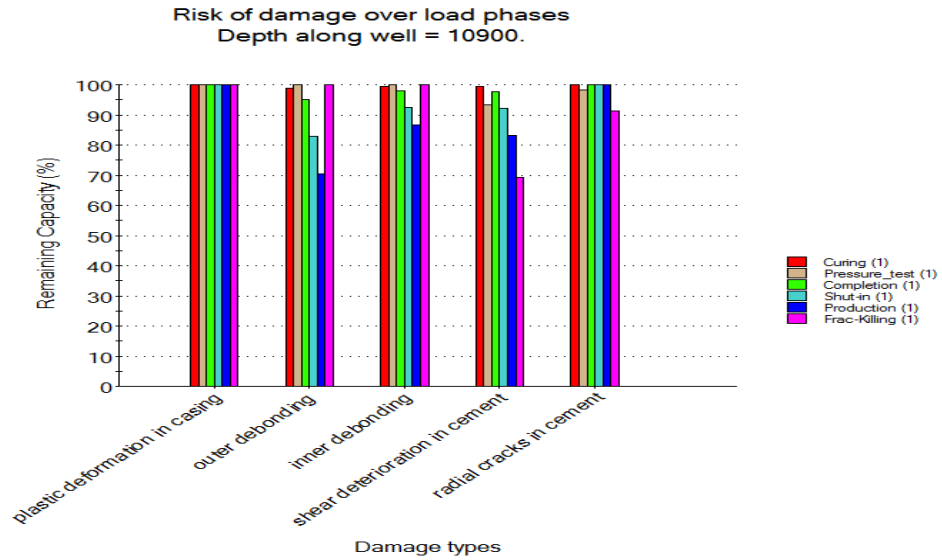

Fig. 6.3—Risk of damage of cement Design 3 at K2 formation of Apiay wells with WellLife software

As shown by the WellLife software, set cements have no risk of debonding, shear deterioration, and radial cracks when their remaining capacity is 60% or higher. In this

scenario, WellLife software indicated that outer debonding was one of the main risks of cement failure in the K1 formation during well production of Apiay wells; the remaining capacity for outer debonding was only 47%. The software showed acceptable cement behavior in the T2 and K2 formations at this field. One of the weaknesses of WellLife software, however, is that the risks of cement damage were not cumulative.

The Abaqus FEM assumed that the casing/cement interface and the cement/rock interface were fully bonded. The model assumed that casing, cement, and rock behave like thermo-elastic-plastic materials, and heat transport was essentially by conduction. The calculation of the stress caused by temperature changes depends on density, specific heat, thermal conductivity, and coefficient of thermal expansion of the casing, cement, and formation.

The FEM expected the wellbore to withstand pressure and temperatures during the life of the wells. The type of failure—either cement debonding or cement cracking—was a function of radial and tangential stresses in downhole conditions. Chapter V of this dissertation showed that cements are stronger in compression than in tension, and therefore cement cracking occurs first in tension. Three critical steps during well life were analyzed in detail: well completion, hydraulic fracturing, and well production.

Wellbore pressure decreases during well completion, and the cement withstands tensile stresses that lead to cement debonding. Radial stresses and tangential stresses were determined using a circumferential system of coordinates where S11 (CSYS-1) and S22 (CSYS-1) are radial and tangential stresses. Tensile stresses are positive and compressive stresses are negative, according to Abaqus software.

Fig. 6.4 clearly shows in the FEA that the maximum tensile radial stress of cement Design 3 after well completion was 179 psi in the top of casing/cement interface. Furthermore, the expected debonding strength of 15.8-ppg Design 3 cement was 392 psi (Table 6.3). Therefore, there were no chances of debonding of 15.8-ppg Design 3 cement from casing and formation during well completion of Apiay wells.

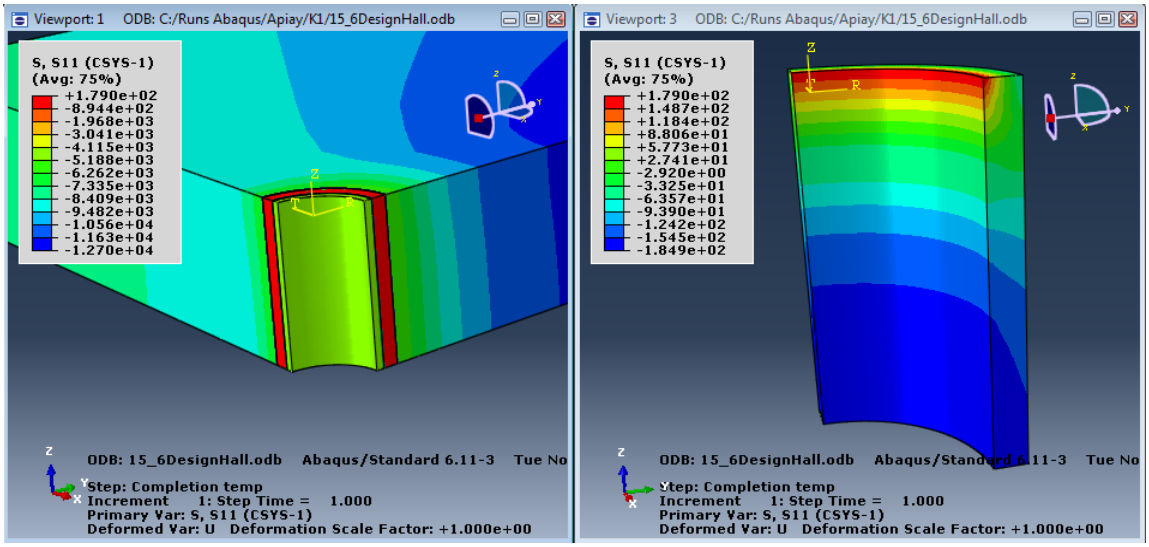

Fig. 6.4—Radial stresses after well completion with cement Design 3 at K1 formation of Apiay wells using FEA. Left: casing, cement and formation. Right: cement.

Hydraulic fracturing jobs can damage the cement sheath seriously because fracturing fluid transfers high pressures inside the casing for hours. To understand the effect on the cement sheath, the FEM included the loading pressure applied to the casing that was not perforated. The phenomenon is more complex in the perforated section, because the formation is fractured and the fracturing fluid is injected into the formation, but this instance was not analyzed in the FEA during this research.

The highest value of tensile tangential stress in the FEA was at the casing/cement interface, where cement cracking failure should occur first (Fig. 6.5). Tensile radial cracks propagate normal to the direction of the maximum tensile stress. The maximum tensile tangential stress at the cement sheath was 396 psi, and the tensile strength of the cement must be higher to avoid cement radial cracking. 15.8-ppg Design 3 cement had a tensile strength value of 473 psi; therefore, this cement design did not have radial cracks. Chapter IV of this dissertation explained that tensile strength requirements increased when cement Young's modulus increased, because tangential stresses are direct functions of Young's modulus.

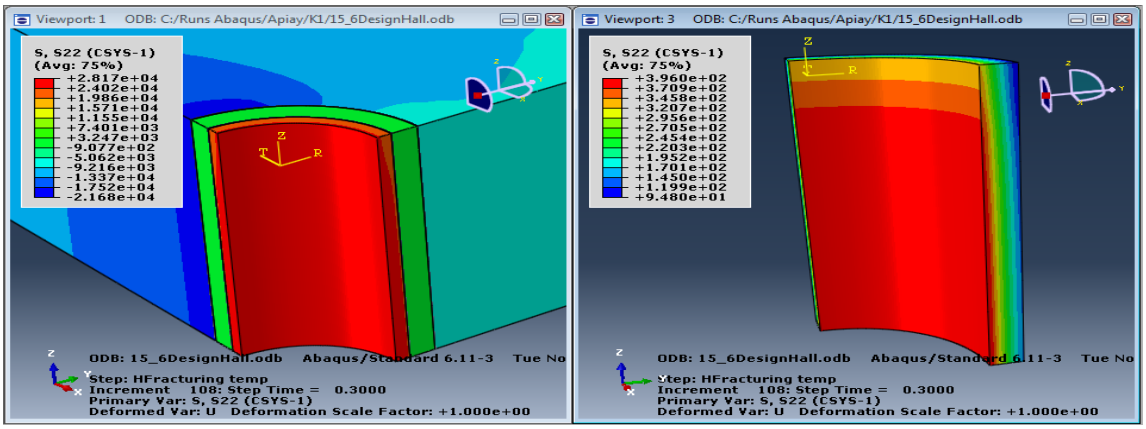

Fig. 6.5—Tangential stresses after hydraulic fracturing with cement Design 3 at K1 formation of Apiay wells using FEA. Left: casing, cement and formation. Right: cement.

Set cement behavior during well production of Apiay wells was simulated with the FEM with a borehole pressure of 1,500 psi. Fig. 6.6 shows that maximum tensile radial stress was 490 psi at the top of the cement sheath. Therefore, cement Design 3 partially debonded from casing because tensile radial stresses were higher than the expected tensile strength of cement. The FEM showed compressive stresses at the cement/formation interface; therefore, cement did not debond from formation. Cement debonding during well production can be eliminated if the wells have a borehole pressure higher than 1,500 psi.

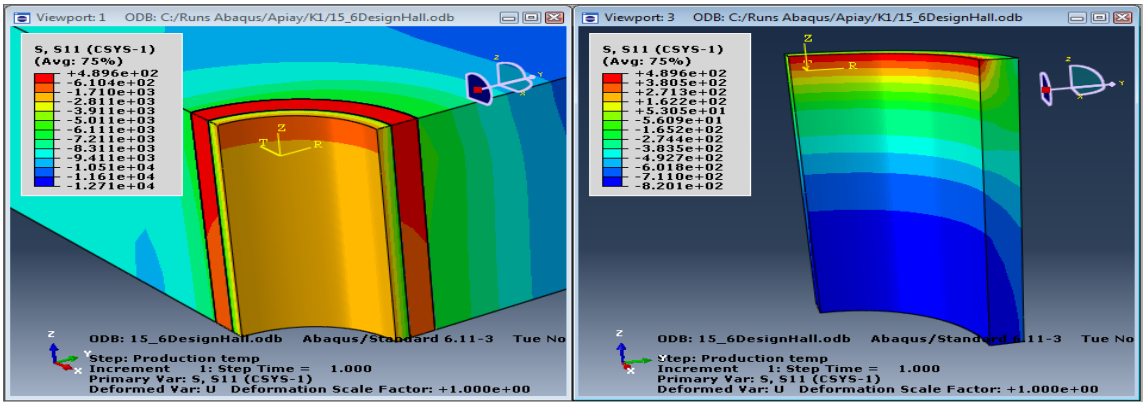

Fig. 6.6—Radial stresses during well production with cement Design 3 at K1 formation of Apiay wells using FEA. Left: casing, cement and formation. Right: cement.

Plastic deformation of rock and cement were designated as PEEQ in Abaqus/implicit. Plastic deformations of cement or rocks can create inner or outer microannuli. Plastic deformations of set cements and rocks are cumulative, and the FEM used in this dissertation integrated all the loads of the well during drilling, completion, hydraulic fracturing and production.

Fig. 6.7 shows no PEEQ of cement or rocks from drilling to production of Apiay wells. Therefore, plastic deformation did not cause either inner or outer microannuli of cement with 15.8-ppg Design 3 cement at the K1 formation of Apiay wells.

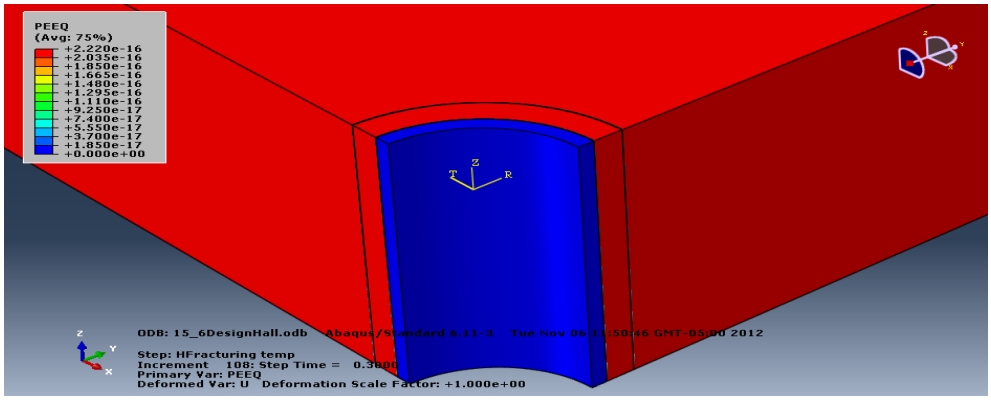

Fig. 6.7—Equivalent plastic deformation after well production with cement Design 3 at K1 formation of Apiay wells using FEA

Appendix E shows the FEA of cement Design 3 in the T2 and K2 formations of Apiay wells. Cement Design 3 did not display radial cracks and plastic deformation, but this set cement partially debonded from casing during well production.

There are two ways to avoid partial cement debonding: increase the debonding strength of 15.6-ppg cement Design 3 to values higher than 550 psi, maintaining their mechanical and thermal properties, or rising borehole production pressure higher than 1,500 psi. K2 formation had higher risk of partial debonding, and water production can upsurge due to the proximity to WOC.

Tables 6.4, 6.5, and 6.6 show clearly that cement Design 3 had the best behavior of the three analyzed cements in front of T2, K1, and K2 formations of Apiay wells. Design 3 had the lowest von Mises stresses (VM), tangential stresses (S22) and radial stresses (S11) during hydraulic fracturing and well production.

TABLE 6.4—FEA WITH DIFFERENT SET CEMENTS AT T2 FORMATION OF APIAY FIELD

	Hydraulic Fracturing					Well Production				
Cement Design	**Max. VM, psi**	**Max. S22, psi**	**Radial cracks**	**Cement PEEQ, %**	**Form. PEEQ, %**	**Max. VM, psi**	**Max. S11 Stress, psi**	**Debond**	**Cement PEEQ, %**	**Form. PEEQ, %**
LifeCem	1,779	769	Yes	0	0	1,694	657	Partial	0	0
Design 3	**1,368**	**418**	**No**	**0**	**0**	**1,292**	**466**	**Partial**	**0**	**0**
Design 7	1,437	712	Yes	0.22	0	1,354	504	Partial	0.22	0

TABLE 6.5—FEA WITH DIFFERENT SET CEMENTS AT K1 FORMATION OF APIAY FIELD

	Hydraulic Fracturing					Well Production				
Cement Design	**Max. VM, psi**	**Max. S22, psi**	**Radial cracks**	**Cem. PEEQ, %**	**Form. PEEQ, %**	**Max. VM, psi**	**Max. S11 Stress, psi**	**Debond**	**Cement PEEQ, %**	**Form. PEEQ, %**
LifeCem	1,874	708	Yes	0	0	1,860	681	Partial	0	0
Design 3	**1,458**	**396**	**No**	**0**	**0**	**1,418**	**489**	**Partial**	**0**	**0**
Design 7	1,546	689	Yes	0.27	0	1,464	521	Partial	0.27	0

TABLE 6.6—FEA WITH DIFFERENT SET CEMENTS AT K2 FORMATION OF APIAY FIELD

	Hydraulic Fracturing					Well Production				
Cement Design	**Max. VM, psi**	**Max. S22, psi**	**Radial cracks**	**Cement PEEQ, %**	**Form. PEEQ, %**	**Max. VM, psi**	**Max. S11 Stress, psi**	**Debond**	**Cement PEEQ, %**	**Form. PEEQ, %**
LifeCem	1,913	693	Yes	0	0	2,016	755	Partial	0	0
Design 3	**1,492**	**392**	**No**	**0**	**0**	**1,528**	**548**	**Partial**	**0**	**0**
Design 7	1,741	772	Yes	0.36	0	1,650	611	Partial	0.36	0

Cement Design 3 did not develop radial cracks during hydraulic fracturing pressures in front of the T2, K1, and K2 formations. However, this set cement had debonding in front of the K1 formation with a well production pressure of 1,500 psi. WellLife software also predicted this cement failure in front of the K1 formation.

Cement Design 7 developed plastic deformations, and this set cement had a lower Young's modulus/tensile strength ratio than 15.6-ppg LifeCem cement. This indicates that set cements with lower Young's modulus/tensile strength ratio are not always the solution, because this ratio does not capture the risk of plastic deformation of the set cements and formations, cement debonding, and radial cracks.

6.2 Simulation of Cement Behavior at Chichimene Field, Colombia

Chichimene wells have an average of 9,200 ft of true vertical depth, and they produce essentially from the T2 and K2 formations. Reservoirs in the field are sandstones interbedded with shale.

Table 6.7 shows the borehole data and loads of Chichimene wells. All data was taken from drilling histories of the wells, temperature logs, and hydraulic fracturing jobs in the field. Table 6.8 shows the mechanical and thermal formation properties at Chichimene field. The mechanical rock properties were determined by electrical logs and calibrated with tri-axial tests done at ICP, Colombia. Thermal rock properties were taken from the library of WellLife software of Halliburton.

TABLE 6.7—BOREHOLE DATA AND LOADS AT CHICHIMENE WELLS

Well Data	Formation Name		
	T2	K1	K2
Formation top, ft	**7,867**	**8,193**	**8,767**
Borehole, in	8.50	8.50	8.50
Casing OD, in	7	7	7
Casing ID, in	6.276	6.276	6.276
Overburden pressure, psi/ft	1.0	1.0	1.0
Maximum horizontal stress pressure, psi/ft	1.19	1.19	1.19
Minimum horizontal stress pressure, psi/ft	0.78	0.78	0.78
Azimuth of maximum horizontal stress direction, deg	110	110	110
Formation pore pressure, psi	**3,067**	**3,191**	**3,642**
Mud gradient, psi/ft	0.468	0.468	0.468
Mud temperature, °F	135	135	135
Cement slurry density, ppg	14.5	14.5	14.5
Completion fluid density, ppg	8.4	8.4	8.4
Hydraulic fracturing pressure, psi	**7,468**	**7,886**	**8,092**
Hydraulic fracturing fluid temperature, °F	135	135	135
Bottom-hole production pressure, psi	1,500	1,500	1,500
Tubular fluid temperature during production, °F	**176**	**181**	**188**
Surface temperature, °F	90	90	90
Formation temperature, °F/100 ft	1.2	1.2	1.2

TABLE 6.8—MECHANICAL AND THERMAL FORMATION PROPERTIES AT CHICHIMENE FIELD

Mechanical and Thermal Properties	Formation Names		
	T2	K1	K2
Formation density, ppg	22.36	21.61	20.86
UCS, psi	5,908	5,643	6,090
Young's modulus, psi	3.0 E+06	2.44 E+06	3.31 E+06
Poisson's ratio	0.23	0.27	0.22
Friction angle, deg	54	50	56
Cohesion, psi	2,482	2,180	2,665
Volumetric specific heat, BTU/ (ft^3.°F)	14.76	14.76	14.76
Specific heat capacity (Btu/(lbm.°F)	0.0882435	0.09131	0,094589
Thermal conductivity, BTU/ (hr.in.°F)	0.0475	0.0475	0.0475
Thermal expansion, 1/°F	5.56E-6	5.56E-6	5.56E-6

Table 6.9 provides the mechanical and thermal properties of 14.5-ppg Portland San Antonio cement of Baker Hughes. Appendixes C shows more details of the cement slurry design of 14.5-ppg San Antonio cement.

TABLE 6.9—MECHANICAL AND THERMAL PROPERTIES OF 14.5-PPG PORTLAND CEMENTS AT CHICHIMENE FIELD

Mechanical and Thermal Properties	14.5-ppg FlexStone Cured at 180°F	14.5-ppg San Antonio
Cement slurrry density, ppg	14.5	14.5
UCS, psi	3,308	6,868
Young's modulus, psi	7.54E+5	1.41e+06
Poisson's ratio	0.19	0.19
Cohesion, psi	1,070	2,200
Friction angle, deg	25	25
Tensile strength, psi	383	675
Expected debonding strength (0.83*To), psi	315	560
Young's modulus /tensile strength	**1,968**	**2,089**
Volumetric specific heat, BTU/(ft^3.°F)	59.4	59.4
Specific heat capacity (Btu/(lbm.°F)	0.5476	0.5476
Thermal conductivity, BTU/ (hr.in.°F)	0.04	0.04
Thermal expansion, 1/°F	6.11E-6	6.11E-6
Tensile fracture energy, BTU/ft^2	0.00607545	0.00607545
Hydration volume change, %	0,0	0,0
Hydration heat, BTU/ft^3	2656.8	2656.8

Figs. 6.8, 6.9, and 6.10 show the risk of damage of 14.5-ppg San Antonio cement at Chichimene field with Halliburton's WellLife Software. The remaining capacity for plastic deformation, debonding, shear deterioration, debonding and radial cracks of set cement were clearly above 60%.

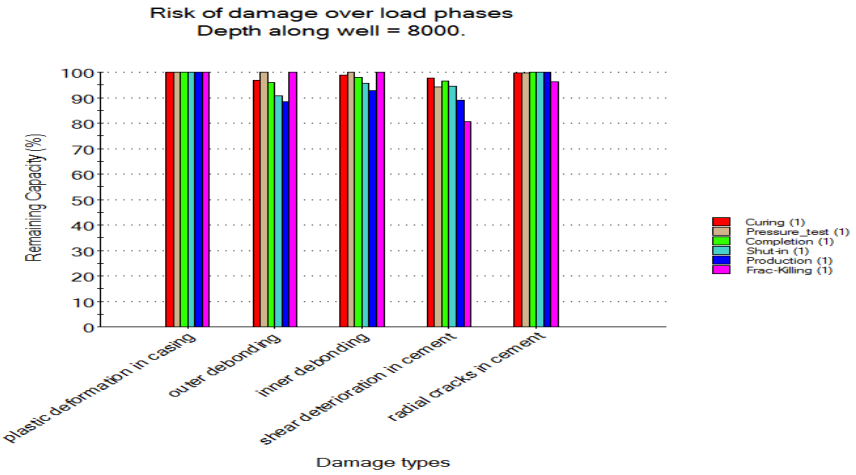

Fig. 6.8—Risk of damage of 14.5-ppg San Antonio cement at T2 formation of Chichimene wells with WellLife software

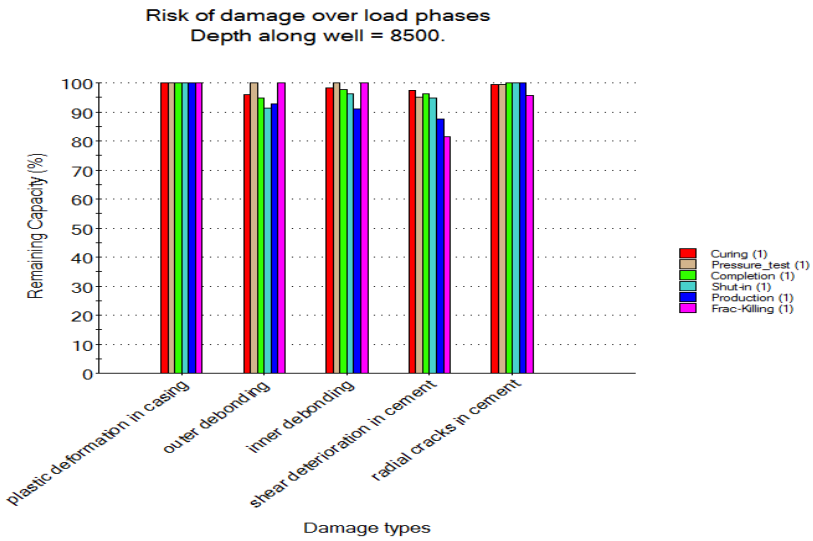

Fig. 6.9—Risk of damage of 14.5-ppg San Antonio cement at K1 formation of Chichimene wells with WellLife software

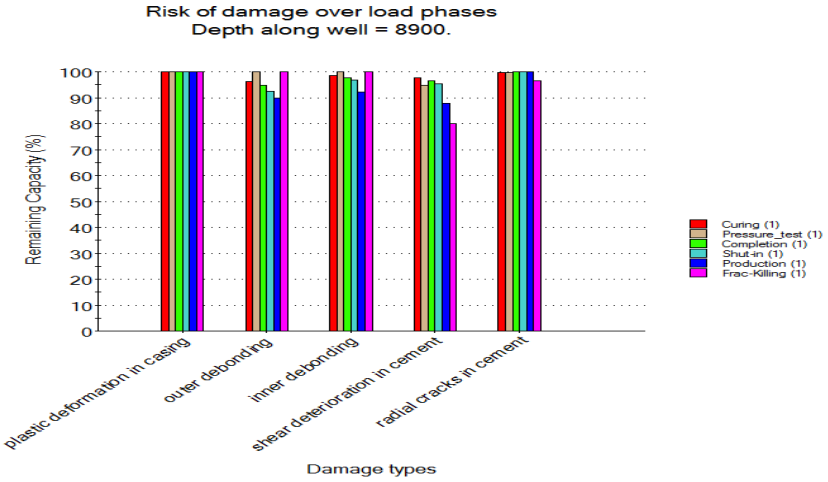

Fig. 6.10—Risk of damage of 14.5-ppg San Antonio cement at K2 formation of Chichimene wells with WellLife software

WellLife software predicted that cement slurry 14.5-ppg San Antonio cement was a good application to avoid cement failure during the life of Chichimene wells. Later in this section, the Abaqus FEM model for Chichimene field showed partial debonding of San Antonio cement after well completion and production in the T2, K1, and K2 formations.

Fig.6.11 illustrates that tensile radial stresses of San Antonio cement reached 652 psi at T2 formation, exceeding the estimated debonding strength of 560 psi. This clearly shows that San Antonio cement debonded from casing at the T2 formation after completion of the Chichimene wells. This debonding was related to the density of drilling and completion fluids. Displacement of the 14.5-ppg San Antonio cement slurry with the completion fluid could be a solution to avoid cement debonding after well completion.

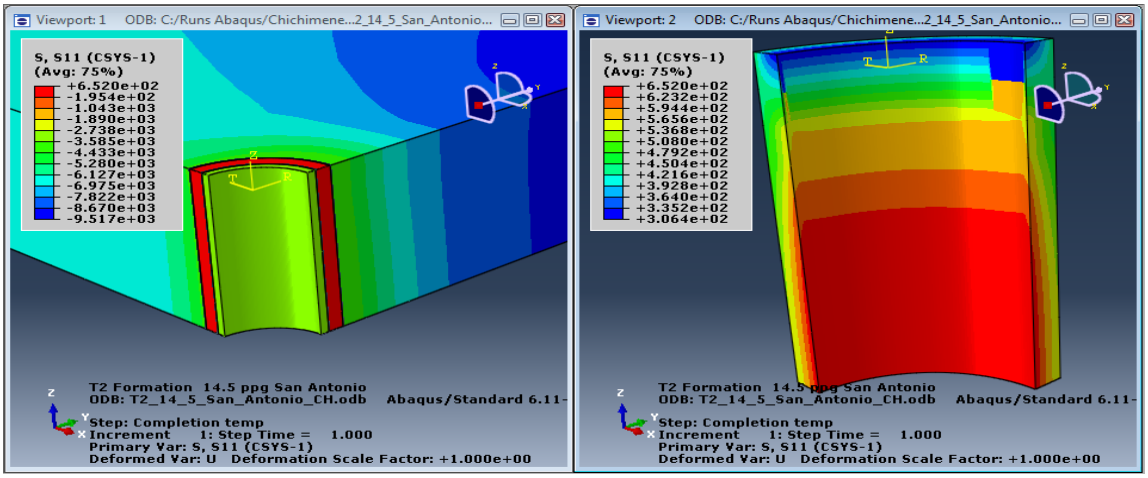

Fig .6.11—Radial stresses with San Antonio cement after well completion at T2 formation of Chichimene wells using FEA. Left: casing, cement and formation. Right: cement

Fig. 6.12 illustrates that tensile tangential stresses of San Antonio cement reached 576 psi at the T2 formation, but it does not exceed its tensile strength of 675 psi. Because tangential stresses of set cement did not exceed the tensile strength of San Antonio cement, there were no chances of cement radial cracking at the T2 formation after hydraulic fracturing of the Chichimene wells. The maximum tensile tangential stresses were clearly in the casing/cement contact, and therefore the cracks started in this point and propagated to the cement/formation contact.

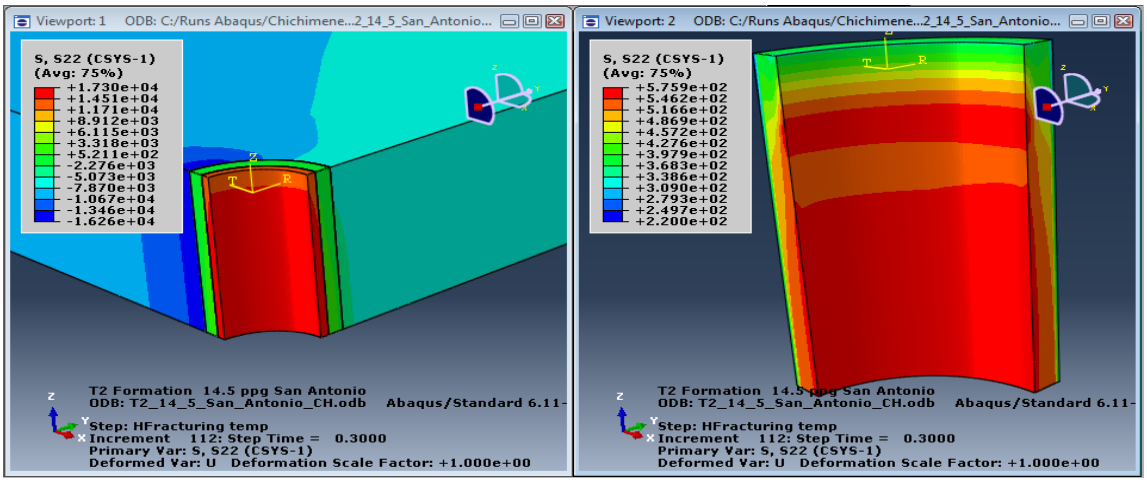

Fig. 6.12—Tangential stresses with San Antonio cement after hydraulic fracturing at T2 formation of Chichimene wells using FEA. Left: casing, cement and formation. Right: cement

Fig. 6.13 illustrates that tensile radial stresses of San Antonio cement reached 689 psi at the T2 formation during production, exceeding the estimated debonding strength of 560 psi. This clearly reveals partial debonding of San Antonio cement from casing at the T2 formation of Chichimene wells at a bottomhole production pressure of 1,500 psi. Cement debonding strength higher than 689 psi is uncommon.

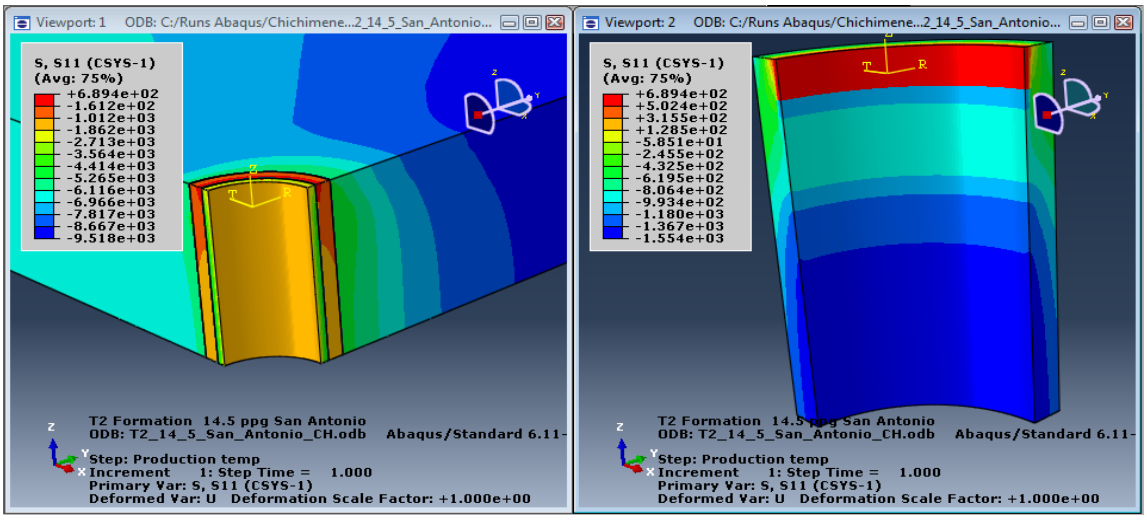

Fig. 6.13—Radial stresses with San Antonio cement during production of T2 formation of Chichimene wells using FEA. Left: casing, cement and formation. Right: cement

Fig. 6.14 reveals a partial plastic deformation of San Antonio cement in the T2 formation at bottomhole production pressure of 1,500 psi. This FEA shows that equivalent plastic deformation (PEEQ) of San Antonio cement was 0.1% at the top of the set cement.

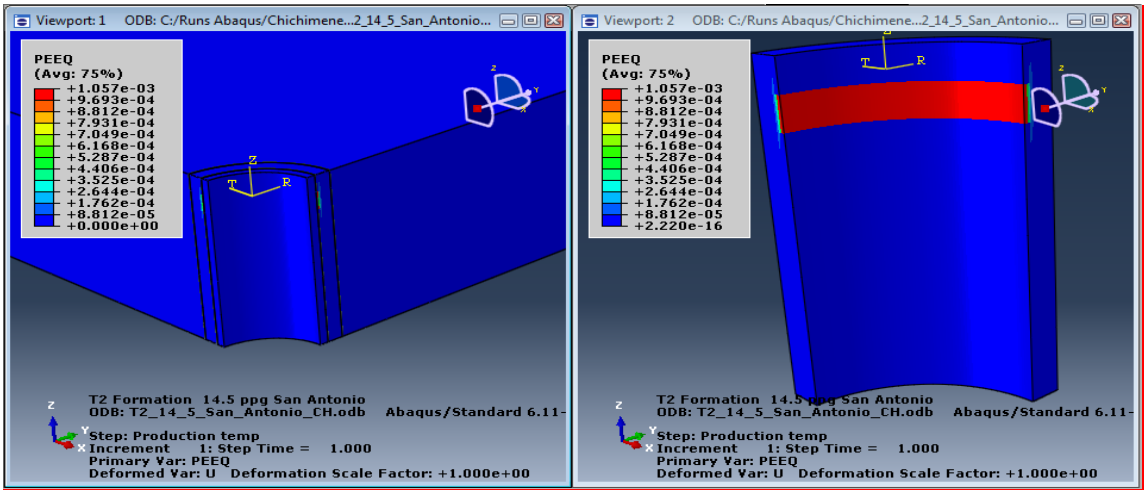

Fig. 6.14—Equivalent plastic deformation with San Antonio cement during well production at T2 formation of Chichimene wells using FEA. Left: casing, cement and formation. Right: cement

Appendix E shows the FEA of 14.5-ppg San Antonio cement behavior in K1 and K2 formations of Chichimente wells. Debonding of 14.5-ppg San Antonio cement from casing was the main risk of cement failure after well completion and well production in the T2, K1, and K2 formations.

Tables 6.10, 6.11, and 6.12 show that San Antonio cement had better zonal isolation than FlexStone cement in front of the T2, K1, and K2 formations of Chichimene wells. San Antonio cement did not have cracks, but it had partial debonding during completion and well production. FlexStone cement had radial cracks at T2 and K2, and higher plastic deformation than San Antonio cement. In this case FlexStone cement had a lower Young's modulus/tensile strength ratio than San Antonio cement. However, San Antonio cement had better zonal isolation than FlexStone cement.

TABLE 6.10—FEA WITH DIFFERENT SET CEMENTS AT T2 FORMATION OF CHICHIMENE FIELD

	Hydraulic Fracturing					Well Production				
Cement Design	Max. VM, psi	Max. S22, psi	Radial cracks	Cement PEEQ, %	Form. PEEQ, %	Max. VM, psi	Max. S11 Stress, psi	Debond	Cement PEEQ, %	Form. PEEQ, %
14.5-ppg FlexStone Cured at 180°F	1,551	970	Yes	0.20	0	2,130	438	Partial	0.38	0
14.5-ppg San Antonio	**1,181**	**576**	**No**	**0.10**	**0**	**2,880**	**689**	**Partial**	**0.10**	**0**

TABLE 6.11—FEA WITH DIFFERENT SET CEMENTS AT K1 FORMATION OF CHICHIMENE FIELD

	Hydraulic Fracturing					Well Production				
Cement Design	Max. VM, psi	Max. S22, psi	Radial cracks	Cement PEEQ, %	Form. PEEQ, %	Max. VM, psi	Max. S11 Stress, psi	Debond	Cement PEEQ, %	Form. PEEQ, %
14.5-ppg FlexStone Cured at 180°F	1,378	270	No	0.56	0	2,604	210	No	0.7	0
14.5-ppg San Antonio	**1,135**	**595**	**No**	**0**	**0**	**2,497**	**855**	**Partial**	**0**	**0**

TABLE 6.12—FEA WITH DIFFERENT SET CEMENTS AT K2 FORMATION OF CHICHIMENE FIELD

	Hydraulic Fracturing					Well Production				
Cement Design	Max. VM, psi	Max. S22, psi	Radial cracks	Cement PEEQ, %	Form. PEEQ, %	Max. VM, psi	Max. S11 Stress, psi	Debond	Cement PEEQ, %	Form. PEEQ, %
14.5-ppg FlexStone Cured at 180°F	1,674	578	Yes	0,28	0	2,250	469	Partial	0,54	0
14.5-ppg San Antonio	**1,128**	**557**	**No**	**0**	**0.1**	**2,850**	**732**	**Partial**	**0.10**	**0**

6.3 Cement Behavior at In-Situ Combustion Project of Chichimene Field

Ecopetrol is carrying out a pilot project of in-situ combustion to recover heavy oil from the T2 formation at Chichimene field, Colombia. The technique consists of ignition in the oil well and injection of air to maintain a flame front that travels from the injection well to production wells. The flame front passes through observation wells. In this process, a small quantity of in-situ oil burns, producing CO_2, water vapor, and heat

that lowers the viscosity of the oil to go to the producer well. When CO_2 comes into contact with the Portland cement, it produces a deterioration phenomenon in the cement called carbonation. Over time, the loss of cement to carbonation can destroy zonal isolation integrity.

The in-situ combustion project had 3 production wells, 2 observation wells, and 1 injection well that were drilled up to K1 formation top (Fig. 6.15). Injection and production wells can reach temperatures of 500°F and higher, and observation wells can reach temperatures from 600°F to 1,200°F. Therefore, a set cement was designed to withstand temperatures higher than 500°F, 15-20% molar fraction of CO_2, and 0.2-1% molar fraction of H_2S.

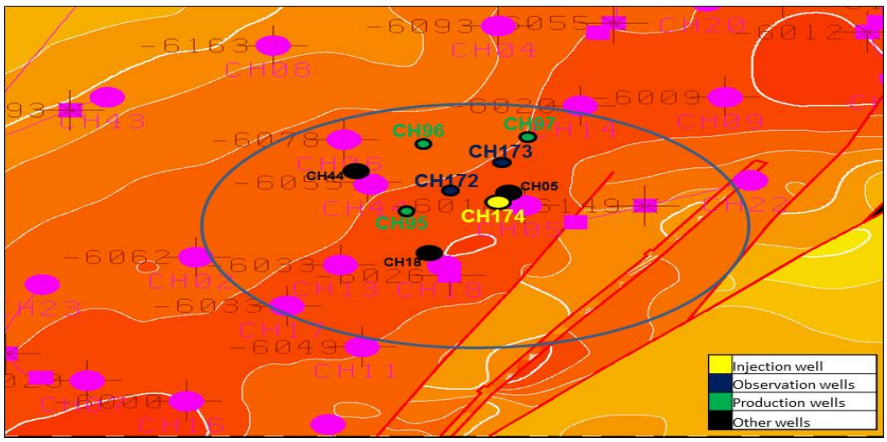

Fig. 6.15—Structural map of T2 formation showing well placement of in-situ combustion project at Chichimene field, Colombia

ThermaLock, a calcium-phosphate cement, is not affected by acid environments and high temperatures because of its composition. In the lab, Thermalock can withstand temperatures above 1,000°F, even in a CO_2 or acid environment.[46]

The 15-ppg ThermaLock cement had only 3% weight loss in 61 days, and it can withstand $C0_2$ environments (Fig. 6.16). Latex can plug small pores in a cement matrix, but it did not protect Class H cement from carbonic acid. Likewise, 50/50 Class H/fly ash with 2 gps of latex had 21% weight loss in 62 days.

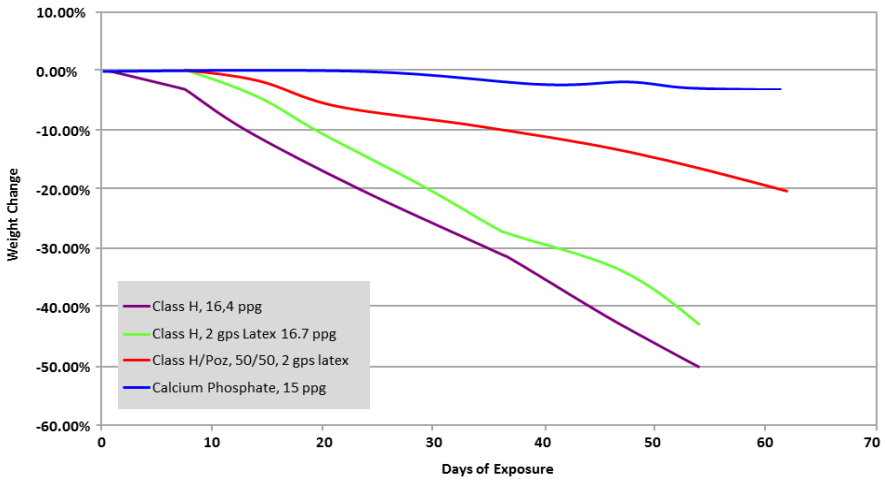

Fig. 6.16—Class H and ThermaLock cements at 140°F in CO_2 environment with pH of 2 (after Ref. 46)

Table 6.13 shows the mechanical and thermal properties of ThermaLock cement Design 5TL for the in-situ combustion process at Chichimene field. Thermalock cement slurry density was decreased from 15.7 ppg to 14.5 ppg with Spherelite (microspheres), and it was further modified to withstand hydraulic fracturing jobs by reducing its Young's modulus and increasing its tensile strength. The 7-in. casing for the in-situ combustion project was sandblasted before running to give a rougher edge and higher bonding strength.

Fig. 6.17 shows the WellLife software interpretation of ThermaLock cement Design 5TL for the in-situ combustion process at Chichimene field. This simulation included well loads described in Table 6.7 and well temperature of 500°F during oil production or gas injection. The ThermaLock cement Design 5TL had a residual capacity up to 70%, and it can withstand all the expected loads during its productive life. WellLife software simulates the in-situ combustion heat flux like a cyclic steam injection process, but this assumption is not correct due to the direction of heat flux. In in-situ combustion process, the heat flux comes from the rock to the well. In cyclic steam injection, the heat flux comes from the well to the formation. During in-situ combustion, stresses and deformations of the rock can squeeze the set cement.

TABLE 6.13—MECHANICAL AND THERMAL PROPERTIES OF THERMALOCK CEMENT WITH 2% BWOC CARBON FIBERS (DESIGN 5TL)

Mechanical and Thermal Properties	Value
Cement slurrry density, ppg	14.5
Young's modulus, psi	0.842 E+6
Poisson's ratio	0.15
Cohesion, psi	1,327
Friction angle, deg	12.1
UCS, psi	3,285
Tensile strength, psi	490.6
Young's modulus / tensile strength	1,716
Volumetric specific heat, BTU/(ft^3.°F)	59.4
Specific heat capacity (Btu/(lbm×°F)	0.54763
Thermal conductivity, BTU/(hr.in. °F)	0.03658
Thermal expansion, 1/°F	6.11E-6
Tensile fracture energy, BTU/ft^2	0.00607545
Hydration volume change, %	0,05
Hydration heat, BTU/ft^3	2656.8
Klikenberg permeability, md	0.014
Water permeability, md	0.01

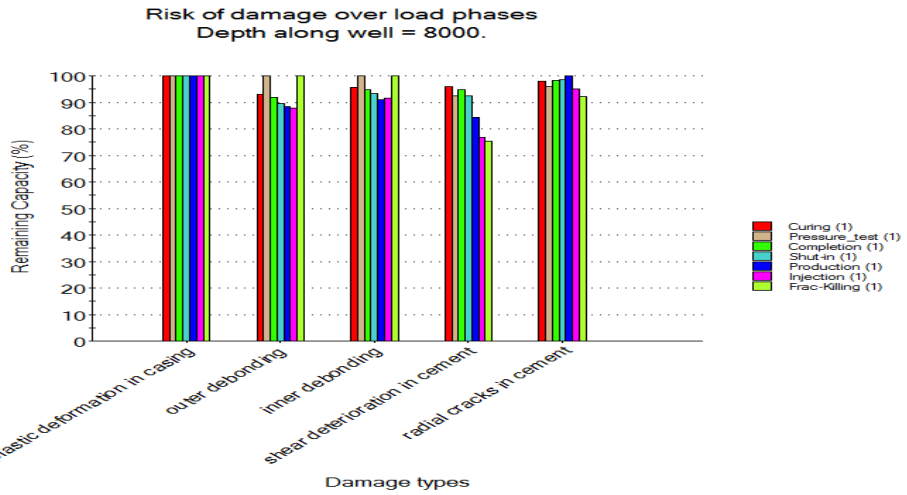

Fig. 6.17—Risk of damage of ThermaLock cement at T2 formation for in-situ combustion project at Chichimene wells

The FEM designed during this research was used to simulate the mechanical behavior of the set cement during the in-situ combustion project. During the hydraulic fracturing of the producing well, the formation was cooled down by the hydraulic fluid, and during in-situ combustion, the formation, cement, and casing were heated up (Fig.

6.18). Temperatures of casing, cement, and formation were in the range of 180°F to 186°F after hydraulic fracturing; and throughout well production, the FEM included 1,500°F at boundary conditions to simulate the in-situ combustion temperatures. Temperatures of the casing, cement, and formation changed from 600°F to 1,500°F, and their effect on the set cement was studied. The set cement remained in the range from 600°F to 692°F during well production (Fig.6.19).

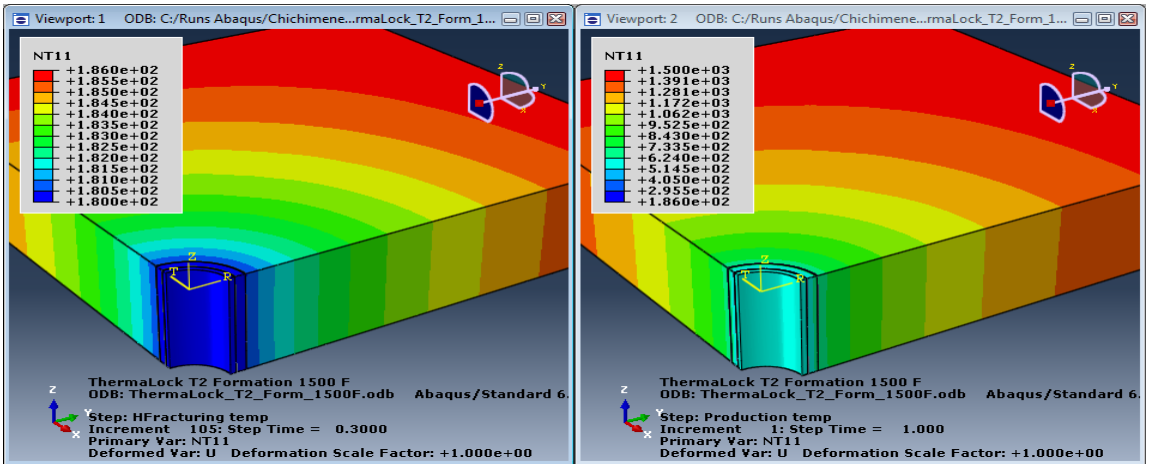

Fig. 6.18—Casing, cement and formation temperature after hydraulic fracturing (left) and during well production (right) at T2 formation of Chichimene field during in-situ combustion process using FEA

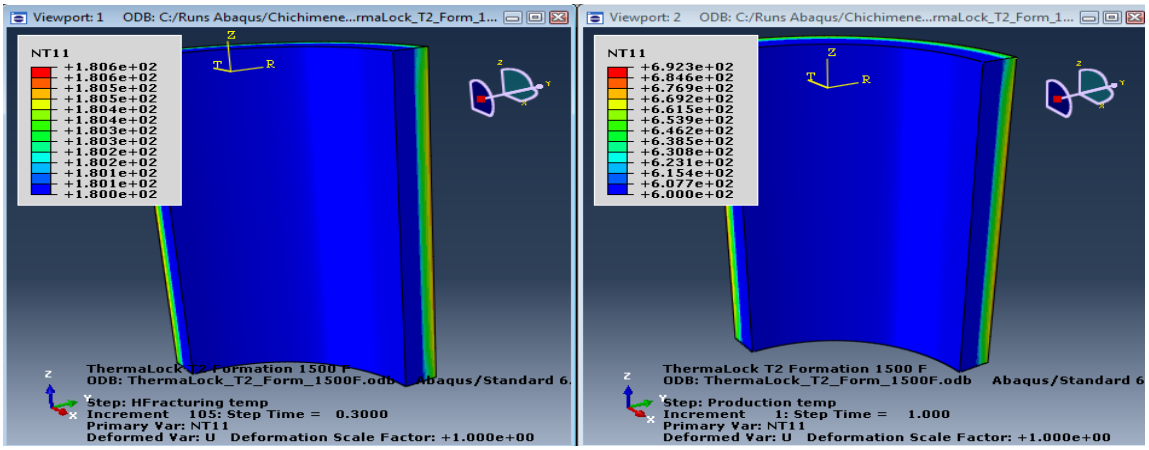

Fig. 6.19—Cement temperature after hydraulic fracturing (left) and during well production (right) at T2 formation of Chichimene field during in-situ combustion using FEA

During hydraulic fracturing, the set cement was in compression (negative values), and therefore there was no risk of debonding of cement from either the casing or the formation (Fig.6.20). However, during well production the minimum debonding strength required can reach 4,186 psi. ThermaLock cement cannot withstand such a high debonding pressure value.

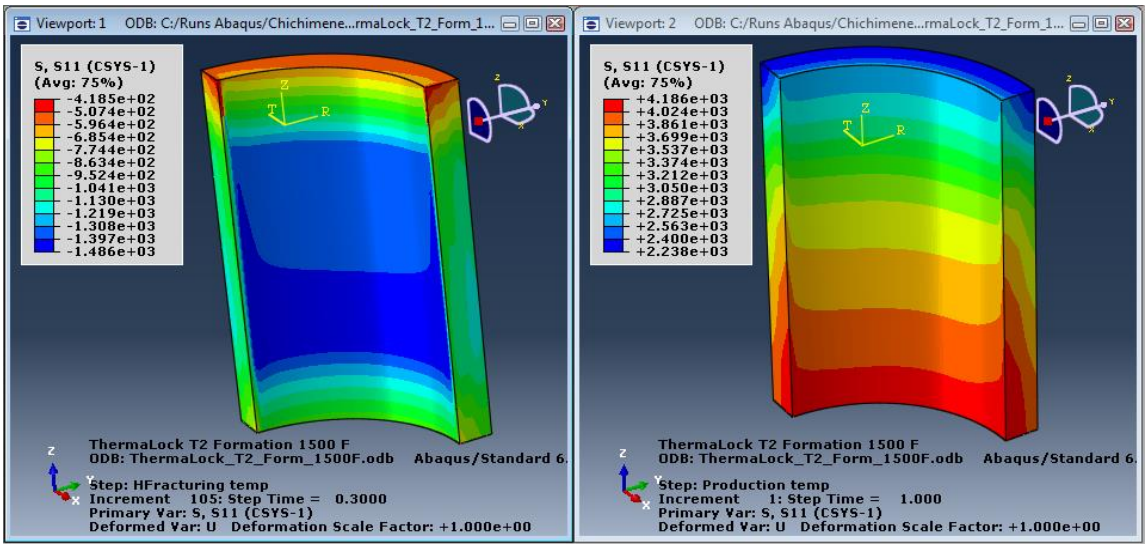

Fig. 6.20—Radial stresses of set cement after hydraulic fracturing (left) and well production (right) at T2 formation of Chichimene field during in-situ combustion using FEA

The tangential stresses created in ThermaLock cement during hydraulic fracturing job and well production were 352 psi and 3,309 psi, one-to-one (Fig.6.21). ThermaLock cement had tensile strength of 490 psi, and it can withstand tangential stresses created during hydraulic fracturing. However, ThermaLock cement failed during well production of in-situ combustion project of Chichimene wells, because tangential stresses surpassed its tensile strength, leading to radial cracks.

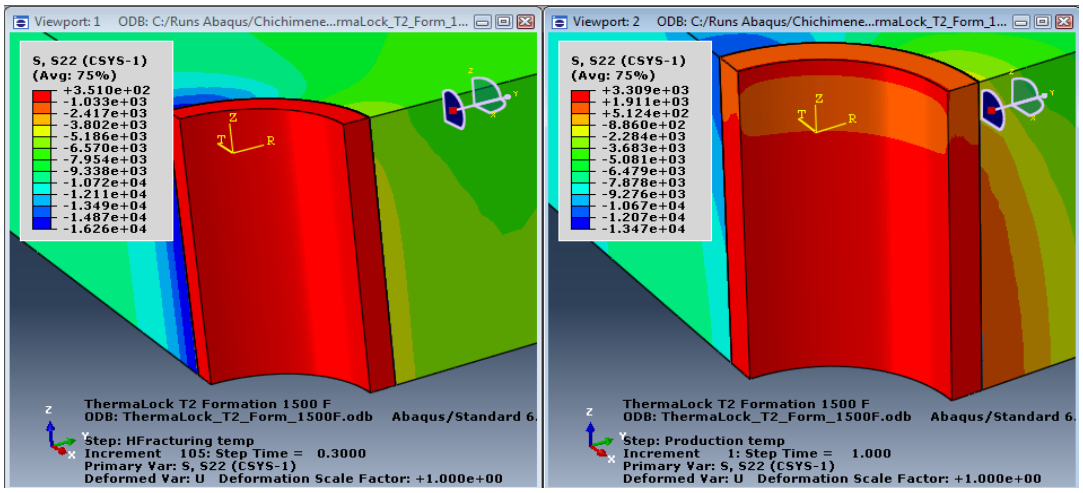

Fig. 6.21—Tangential stresses of cement and formation after hydraulic fracturing (left) and well production (right) at T2 formation of Chichimene field during in-situ combustion using FEA

No plastic deformation appeared in the cement and rock during hydraulic fracturing in the Chichimene wells (Fig.6.22). However, the FEM showed that ThermaLock cement Design 5TL had plastic deformations up to 2.29% during well production at temperature higher than 600°F. The FEM showed that ThermaLock cement had radial cracks and plastic deformation during well production at 692°F.

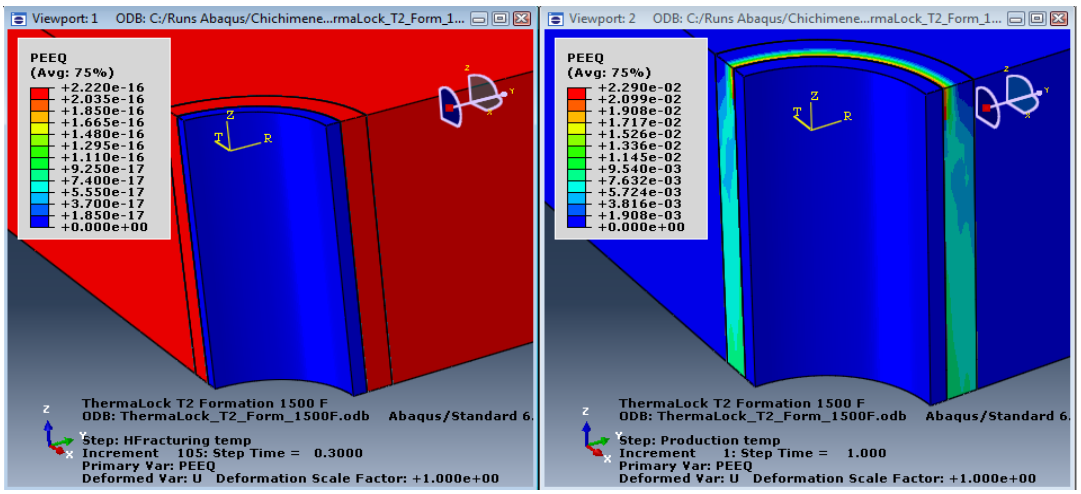

Fig. 6.22—Equivalent plastic deformation after hydraulic fracturing (left) and well production (right) at T2 formation of Chichimene field during in-situ combustion using FEA

Fig.6.23 schematically shows typical designs for production and injection wells at in-situ combustion project at Chichimene field. 13-3/8-in casing was cemented with 15.6-ppg cement with 35% of silica flour from 1,000 ft to surface, and 9-5/8-in. casing was cemented with 14.5-ppg cement with 35% of silica flour from 7,740 ft to surface. Well designs included liner hanger for HTHP conditions, and 7-in. 32-lb L80 liner with 13% (by weight) chromium to withstand high oxidation and $C0_2$ and H_2S. 7-in liners were cemented with 14.5-ppg ThermaLock cement (Design 5TL).

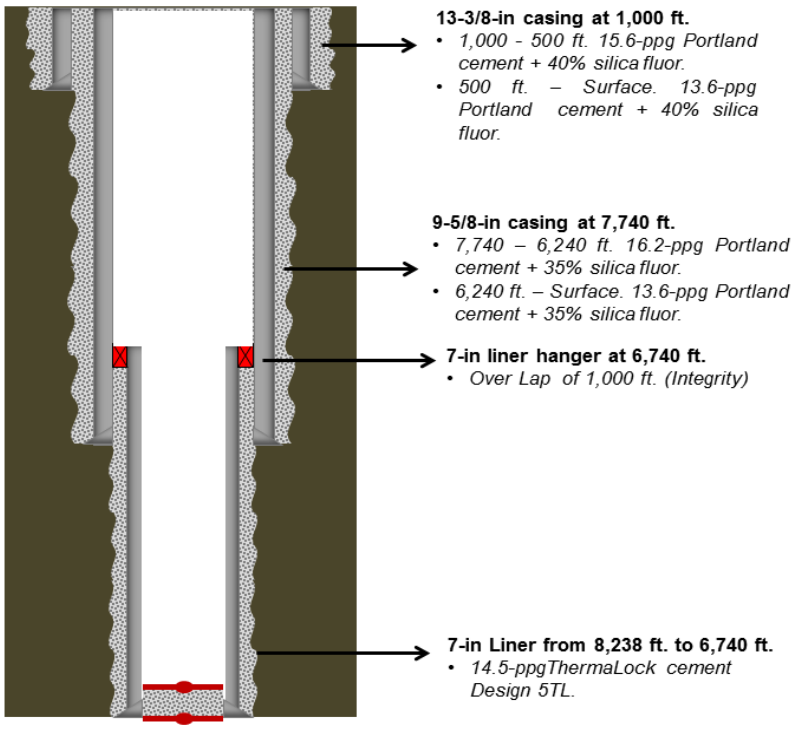

Fig. 6.23—Well design for production and observation wells (left) and injection wells (right) for in-situ combustion at Chichimene field

Two types of liner hangers were used during the in-situ combustion project: a TIW XPak expandable liner hanger/packer and a Baker Hughes system with a mechanical rotating flex-lock liner hanger and ZXP Ultra HP/HT compression set liner top packer. These liner hanger systems were chosen because they did not have hydraulic

chambers or ports, and they did not use a setting ball to set the liner hanger. This eliminated the risk of lost circulation when the ball seat shears with the applied pressure. Also, Ultra HP/HT liner hangers could be a barrier in the event of cement failure observed with the FEA.

Wellhead and Christmas tree designs of observation, production and injection wells were completely different (Fig.6.24), and they were designed to withstand temperatures up to 650°F along with $C0_2$, H_2S, and 9,000 ppm of chlorides.

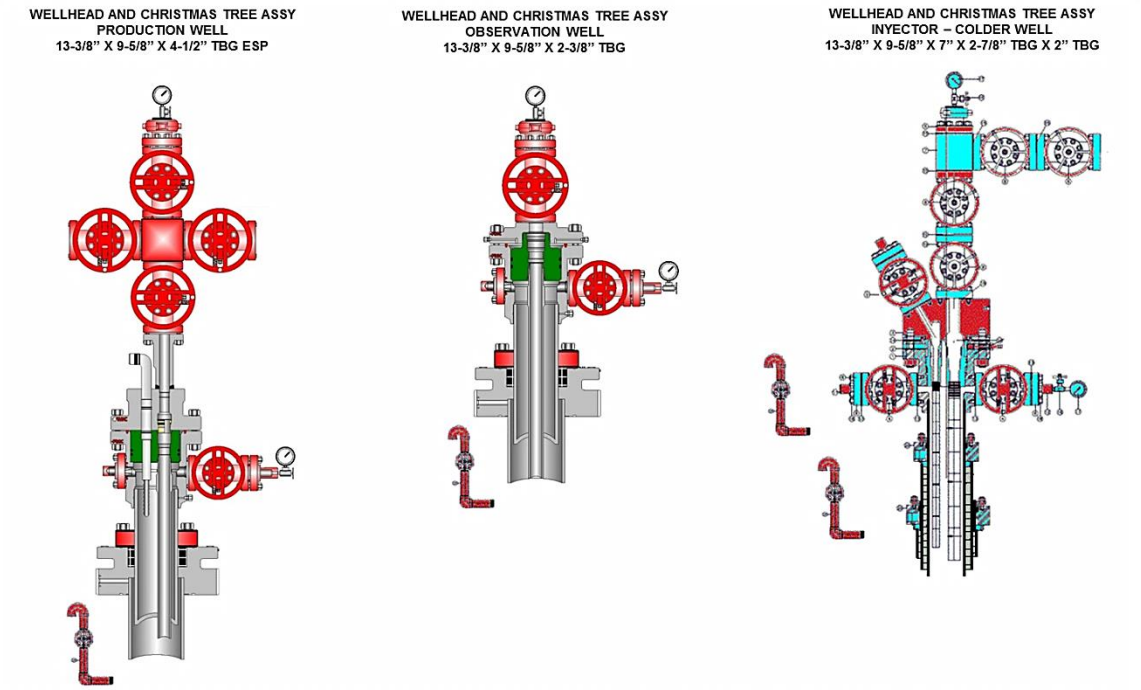

Fig. 6.24—Wellhead and Christmas tree designs for production wells (left), observation wells (middle) and injection well (right) for in-situ combustion at Chichimene field

Ultrasonic logs are generally easier to interpret and less ambiguous than sonic logs, but the combination of sonic and ultrasonic cement logs was essential. The acoustic impedance of ThermaLock cement Design 5TL was 4.45 mega-Rayleigh (MRayl), and this value was included to correct cement ultrasonic logs.

Cement evaluation logs for the Chichimene 95 well after 7 and 25 days (Fig. 6.25) show that the cement did not set in the scheduled time. In this well, cement retarder was added to the ThermaLock Design 5TL, which was expected to keep the cement from setting prematurely. However, the cement did not set in 7 days, so it was decided to suspend cement retarder. The cement slurry did not include any accelerator because its thickening time is limited to 4 hrs.

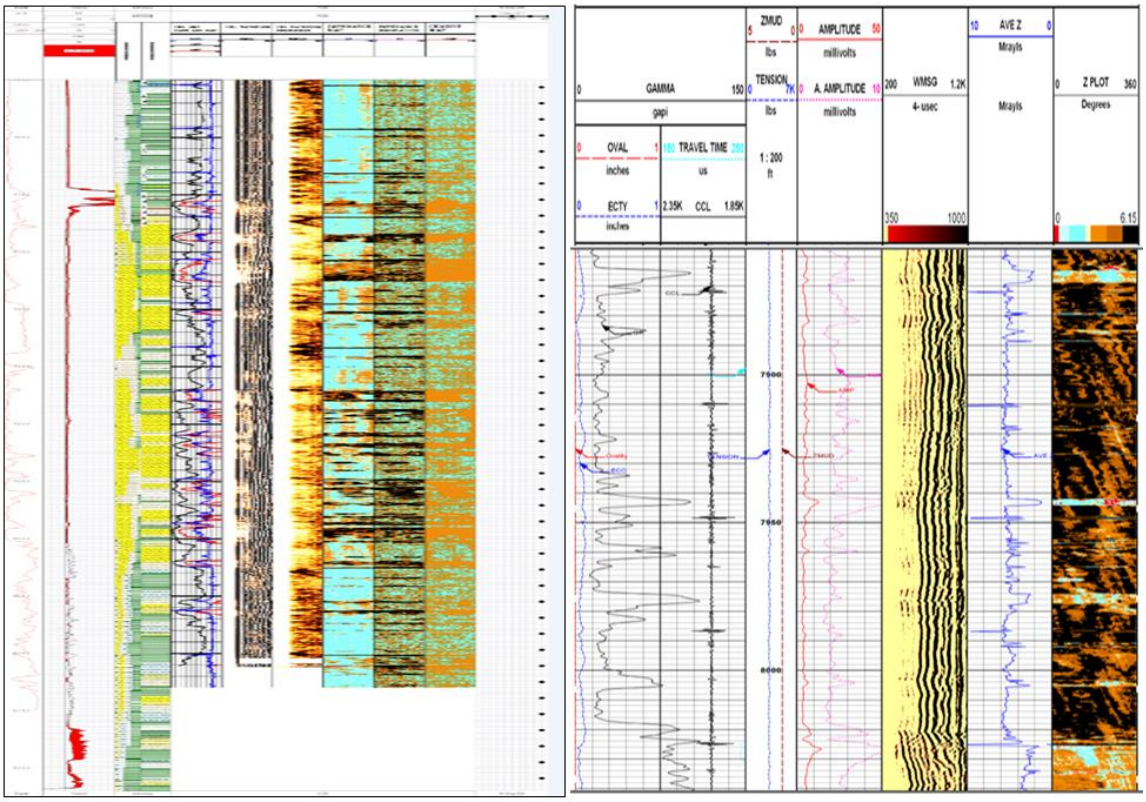

Fig. 6.25—Cement evaluation after 7 days (left) and 25 days (right) of WOC at Chichimene-95 well

Fig. 6.26 shows cement evaluation logs of the Chichimene 97 and 172 wells after 7 days and 30 days. Six Chichimene wells were drilled for the in-situ combustion pilot project in year 2012, and continuous lessons learned were applied after each well. Best practices were used in job design, like good casing centralization (7-in. casing with

standoff higher than 75%), liner rotation, and density and viscosity hierarchies of fluids to optimize mud displacement during cementing operations. Cement evaluation logs were considered adequate for the six Chichimene wells drilled for the in-situ combustion project.

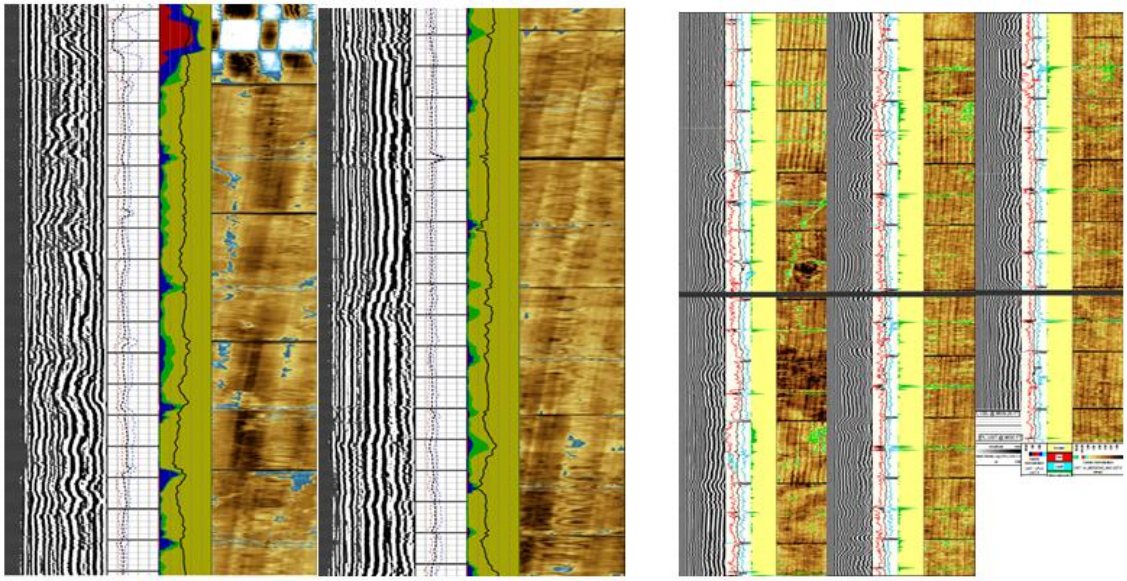

Fig. 6.26—Cement evaluation after 7 days of WOC at Chichime-97 (left) and 30 days of WOC Chichimene 172 (right) wells

6.4 Simulation of Cement Behavior at Cupiagua Field, Colombia

Cupiagua wells have three oil-productive formations: Mirador, Barco, and Guadalupe. Barco and Mirador formations can reach UCS values above 30,000 psi. The reservoirs are sandstone with some intervals of shale. The Cuervos formation, located in the middle of the Mirador and Barco formations, is mainly shale. The productive zones of Cupiagua field are the Mirador, Barco, and Guadalupe formations, and this field produces light crude oil from sandstones.

Mirador and Cuervos formations are drilled with an $8^1/_2$-in. borehole size, and Barco and Guadalupe formations are drilled with a $6^1/_2$-in. borehole size. All four

formations are cemented with 14.5-ppg cement slurry. The Cuapiagua field is located in a high-tectonic-stress area of the foothills of Eastern Cordillera in Colombia.

Table 6.14 presents borehole data and loads at Cupiagua wells. All data was taken from the drilling history of the wells, temperature logs, and hydraulic fracturing jobs in the field. The true vertical depth of Cupiagua wells is about 15,000 ft.

TABLE 6.14—BOREHOLE DATA AND LOADS AT CUPIAGUA WELLS

Well Data	Formation Name			
	Mirador	Cuervos	Barco	Guadalupe
Formation top, ft	**12,730**	**13,318**	**14,045**	**14,588**
Borehole, in.	**8.5**	**8.5**	**6.5**	**6.5**
Casing OD, in.	**7.0**	**7.0**	**5.5**	**5.5**
Casing ID, in.	**6.276**	**6.276**	**4.948**	**4.948**
Overburden pressure, psi/ft	1.1	1.1	1.1	1.1
Maximum horizontal stress pressure, psi/ft	1.3	1.3	1.3	1.3
Minimum horizontal stress pressure, psi/ft	0.8	0.8	0.8	0.8
Azimuth of maximum horizontal stress direction, deg	120	120	120	120
Formation pore pressure, psi	**3,574**	**3,656**	**3,739**	**7,157**
Mud gradient, psi/ft	**0.416**	**0.546**	**0.546**	**0.546**
Mud temperature, °F	**198**	**200**	**204**	**211**
Cement slurry density, ppg	14.5	14.5	14.5	14.5
Completion fluid density, ppg	8.4	8.4	8.4	8.4
Hydraulic fracturing pressure gradient, psi/ft	0.9	0.9	0.9	0.9
Hydraulic fracturing fluid temperature, °F	**198**	**200**	**204**	**211**
Bottomhole production pressure, psi	1,000	1,000	1,000	1,000
Tubular fluid temperature during production, °F	**233**	**236**	**240**	**248**
Surface temperature, °F	80	80	80	80
Formation temperature, °F/100 ft	1.2	1.2	1.2	1.2

Table 6.15 displays the mechanical and thermal formation properties of the payzones and Cuervos formation at Cupiagua field. The mechanical properties of formations were calculated and calibrated with laboratory tests. Thermal rock properties were taken from the library of Halliburton's WellLife software. The thermal expansion of shale was higher than sandstone. Cuervos formation is a nonproductive formation, but it has to withstand hydraulic fracturing pressure of the well. More specific information about mechanical rock properties and in-situ stresses of the studied fields is included in Appendix D.

TABLE 6.15—MECHANICAL AND THERMAL FORMATION PROPERTIES AT CUPIAGUA FIELD

Mechanical and Thermal Properties	Formation Names			
	Mirador	Cuervos	Barco	Guadalupe
Density, ppg	20.86	19.61	20.03	21.95
UCS, psi	36,207	11,500	31,000	24,858
Young's modulus, psi	6.29 E+06	3.0E+06	8.3E+06	2,94E+06
Poisson's ratio	0.13	0.25	0.25	0.19
Friction angle, deg	50	25	45	51
Cohesion, psi	5,776	4,000	5,700	7,246
Volumetric specific heat, BTU/(ft^3.°F)	33.0624	44.28	33.0624	33.0624
Specific heat capacity (Btu/(lbm×°F)	0.21187	0.3018	0.22065	0.20135
Thermal conductivity, BTU/(hr.in.°F)	0.1108	0.08191	0.1108	0.1108
Thermal Expansion, 1/°F	5.56E-6	1.667E-5	5.56E-6	5.56E-6

Table 6.16 shows the mechanical and thermal properties of set cement used in Cupiagua wells. Set cement samples were cured at 211°F and 3,000 psi for 24 hrs. before doing triaxial tests. Specific composition of the cement slurries and their mechanical properties are included in Appendix B and C.

TABLE 6.16—MECHANICAL AND THERMAL PROPERTIES OF SET CEMENT OF CUPIAGUA WELLS

Mechanical and Thermal Property	Cupiagua	Yopal
Cement slurrry density, ppg	14.5	14.5
UCS, psi	5,713	5,541
Young's modulus, psi	1.02 E+6	1.46 E+6
Poisson's ratio	0.19	0.23
Cohesion, psi	2,270	1,200
Friction angle, deg	13.0	38
Tensile strength, psi	597	536
Young's modulus / tensile strength ratio	1,708	2,723
Expected debonding strength (0.83*To), psi	495	445
Volumetric specific heat, BTU/(ft^3.°F)	59.4	59.4
Specific heat capacity (Btu/(lbm×°F)	0,54763	0,54763
Thermal conductivity, BTU/(hr.in. °F)	0,04	0,04
Thermal expansion, 1/°F	6.11E-6	6.11E-6
Tensile fracture energy, BTU/ft^2	0.00607545	0.00607545
Hydration volume change, %	0,0	0,0
Hydration heat, BTU/ft^3	2656.8	2656.8

Mirador and Cuervos formations show a minor risk of cement outer debonding during production of Cupiagua wells (Figs. 6.27 and 6.28). According to WellLife software, Yopal cement had good zonal isolation at the Mirador and Cuervos formations.

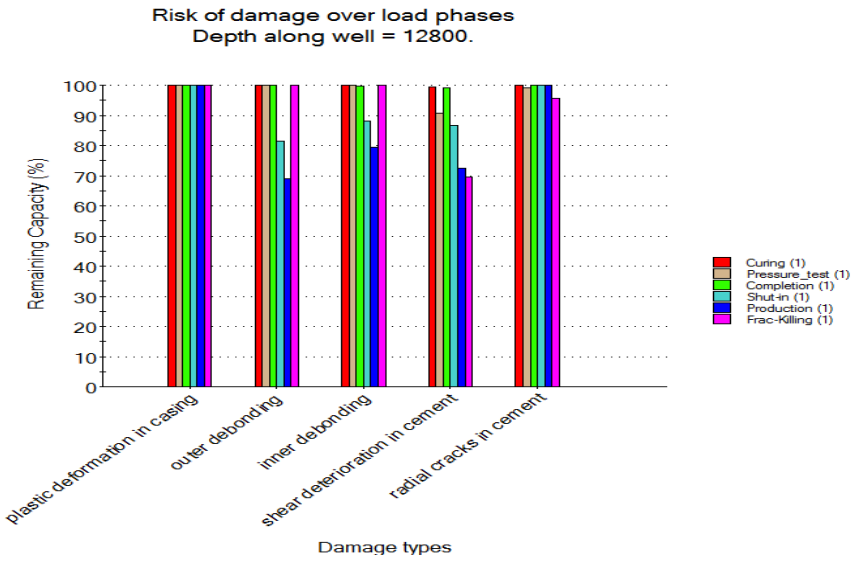

Fig. 6.27—Risk of damage of Yopal cement at Mirador formation of Cupiagua wells with WellLife software

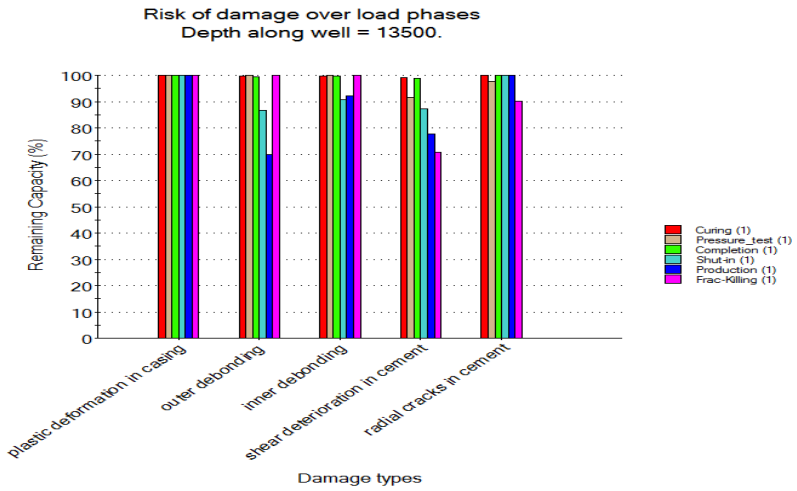

Fig. 6.28—Risk of damage of Yopal cement at Cuervos formation at Cupiagua wells with WellLife software

The Barco and Guadalupe formations show high risk of plastic deformation of the casing and cement outer debonding (Figs. 6.29 and 6.16) and risk of shear deterioration after hydraulic fracturing at both formations. The casing design must be reviewed because of the risk of plastic deformation of $5^1/_2$–in. casing.

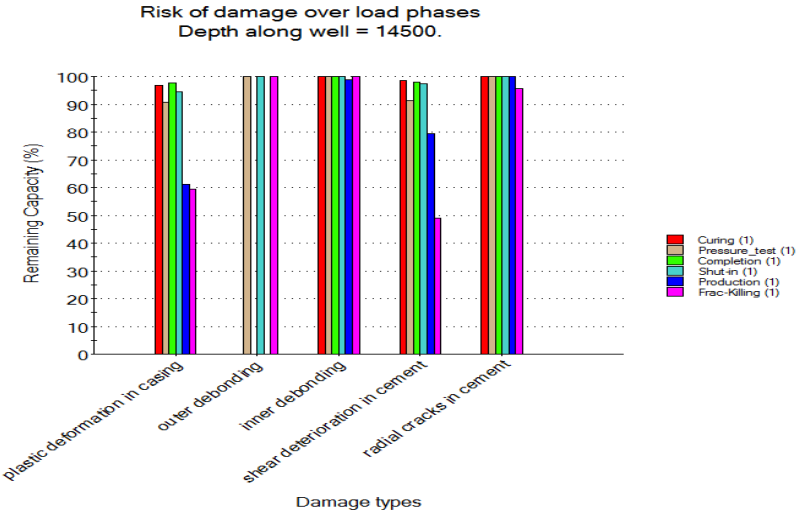

Fig. 6.29—Risk of damage of Yopal cement at Barco formation at Cupiagua field with WellLife software

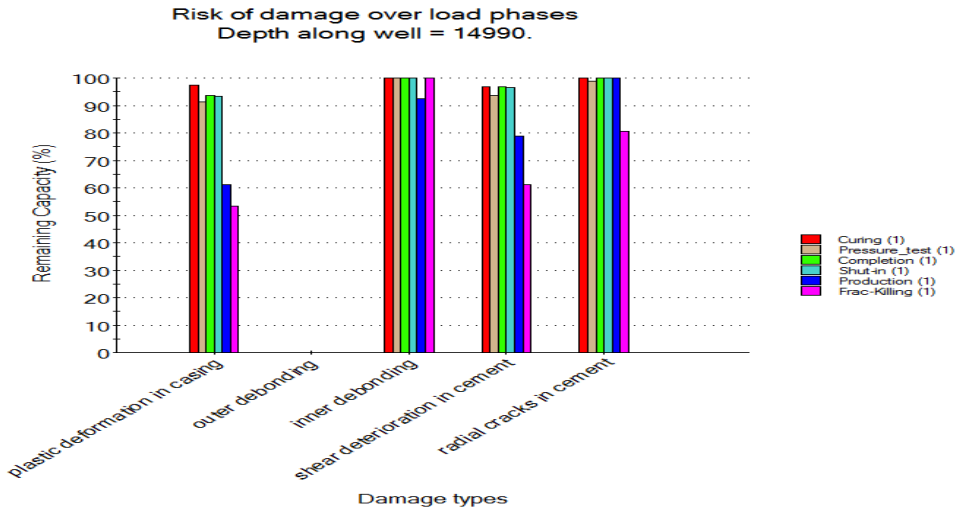

Fig. 6.30—Risk of damage of Yopal cement at Guadalupe formation at Cupiagua field with WellLife software

According to WellLife software, 14.5-ppg Yopal cement did not have the mechanical properties to give zonal isolation at the Barco and Guadalupe formations of Cupiagua wells. The remaining outer debonding and shear strength capacity of the cement was lower than 60%.

The FEA developed in this research was applied to understand the performance of 14.5-ppg Cupiagua and 14.5-ppg Yopal cements at Cupiagua wells. Partial debonding occurred in both set cements from casing and the Guadalupe formation after well completion of Cupiagua wells (Fig. 6.31). However, the 14.5-ppg Cupiagua cement was more likely to debond from casing and formation than the 14.5-ppg Yopal cement. The tensile radial stresses of the 14.5-ppg Yopal cement were in the range of 6 to 1,045 psi at Guadalupe formation, exceeding the estimated debonding strength of 445 psi.

Cement debonding from casing was related to the density of drilling and completion fluids. The Barco and Guadalupe formations are drilled in the same section, which ended with 10.5-ppg drilling fluid, and wells are completed with an 8.4-ppg completion fluid. Displacement of cement slurries with completion fluid could be a solution to avoid cement debonding after well completion.

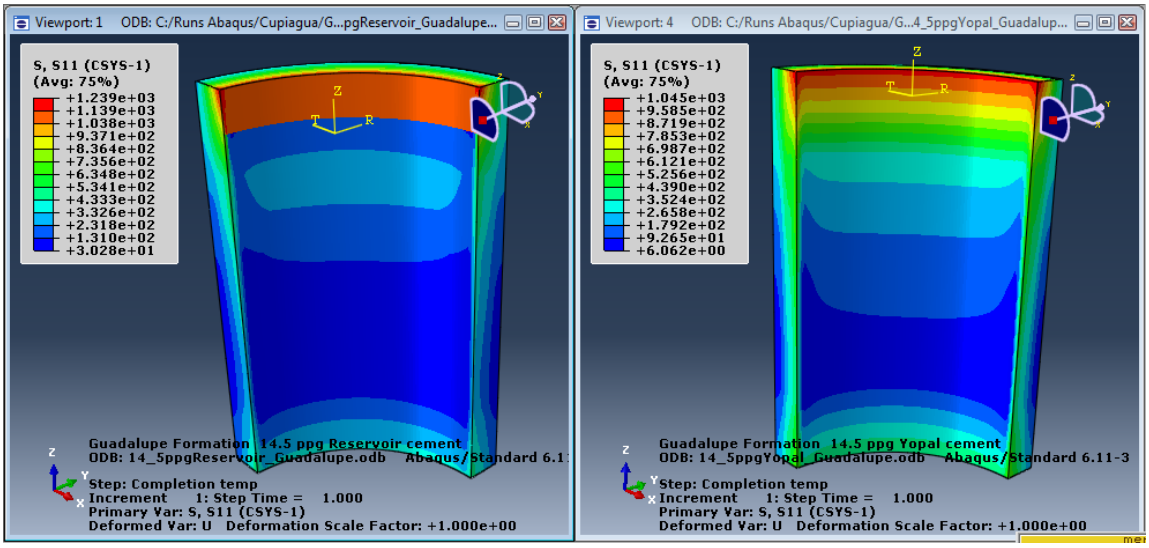

Fig . 6.31—Radial stresses after well completion at Guadalupe formation of Cupiagua wells using FEA. Left: Cupiagua cement. Right: Yopal cement

Tangential stresses of 14.5-ppg Yopal cement reached 832 psi at Guadalupe formation (Fig. 6.32), and it exceeded its tensile strength of 536 psi, increasing chances of radial cracks during hydraulic fracturing jobs. 14.5-ppg Yopal cement can have cracks in the whole set cement, which led to a serious failure of set cement. 14.5-ppg Cupiagua cement does not exceed its tensile strength of 597 psi, and therefore there were no chances of radial cracks of the set cement.

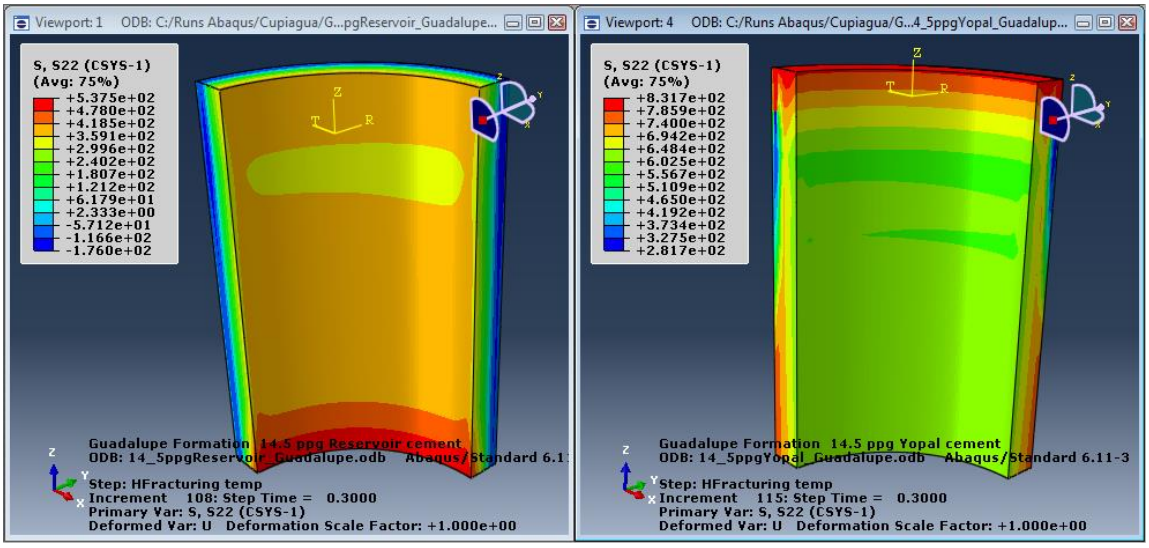

Fig. 6.32—Tangential stresses after hydraulic fracturing at Guadalupe formation of Cupiagua wells using the FEA. Left: Cupiagua cement. Right: Yopal cement

Radial stresses of 14.5-ppg Cupiagua and 14.5-ppg Yopal cements were tensile at the top of set cement at Guadalupe formation during production with a bottomhole production pressure of 1,000 psi (Fig.6.33). This clearly reveals partial debonding of both cements from casing at the Guadalupe formation because cement tensile radial stresses were higher than the debonding strength. There was no cement debonding from formation.

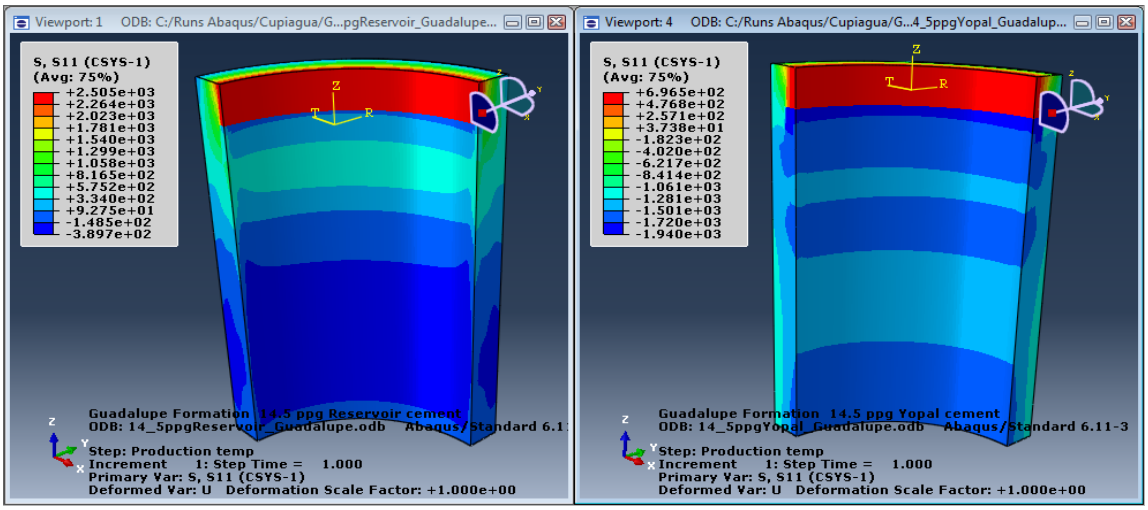

Fig. 6.33—Radial stresses Guadalupe formation production of Cupiagua wells using FEA. Left: Cupiagua cement. Right: Yopal cement

Partial plastic deformation of 14.5-ppg Yopal cement was wider and higher than 14.5-ppg Cupiagua cement at Guadalupe formation during well production (Fig. 6.34). Most of the plastic deformations of the set cements were initiated during hydraulic fracturing, but minor increments of cement PEEQ occurred during well production with bottomhole production pressure of 1,000 psi.

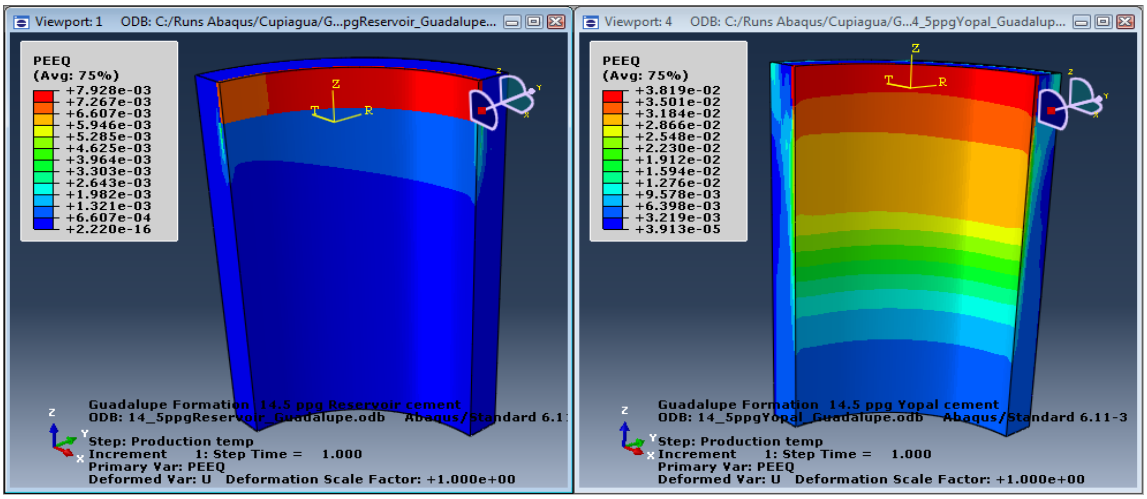

Fig. 6.34—Equivalent plastic deformation during well production at Guadalupe formation of Cupiagua wells with two set cements using FEA. Left: Cupiagua cement. Right: Yopal cement

Tables 6.17, 6.18, 6.19, 6.20, and Appendix F show the FEA results for two set cements designed for Cupiagua wells. 14.5-ppg Cupiagua cement clearly had better zonal isolation than 14.5-ppg Yopal cement, which was in concordance with their Young's modulus /tensile strength ratio. Neither of the two set cements had a perfect zonal isolation.

14.5-ppg Yopal cement had more chances of developing cracks and plastic deformation during hydraulic fracturing jobs than 14.5-ppg Cupiagua cement. This phenomenon was explained by the lower Young's modulus and higher cement cohesion of 14.5-ppg Cupiagua cement than 14.5-ppg Yopal cement. During hydraulic fracturing jobs, Cuervos formation had plastic deformation in the minimum horizontal stress direction with 14.5-ppg Cupiagua cement that could initiate an outer microannulus. 14.5-ppg Cupiagua cement had more chances of partial cement debonding during bottomhole production pressure of 1,000 psi than 14-5-ppg Yopal cement.

The FEA developed during this dissertation is clearly more comprehensive than WellLife software. This information was useful to design cement slurries of different wells.

TABLE 6.17—FEA WITH DIFFERENT SET CEMENTS AT MIRADOR FORMATION OF CUPIAGUA WELLS

	Hydraulic Fracturing					Well Production				
Cement Design	Max. VM, psi	Max. S22, psi	Radial cracks	Cement PEEQ, %	Form. PEEQ, %	Max. VM, psi	Max. S11 Stress, psi	Debond	Cement PEEQ, %	Form. PEEQ, %
14.5-ppg Cupiagua	1,924	437	No	0.15	0	4,065	1,286	Partial	0.42 (small area)	0
14.5-ppg Yopal	3,433	538	Initial	3.13	0	5,470	-606	No	3.13	0

TABLE 6.18—FEA WITH DIFFERENT SET CEMENTS AT CUERVOS FORMATION OF CUPIAGUA WELLS

	Hydraulic Fracturing					Well Production				
Cement Design	Max. VM, psi	Max. S22, psi	Radial cracks	Cement PEEQ, %	Form. PEEQ, %	Max. VM, psi	Max. S11 Stress, psi	Debond	Cement PEEQ, %	Form. PEEQ, %
14.5-ppg Cupiagua	1,120	475	No	0	0.1	3,928	2,224	Partial	0.63	0.1
14.5-ppg Yopal	2,650	865	Yes	2.93	0	5,158	-416	No	3.44	0

TABLE 6.19—FEA WITH DIFFERENT SET CEMENTS AT BARCO FORMATION OF CUPIAGUA WELLS

	Hydraulic Fracturing					Well Production				
Cement Design	Max. VM, psi	Max. S22, psi	Radial cracks	Max. Cement PEEQ, %	Form. PEEQ, %	Max. VM, psi	Max. S11 Stress, psi	Debond	Max. Cement PEEQ, %	Form. PEEQ, %
14.5-ppg Cupiagua	1,815	589	No	0.31	0	3,908	2,044	Minor	1.53	0
14.5-ppg Yopal	4,139	350	No	2.45	0	6,340	-881	No	2.55	0

TABLE 6.20—FEA WITH DIFFERENT SET CEMENTS AT GUADALUPE FORMATION OF CUPIAGUA WELLS

	Hydraulic Fracturing					Well Production				
Cement Design	Max. VM, psi	Max. S22, psi	Radial cracks	Max. Cement PEEQ, %	Form. PEEQ, %	Max. VM, psi	Max. S11 Stress, psi	Debond	Max. Cement PEEQ, %	Form. PEEQ, %
14.5-ppg Cupiagua	1,265	538	No	0	0	3,942	2,505	Partial	0.79	0
14.5-ppg Yopal	2,736	832	Yes	3.03	0	3,832	697	Partial	3.82	0

A FEM in Abaqus software was built to understand cement failures at HPHT conditions during this dissertation, and numerous uniaxial, triaxial, Brazilian, permeability and thermal tests of different Portland and non-Portland cements were done to know their mechanical and thermal properties. Also, the FEM was applied in three oil fields of Ecopetrol, including an in-situ combustion project. Finally, the FEM built in Abaqus was compared with the WellLife Software of Halliburton.

CHAPTER VII

CONCLUSIONS AND RECOMMENDATIONS

The primary goal of this research has been to understand the behavior of cement sheaths of high-pressure and high-temperature (HPHT) oil wells. Lab tests of several oil cement designs, including cements for in-situ combustion, were carried out to determine their permeability and mechanical and thermal properties. The cement failure in HPHT well conditions was simulated by Abaqus software, a commercial finite-element software. Simulations of cement failures were completed for three oil fields in Colombia, South America.

Glass fibers, carbon fibers, and elastomers were incorporated in the cement slurry designs to improve tensile strength and mechanical properties of oil cements to withstand hydraulic fracturing pressures or HPHT conditions. Also, expansive and self-healing additives were included in the cement slurries to seal possible microannuli of the cement sheath.

7.1 Conclusions

The results obtained during these finite-element analyses (FEA) and uniaxial and triaxial tests done for several set cements led to the following conclusions:

1. Set cements with the lowest Young's modulus/tensile strength ratio were not the solution for zonal isolation of hard formations, and FEA was essential to select the appropriate set cement. Young's modulus/tensile strength ratio does not take into account possible plastic deformations of the set cements and formations.
2. FEA indicated that set cements with high Young's modulus, low Poisson's ratio and low cohesive strength can have the highest plastic deformation, especially when the oil wells have hydraulic fracturing jobs in HPHT conditions. Cohesion and Young's modulus played an important role in the plastic deformation of set cement during the life of the well.

3. FEA showed that hydraulic fracturing jobs were the main cause of plastic deformation in set cements and rocks during the life of the well. Several cement slurries were designed to improve mechanical properties to minimize plastic deformations of set cements and rocks at three oil fields of Ecopetrol in Colombia.
4. FEA showed that cement plastic deformation was bigger in hard rocks (high Young's modulus) than in soft rocks (low Young's modulus). Most of the cement plastic deformation was in the casing/cement boundary. Plastic deformations created inner microannuli.
5. Set cements in front of soft rocks were more likely to debonding and radial cracks than in front of hard rocks. Likewise, set cements in front of soft formations had lower plastic deformations than in hard rocks during hydraulic fracturing jobs.
6. FEA showed that cement slurries should be designed with Young's modulus lower than the surrounding rocks and with tensile strength high enough to reduce the chances of tensile cracking when the pressure and temperature inside the casing is increased.
7. FEA showed that rocks with low formation cohesive strength can have higher formation plastic deformation after hydraulic fracturing jobs than rocks with high cohesive strength. Also, the maximum formation plastic deformation was oriented in the maximum horizontal stress direction. Formation plastic deformations were responsible for outer microannuli.
8. FEM indicated that set cements with a Young's modulus between 0.5 E+6 and 1.0 E+6 psi have less plastic deformation than set cements with Young's modulus higher than 1.0 E+6 psi. However, FEA is necessary for specific applications.
9. Triaxial tests showed that set cements exhibit plastic flow behavior under confining pressures of 12,000 psi, so they fail only under very high axial load pressures. Ductile failure of set cements would be the principal deformation and failure mechanisms.
10. Uniaxial and triaxial tests showed that carbon fibers increase the tensile strength property of calcium phosphate cements by 28.8% without affecting its compressive

strength or Young's modulus. Glass fibers showed a significant improvement in tensile strength of Portland cements. Carbon fibers can resist high temperatures required in calcium phosphate cements used for in-situ combustion.

11. Lab tests confirmed that curing time of set cements played an important role in the development of its mechanical properties. Set cements cured for 7 days improved their tensile strength more than three times with respect to set cement that was cured for only 1 day at 200°F.
12. Uniaxial tests of set cements showed a failure plane parallel to the axial load. In triaxial strength tests with confining pressure of 500 psi or higher, the set cements showed an inclined failure plane with the axial load. Analogous behavior was observed in rocks.
13. The mechanical, thermal and permeability tests of ThermaLock cement done in laboratory were suitable for wells for in-situ combustion wells. However, FEA simulation of cement behavior showed that mechanical and thermal properties of ThermaLock cement with 2% and 2.5% BWOC of carbon fibers had radial cracks and plastic deformation during well production at 692°F. It is convenient that the fire front does not reach the production well to maintain its integrity. HP/HT liner hangers are the second barrier in the event of cement failure observed with the FEA.
14. Results of finite-element analyses done in Abaqus during this research were in concordance with WellLife software of Halliburton except for in-situ combustion project of Chichimene field. WellLife software simulates the in-situ combustion heat flux like a cyclic steam injection process, but this assumption is not correct due to the direction of heat flux in the in-situ combustion process.

7.2 Recommendations

1. Uniaxial, triaxial, and permeability tests of set cement and formations should be run to determine static mechanical and thermal properties, and use this data to run a finite-element model (FEM) to simulate the behavior of cement sheath. This FEM can simulate if the cement sheath can withstand the loads during the life of the well, including in-situ combustion processes.

2. Additional work is necessary to include shrinkage, expansion, porosity, and permeability of set cements in the FEM developed with Abaqus software to couple these variables in the results of the simulation of cement behavior.
3. Use of extended-finite elements could be used in the future to improve the visualization of debonding and radial cracks of the cement. Today, extended-finite elements handle elements with temperature or pressure, but not couple analysis of temperature and pressure.

REFERENCES

1. Moroconi, N., Repetto C. and Ravi, K.: "Zonal Isolation in Reservoir Containing CO_2 and H_2S," paper SPE 112703 presented at the 2008 IADC/SPE Drilling Conference, Orlando, Florida, 4-6 March.
2. Newman, K., and Wojtanowicz, A.: "Cement pulsation improves gas well cementing," World Oil Magazine, July 2001.
3. Ravi, K., Bosma, M. and Gastebled, O.: "Improve the Economics of Oil and Gas Wells by Reducing the Risk of Cement Failure," paper SPE 74497 presented at the 2002 IADC/SPE Drilling Conference, Dallas, Texas, 26-28 February.
4. Jaeger, J.C. and Cook, N.G.W.: Fundamentals of Rock Mechanics, third ed. Chapman and Hall, London (1979).
5. Desai, C.S. and Christian, J.T.: Numerical Methods in Geotechnical Engineering, McGraw-Hill, New York (1977).
6. Fjaer, E., Holt, R.M., and Horsrud, P.: Petroleum Related Rock Mechanics, Elsevier, Amsterdam (1992).
7. McClintock, F.A. and Argon, A.S.: Mechanical Behavior of Material, Addison-Wesley Publishing Company, Inc., Massachusetts (1966).
8. Economides, M.J. and Nolte, K.G.: Reservoir Simulation, Schlumberger Educational Services, Houston (1989).
9. Log Interpretation Principles/Applications, Schlumberger, Houston (1996).
10. Terzaghi, K.V.: Theoretical Soil Mechanics, John Wiley and Sons Inc., New York (1943).
11. Biot, M.A.: "Theory of Elasticity and Consolidation for a Porous Anisotropic Solid," J. of Applied Physics Research (1955) 26.
12. Nelson, E.B. and Guillot, D.: Well Cementing, second ed. Schlumberger, Sugar Land, Texas (2006).
13. Abaqus, 2011. Reference Manuals v6.11. Dassault Systèmes Simulia Corp.
14. Carslaw, H.S. and Jaeger, J.C.: Conduction of Heat in Solids, second ed. Oxford University Press, Great Clarendon Street, Oxford, New York, (1959).

15. Ayres, F. Jr. and Mendelson, E.: Theory and Problems of Differential and Integral Calculus, third ed. Schaum's Outline Series, McGraw-Hill, USA (1990).
16. Goodman, R.E.: Introduction to Rock Mechanics, John Wiley & Sons, New York, (1989).
17. Ramos, X., Martinez, C., Hunter, W. and Ravi, K.: "Three Levels of Zonal-Isolation Assurance Deployed To Maximize Life of Well Cement-Sheath Reliability and Value: Case Histories From Latin America," paper SPE 121310 presented at the 2009 Latin American and Caribbean Petroleum Engineering Conference, Cartagena, Colombia, 31 May-3 June.
18. Menetrey, P. and Willam, K.: "A triaxial failure criterion for concrete and its generalization," ACI Structural Journal, 1995.
19. Modeling Fracture and Failure with Abaqus Course. Dessault Systems, USA (2008).
20. Lacy, L.L.: "Dynamic Rock Mechanics Testing for Optimized Fracture Designs," paper SPE 38716 presented at the 1996 SPE Annual Technical Conference and Exhibition, San Antonio, Texas, 5-8 October.
21. Morales, R.H. and Marcinew, R.P.: "Fracturing of High-Permeability Formations: Mechanical Properties Correlations," paper SPE 26561 presented at the 1993 SPE Annual Technical Conference and Exhibition, Houston, 3-6 October.
22. Baumgarte, C., Thiercelin, M. and Klaus, D.: "Case Studies of Expanding Cement To Prevent Microannular Formation," paper SPE 56535 presented at the 1999 SPE Annual Technical Conference and Exhibition, Houston, 3-6 October.
23. Backe, K.R., Lile, O.B., Lyomov, S.K., Elvebakk, H. and Skalle, P.: "Characterising Curing Cement Slurries by Permeability, Tensile Strength and Shrinkage," paper SPE 38267 presented at the 1997 SPE Western Regional Meeting, Long Beach, California, 25-27 June.
24. Reddy, B.R., Xu, Y., Ravi, K., Gray, D. and Pattillo, P.D.: "Cement-Shrinkage Measurement in Oilwell Cementing-A Comparative Study of Laboratory Methods and Procedures," paper SPE 103610 presented at the 2007 Rocky Mountain Oil & Gas Technology Symposium, Denver, 16-18 April.

25. Belytschko, T., Black, T. Elastic Crack Growth in Finite Elements with Minimal Remeshing. Int. J. Numer. Meth. Engng. John Wiley & Sons, Ltd., Evanston, Illinois (1999).
26. Thiercelin, M., Baumgarte, C. and Guillot, D.: "A Soil Mechanics Approach To Predict Sheath Behavior," paper SPE 47375 presented at the SPE/ISRM Eurock '98, Trondheim, 8-10 July.
27. Moran, L.K., Murray, T.R. and Moyer, W.R.: "Cement Expansion: A Laboratory Investigation," paper SPE 21685 presented at the 1991 Production Operations Symposium, Oklahoma City, 7-9 April.
28. Parcevaux, P.A. and Sault, P.H.: "Cement Shrinkage and Elasticity: A New Approach for a Good Zonal Isolation," paper SPE 13176 presented at the 1984 59th Annual Technical Conference and Exhibition, Houston, 16-19 September.
29. Hunter, L., Kinnaird, B., and MacLean, K.: "Life of Well Isolation in Major Sea Development," paper SPE 110804 presented at the 2007 SPE Annual Technical Conference and Exhibition, Anaheim, California, 11-14 November.
30. Tahmourpour, F., Exner, M. and Khallad, I.: "Design and Operational Factors for the Life of the Well and Abandonment," paper SPE 114866 presented at the CIPC/SPE Gas Technology Symposium 2008 Joint Conference, Calgary, 16-19 June.
31. Deeg, W.F., Griffith. R., and Benge, G.: "How Foamed Cement Advantages Extend to Hydraulic Fracturing Operations," World Oil (November 1999).
32. Krusche, K., Johnson, C.R., Braud, N.Y. and Ghazi, H.B.: "Application of Engineered Cementing Solution to Solve Long-Term Cement Integrity Issues in Tunisia," paper SPE 100390 presented at the 2006 Annual Technical Conference and Exhibition, San Antonio, Texas, 24-27 September.
33. Di Lullo, G. and Rae, P.: "Cements for Long Term Isolation – Design Optimization by Computer Modelling and Prediction," paper SPE 62745 presented at the 2000 IADC/SPE Asia Pasific Drilling Technology, Kuala Lumpur, Malaysia, 11-13 September.

34. Moroconi, N., Zanchi, A., Barbieri, E., Ravi, K., Mesmacque, A. and D'Ancona, E.: "Intelligent and Interventionless Zonal Isolation for Well Integrity in Italy," paper SPE 119869 presented at the 2009 Middle East Oil & Gas Show and Conference, Bahrain, 15-18 March.
35. Hunter, L., Kinnaird, B., and MacLean, K.: "Life of Well Isolation in Major Sea Development," paper SPE 110804 presented at the 2007 SPE Annual Technical Conference and Exhibition, Anaheim, California, 11-14 November.
36. Griffith, J., Lende, G., Ravi, K., Saasen, A., Nodland, N. and Jordal, O.: "Foam Cement Engineering and Implementation for Cement Sheath Integrity at high Temperature and High Pressure," paper SPE 87194 presented at the 2004 IADC/SPE Drilling Conference, Dallas, 2-4 March.
37. Rozleres, J. and Ferriere, R.: "Foamed-Cement Charactetization under Downhole Conditions and Its Impact on Job Design," paper SPE 19935 presented at the 1990 IADC/SPE Drilling Conference, Houston, 27 February – 2 March.
38. Roth, J., Reeves, C., Johnson, C.R., De Bruijin, G., Bellabarba, M., Le Roy-Delage, S. and Bulte-Loyer, H.: "Innovation Hydraulic Isolation Material preserves Well Integrity," paper SPE 112715 presented at the 2008 IADC/SPE Drilling Conference, Orlando, Florida, 4-6 March.
39. Gray, K.E., Podnos, E. and Becker, E.: "Finite Element Studies of Near-Wellbore Region During Cementing Operations: Part I ," paper SPE 106998 presented at the 2007 Production and Operations Symposium, Oklahoma City, 31 March-3 April.
40. Berger, A., Fleckenstein, W.W., Eustes, A.W., and Tronhauser, G.: "Effect of Eccentricity, Voids, Cement Channels, and Pore Pressure Decline on Collapse Resistance of Casing" paper SPE 90045 presented at the SPE Annual Technical Conference and Exhibition held in Houston, 26-29 September 2004.
41. Teodoriu, C., Ugwu, I., Schubert, J.: "Estimation of Casing-Cement-Formation Interaction using a new Analytical Model" paper SPE 131335 presented at the SPE EUROPEC/EAGE Annual Conference and Exhibition held in Barcelona, Spain, USA, 14-17 June 2010.

42. Suyan, K.M., Dasgupta, D., Garg, S.P., and Jain, V.K.: "Novel Cement Composition for Completion of Thermal Recovery (ISC) Wellbores," paper SPE 101848 presented at the 2006 SPE /IADC Indian Drilling Technology Conference and Exhibition, Mumbai, India, 16-18 October.
43. Doherty, D.R. and Brandl, A.: "Pushing Portland Cement beyond the Norm of Extreme High Temperature," paper SPE 134422 presented at the 2010 IADC/SPE Asian Pacific Drilling Technology Conference and Exhibition, Ho Chi Minh city, Vietnam, 1-3 November.
44. ElastiCem Cement, http://www.halliburton.com/public/cem/contents/Brochures/web/WellLife%20III_H07578.pdf.
45. Zoback, M.D.: Reservoir Geomechanics, first ed. United Kingdom at the University Press, Cambridge (2007).
46. ThermaLockCement, http://halliburton.com/public/cem/contents/Data_Sheets/web/H/H01458Thermalock.pdf
47. Molina, M., Peralta, R. and Martinez, O.: Caracterización Geomecánica del Campo Cupiagua, Bucaramanga, Colombia (2004).

APPENDIX A

SENSITIVITY ANALYSIS FOR SET CEMENTS WITH DIFFERENT MECHANICAL PROPERTIES AND "A" ROCK OF TABLE 4.3

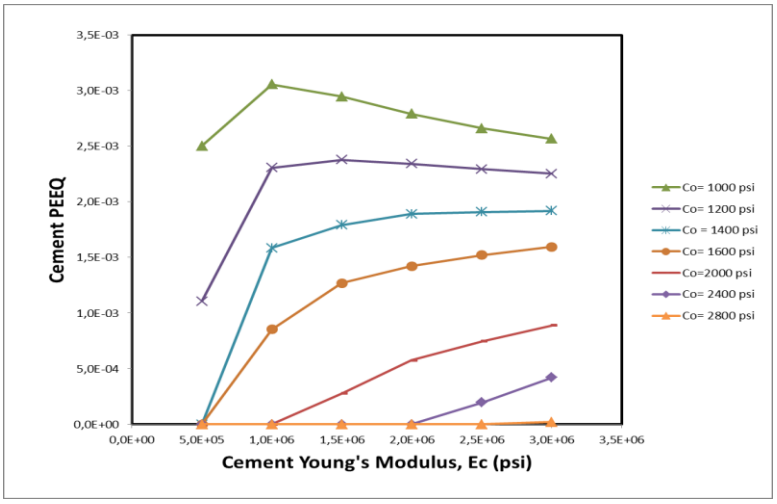

Fig. A-1. Cement Young's Modulus, Ec (psi) vs. Cement PEEQ after well completion with cement Poisson's ratio of 0.05. Cement plastic deformation increased for low values of cement cohesions and high values of cement Young's moduli.

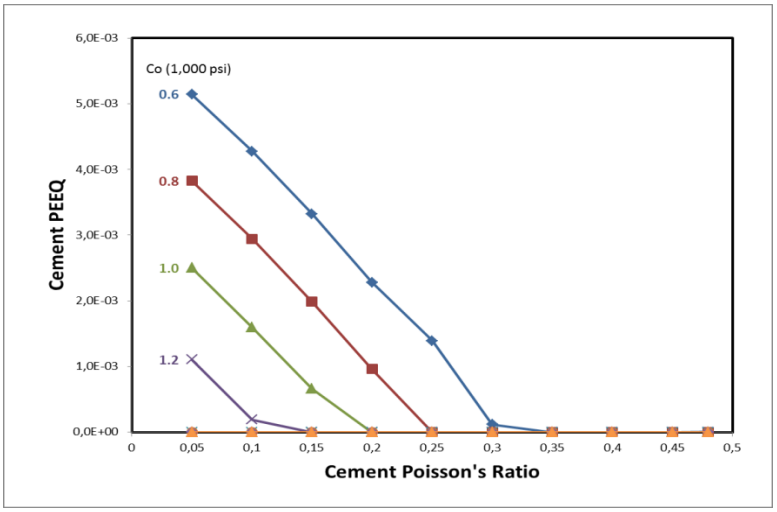

Fig. A-2. Cement Poisson's Ratio vs. Cement PEEQ after well completion with cement Young's modulus of 0.5 E+6 psi. Cement plastic deformation increased for low values of cement cohesion and low values of cement Poisson's ratio.

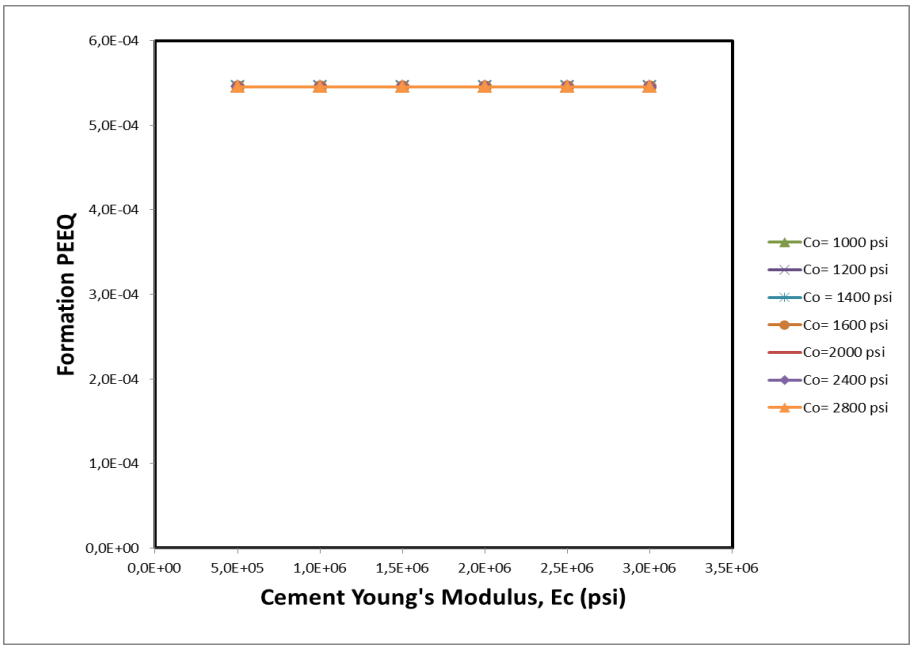

Fig. A-3. Cement Young's Modulus, Ec (psi) vs. Formation PEEQ after well completion with cement Poisson's ratio of 0.05. Formation plastic deformation was low and constant for different cement cohesions and cement Young's moduli.

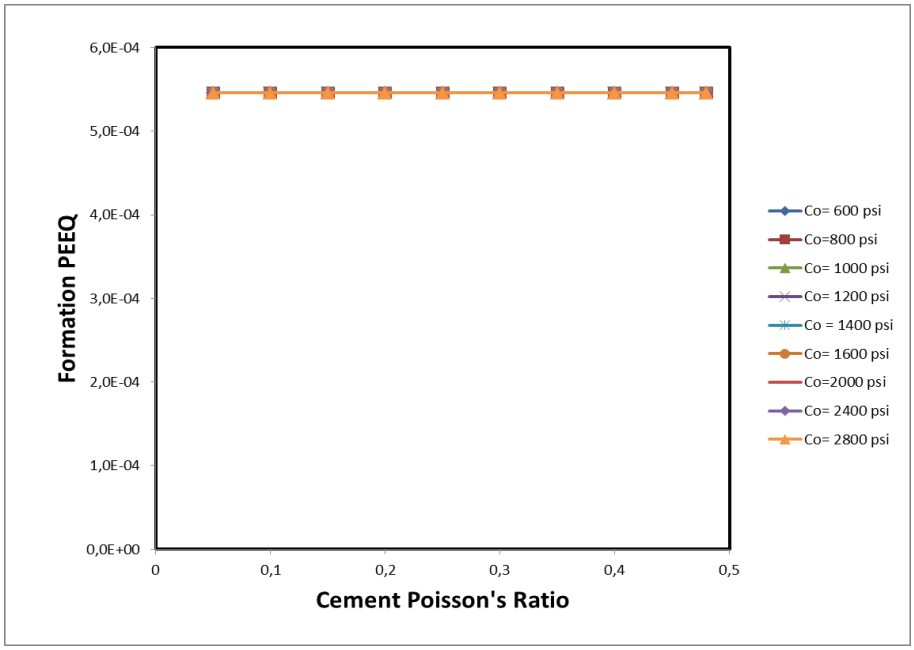

Fig. A-4. Cement Poisson's Ratio vs. Formation PEEQ after well completion with cement Young's modulus of 0.5 E+6 psi. Formation plastic deformation was low and constant for different cement cohesions and cement Poisson's ratios.

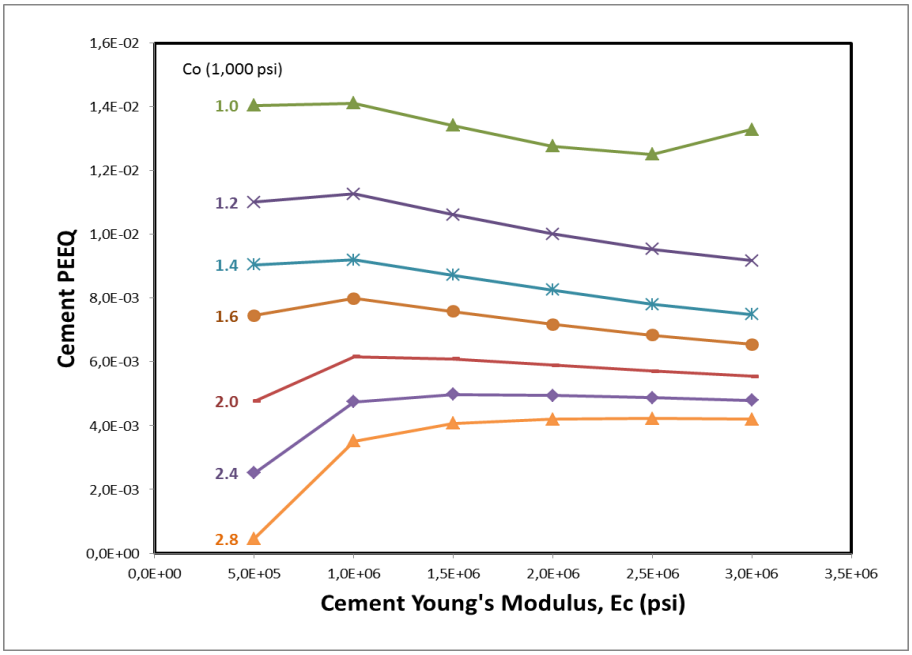

Fig. A-5. Cement Young's Modulus, Ec (psi) vs. Cement PEEQ after hydraulic fracturing job with cement Poisson's ratio of 0.05. Cement plastic deformation increased for low values of cement cohesion.

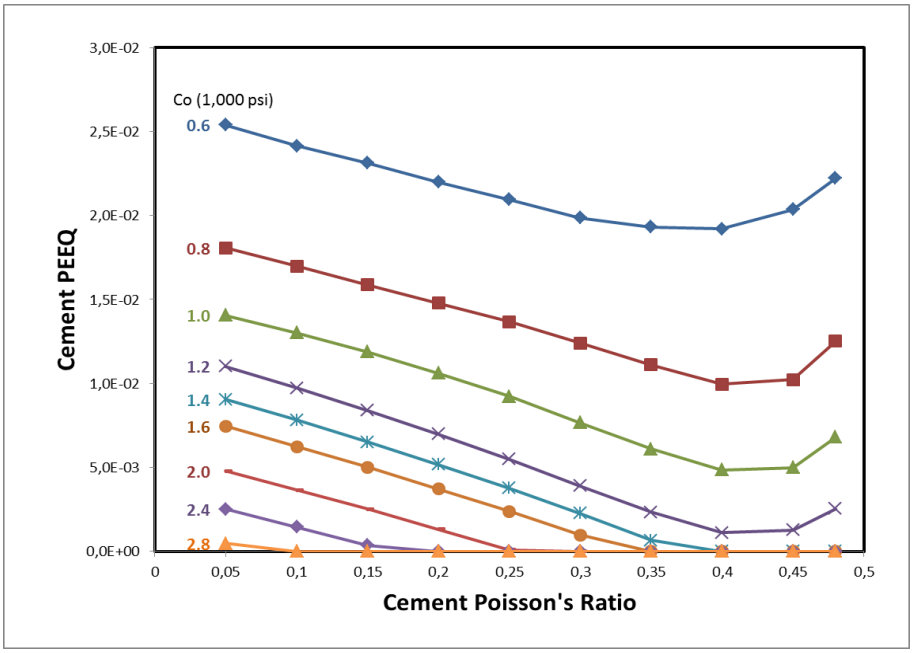

Fig. A-6. Cement Poisson's Ratio vs. Cement PEEQ after hydraulic fracturing job with cement Young's modulus of 0.5 E+6 psi. Cement plastic deformation increased for low values of cement cohesion and low values of cement Poisson's ratio.

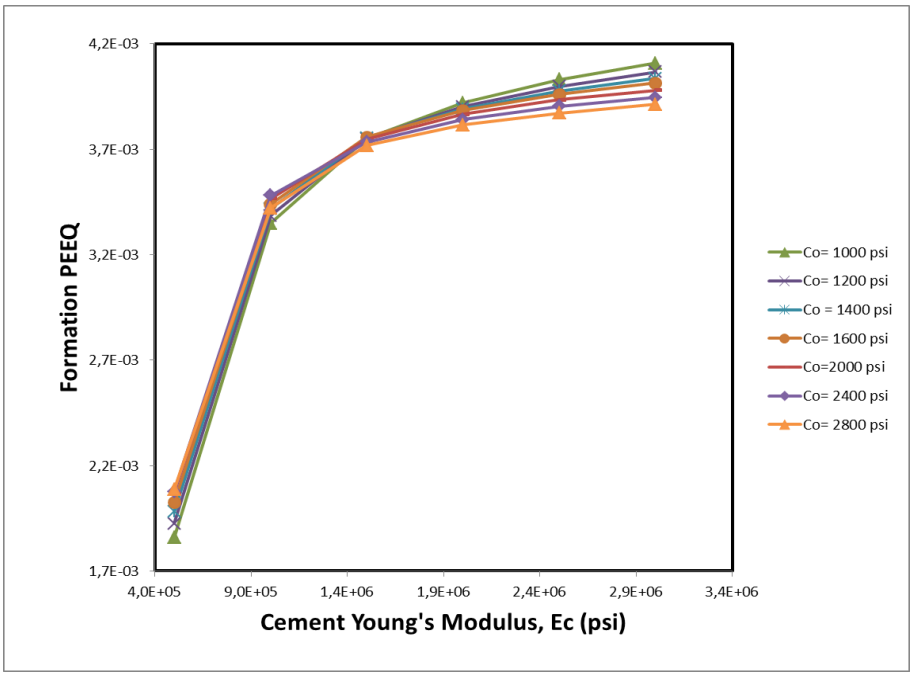

Fig. A-7. Cement Young's Modulus, Ec (psi) vs. Formation PEEQ after hydraulic fracturing job with cement Poisson's ratio of 0.05. The higher Young's modulus of set cements, the higher formation plastic deformation.

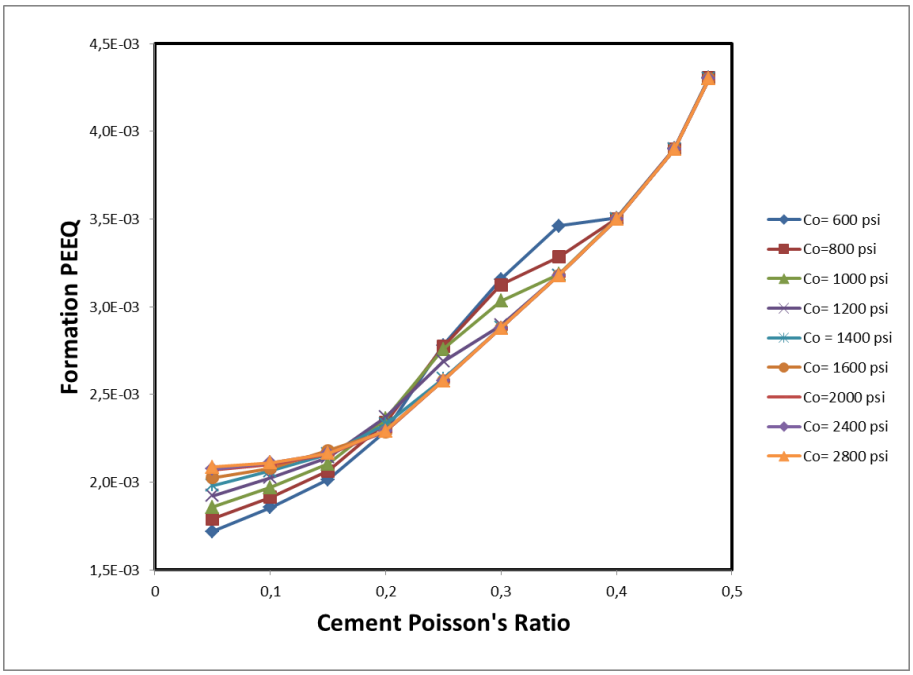

Fig. A-8. Cement Poisson's Ratio vs. Formation PEEQ after hydraulic fracturing job with cement Young's modulus of 0.5 E+6 psi. The higher Poisson's ratio of set cements, the higher formation plastic deformation.

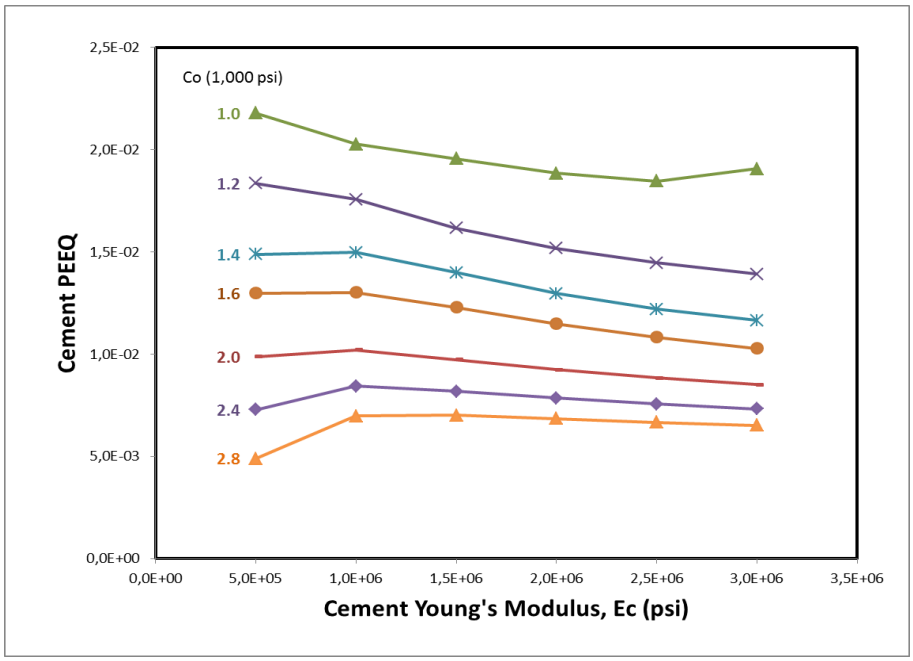

Fig. A-9. Cement Young's Modulus, Ec (psi) vs. Cement PEEQ during well production with cement Poisson's ratio of 0.05. Cement plastic deformation increased for low values of cement cohesion.

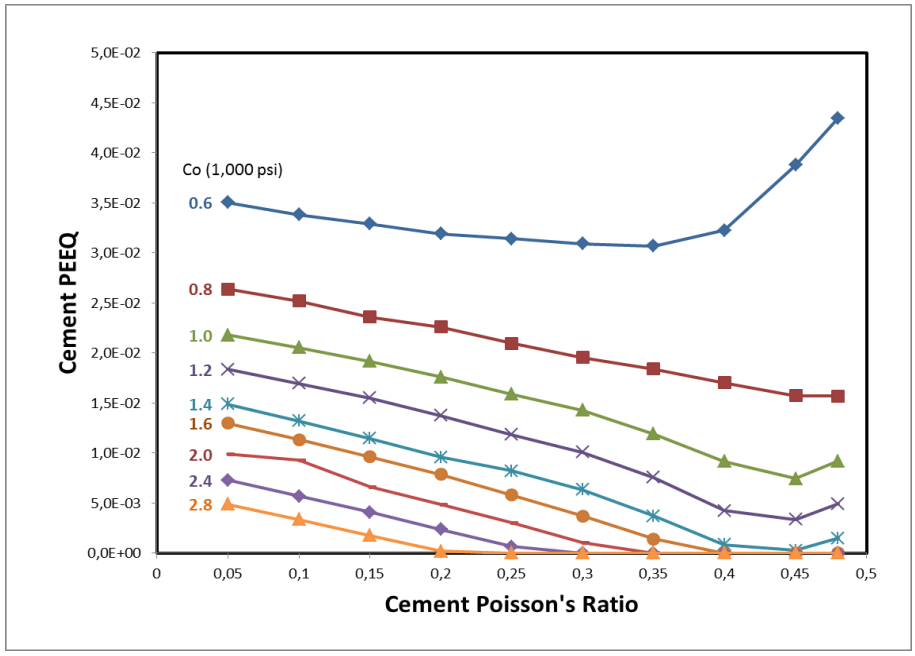

Fig. A-10. Cement Poisson's Ratio vs. Cement PEEQ during well production with cement Young's modulus of 0.5 E+6 psi. Cement plastic deformation increased for low values of cement cohesion and low values of cement Poisson's ratio.

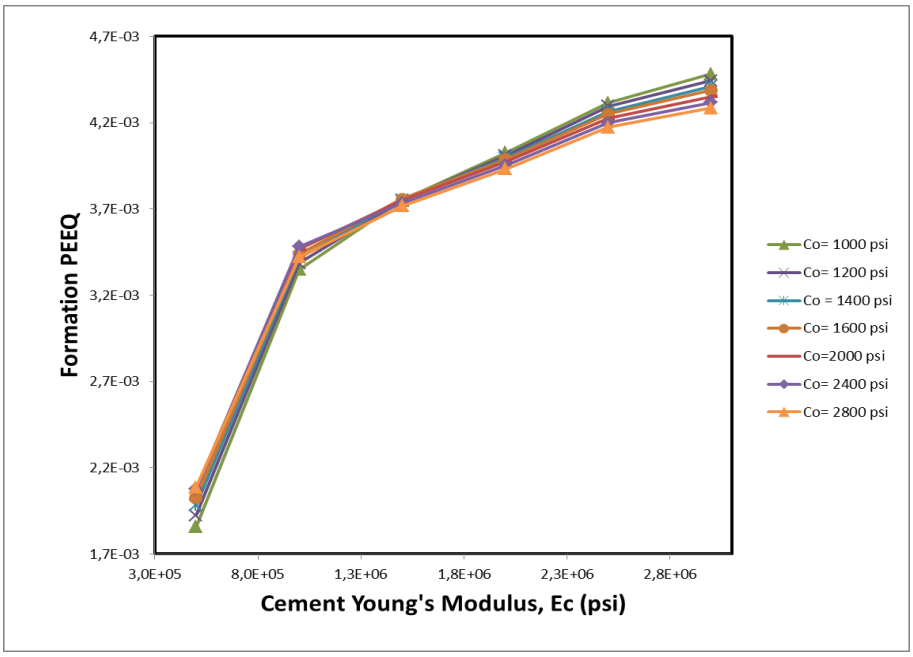

Fig. A-11. Cement Young's Modulus, Ec (psi) vs. Formation PEEQ during well production with cement Poisson's ratio of 0.05. The higher Young's modulus of set cements, the higher formation plastic deformation.

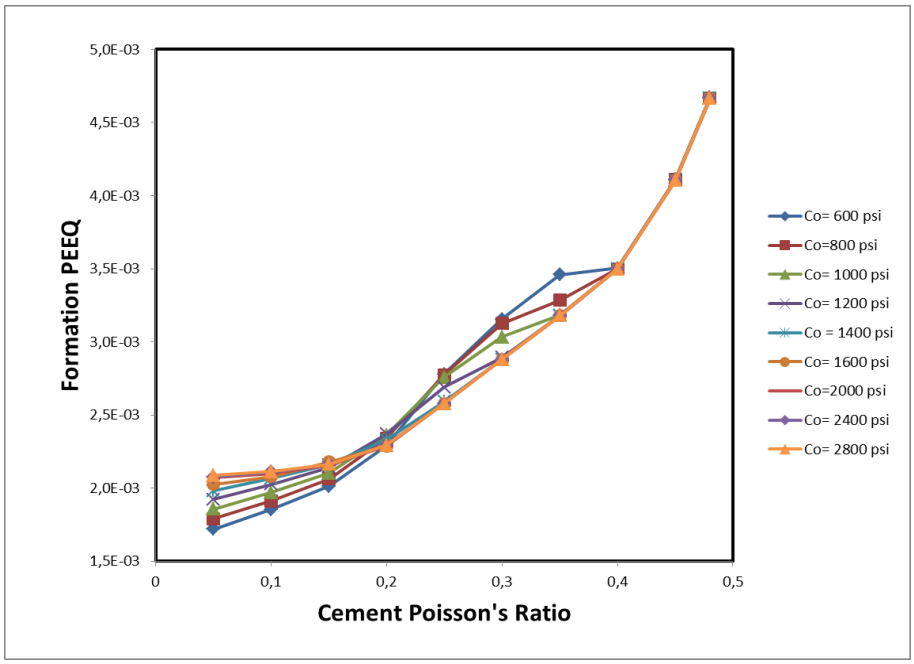

Fig. A-12. Cement Poisson's Ratio vs. Formation PEEQ during well production with cement Young's modulus of 0.5 E+6 psi. Formation plastic deformation increased for high values of cement Poisson's ratio.

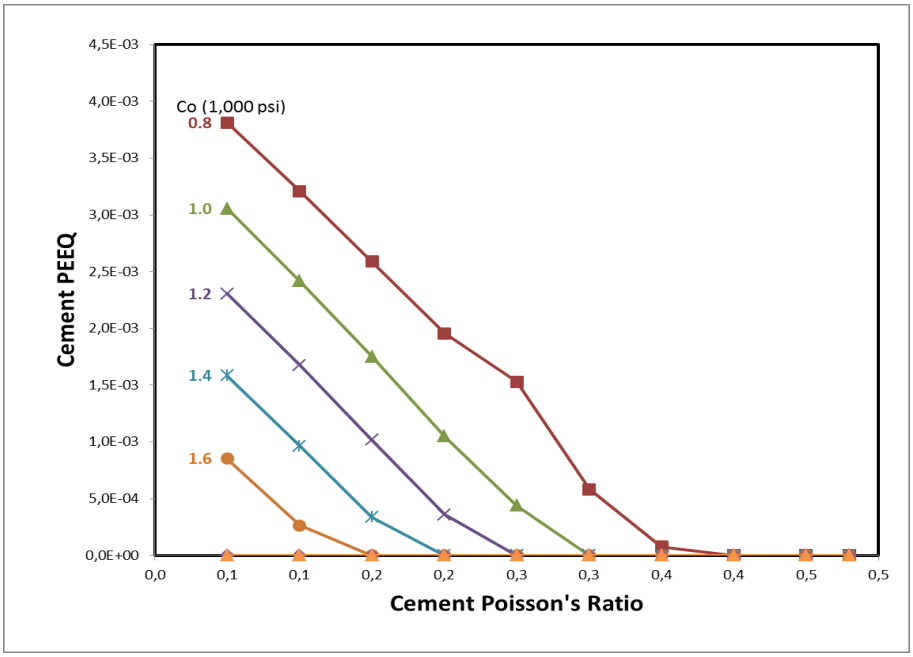

Fig. A-13. Cement Poisson's Ratio vs. Cement PEEQ after well completion with cement Young's modulus of 1.0 E+6 psi. Cement plastic deformation increased for low values of cement cohesions and high values of cement Young's moduli.

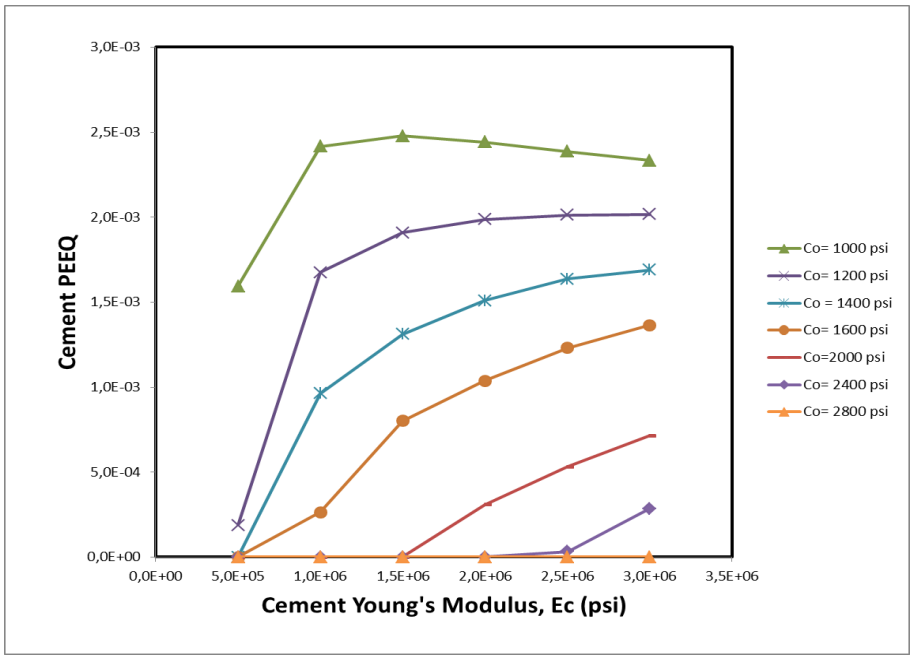

Fig. A-14. Cement Young's Modulus, Ec (psi) vs. Cement PEEQ after well completion with cement Poisson's ratio of 0.1. Cement plastic deformation increased for low values of cement cohesion and low values of cement Poisson's ratio.

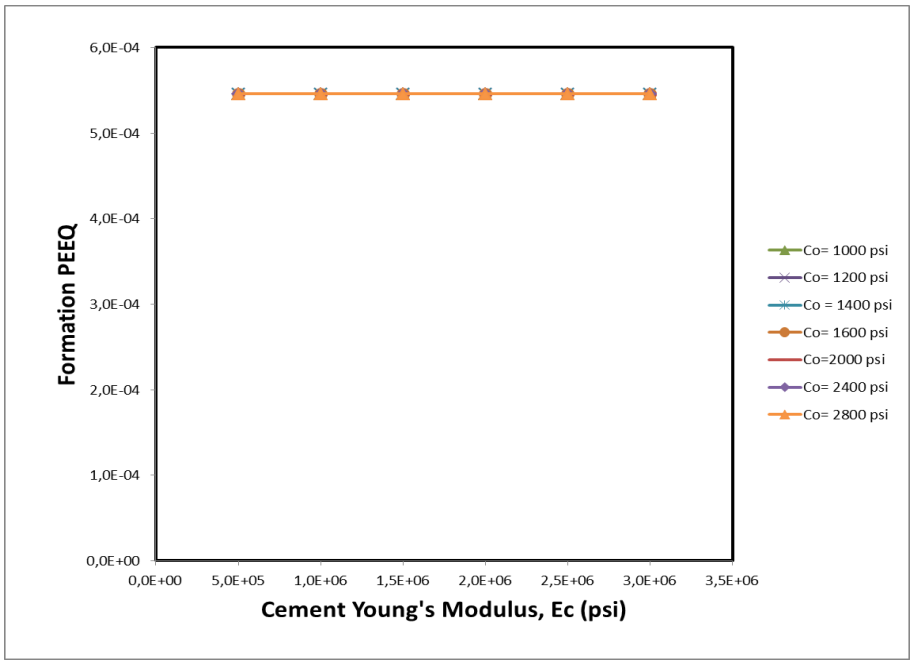

Fig. A-15. Cement Young's Modulus, Ec (psi) vs. Formation PEEQ after well completion with cement Poisson's ratio of 0.1. Formation plastic deformation was low and constant for different cement cohesions and cement Young's moduli.

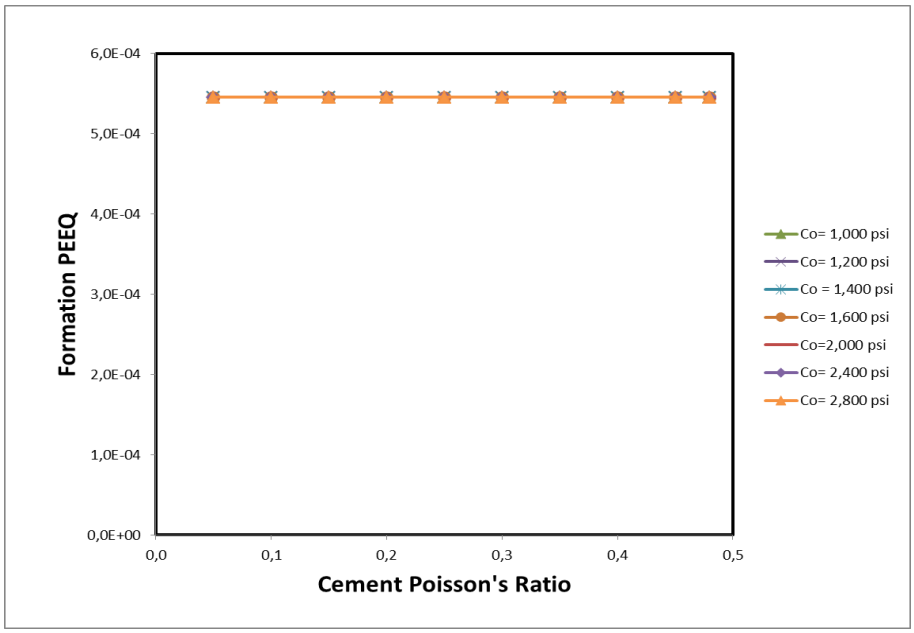

Fig. A-16. Cement Poisson's Ratio vs. Formation PEEQ after well completion with cement Young's modulus of 1.0 E+6 psi. Formation plastic deformation was low and constant for different cement cohesions and cement Poisson's ratios.

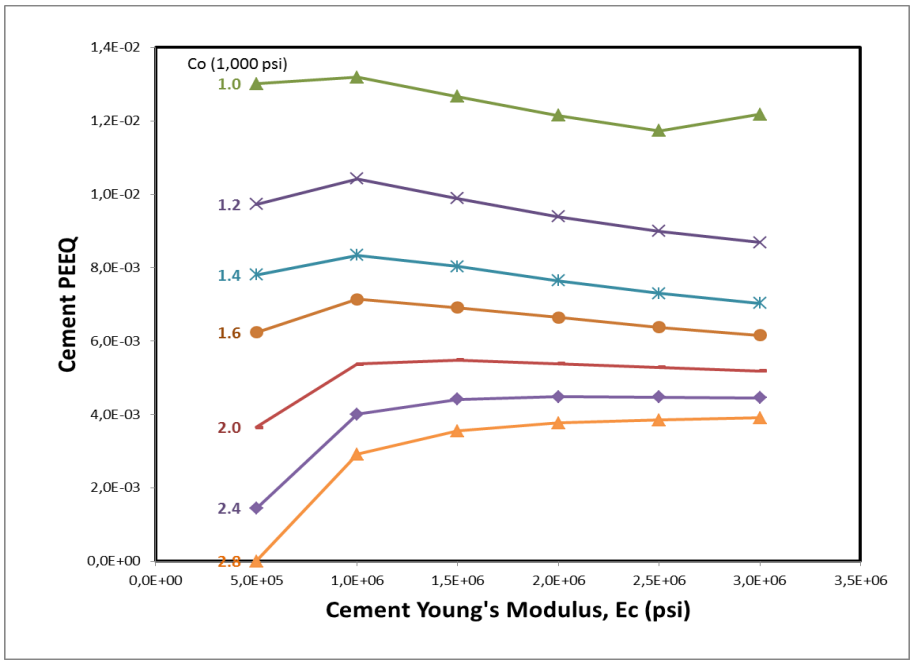

Fig. A-17. Cement Young's Modulus, Ec (psi) vs. Cement PEEQ after hydraulic fracturing job with cement Poisson's ratio of 0.1. Cement plastic deformation increased for low values of cement cohesion.

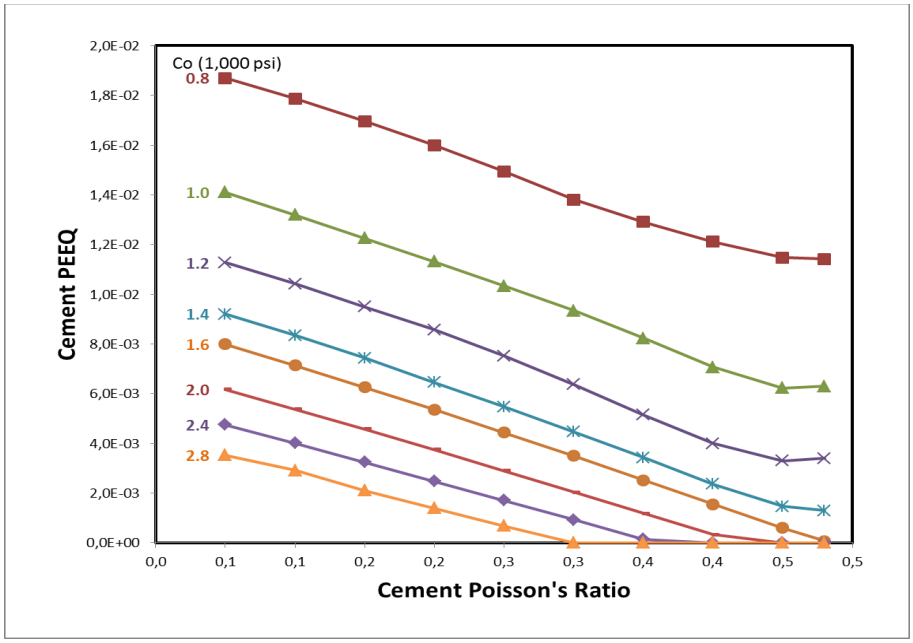

Fig. A-18. Cement Poisson's Ratio vs. Cement PEEQ after hydraulic fracturing job with cement Young's modulus of 1.0 E+6 psi. Cement plastic deformation increased for low values of cement cohesion and low values of cement Poisson's ratio.

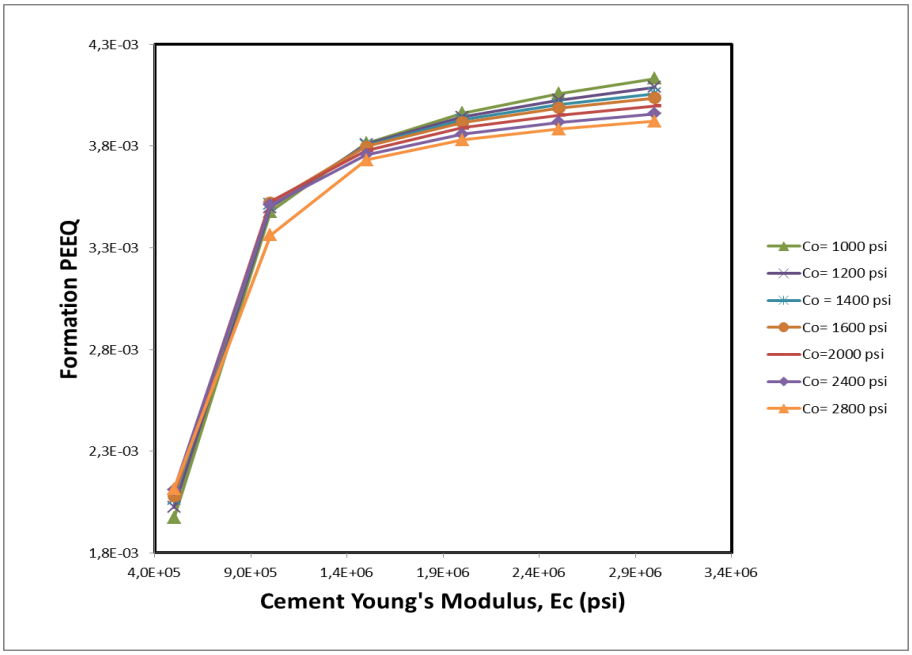

Fig. A-19. Cement Young's Modulus vs. Formation PEEQ after hydraulic fracturing job with cement Poisson's ratio of 0.1. The higher Young's modulus of set cements, the higher formation plastic deformation.

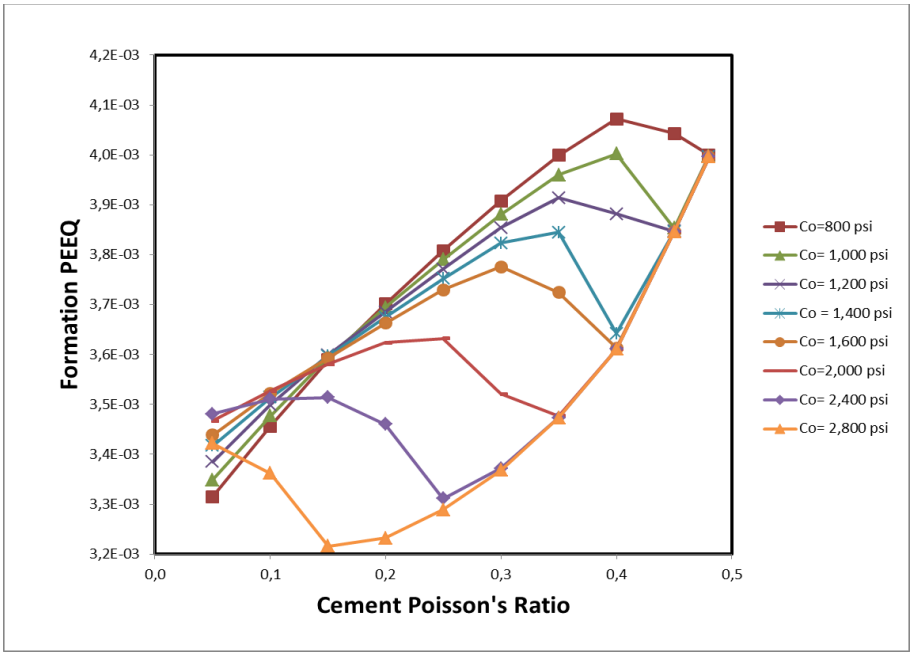

Fig. A-20. Cement Poisson's Ratio vs. Formation PEEQ after hydraulic fracturing job with cement Young's modulus of 1.0 E+6 psi. Cement Poisson's ratio and formation PEEQ did not have a linear relationship.

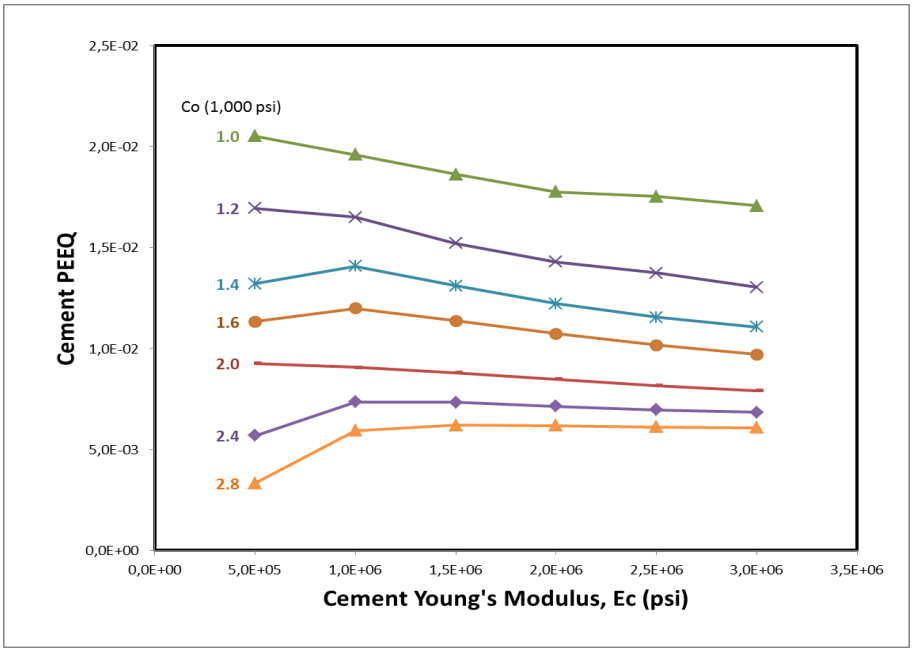

Fig. A-21. Cement Young's Modulus, Ec (psi) vs. Cement PEEQ during well production with cement Poisson's ratio of 0.1. Cement plastic deformation increased for low values of cement cohesion.

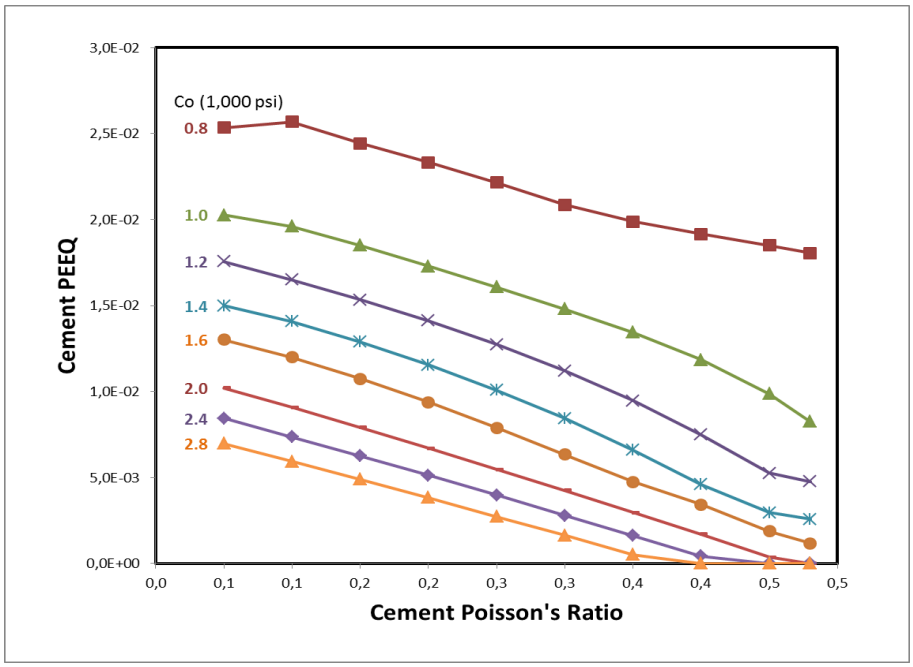

Fig. A-22. Cement Poisson's Ratio vs. Cement PEEQ during well production with cement Young's modulus of 1.0 E+6 psi. Cement plastic deformation increased for low values of cement cohesion and low values of cement Poisson's ratio.

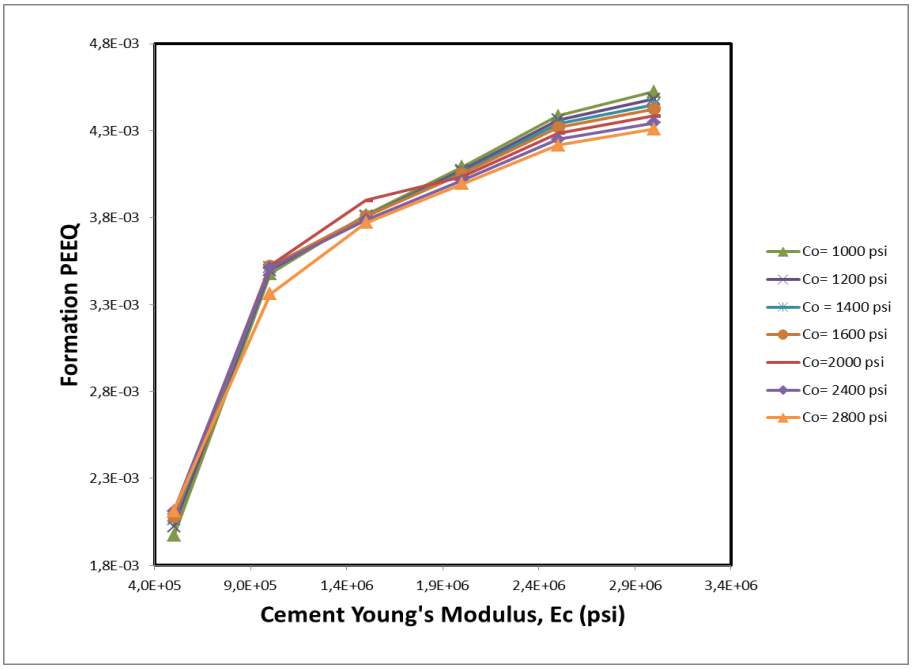

Fig. A-23. Cement Young's Modulus, Ec (psi) vs. Formation PEEQ during well production with cement Poisson's ratio of 0.1. The higher Young's modulus of set cements, the higher formation plastic deformation.

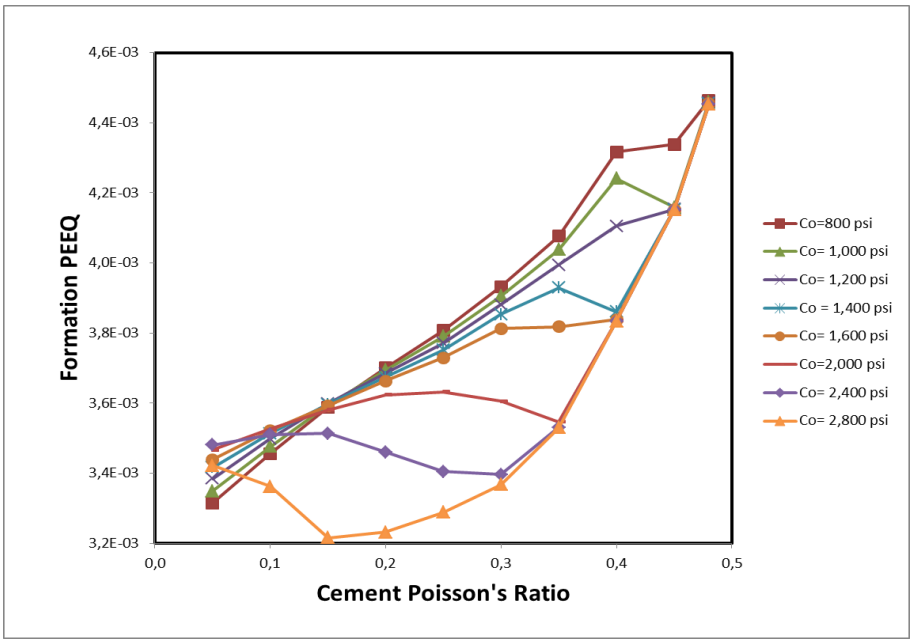

Fig. A-24. Cement Poisson's Ratio vs. Formation PEEQ during well production with cement Young's modulus of 1.0 E+6 psi. Poisson's ratio and formation plastic deformation did not have a linear relationship.

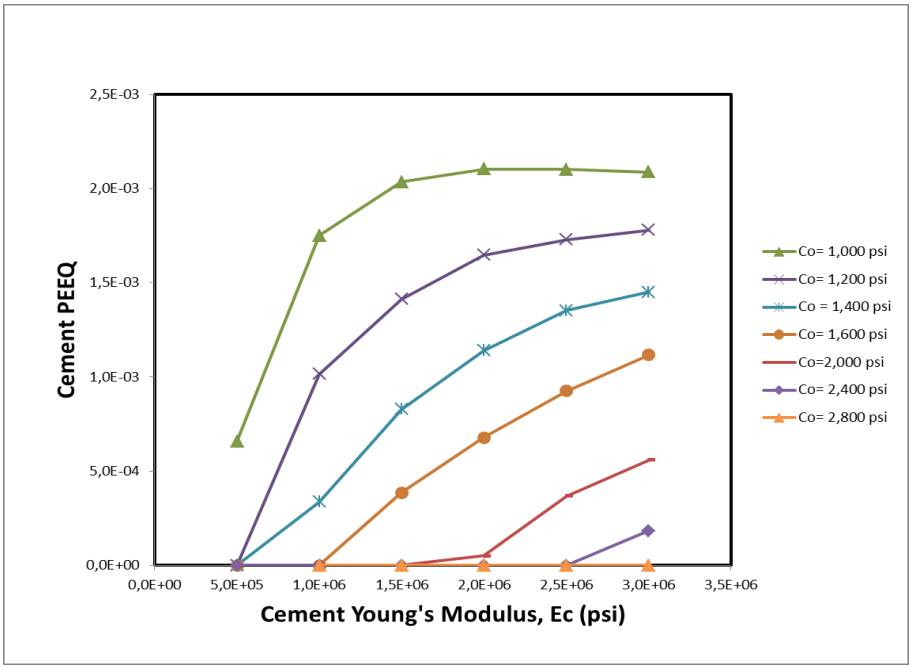

Fig. A-25. Cement Young's Modulus, Ec (psi) vs. Cement PEEQ after well completion with cement Poisson's ratio of 0.15. Cement plastic deformation increased for low values of cement cohesions and high values of cement Young's moduli.

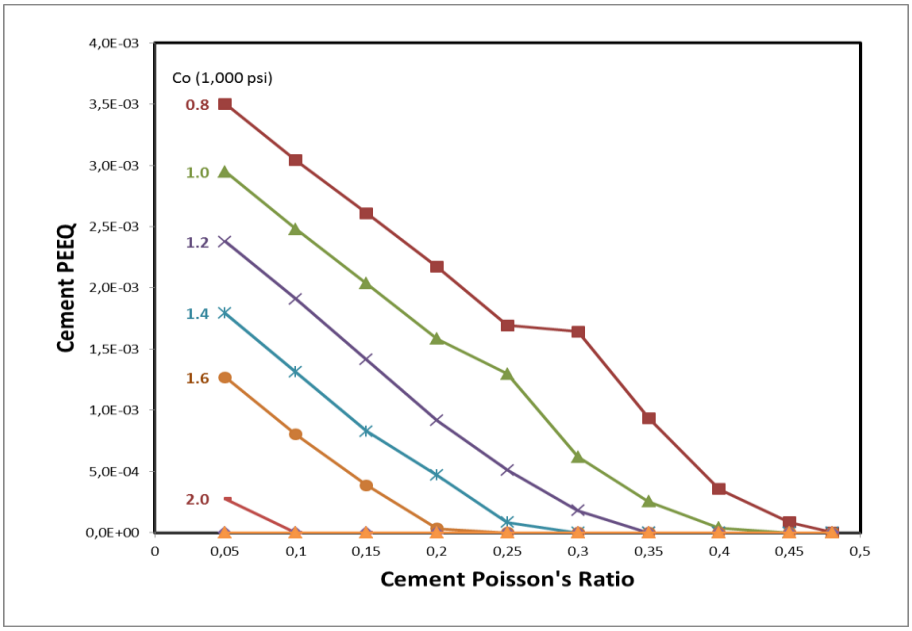

Fig. A-26. Cement Poisson's Ratio vs. Cement PEEQ after well completion with cement Young's modulus of 1.5 E+6 psi. Cement plastic deformation increased for low values of cement cohesion and low values of cement Poisson's ratio.

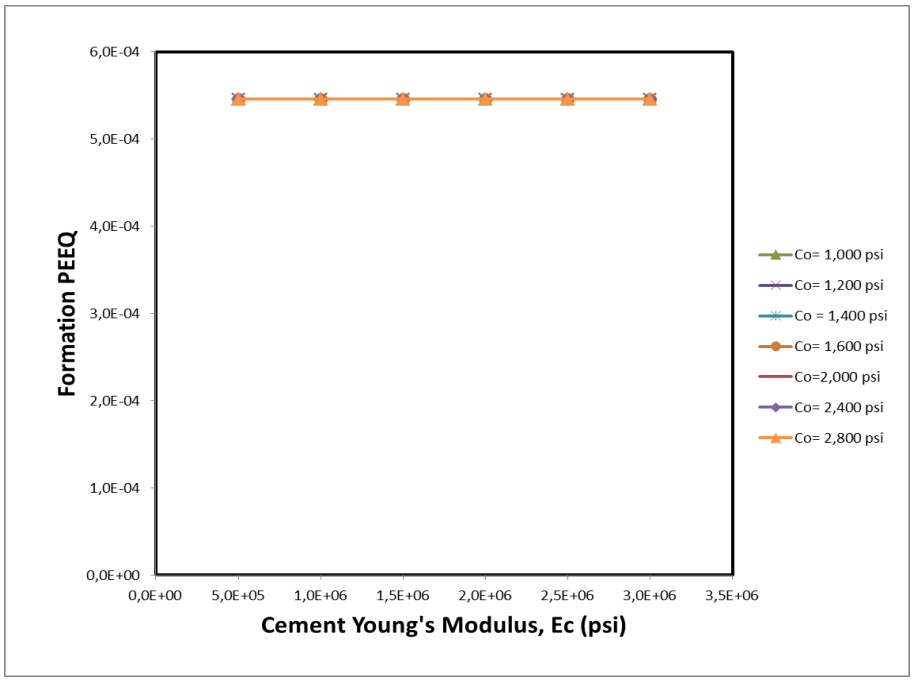

Fig. A-27. Cement Young's Modulus, Ec (psi) vs. Formation PEEQ after well completion with cement Poisson's ratio of 0.15. Formation plastic deformation was low and constant for different cement cohesions and cement Young's moduli.

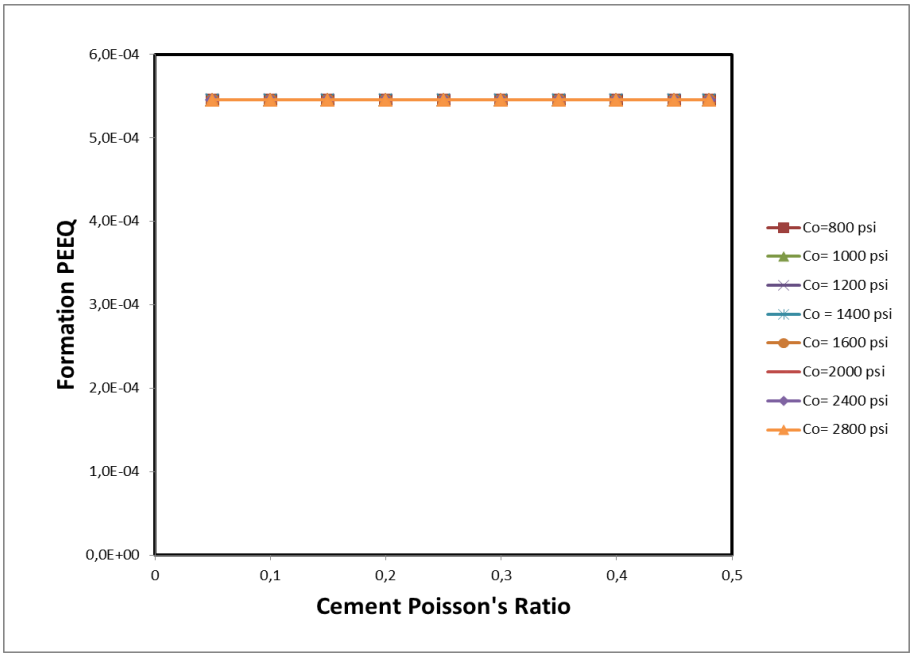

Fig. A-28. Cement Poisson's Ratio vs. Formation PEEQ after well completion with cement Young's modulus of 1.5 E+6 psi. Formation plastic deformation was low and constant for different cement cohesions and cement Poisson's ratios.

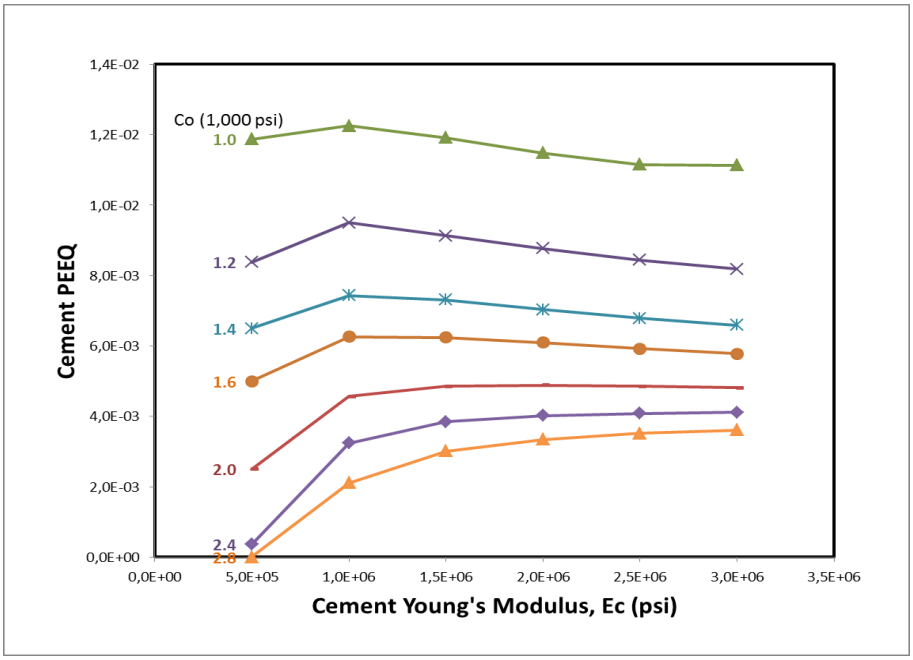

Fig. A-29. Cement Young's Modulus, Ec (psi) vs. Cement PEEQ after hydraulic fracturing job with cement Poisson's ratio of 0.15. Cement plastic deformation increased for low values of cement cohesion.

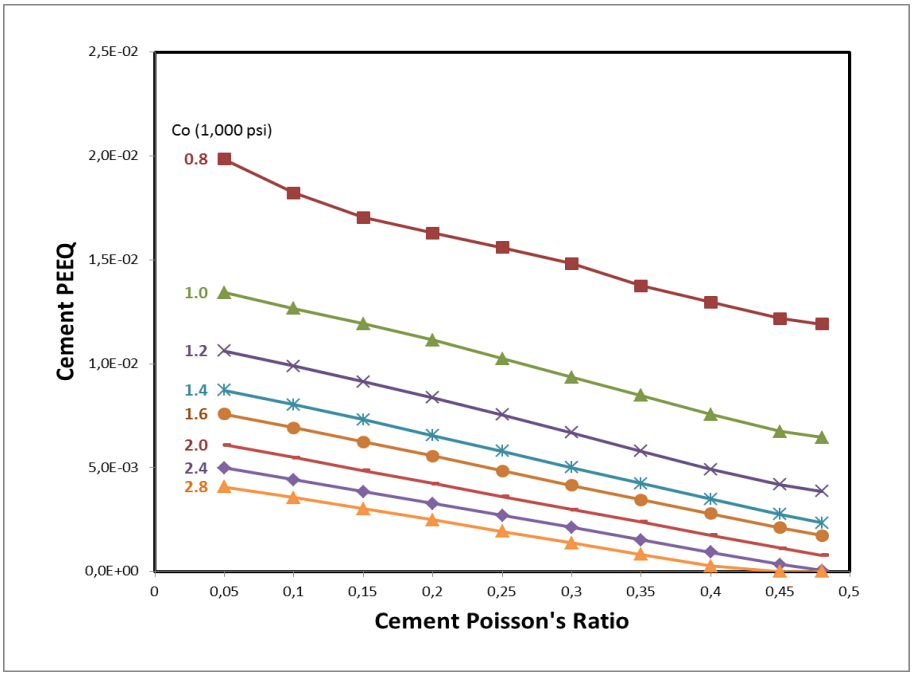

Fig. A-30. Cement Poisson's Ratio vs. Cement PEEQ after hydraulic fracturing job with cement Young's modulus of 1.5 E+6 psi. Cement plastic deformation increased for low values of cement cohesion and low values of cement Poisson's ratio.

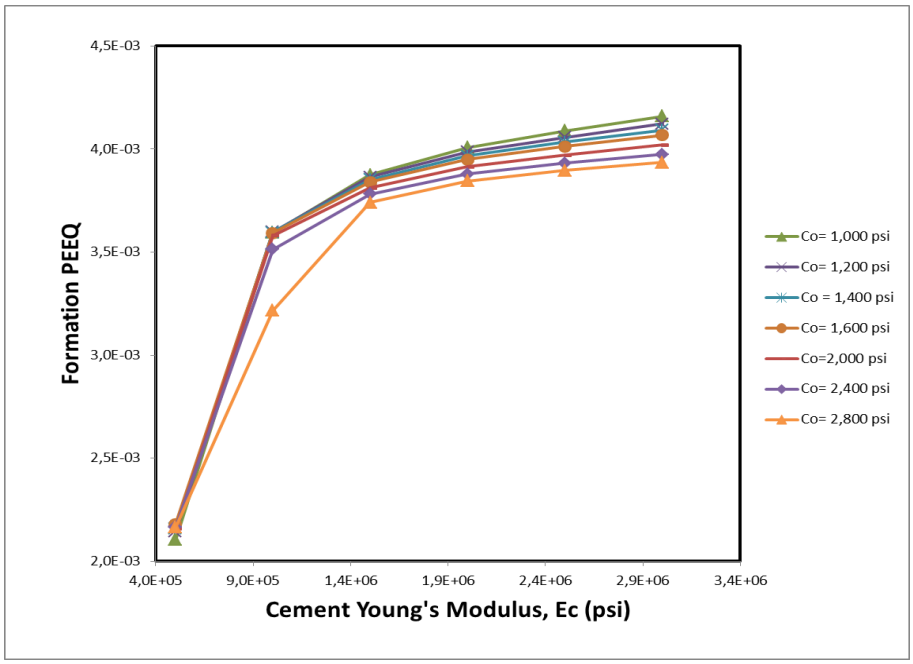

Fig. A-31. Cement Young's Modulus, Ec (psi) vs. Formation PEEQ after hydraulic fracturing job with cement Poisson's ratio of 0.15. The higher Young's modulus of set cements, the higher formation plastic deformation.

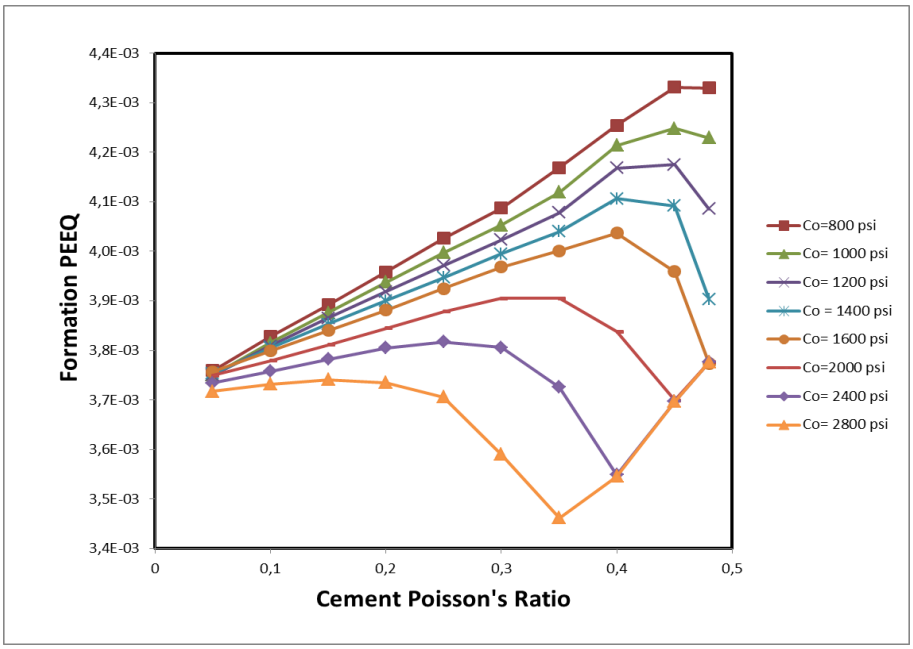

Fig. A-32. Cement Poisson's Ratio vs. Formation PEEQ after hydraulic fracturing job with cement Young's modulus of 1.5 E+6 psi. No linear relationship occurred between cement Poisson's ratio and formation plastic deformation.

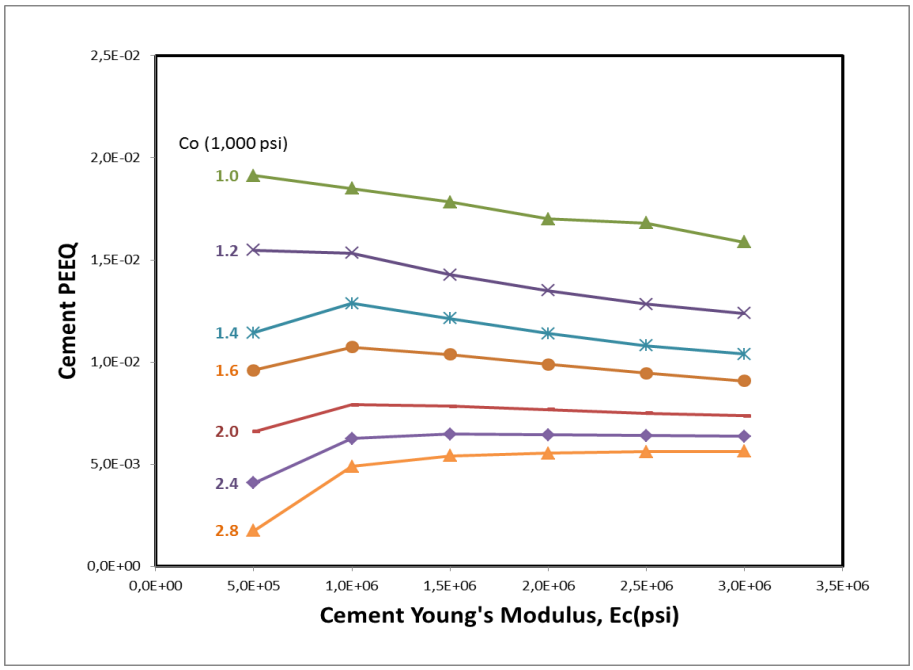

Fig. A-33. Cement Young's Modulus, Ec (psi) vs. Cement PEEQ during well production with cement Poisson's ratio of 0.15. Cement plastic deformation increased for low values of cement cohesions.

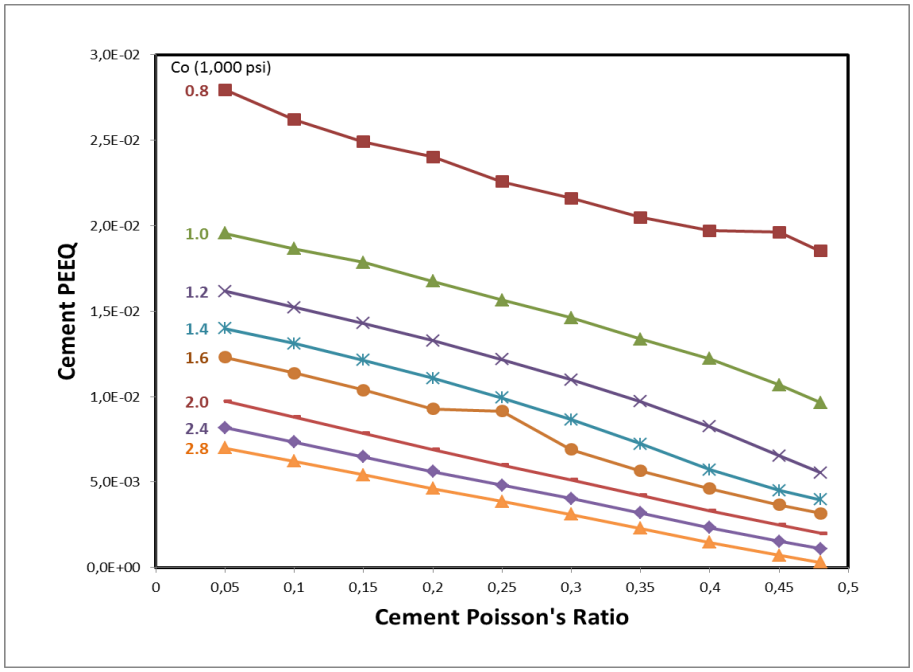

Fig. A-34. Cement Poisson's Ratio vs. Cement PEEQ during well production with cement Young's modulus of 1.5 E+6 psi. Cement plastic deformation increased for low values of cement cohesions and low values of cement Poisson's ratios.

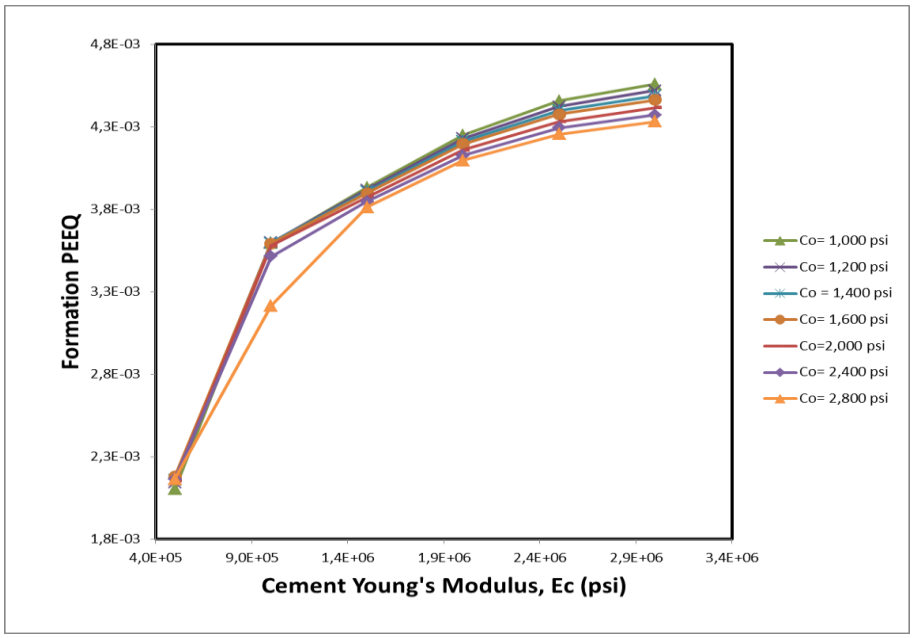

Fig. A-35. Cement Young's Modulus, Ec (psi) vs. Formation PEEQ during well production with cement Poisson's ratio of 0.15. The higher Young's modulus of set cements, the higher formation plastic deformation.

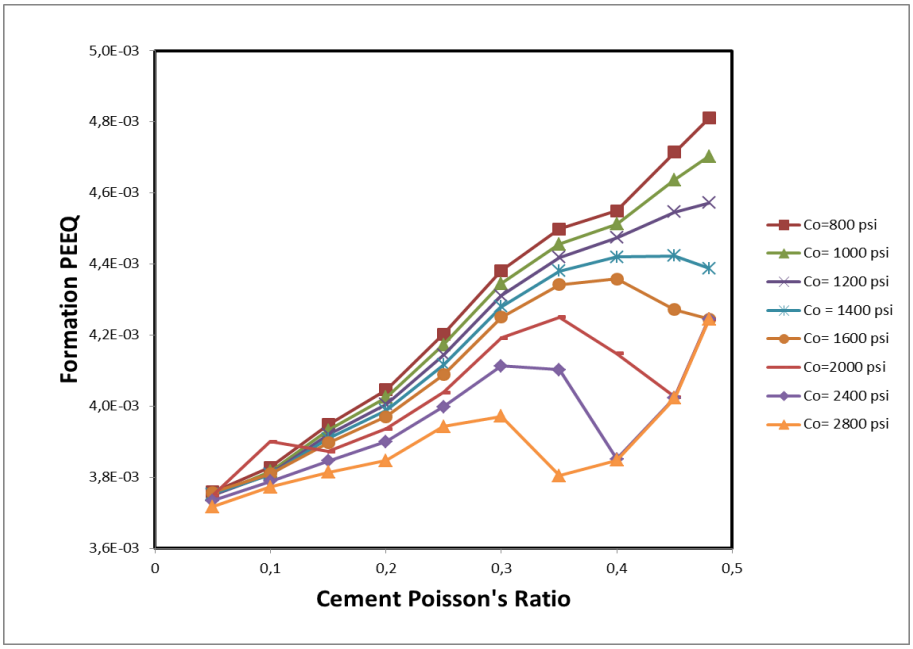

Fig. A-36. Cement Poisson's Ratio vs. Formation PEEQ during well production with cement Young's modulus of 1.5 E+6 psi. Cement Poisson's ratio and Formation plastic deformation did not have a linear relationship.

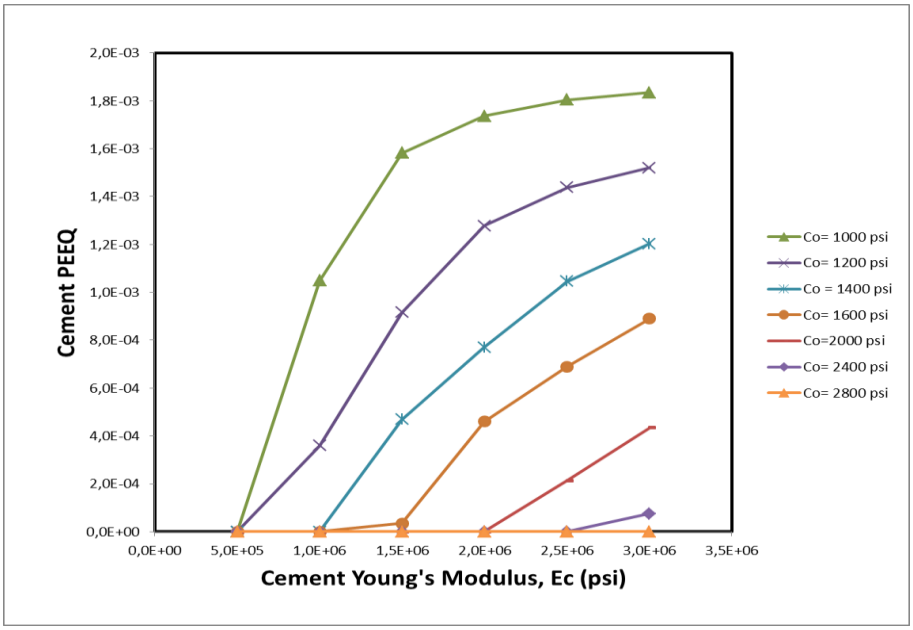

Fig. A-37. Cement Young's Modulus, Ec (psi) vs. Cement PEEQ after well completion with cement Poisson's ratio of 0.2. Cement plastic deformation increased for low values of cement cohesions and high values of cement Young's moduli.

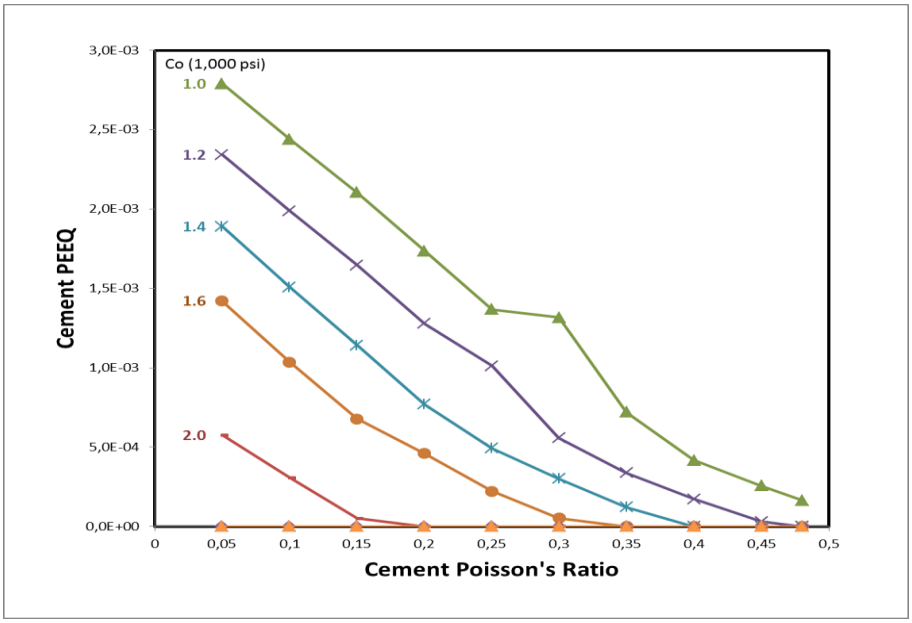

Fig. 38A. Cement Poisson's Ratio vs. Cement PEEQ after well completion with cement Young's modulus of 2.0 E+6 psi. Cement plastic deformation increased for low values of cement cohesions and low values of cement Poisson's ratio.

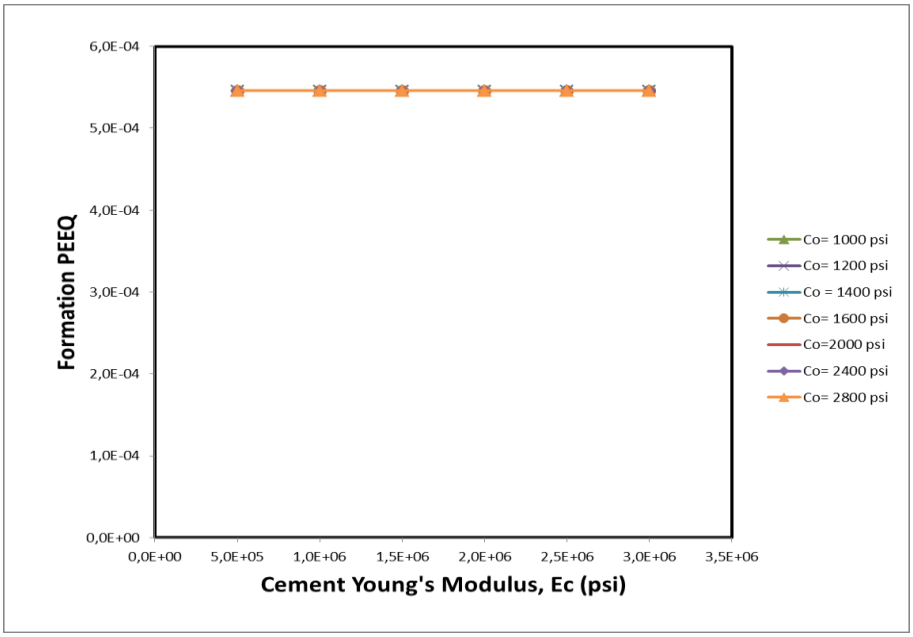

Fig. A-39. Cement Young's Modulus, Ec (psi) vs. Formation PEEQ after well completion with cement Poisson's ratio of 0.2. Formation plastic deformation was low and constant for different cement cohesions and cement Young's moduli.

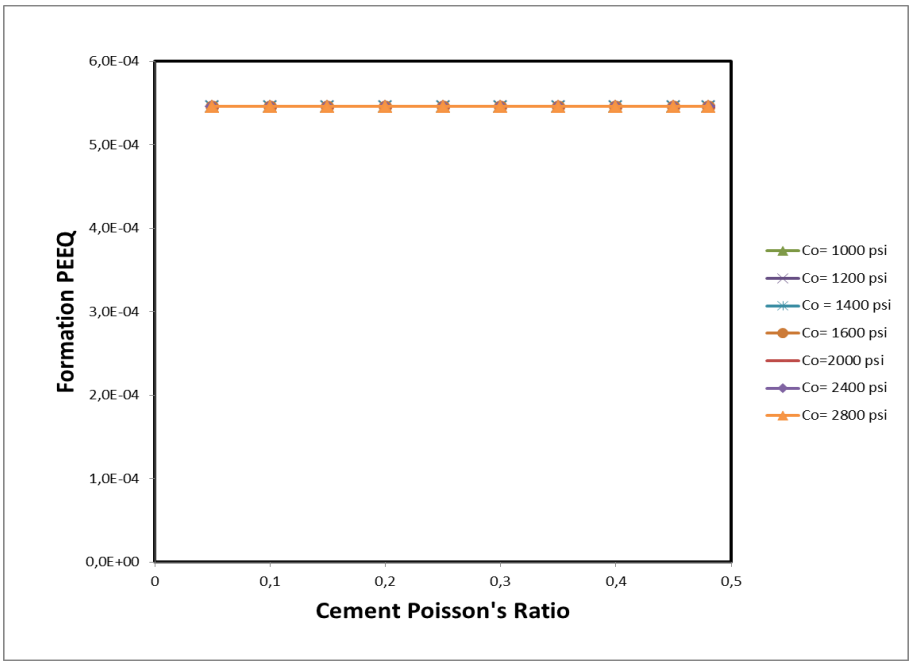

Fig. A-40. Cement Poisson's Ratio vs. Formation PEEQ after well completion with cement Young's modulus of 2.0 E+6 psi. Formation plastic deformation was low and constant for different cement cohesions and cement Poisson's ratios.

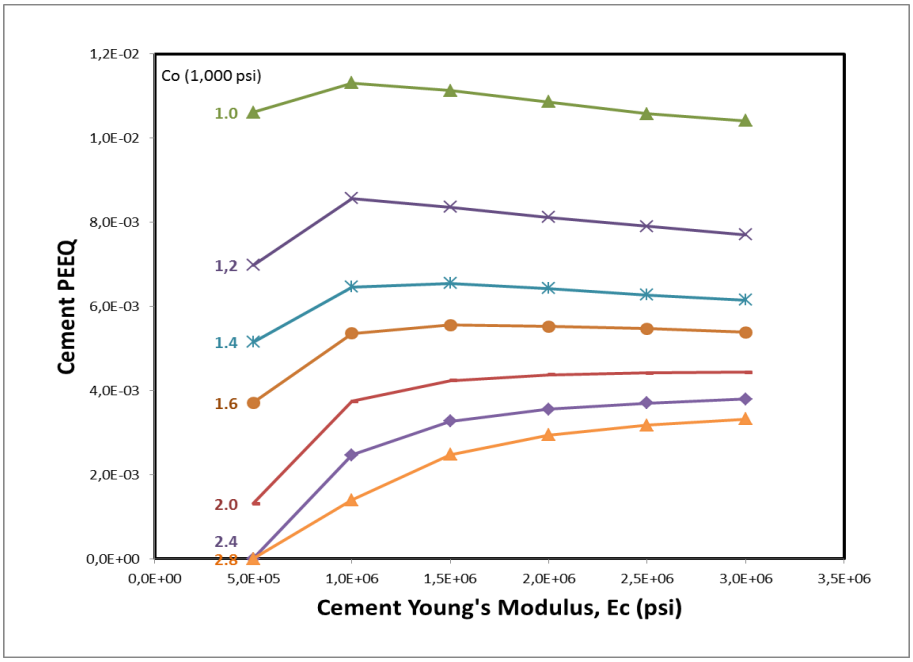

Fig. A-41. Cement Young's Modulus, Ec (psi) vs. Cement PEEQ after hydraulic fracturing job with cement Poisson's ratio of 0.2. Cement plastic deformation increased for low values of cement cohesion.

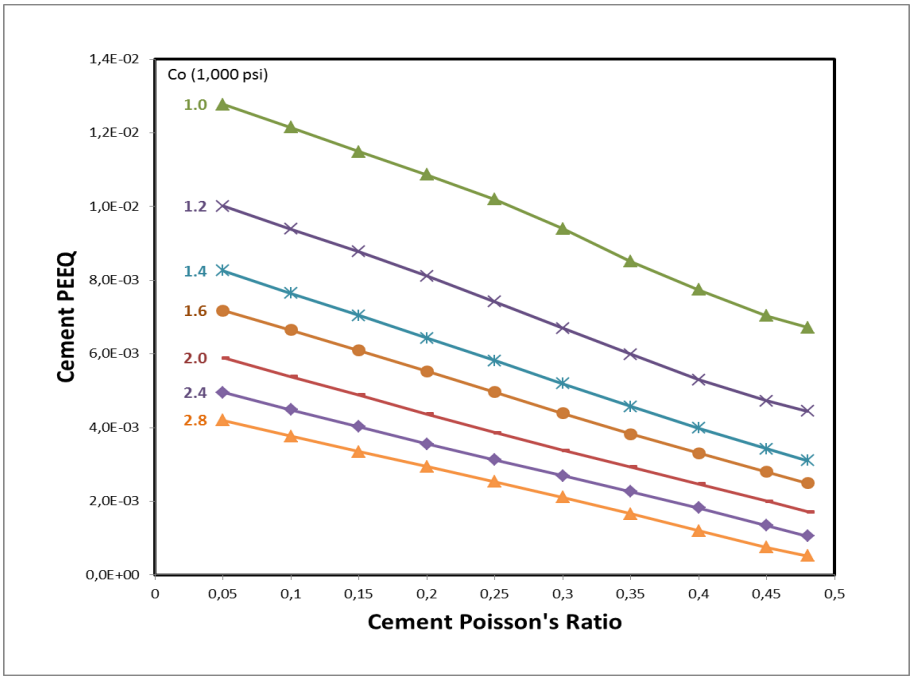

Fig. A-42. Cement Poisson's Ratio vs. Cement PEEQ after hydraulic fracturing job with cement Young's modulus of 2.0 E+6 psi. Cement plastic deformation increased for low values of cement cohesion and low values of cement Poisson's ratio.

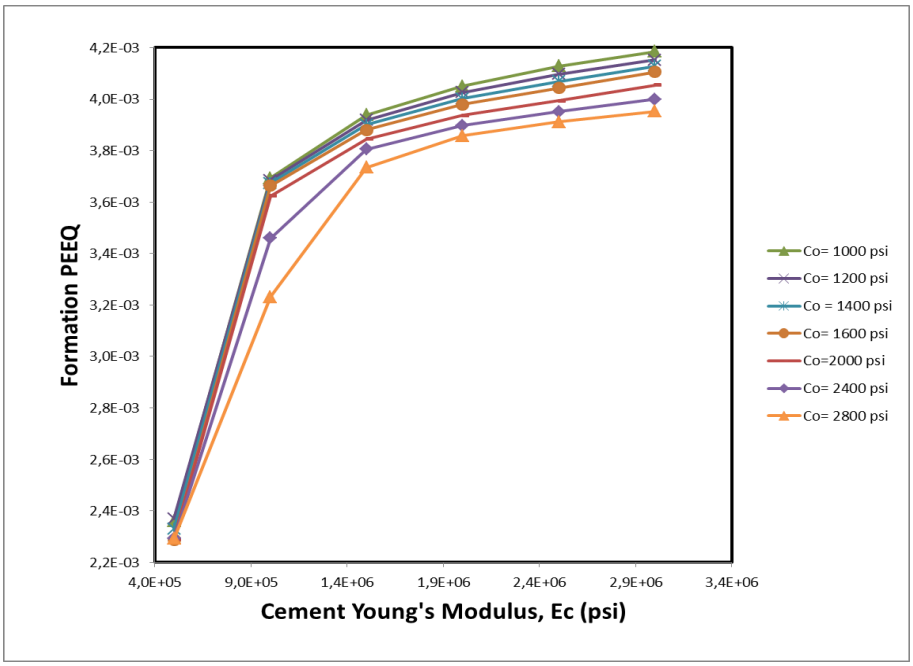

Fig. A-43. Cement Young's Modulus, Ec (psi) vs. Formation PEEQ after hydraulic fracturing job with cement Poisson's ratio of 0.2. The higher Young's modulus of set cements, the higher formation plastic deformation.

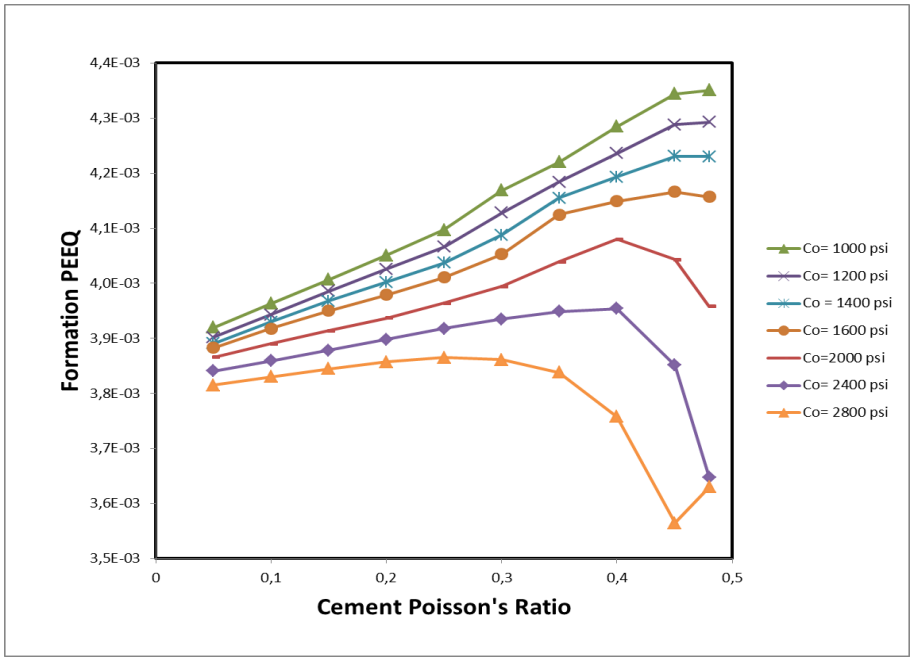

Fig. A-44. Cement Poisson's Ratio vs. Formation PEEQ after hydraulic fracturing job with cement Young's modulus of 2.0 E+6 psi. Cement Poisson's ratio and Formation PEEQ did not have a linear relationship.

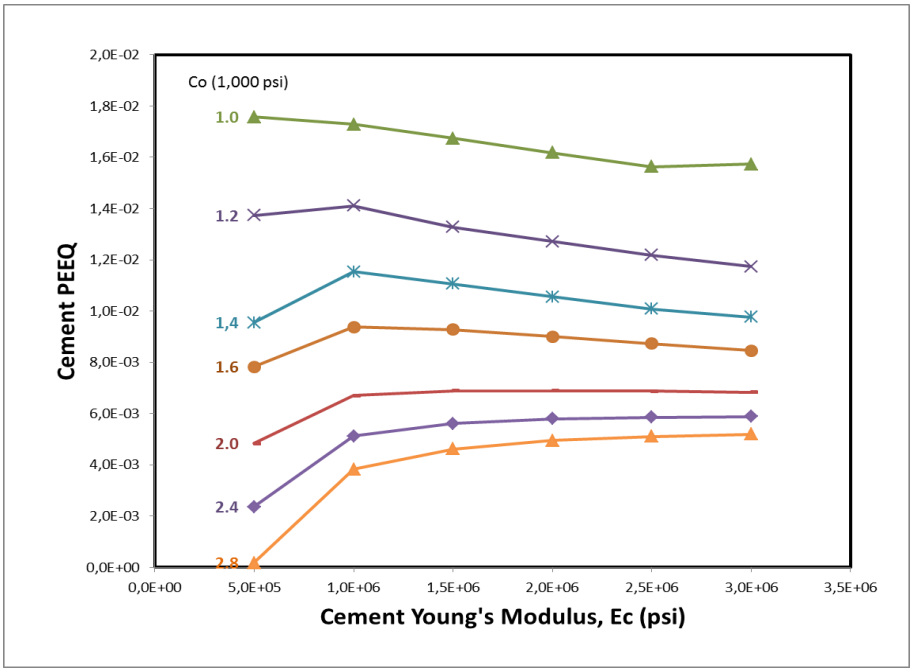

Fig. A-45. Cement Young's Modulus, Ec (psi) vs. Cement PEEQ during well production with cement Poisson's ratio of 0.2. Cement plastic deformation increased for low values of cement cohesion.

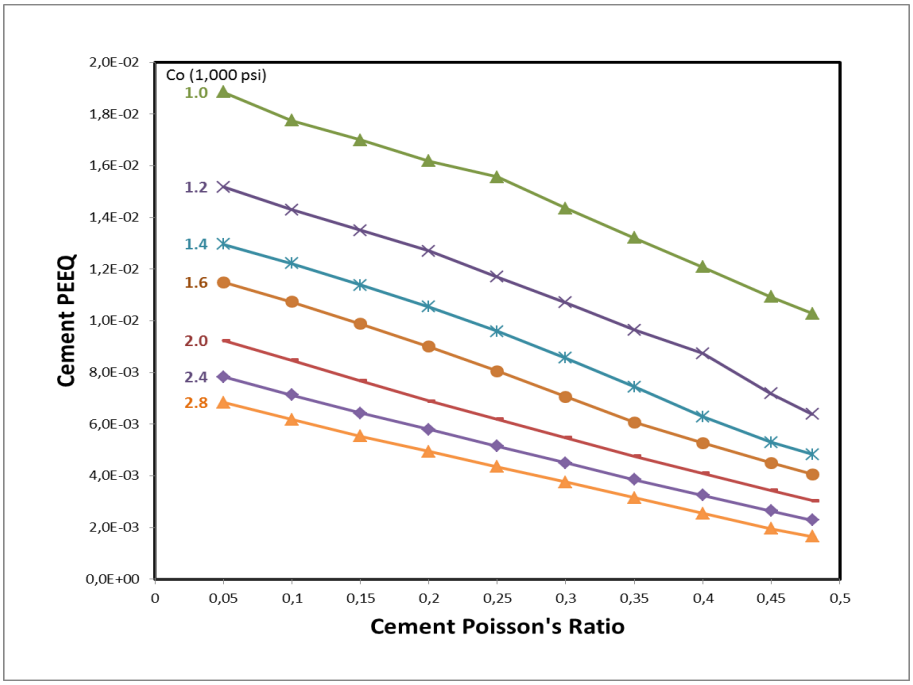

Fig. A-46. Cement Poisson's Ratio vs. Cement PEEQ during well production with cement Young's Modulus of 2.0 E+6 psi. Cement plastic deformation increased for low values of cement cohesion and low values of cement Poisson's ratio.

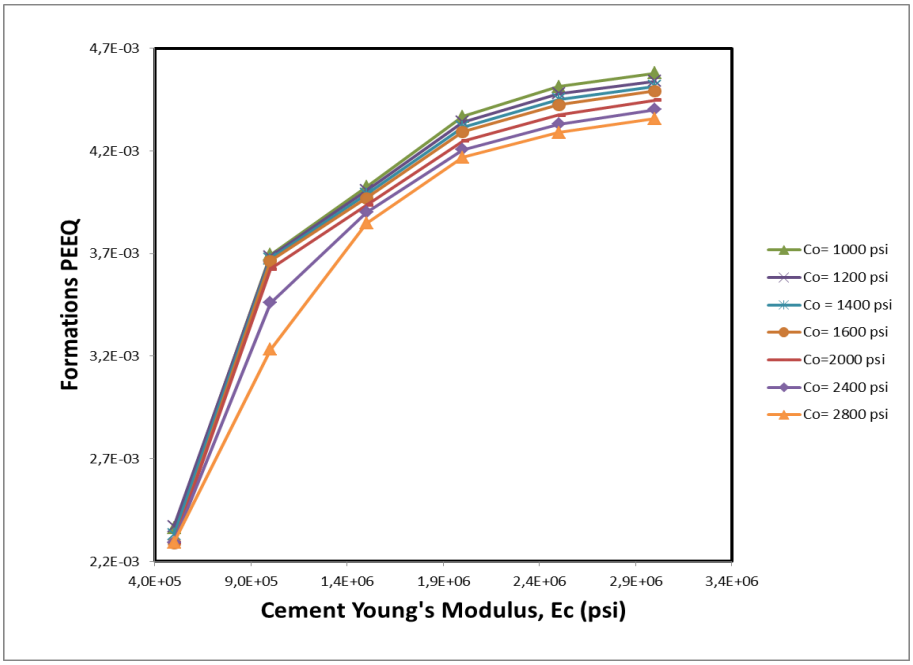

Fig. A-47. Cement Young's Modulus, Ec (psi) vs. Formation PEEQ during well production with cement Poisson's ratio of 0.2. The higher Young's modulus of set cements, the higher formation plastic deformation.

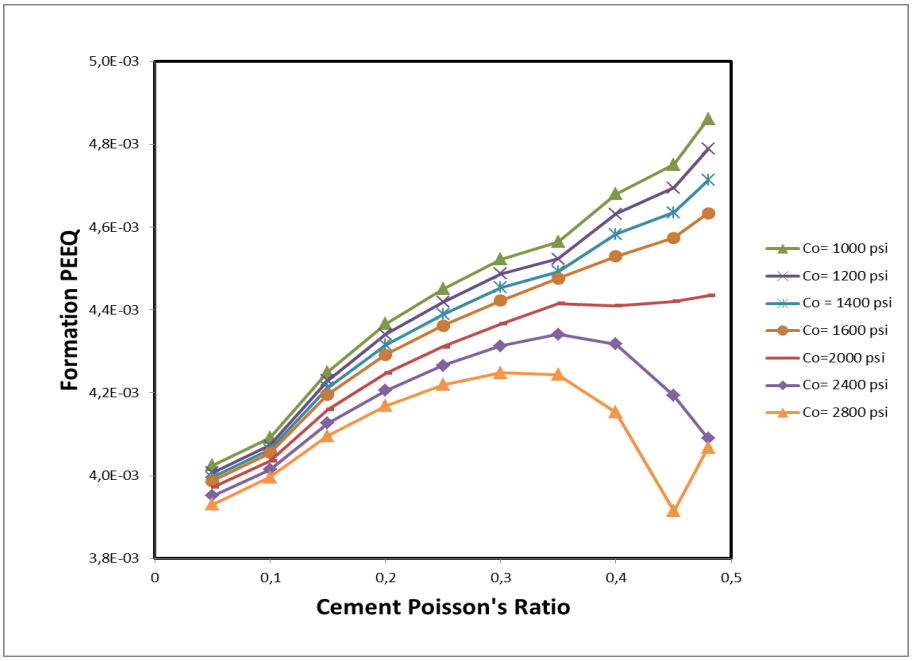

Fig. A-48. Cement Poisson's Ratio vs. Formation PEEQ during well production with cement Young's modulus of 2.0 E+6 psi. Cement Poisson's ratio and formation PEEQ did not have a linear relationship.

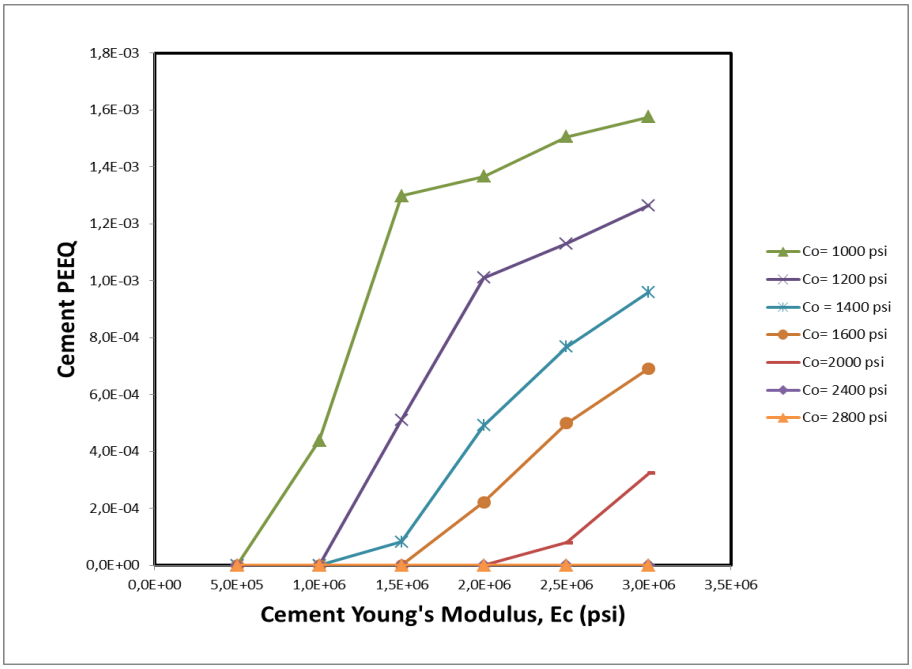

Fig. A-49. Cement Young's Modulus, Ec (psi) vs. Cement PEEQ after well completion with cement Poisson's ratio of 0.25. Cement plastic deformation increased for low values of cement cohesion and high values of cement Young's modulus.

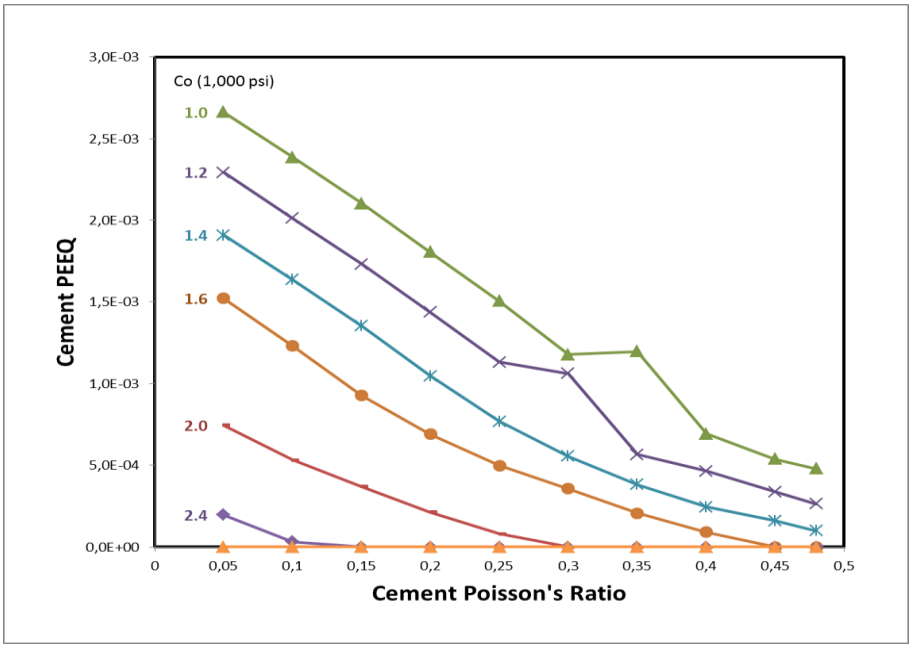

Fig. A-50. Cement Poisson's Ratio vs. Cement PEEQ after well completion with cement Young's Modulus of 2.5 E+6 psi. Cement plastic deformation increased for low values of cement cohesion and low values of cement Poisson's ratio.

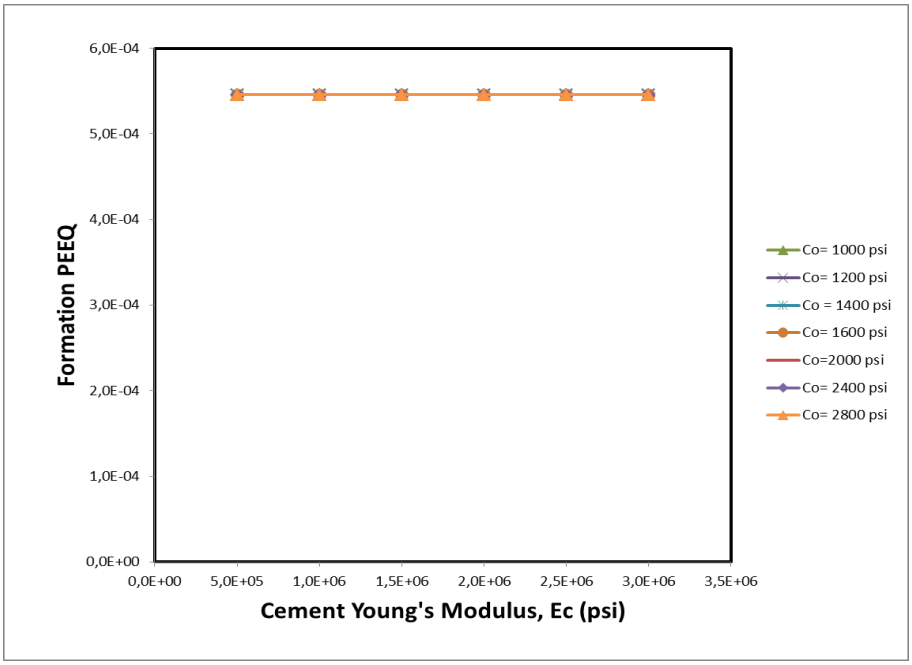

Fig. A-51. Cement Young's Modulus, Ec (psi) vs. Formation PEEQ after well completion with cement Poisson's ratio of 0.25. Formation plastic deformation was low and constant for different cement cohesions and cement Young's moduli.

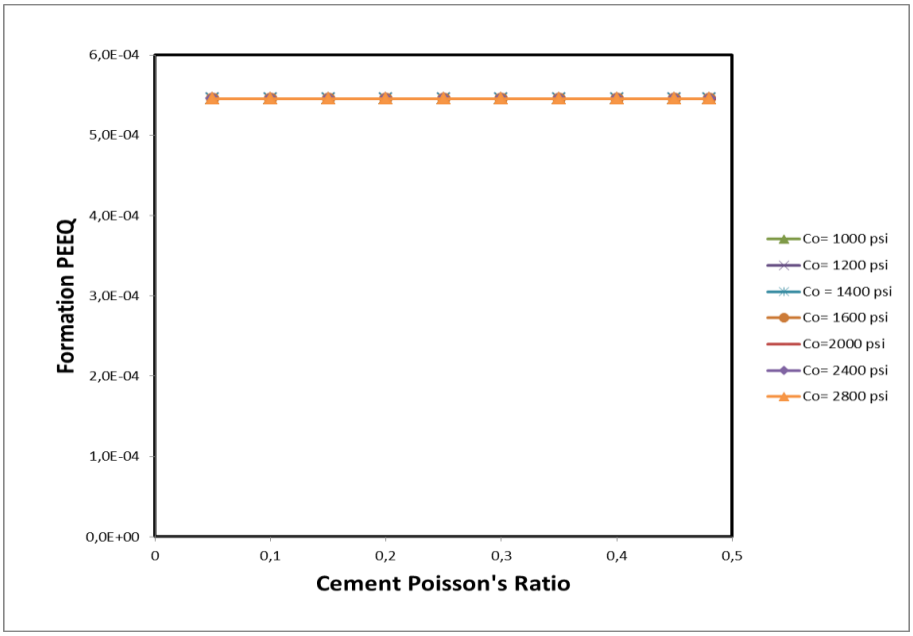

Fig. A-52. Cement Poisson's Ratio vs. Formation PEEQ after well completion with cement Young's Modulus of 2.5 E+6 psi. Formation plastic deformation was low and constant for different cement cohesions and cement Poisson's ratios.

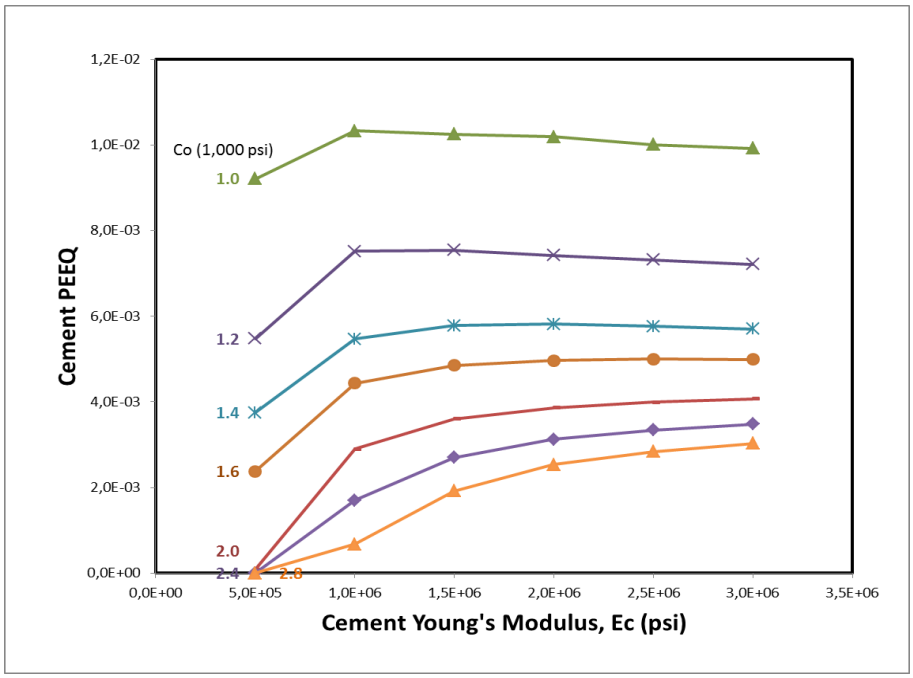

Fig. A-53. Cement Young's Modulus, Ec (psi) vs. Cement PEEQ after hydraulic fracturing job with cement Poisson's ratio of .25. Cement plastic deformation increased for low values of cement cohesion.

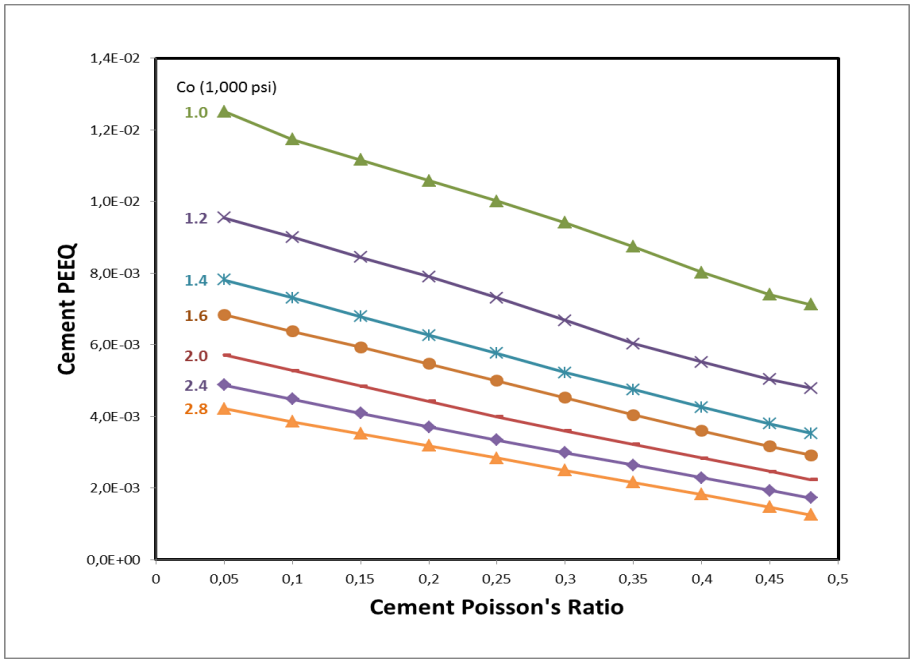

Fig. A-54. Cement Poisson's Ratio vs. Cement PEEQ after hydraulic fracturing job with cement Young's modulus of 2.5 E+6 psi. Cement plastic deformation increased for low values of cement cohesion and low values of cement Poisson's ratio.

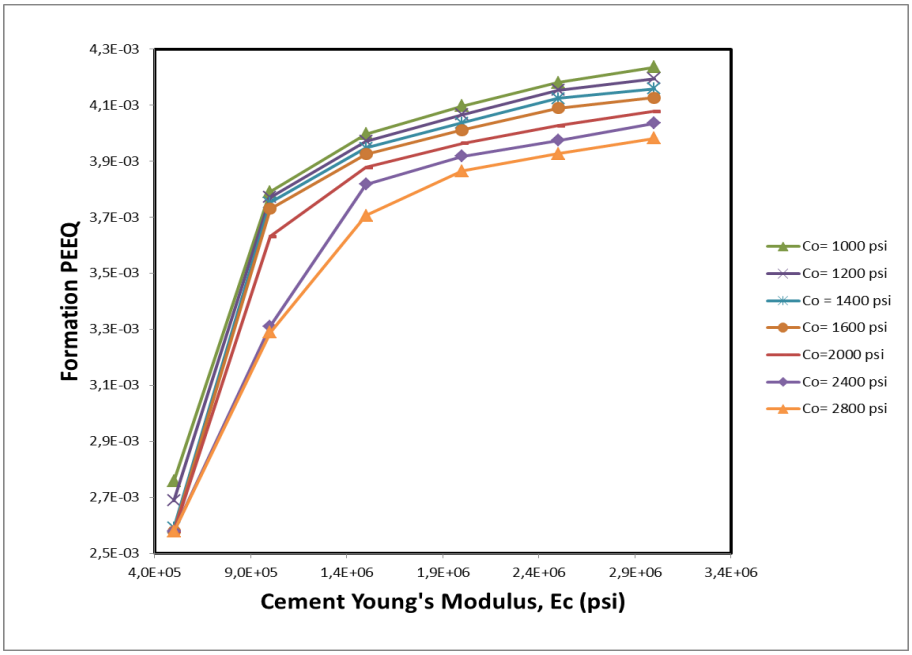

Fig. A-55. Cement Young's Modulus, Ec (psi) vs. Formation PEEQ after hydraulic fracturing job with cement Poisson's ratio of 0.25. The higher Young's modulus of set cements, the higher formation plastic deformation.

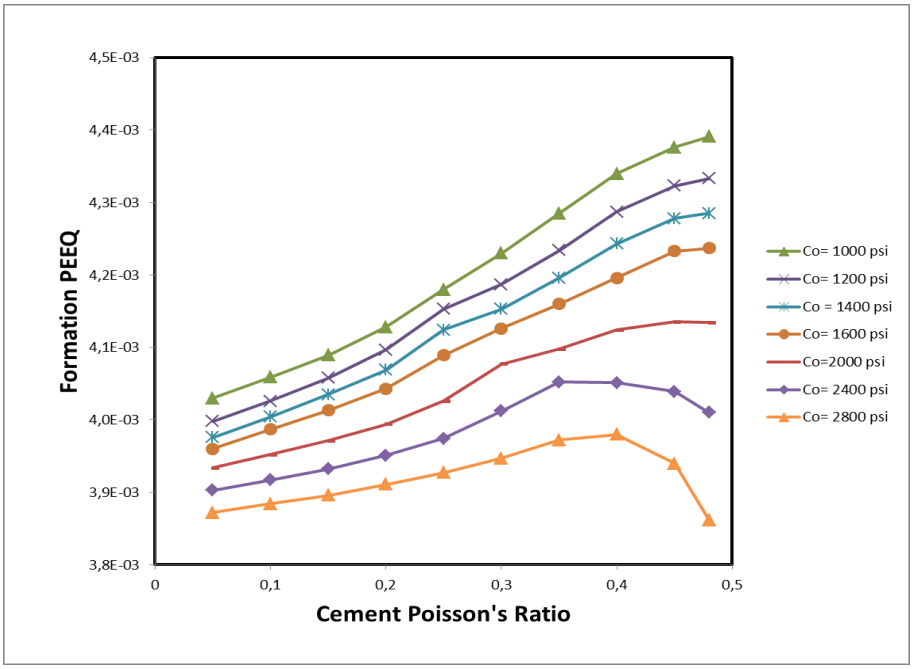

Fig. A-56. Cement Poisson's Ratio vs. Formation PEEQ after hydraulic fracturing job with cement Young's modulus of 2.5 E+6 psi. Cement plastic deformation increased for low values of cement cohesion.

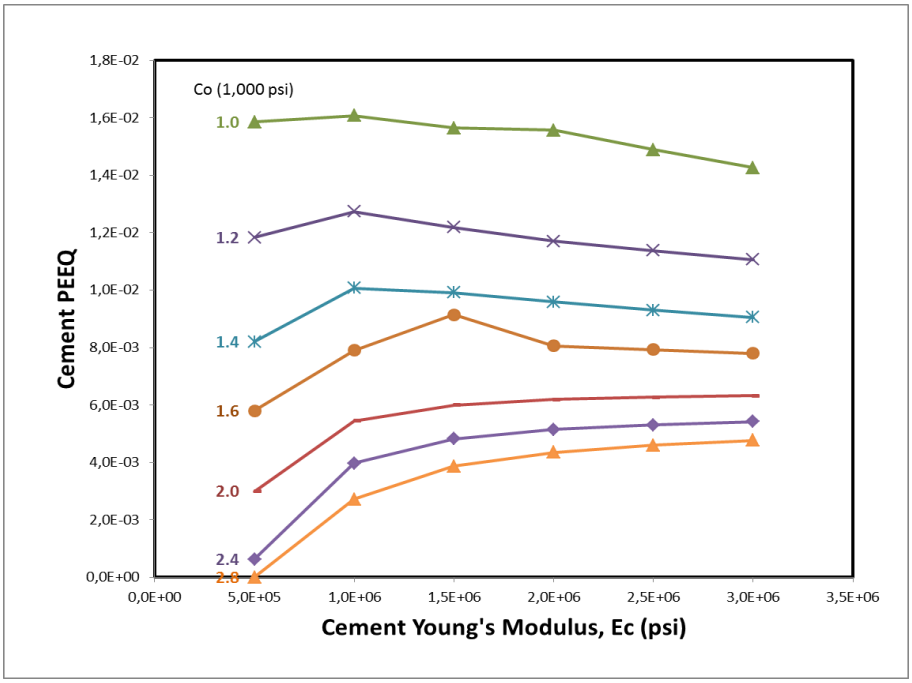

Fig. A-57. Cement Young's Modulus, Ec (psi) vs. Cement PEEQ during well production with cement Poisson's ratio of 0.25. Cement plastic deformation increased for low values of cement cohesion.

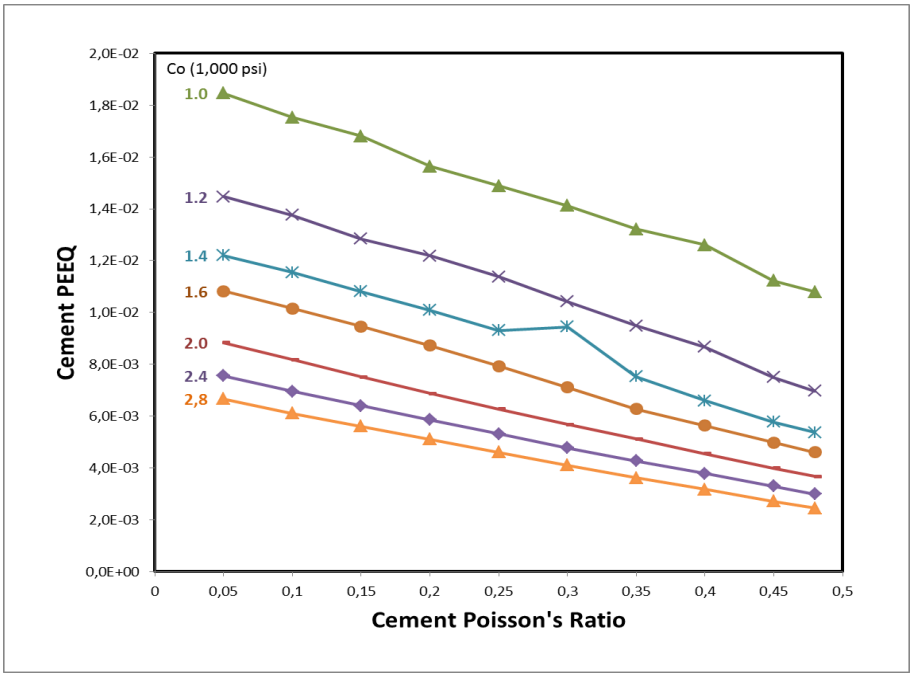

Fig. A-58. Cement Poisson's Ratio vs. Cement PEEQ during well production with cement Young's modulus of 2.5 E+6 psi. Cement plastic deformation increased for low values of cement cohesion and low values of cement Poisson's ratio.

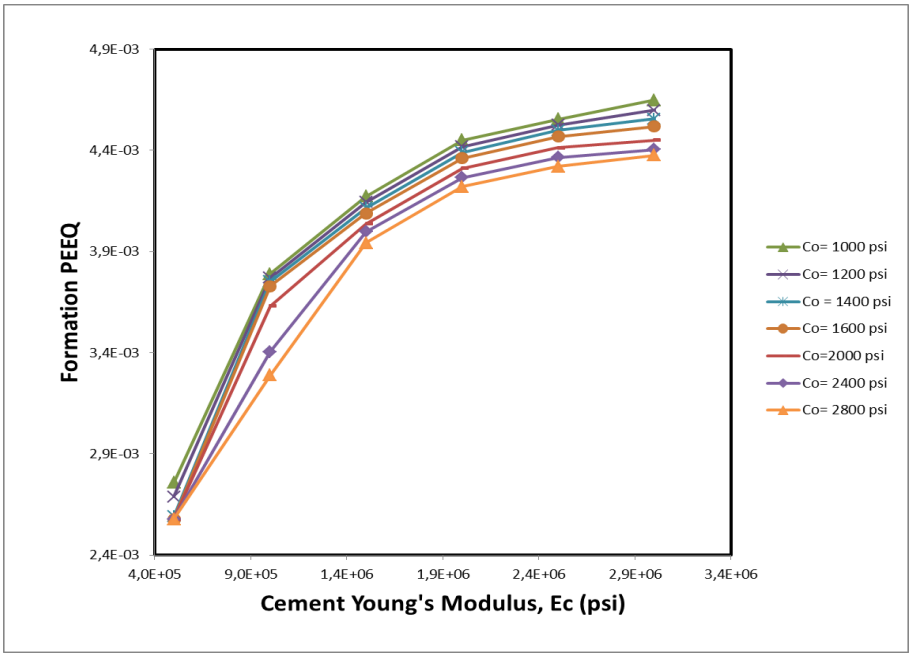

Fig. A-59. Cement Young's Modulus, Ec (psi) vs. Formation PEEQ during well production with cement Poisson's ratio of 0.25. The higher Young's modulus of set cements, the higher formation plastic deformation.

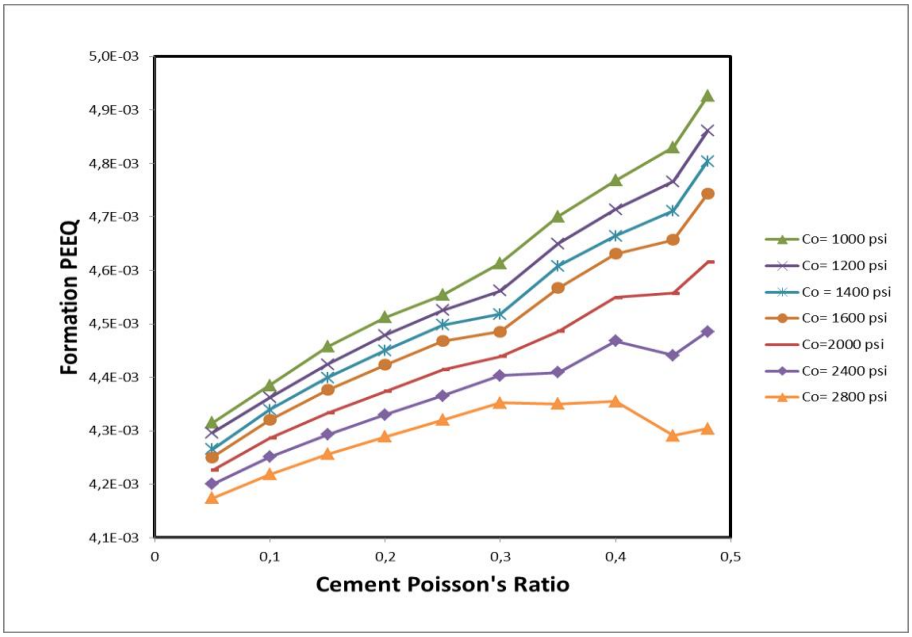

Fig. A-60. Cement Poisson's Ratio vs. Formation PEEQ during well production with cement Young's modulus of 2.5 E+6 psi. Formation plastic deformation increased for low values of cement cohesion and high values of cement Poisson's ratio.

APPENDIX B

CEMENT SLURRY DESIGNS

TABLE B-1—DESIGN OF HALLIBURTON PORTLAND CEMENT (2010)

	14.5-ppg ElastiCem	14.5-ppg Non-ElastiCem	15.6-ppg ElastiCem
Density, ppg	14.5	14.5	15.8
Curing temperature, °F	122	122	122
Dyckerhoff cement, lbs/sx	94	94	94
Micro Matrix (ultrafine) cement, % BWOC.	10	5	---
Spherilite extender, % BWOC.	10	8	---
Silicalite extender and permeability reducer (silica), % BWOC.	5	5	---
LifeCem 100 elastomer, % BWOC	---	12	12
CFR-3 dispersant, % BWOC	---	0.15	0.4
HR-5 retarder, % BWOC	0.2	0.2	0.2
HALAD-400L fluid-loss additive, gps	0.2	0.15	---
HALAD-344 fluid-loss additive, % BWOC	0.1	---	---

TABLE B-2—DESIGNS OF HALLIBURTON PORTLAND CEMENT (2011 - 2012)

	Design 1	Design 2	Design 3	Design 4
Density, ppg	15.8	15.8	15.8	15.8
Curing temperature, °F	122	122	122	122
Dyckerhoff cement, lbs/sx	94	94	94	94
Micromax weight additive, % BWOC	3		3	
LifeCem 100 elastomer, % BWOC	8		8	
Scr-100 retarder, % BWOC	0.45	0.4	0.45	0.4
HR-5 retarder, % BWOC				
HALAD-344 fluid-loss additive, % BWOC	0.3	0.3	0.3	0.7
HALAD-400L fluid-loss additive, gps				
HALAD-413 Fluid-Loss Additive, % BWOC	0.55	0.55	0.55	
Microbond HT expansive cement additive, % BWOC	3		3	3
WellLife 684 carbon fibers, % BWOC				3
WellLife 734 glass fibers, % BWOC	0.5		0.5	
FDP-C930 fluid loss additive, % BWOC				20
Latex 3000 elastomer, gps			1	

TABLE B-2—DESIGNS OF HALLIBURTON PORTLAND CEMENT (2011 - 2012) (CONTINUED)

	Design 5	Design 6	Design 7	Design 8	Design 9	Design 10
Density, ppg	15.8	15.8	15.8	14.5	14.5	15.8
Curing temperature, °F	122	122	122	122	122	122
Dyckerhoff cement, lbs/sx	94	94	94	94	94	94
Micromax weight additive, % BWOC		3	3			
Spherilite extender, % BWOC.				10	10	
Silicalite extender and permeability reducer (silica), % BWOC.				7	7	
Scr-100 retarder, % BWOC	0.4	0.4	0.4	0.4	0.4	0.4
HR-5 retarder, % BWOC						
HALAD-344 fluid-loss additive, % BWOC	0.7	0.3	0.3	0.7	0.7	0.7
HALAD-413 Fluid-Loss Additive, % BWOC		0.55	0.55			
Microbond HT expansive cement additive, % BWOC	3	3	3	3	3	3
WellLife 665 elastomer, % BWOC		8	8			
WellLife 684 carbon fibers, % BWOC	3			3	3	3
WellLife 734 glass fibers, % BWOC		0.5	0.5			
FDP-C930 (weighted WellLife 809), high performing elastomer, % BWOC	20			20		
FDP-C987 (weighted WellLife 665), High performing elastomer % BWOC					20	15
Latex 3000 elastomer, gps	1		1			

TABLE B-3—DESIGN OF THERMALOCK CEMENTS (2011 – 2012)

	Design 1TL	Design 2TL	Design 3TL	Design 4TL	Design 5TL	Design 6TL
Density, ppg	15.5	14.5	14.5	14.5	14.5	14.5
ThermaLock, %	100	100	100	100	100	100
Versaset accelerator, % BWOC	3	3	0.4	0.4	0.4	0.4
Latex 3000 elastomer, gps	1.5	1.5	1.5	1.5	1.5	1.5
Spherilite extender, % BWOC	---	5	5	5	5	5
WellLife-734 glass fibers, % BWOC.	---	---	---	2	---	---
WellLife-684 carbon fibers, % BWOC	---	---	---	---	2	2.5

TABLE B-4—DESIGN OF 14.55 PPG FEXSTONE CEMENT (2012)

	14.55-ppg FlexStone
Density, ppg	14.67
Blend 14.55 ppg FlexStone (Portland Cement G, silica, extender and expansive), yield, ft^3/sx	1.23
D153 antisettling, % BWOC	0.10
D047 antifoam, % BWOC	0.02
D167 fluid loss, % BWOC	0.20
D800 retarder, % BWOC	0.38

TABLE B-5—DESIGN OF BAKERS CEMENTS (2011 – 2012)

	San Antonio	Yopal	Reservoir	Fire Set
Density, ppg	14.5	14.5	14.5	14.5
Fire Set, %				100
FP-6L antifoam, gps	0.01	0.01	0.02	0.02
CD-Ultra LB dispersant, gps	0.08	0.08	0.35	0.35
FL-67L fluid-loss control, gps	0.20	0.20	0.80	0.6
R-3 retarder, % BWOC	0.37	0.37		0.45
A-3L gel stabilizer, gps	0.01	0.01		0.02
FL-52 fluid loss, % BWOC	0.1	0.1	0.1	
LW-7-10 Spherelite, % BWOC	7	7	13	3
MPA-1 Multipurpose agent (increases tensile strength and early compressibility strength), % BWOC	6	6		
BA-86L latex, gps	---	0.5		
BA-10 gas migration additive, % BWOC			1	0.5
S-8 Anti-retrogression, % BWOC			40	
BJ-Ultra LB Multipurpose agent, gps			0.2	
Ultra-fine cement, % BWOC			15	

APPENDIX C

MECHANICAL AND THERMAL PROPERTIES OF SET CEMENTS

Halliburton Cements

TABLE C-1—TENSILE STRENGTH TESTS OF HALLIBURTON PORTLAND CEMENTS TESTS (2010)

Sample ID	Sample Name	Tensile Strength, psi
200550406	14.5-ppg ElastiCem cement	396.6
200550410	14.5-ppg non-ElastiCem	377.4
200550413	15.6-ppg ElastiCem cement	318.3
200550414	15.8-ppg ElastiCem cement	283.6
200551241	14.5-ppg ElastiCem cement	328.4
200551242	14.5-ppg ElastiCem cement	366.1
200551243	14.5-ppg non-ElastiCem cement	314.8
200551244	14.5-ppg non-ElastiCem cement	350.4
200551245	15.6-ppg ElastiCem cement	352.4
200551246	15.6-ppg ElastiCem cement	385.9
200551247	15.8-ppg ElastiCem cement	372.1
200551248	15.8-ppg ElastiCem cement	452.9

TABLE C-2—UNIAXIAL TESTS OF HALLIBURTON PORTLAND CEMENTS TESTS (2010)

Sample ID	Sample Name	UCS, psi	Average Young's Modulus, psi	Average Poisson's Ratio
200550409	14.5-ppg ElastiCem cement	3,126	1.16E+06	0.218
200550411	14.5-ppg non-ElastiCem	5,250	1.18E+06	0.217
200550415	15.8-ppg ElastiCem cement	4,430	1.14E+06	0.209

TABLE C-3—TENSILE STRENGTH TESTS OF HALLIBURTON PORTLAND CEMENTS TESTS (2011 – 2012)

Sample ID	Design	Length, mm	Diameter, mm	Tensile Strength, psi
200709430	3	19.059	38.096	414.6
200709431	3	19.070	37.970	581.2
200709432	3	19,319	37.952	424.1
200709421	6	19.046	37.986	548.8
200709422	6	18.445	37.930	495.5
200709423	6	18.936	37.942	580.5
200709412	7	18.754	37.328	464.1
200709413	7	18.931	37.498	476.7
200709414	7	18.350	37.376	408.5
200777519	9	19.084	37.914	349.52
200777520	9	18.815	37.792	376.75
200777521	9	19.218	37.872	382.91
200802516	10	21,466	37,978	438,466
200802517	10	21,746	37,876	396,819

TABLE C-4—UNIAXIAL TESTS OF HALLIBURTON PORTLAND CEMENTS TESTS (2011 – 2012)

Sample ID	Design	Length, mm	Diameter, mm	UCS, psi	Young's Modulus, psi	Poisson's Ratio
200709424	3	76.462	37.865	5,933	6.63E+05	0.121
200709425	3	76.411	37.913	3,693	6.67E+05	0.042
200709426	3	75.604	37.666	5,459	5.98E+05	0.105
200709415	6	76.211	37.981	5,698	5.84E+05	0.103
200709416	6	76.51	38.019	5,197	9.06E+05	0.076
200709417	6	76.259	37.963	3,180	7.28E+05	0.036
200709406	7	76.405	37.804	4,330	6.92E+05	0.053
200709407	7	75.636	37.864	3,669	---	---
200777522	9	75.953	37.855	2,926	5.53E+05	0.126
200777523	9	75.831	37.879	2,915	5.53E+05	0.100
200777524	9	75.506	37.804	2,815	5.36E+05	0.114
200802519	10	77.023	37.879	3312	8.521E+05	0.121
200802520	10	77.773	37.851	3440	8.407E+05	0.108

TABLE C-5—TRIAXIAL TESTS OF HALLIBURTON PORTLAND CEMENTS TESTS (2011 – 2012)

Sample ID	Design	Length, mm	Diameter, mm	Confining Pressure, psi	Confined Compressive Strength, psi	Young's Modulus, psi	Poisson's Ratio
200709402	1	75.989	37.985	500	4,858	5.24E+05	0.187
200709429	3	76.264	37.817	500	6,013	7.17E+05	0.134
200709427	3	76.159	37.823	1000	7,279	8.56E+05	0.173
200709418	6	76.575	37.974	500	4,399	3.89E+05	0.322
200709419	6	76.166	38.018	1000	6,746	6.05E+05	0.139
200709420	6	48.769	25.216	1500	4,188	1.40E+05	0.205
200709410	7	74.011	38.016	500	3,397	4.29E+05	0.136
200709409	7	71.593	37.924	1000	2,816	2.13E+05	0.093
200709411	7	50.555	25.226	750	6,110	5.23E+05	0.144
200777525	9	75.763	37.856	500	3,046	4.08E+05	0.123
200777526	9	75.636	37.813	250	2,370	5.41E+05	0.239
200777527	9	76.155	37.801	100	3,524	7.63E+05	0.143
200802521	10	76.907	37.832	500	4,668	9.19E+05	0.184
200802522	10	75.838	37.828	250	3,526	8.22E+05	0.170
200802523	10	75.855	37.914	250	4,092	9.76E+05	0.218

TABLE C-6—TENSILE STRENGTH RESULTS FOR THERMALOCK CEMENT, HALLIBURTON - DUNCAN

Sample Number	Average Tensile Strength, psi	
	9-5/8" Intermediate Casing, Design 1TL (15.5-ppg)	7" Production Liner, Design 2TL (15.5-ppg)
1	296	385
2	210	470
3	614	544
4	504	653
Average	406	513

TABLE C-7—UNIAXIAL AND TRIAXIAL TESTS OF 15.5-PPG THERMALOCK CEMENT, HALLIBURTON - DUNCAN

ThermaLock Cement	Intermediate Casing, Sample 1 Design 1TL (15.5-ppg)			Intermediate Casing, Sample 2 Design 1TL (15.5-ppg)		
Density,-ppg	15.5	15.5	15.5	15.5	15.5	15.5
Confining Pressure, psi	0	500	1,000	0	500	1,000
Compressive strength, psi	2,916	4,222	4,160	3,730	3,975	4,153
Young's Modulus, psi	1.35E6	1.46E6	1.54E6	1.33E6	1.25E6	2.55E6
Poisson's Ratio	0.12	0.14	0.22	0.12	0.132	0.238

TABLE C-8—UNIAXIAL AND TRIAXIAL TESTS OF 14.5-PPG THERMALOCK CEMENT, HALLIBURTON - DUNCAN

ThermaLock Cement Design	7" Production Liner Sample 1, Design 2TL (15.5-ppg)			7" Production Liner Sample 2, Design 2TL (15.5-ppg)		
Density,-ppg	14.5	14.5	14.5	14.5	14.5	14.5
Confining pressure, psi	0	500	1,000	0	500	1,000
Compressive strength, psi	3,621	3,839	4,176	3,212	3,568	3,816
Young's modulus, psi	1.17E6	1.41E6	1.27E6	1.11E6	1.44E6	1.24E6
Poisson's ratio	0.13	0.2	0.19	0.14	0.19	0.17

TABLE C-9—UNIAXIAL TESTS OF THERMALOCK CEMENT (2011 – 2012)

14.5-ppg ThermaLock Cement	Sample ID	Length, mm	Diameter, mm	UCS, psi	Young's Modulus, psi	Poisson's Ratio
Cured for 1 day (Design 3TL)	200712525	75.355	37.743	1938.7	4.19E+05	0.14
	200712526	74.845	37.598	2880.5	3.49E+05	0.11
	200712527	75.76	37.823	2552.1	3.87E+05	0.19
	200712529	76.605	38.041	2280.2	4.11E+05	0.19
Cured for 7 days with 2% BWOC glass fibers (Design 4TL)	200723063	75.329	37.768	1973.2	7.97E+05	0.09
Cured for 7 days with 2% BWOC carbon fibers (Design 5TL)	200730387	75.719	37.723	3284.7	8.42E+05	0.15

TABLE C-10—TRIAXIAL TESTS OF THERMALOCK CEMENT (2011 -2012)

14.5-ppg ThermaLock Cement	Sample ID	Length, mm	Diameter, mm	CCS, psi	Young's Modulus, psi	Poisson's Ratio	Confinement pressure, psi
Cured for 1 day (Design 3TL)	200712528	74.08	37.76	4,335	3.95E+05	0.037	1,500
	200712530	75.69	37.81	2,128	1.91E+05	0.082	500
With 2% BWOC carbon fibers (Design 5TL)	200730386	76.01	37.80	4,037	7.03E+05	0.151	500

TABLE C-11—BRAZILIAN TESTS OF THERMALOCK CEMENT (2011 -2012)

14.5-ppg ThermaLock Cement	Sample ID	Length, mm	Diameter, mm	Tensile Strength, psi
Cured for 1 day (Design 3TL)	200712531	19.33	37.98	75.1
	200712532	19.26	38.04	118.4
	200712533	19.36	38.04	112.8
	Average	19.31	38.02	**102.1**
	Standard Deviation	0.05	0.04	23.5
Cured for 7 days (Design 3TL)	200749709			398.5
	200749710			445.2
	200749711			339.2
	200749712			352.3
	200749713			301.6
	200749714			445.7
	200749715			356.1
	Average			**377**
	Standard Deviation			54.8
With 2% BWOC glass fibers (Design 4TL)	200723056	17.07	37.72	418.8
	200723057	19.30	37.68	400.3
	200723058	18.70	37.90	384.5
	200723059	18.77	37.80	349.0
	200723060	19.00	37.76	338.8
	200723061	18.71	37.65	433.7
	200723062	19.00	37.60	351.4
	200723064	18.28	37.82	382.9
	200730379	20.10	37.91	432.1
	200730380	19.25	37.95	322.8
	Average	**18.82**	**37.78**	**381.4**
	Standard Deviation	0.91	0.06	39.8
With 2% carbon fibers (Design 5TL)	200730381	19.14	37.90	479.2
	200730382	18.99	37.85	461.0
	200730383	18.22	37.67	448.8
	200730384	19.65	37.82	425.5
	200730385	19.74	37.87	518.4
	Average	19.15	37.82	**466.6**
	Standard Deviation	0.61	0.09	34.9

TABLE C-12—SHEAR-BOND TEST OF THERMALOCK CEMENT OF 14.5 PPG AND 2.5% CARBON FIBERS BWOC (DESIGN 6TL) – HALLIBURTON, HOUSTON

Shear Bond (Cured Samples at 170°F)					
Sample Number	Diameter, in	Specimen Height, in	Surface Area, in^2	Ultimate Force, lbf	Ultimate Stress, psi
1	1.511	4.017	19.1	11.099	582
2	1.509	4.055	19.2	6.393	333
3	1.505	3.997	18.9	10.404	551
Average					**488**

TABLE C-13—UNIAXIAL COMPRESSION TESTS OF THERMALOCK CEMENT OF 14.5 PPG AND 2.5% CARBON FIBERS BWOC (DESIGN 6TL) – HALLIBURTON, HOUSTON

Sample Number	Cylinder Compressive Strength [cured samples at 170°F (ATM)], psi	Cylinder Compressive Strength [cured samples at 550°F and 4.000 psi (HPHT)], psi	Cube Compressive Strength [cured samples at 170°F (ATM)], psi
1	1,814		
2	2,439		
3		4,053	
4		2,883	
5		3,432	
6			3,169
7			3,037
9			2,667
Average	**2,126.5**	**3,456**	**2,958**

TABLE C-14 – BRAZILIAN TESTS OF THERMALOCK CEMENT OF 14.5 PPG AND 2.5% OF CARBON FIBERS BWOC (DESIGN 6TL) – HALLIBURTON, HOUSTON

Sample Number	Tensile Strength [cured samples at 170°F (ATM)], psi	Tensile Strength [cured samples at 550°F and 4.000 psi (HPHT)], psi
1	688	
2	556	
3	644	
4	455	
5		841
6		819
Average	**586**	**830**

TABLE C-15—THERMAL CONDUCTIVITY TESTS OF THERMALOCK CEMENT OF 14.5 PPG AND 2.5% CARBON FIBERS BWOC (DESIGN 6TL) – HALLIBURTON, HOUSTON

Sample Number	Thermal Conductivity [cured samples at 170°F (ATM)] (BTU/hr/ft/°F)
1	0.4472
2	0.4316
Average	**0.4394**

TABLE C-16—WATER PERMEABILITY TESTS OF THERMALOCK CEMENT OF 14.5 PPG AND 2.5% CARBON FIBERS BWOC (DESIGN 6TL) –HALLIBURTON, HOUSTON

Sample Number	Water Permeability [cured samples at 170°F (ATM)], md	Water Permeability [cured samples at 550°F and 4,000 psi (HPHT)], md
1	0.002	
2		0.008
3		0.005
Average	**0.02**	**0.007**

TABLE C-17—TENSILE STRENGTH TESTS OF SCHLUMBERGER CEMENTS TESTS (2010)

Sample ID	Sample Name	Tensile Strength, psi
200523633	14.5-ppg cement class GD 907	297.3
200523634	14.5-ppg cement class GD 907	352.5
200523635	14.5-ppg cement class GD 907	323.8
200523636	14.5-ppg cement class GD 907	342.6
200523637	14.5-ppg cement class GD 907	281.2
200523638	14.5-ppg cement class GD 907	318.4
200523639	14.5-ppg cement class GD 907	288.8
200528033	14.2-ppg FlexStone cement	217.4
200528034	14.2-ppg FlexStone cement	236.3
200528035	14.2-ppg FlexStone cement	220.3
200528036	14.2-ppg FlexStone cement	260.4
200528037	14.2-ppg FlexStone cement	261.7
200528038	14.2-ppg FlexStone cement	242.8
200528039	14.2-ppg FlexStone cement	194.2
200530571	15.6-ppg FlexStone cement	415.4
200530572	15.6-ppg FlexStone cement	369.6
200530573	15.6-ppg FlexStone cement	381.9
200530574	15.6-ppg FlexStone cement	387.3
200530575	15.6-ppg FlexStone cement	347.9
200530576	15.6-ppg FlexStone cement	349.9
200530577	15.6-ppg FlexStone cement	339.9

TABLE C-18—UNIAXIAL TESTS OF SCHLUMBERGER PORTLAND CEMENTS TESTS (2010)

Sample ID	Sample Name	UCS, psi	Young's Modulus, psi	Poisson's Ratio
200523640	14.5-ppg cement class GD 907	3,061	---	---
200523641	14.5-ppg cement class GD 907	3,255	9.28E+05	0.196
200523642	14.5-ppg cement class GD 907	2,999	8.65E+05	0.182
200523643	14.5-ppg cement class GD 907	2,877	8.18E+05	0.168
200523644	14.5-ppg cement class GD 907	2,975	7.38E+05	0.175
200523645	14.5-ppg cement class GD 907	3,128	8.53E+05	0.198
200523646	14.5-ppg cement class GD 907	2,993	7.84E+05	0.174
200524913	14.5-ppg cement class GD 907	3,066	8.35E+05	0.177
200528040	14.2-ppg FlexStone cement	4,716	1.00E+06	0.214
200528041	14.2-ppg FlexStone cement	4,579	7.56E+05	0.176
200528042	14.2-ppg FlexStone cement	4,710	1.16E+06	0.247
200528043	14.2-ppg FlexStone cement	4,689	---	---
200528044	14.2-ppg FlexStone cement	4,174	9.91E+05	0.202
200528045	14.2-ppg FlexStone cement	4,896	9.83E+05	0.218
200528046	14.2-ppg FlexStone cement	4,750	9.78E+05	0.220
200538004	14.2-ppg cement - high UCS	4,907	1.00E+06	0.210
200530578	15.6-ppg FlexStone cement	3,422	7.81E+05	0.255
200530579	15.6-ppg FlexStone cement	3,808	8.46E+05	0.210
200530580	15.6-ppg FlexStone cement	3,855	9.11E+05	0.203
200530581	15.6-ppg FlexStone cement	4,153	8.36E+05	0.188
200530582	15.6-ppg FlexStone cement	3,688	7.96E+05	0.198
200530583	15.6-ppg FlexStone cement	3,684	7.60E+05	0.202
200530584	15.6-ppg FlexStone cement	3,646	7.33E+05	0.188

TABLE C-19—TENSILE STRENGTH TESTS OF 14.55 FLEXSTONE CEMENT (2012)

Sample ID	Cured Temperature, F°	Length, mm	Diameter, mm	Tensile Strength, psi
200800411	180	20.215	38.476	401.6
200800412	180	19.046	38.492	375.2
200800413	180	20.263	38.468	372.7
200802536_R	240	19.711	38.476	355.2
200802537	240	21.613	38.496	346.1
200802538	240	21.682	38.488	279.0

TABLE C-20—UNIAXIAL COMPRESSION TESTS OF 14.55-PPG FLEXSTONE CEMENT (2012)

Sample ID	Cured Temperature, F°	Length, mm	Diameter, mm	UCS, psi	Young's Modulus, psi	Poisson's Ratio
200800414	180	77.40	38.49	3,297.3	7.536E+05	0.199
200800416	180	71.82	38.49	3,285.7	7.796E+05	0.187
Average				**3,291**	**7.67E+05**	**0.19**
200802539	240	77.633	38.478	2,926.2	7.664E+05	0.179
200802540	240	77.145	38.471	3,153.1	7.632E+05	0.173
200802541	240	77.387	38.479	2,945.4	7.197E+05	0.142
Average				3008	**7.50E+05**	**0.165**

TABLE C-21—TRIAXIAL COMPRESSION TESTS OF 14.55-PPG FLEXSTONE CEMENT (2012)

Sample ID	Cured Temperature, F°	Length, mm	Diameter, mm	Confining Pressure, psi	CCS, psi	Average CCS, psi
200800418	180	77.527	38.476	100	3,561	**3,950**
200800417	180	75.864	38.478	250	4,027	
200800419	180	74.715	38.470	400	4,263	
200802543	240	77.836	38.469	100	3,216	**3,675**
200802542	240	77.410	38.481	250	3,715	
200802544	240	77.524	38.484	400	4,093	

TABLE C-22—TENSILE STRENGTH TESTS OF BAKER CEMENTS TESTS (2010)

Sample ID	Sample Name	Tensile Strength, psi
200556649	14.5-ppg San Antonio	675.3
200556650	14.5-ppg San Antonio	627.0
200556651	14.5-ppg San Antonio	723.2
200560758	14.5-ppg Yopal	367.1
200560759	14.5-ppg Yopal	649.6
200560760	14.5-ppg Yopal	589.9

TABLE C-23—UNIAXIAL TESTS OF SCHLUMBERGER PORTLAND CEMENTS TESTS (2010)

Sample ID	Sample Name	UCS, psi	Young's Modulus, psi	Poisson's Ratio
200556655	14.5-ppg San Antonio	7,468	1.4E+06	0.170
200556656	14.5-ppg San Antonio	5,354	1.27E+06	0.163
200556657	14.5-ppg San Antonio	7,782	1.93E+06	0.248
200560750	14.5-ppg Yopal	4,866	2.40E+06	0.222
200560751	14.5-ppg Yopal	6,012	9.33E+05	0.213
200560753	14.5-ppg Yopal	5,745	1.05E+06	0.253

TABLE C-24—BRAZILIAN TESTS OF CUPIAGUA CEMENT (2012)

Sample ID	Length, mm	Diameter, mm	Tensile Strength, psi
200786151	19.92	38.238	597

TABLE C-25—UNIAXIAL COMPRESSION TESTS OF CUPIAGUA CEMENT (2012)

Sample ID	Length, mm	Diameter, mm	UCS, psi	Young's Modulus, psi	Poisson's Ratio
200786152	77.123	37.978	5,842.7	1.103E+06	0.183
200820073	76.65	38.0	5,583.5	9.362E+05	0.203
Average			**5,713**	**1.019E+06**	**0.19**
Standard deviation			183.3	117,772	0.014
Error (%)			3.2	11.6	7.43

TABLE C-26—TRIAXIAL COMPRESSION TESTS OF CUPIAGUA CEMENT (2012)

Sample ID	Length, mm	Diameter, mm	CCS, psi	Young's Modulus, psi	Poisson's Ratio	Confining Pressure, psi
200786153	75.699	38.151	5,655.7	1.001E+06	0.18	500
200786154	77.04	37.998	6,453.7	1.155E+06	0.19	500
200820074	76.657	38.006	4,576.1	7.101E+05	0.19	250
Average			**5,562**	9.553E+05	0.19	
Standard Deviation			942.3	225,946	0.0097	
Error (%)			16.9	23.7	5.3	

TABLE C-27— BRAZILIAN TESTS OF FIRE-SET CEMENT CURED AT 211°F (2012)

Sample ID	Length (mm)	Diameter (mm)	To (psi)
200761497	19.530	37.708	299.852
200761498	19.606	37.804	254.185
200761499	18.899	38.026	347.119
200761500	19.655	37.960	349.010
200761501	19.261	37.816	355.777
Average	**19.390**	**37.863**	**321.189**
Standard Deviation	0.314	0.128	43.553
Error (%)	1.619	0.338	13.560

TABLE C-28— UNIAXIAL COMPRESSION TESTS OF FIRE SET CEMENT CURED AT 211 °F (2012)

Sample ID	Length (mm)	Diameter (mm)	UCS (psi)	Young's Modulus (psi)	Poisson's Ratio
200761495	75.238	37.705	4,546.2	5.44E+05	0.151
200774415	76.109	37.878	3,697.6	5.79E+05	0.20
200774417	76.119	37.902	3,571.5	5.53E+05	0.161
Average			**3,938.4**	**5.58E+05**	**0.171**
Standard deviation			530.1	18,093.97	0.026
Error (%)			13.46	3.24	15.1

TABLE C-29— TRIAXIAL COMPRESSION TESTS OF FIRE SET CEMENT CURED AT 211 °F (2012)

Sample ID	Length (mm)	Diameter (mm)	CCS (psi)	Young's Modulus (psi)	Poisson's Ratio	Confining Pressure (psi)
200761496	75.227	37.721	5,155	2.58E+05	0.142	500
200774416	76.481	38.02	4,061	2.80E+05	0.143	500
Average			**4,608**	**2.69E+05**	**0.142**	
Standard Deviation			774	15,836.4	0.001	
Error (%)			16.8	5.889	0.439	

TABLE C-30—BRAZILIAN TESTS OF FIRE-SET CEMENT CURED AT 500 °F(2012)

Sample ID	Length, mm	Diameter, mm	Tensile Strength, psi
200806448	18.393	38.130	145.7

TABLE C-31—UNIAXIAL COMPRESSION TESTS OF FIRE SET CEMENT CURED AT 500 °F (2012)

Sample ID	Length, mm	Diameter, mm	UCS, psi	Young's Modulus, psi	Poisson's Ratio
200806445	69.266	37.895	1,711.6	5.84E+05	0.151

TABLE C-32—TRIAXIAL COMPRESSION TESTS OF FIRE SET CEMENT CURED AT 500 °F (2012)

Sample ID	Length, mm	Diameter, mm	CCS, psi	Young's Modulus, psi	Poisson's Ratio	Confining Pressure, psi
200806446	65.266	37.974	2,551.8	3.24E+05	0.121	250
200806447	70.19	38.144	3,358.5	6.90E+05	0.114	500
Average			**2,955.1**	**5.07E+05**	**0.117**	
Standard Deviation			570,388	258,878	0.005	
Error (%)			19,3	51.0	4.586	

APPENDIX D

TRIAXIAL AND BRAZILIAN TESTS, FRACTURE GRADIENT, IN-SITU STRESS DIRECTIONS OF STUDIED OIL FIELDS

TABLE D-1—ESTIMATED FORMATION MECHANICAL PROPERTIES OF APIAY FIELD, COLOMBIA

Formation Name	Top (TVD), ft	Young's Modulus , psi	UCS, psi	Poisson's Ratio	Friction Angle, deg	Cohesion, psi	Pore Pressure, ppg
Guayabo (Claystone)	0	3.2E+05	3,242	0.42	33.6	823	8.2
Leon (Shale)	3869	3.2E+05	3,332	0.42	45.5	1,157	9.2
C1 Sup (Sandstone)	4350	1.1E+06	4,515	0.34	42.5	1,468	7.3
Lutita E (Shale)	5800	6.5E+05	3,876	0.38	43.8	1,310	9.4
C1 Inf (Sandstone)	6100	1.4E+06	5,428	0.33	42.5	1,540	8.0
Sands Carbonera	7050	1.9E+06	6,965	0.28	41.5	1,639	7.5
C2 (Shale)	7400	1.7E+06	5,930	0.29	43.4	1,688	8.6
E3 (Shale)	9250	9.5E+05	4,928	0.34	45.4	1,510	10.6
T1 (Sandstone)	9700	2.7E+06	8,218	0.25	48.1	2,144	6.3
E4 (Shale)	9800	1.4E+06	5,515	0.32	45.7	1,675	10.4
T2 (Sandstone)	10050	2.9E+06	8,721	0.25	49.1	2,152	6.5
K1 (Sdtone/ Shale)	10250	3.5E+06	7,885	0.23	48.4	2,343	8.2
K2 (Sandstone)	10750	3.8E+06	10,057	0.21	50.0	2,505	6.7

TABLE D-2—TRIAXIAL AND BRAZILIAN TEST RESULTS OF K2 FORMATION IN APIAY FIELD AREA (GAVAN-1 WELL)

Sample Depth, ft	UCS, psi	Friction Angle, deg	Cohesion, psi	Tensile Strength, psi
10,823.00	7,732	40.0	1,803	
10,824.00	9,038	50.1	1,640	914
10,825.00	8,834	29.7	2,565	1,304
10,837.67	5,269	29.6	1,533	2,185
10,849.00	7,595	73.8	540	
10,850.75	11,962	57.1	1,766	1,439
10,851.50	9,550	56.9	1,419	1,120
10,853.08	7,831	49.0	1,464	1,195
10,866.00	7,511	43.5	1,613	
10,880.50	7,268	53.9	1,184	1,121
10,885.58	9,823	63.3	1,165	1,134
10,900.00	10,129	64.2	1,160	1,949
10,900.29	1,774	64.7	199	2,148
10,900.92	7,204	62.9	868	

TABLE D-3—FRACTURE GRADIENT FROM HYDRAULIC FRACTURING JOBS IN APIAY FIELD AREA

Well Name	Average Depth of the Job, ft	Fracture Gradient, psi/ft
Apiay-20	10,622	0.72
Apiay-20	10,557	1.24
Apiay-20	10,518	1.04
Apiay-20	10,470	1.03
Austral-1R	10,518	0.95
Austral-1R	10,440	0.85
Austral-1R	10,406	1.30
Gavan-4	10,833	0.87
Gavan-4	10,833	0.83
Gavan-4	10,766	0.87
Gavan-4	10,766	0.79
Gavan-4	10,722	0.89
Gavan-4	10,722	0.86
Gavan-4	10,668	0.96
Suria Sur-17	10,572	1.05
Suria Sur-17	10,440	0.88
Suria Sur-17	10,440	1.13
Suria Sur-17	10,353	0.99
Suria Sur-17	10,353	1.16
Suria Sur-5	10,212	1.01
Suria Sur-8	10,346	0.79
Suria-14	10,489	0.81
Suria-14	10,489	0.79
Suria-14	10,390	0.98
Suria-14	10,390	1.13
Suria-14	10,300	0.86
Average	**10,524**	**0.95**

TABLE D-4—BREAKOUT AND DRILLING-INDUCED TENSILE FRACTURE AZIMUTH IN APIAY FIELD

Well Name	Minimum Horizontal Stress Direction	
	Breakout Azimuth, deg	Azimuth of Drilling Induced Tensile Fractures, deg
Apiay-20	173±18	108 ± 0
Apiay-22	18 ± 16	102 ± 24
Apiay-24	41 ± 16	
Apiay-28	8 ± 12	
Apiay-29	12 ± 19	115 ± 5
Gavan-2	174 ± 15	
Austral-1R	177 ± 12	
Suria-12	4 ± 13	
Suria-13	2 ± 12	83 ± 5
Suria Sur-17	23 ± 30	
Suria Sur-18	13 ± 11	153 ± 15

TABLE D-5—ESTIMATED FORMATION MECHANICAL PROPERTIES OF CHICHIMENE FIELD, COLOMBIA

Formation Name	Top (TVD), ft	Young's Modulus, psi	UCS, psi	Poisson's Ratio	Friction Angle, deg	Cohesion, psi	Pore Pressure, ppg
Guayabo (Clay and sands)	0	8.13E+05	4,188	0.40	37	1,151	8.8
Lutita E (Shale)	3,096	1.29E+06	4,763	0.33	36	1,292	9.3
C1 (Sandstone)	3,461	1.50E+06	4,953	0.31	38	1,427	9.2
Carbonera Sandstone	3,971	1.46E+06	4,921	0.31	38	1,405	8.1
C2 (Shale)	4,605	1.30E+06	4,757	0.33	37	1,326	9.9
E3 (Shale)	6,492	7.99E+05	4,204	0.36	37	1,161	11
T1 (Sandstone)	7,045	1.51E+06	4,966	0.31	38	1,447	8.9
E4 (Shale)	7,223	1.24E+06	4,656	0.33	37	1,321	10.8
T2 (Sandstone	7,867	3.00E+06	5,908	0.23	54	2,482	7.8
K1 (Sandstone/ Shale)	8,193	2.44E+06	5,643	0.27	50	2,180	8
K2 (Sandstone)	8,767	3.31E+06	6,090	0.22	56	2,665	7.3

TABLE D-6—ESTIMATED FORMATION MECHANICAL PROPERTIES OF CUPIAGUA FIELD, COLOMBIA

Formation Name	Top (TVD), ft	Young's Modulus, psi	UCS, psi	Poisson's Ratio	Friction Angle, deg	Cohesion, psi	Pore Pressure, ppg
Guayabo (Claystone)	0	3.65E+05	3,801	0.31	22	1,439	8.3
Charte (Claystone)	3,395	7.25E+05	5,507	0.28	25	1,782	8.5
Leon(Shale)	5,354	2.25E+05	5,227	0.31	21	1,615	10
C1 (Sandstone)	6,627	8.65E+05	6,192	0.30	35	2,313	9.5
C2 (Shale)	8,489	1.95E+05	5,088	0.32	20	1,622	11
C3 (Sandstone)	8,953	7.45E+05	8,747	0.23	35.3	2,890	10.1
C4 (Shale)	9,321	3.25E+05	6,199	0.29	22	1,697	11.2
C5 (Sandstone)	9,513	1.05E+06	8,341	0.22	39	2,854	10.3
C6 (Shale)	10,847	7.35E+05	5,435	0.31	21.7	1,750	13.9
C7 (Sandstone)	11,511	1.03E+06	9,868	0.24	36	2,939	14.3
C8 (Shale)	12,222	6.85E+05	8,948	0.26	25	2,637	14.6
Mirador (Sandstone)	12,730	6.29E+06	36,200	0.13	50	5,776	5.4
Cuervos (Shale)	13,318	3.0E+06	11,500	0.25	25	4,000	9.8
Barco (Sandstone)	14,045	8.3E+06	31,000	0.25	45	5,700	5.8
Guadalupe (Sandstone/Shale)	14,588	2.94E+06/ 2.05E+06	24,800/ 19,537	0.19/ 0.25	51/ 42	7,246/ 4,873	4.8/ 8.5

TABLE D-7—GEOMECHANICAL PROPERTIES OF PAYZONES AT CUPIAGUA FIELD (AFTER REF. 47)

Mechanical Property		Formation		
		Mirador	Barco	Guadalupe
UCS, psi		36,207	31,204	24,858
Poisson's Ratio	Tangent (25%-75%)	0.29	0.24	0,30
	Average (20%-80%)	0.31	0.25	0,30
	Secant (0%-50%)	0.14	0.12	0,06
Young's Modulus, Mpsi	Tangent (25%-75%)	8.4	8.5	6,0
	Average (20%-80%)	8.3	8.3	5,9
	Secant (0%-50%)	6.0	6.9	3,5
Cohesion (psi)		6593	*	4485
Internal Friction Angle (deg)		50.0	*	50.3

* tests were not completed due to high strength of the rock

TABLE D-8—ESTIMATED MAGNITUDE AND AZIMUTH OF IN-SITU STRESS AT APIAY, CHICHIMENE AND CUPIAGUA FIELDS

Field	Vertical Stress Magnitude, psi/ft	Maximum Horizontal Stress Magnitude, psi/ft	Minimum Horizontal Stress Magnitude, psi/ft	Maximum Horizontal Stress Azimuth, deg	Minimum Horizontal Stress Azimuth, deg
Apiay	1.0	1.21	0.81	115 ± 5	25 ± 5
Chichimene	1.0	1.19	0.76	110±10	20
Cupiagua	1.1	1.3	0.8	120	30

TABLE D-9—SURFACE TEMPERATURE AND TEMPERATURE GRADIENT OF APIAY, CHICHIMENE AND CUPIAGUA FIELDS

Field	Surface Temperature, °F	Temperature Gradient, °F/100 ft
Apiay	90	1.13
Chichimene	90	1.15
Cupiagua	80	1.2

APPENDIX E

APPLICATION OF THE FEM TO THREE ECOPETROL'S WELLS

FEA at T2 Formation of Apiay Wells with 15.8-PPG Design 3 Cement of Halliburton Company

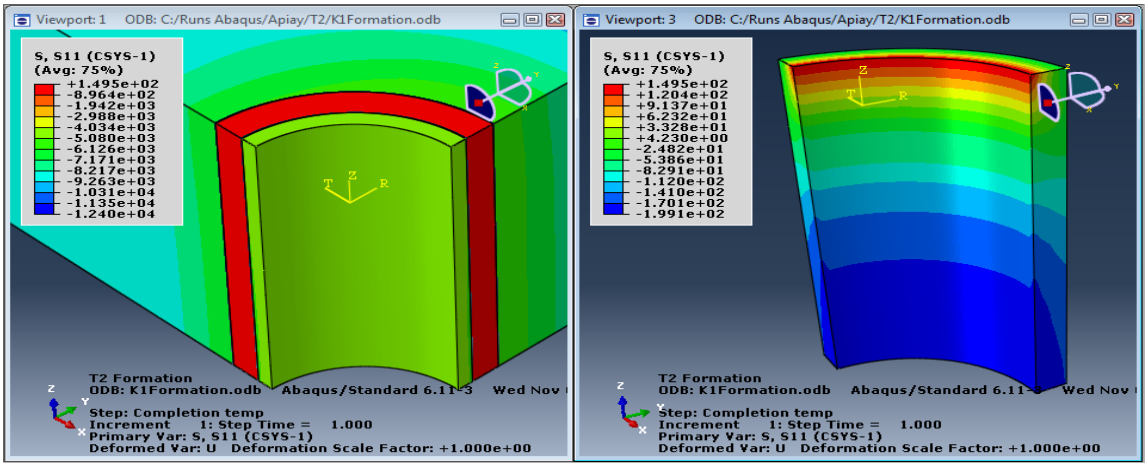

Fig. E-1—Radial stresses after well completion at T2 formation of Apiay well using FEA. Left: casing, cement and formation. Right: cement. Low chances of cement debonding from casing and formation because tensile radial stresses in the cement are lower than debonding strength of Design 3 (392 psi).

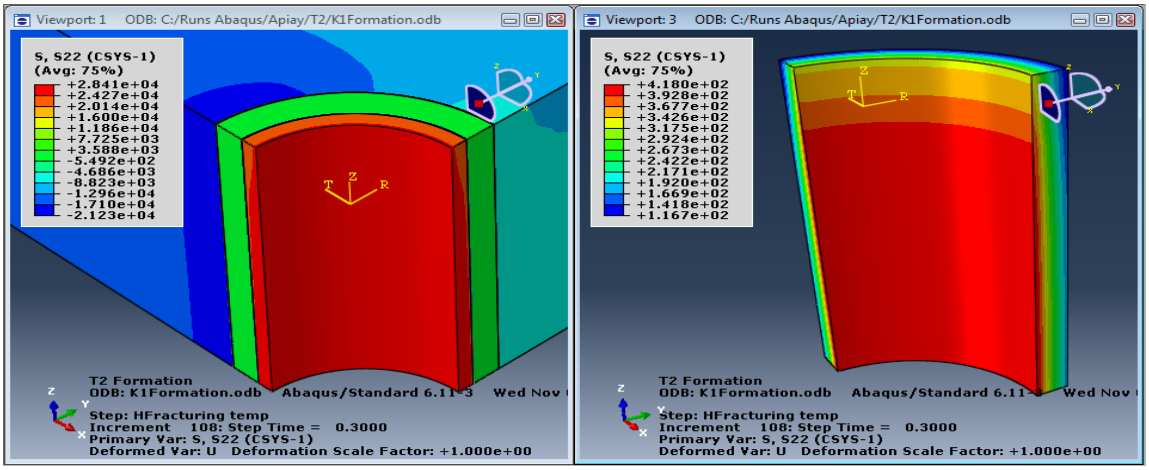

Fig. E-2—Tangential stresses after hydraulic fracturing at T2 formation of Apiay well using FEA. Left: casing, cement and formation. Right: cement. This cement design does not have radial cracks because maximum tangential stresses at cement were 418 psi, and the cement had a tensile strength of 473 psi.

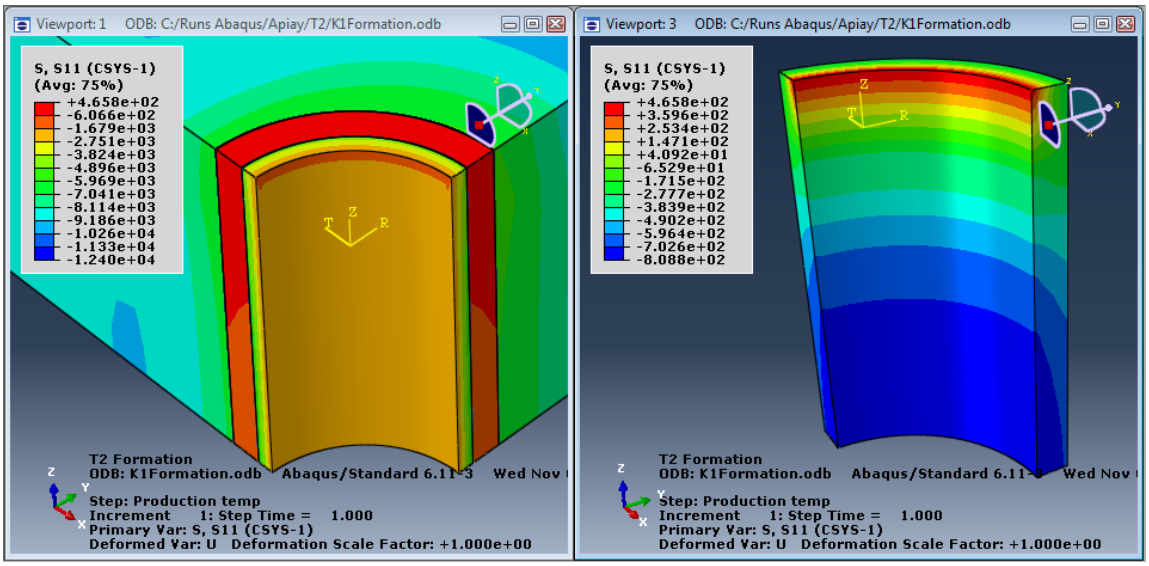

Fig. E-3—Radial stresses during well production at T2 formation of Apiay well using FEA. Left: casing, cement and formation. Right: cement. The maximum tensile radial stress was 466 psi at top of the cement sheath, and cement Design 3 partially debonds from casing, because the expected debonding strength of Design 3 cement was 392 psi.

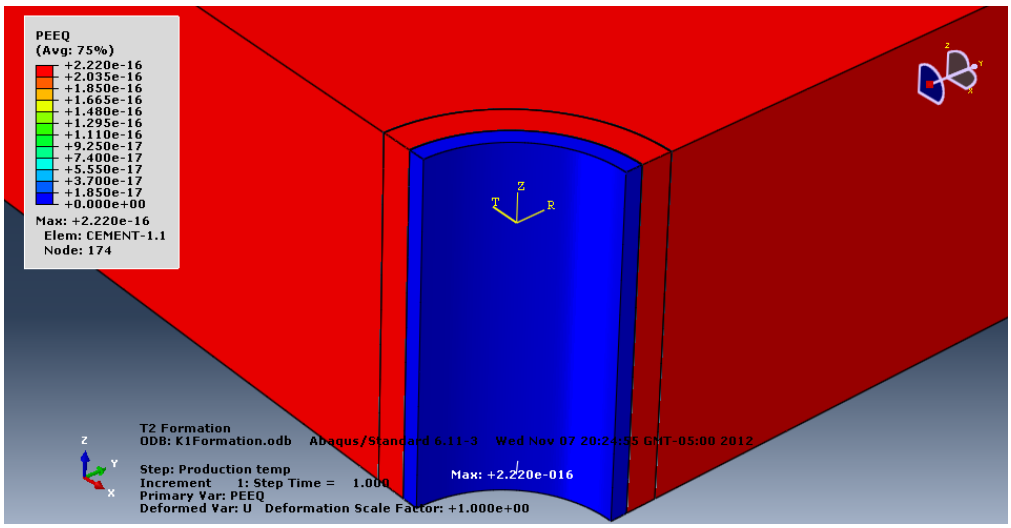

Fig. E-4—Equivalent plastic deformation (PEEQ) after well production at T2 formation of Apiay well using FEA. There was not plastic deformation of set cement or rocks.

FEA at K2 Formation of Apiay Wells with 15.8-ppg Design 3 Cement of Halliburton Company

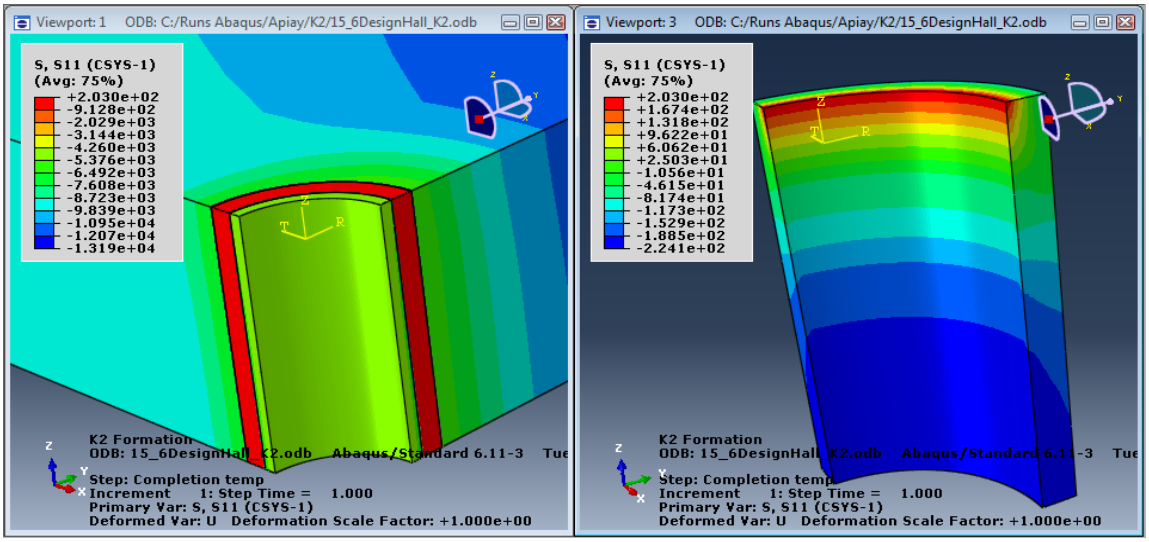

Fig. E-5—Radial stresses after well completion at K2 formation of Apiay well using FEA. Left: casing, cement and formation. Right: cement. Low chances of cement debonding from casing and formation because tensile radial stresses of cement were lower than expected cement debonding strength of 392 psi.

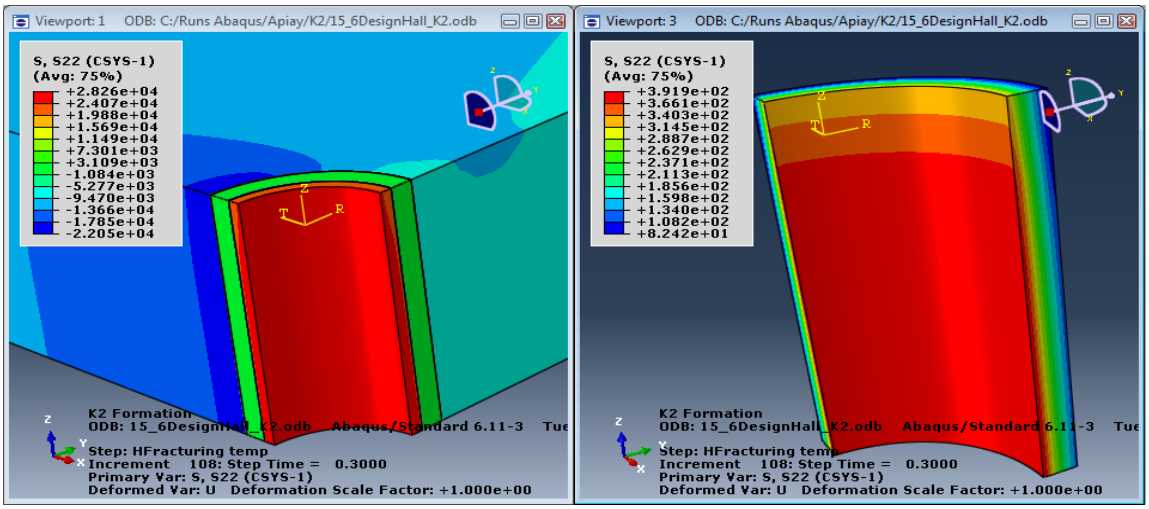

Fig. E-6—Tangential stresses after hydraulic fracturing at K2 formation of Apiay well using FEA. Left: casing, cement and formation. Right: cement. This cement design did not show radial cracks because the maximum tangential stress at cement was 392 psi, and the cement had a tensile strength of 473 psi.

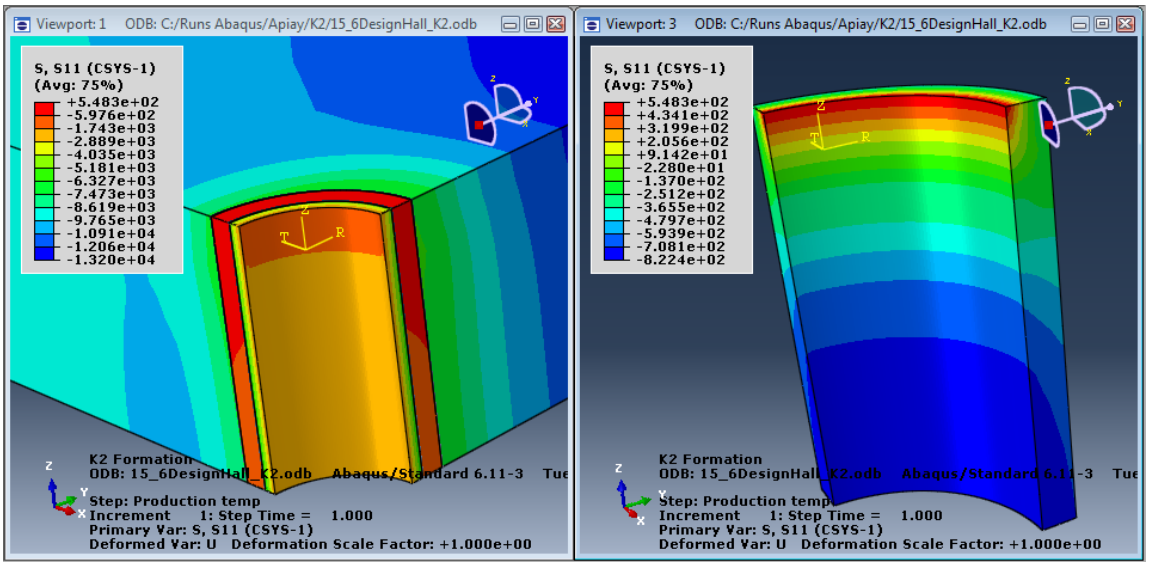

Fig. E-7—Radial stresses after well production at K2 formation of Apiay field using FEA. Left: casing, cement and formation. Right: cement. The maximum tensile radial stress of set cement was 549 psi at the top, and cement Design 3 partially debonds from casing, because the expected debonding strength of Design 3 cement was 392 psi.

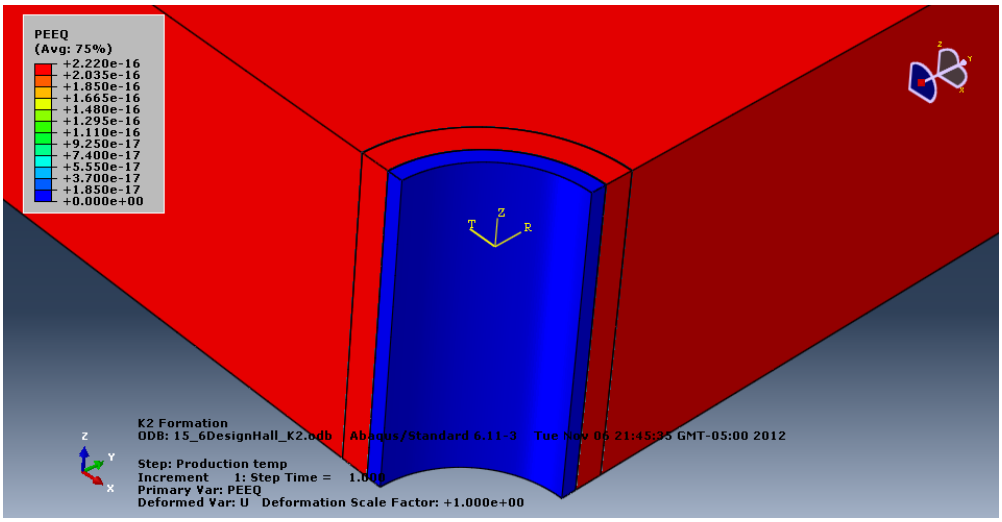

Fig. E-8—Equivalent plastic deformation (PEEQ) after well production at K2 formation of Apiay well using FEA. There was not plastic deformation of set cement or rocks.

FEA at K1 Formation of Chichimene Wells with 14.5-ppg San Antonio Cement of Baker Company

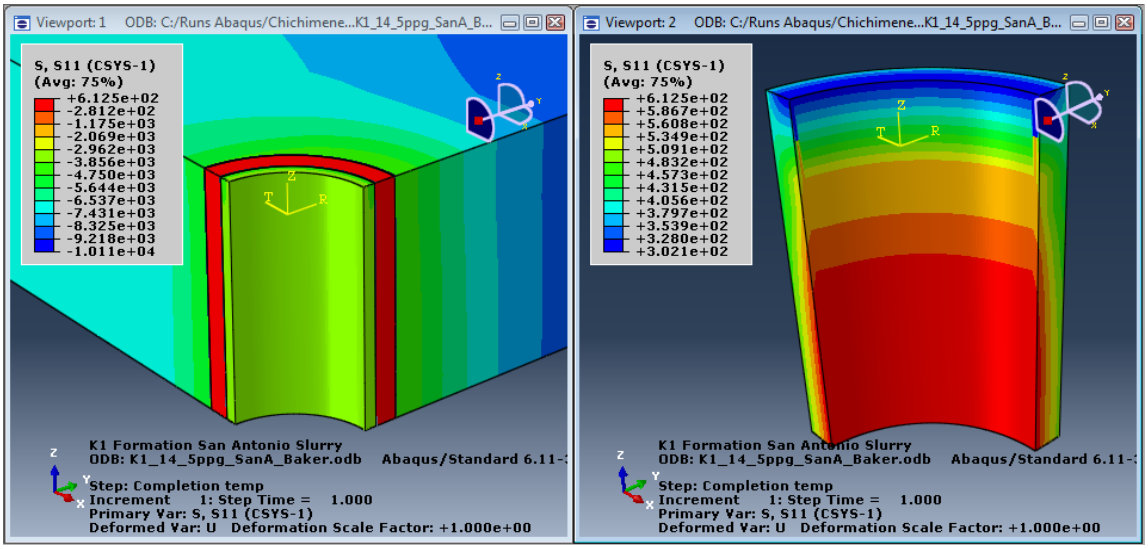

Fig. E-9—Radial stresses after well completion at K1 formation of Chichimene wells using FEA. Left: casing, cement and formation. Right: cement. There is cement debonding from casing, because tensile radial stresses of San Antonio cement had a value of 613 psi and its estimated debonding strength was 560 psi.

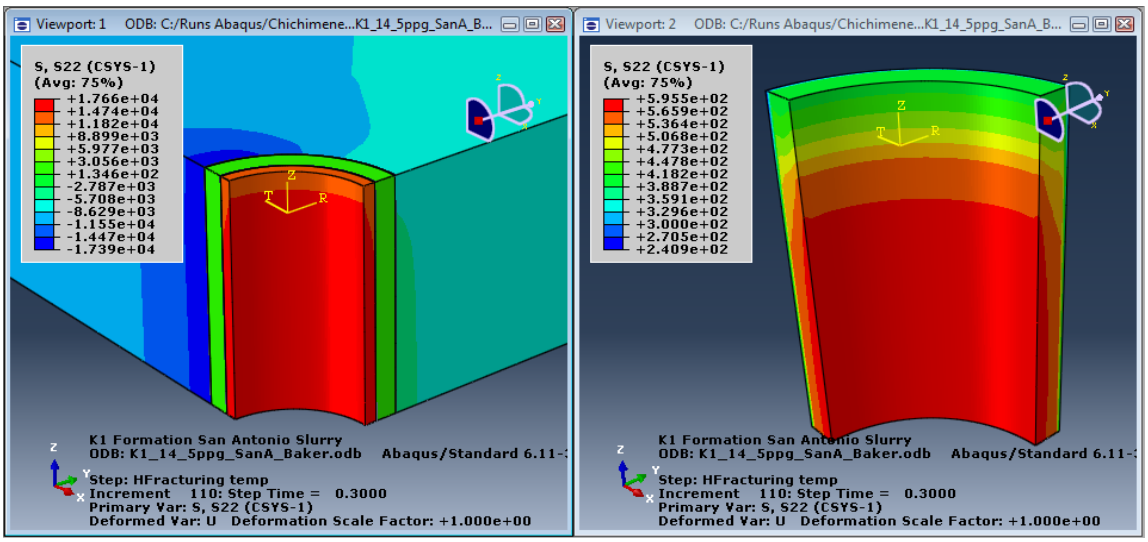

Fig. E-10—Tangential stresses after hydraulic fracturing at K1 formation of Chichimene well using FEA. Left: casing, cement and formation. Right: cement. San Antonio cement design did not have radial cracks, because its maximum tangential stress was 595 psi, and its tensile strength was 675 psi.

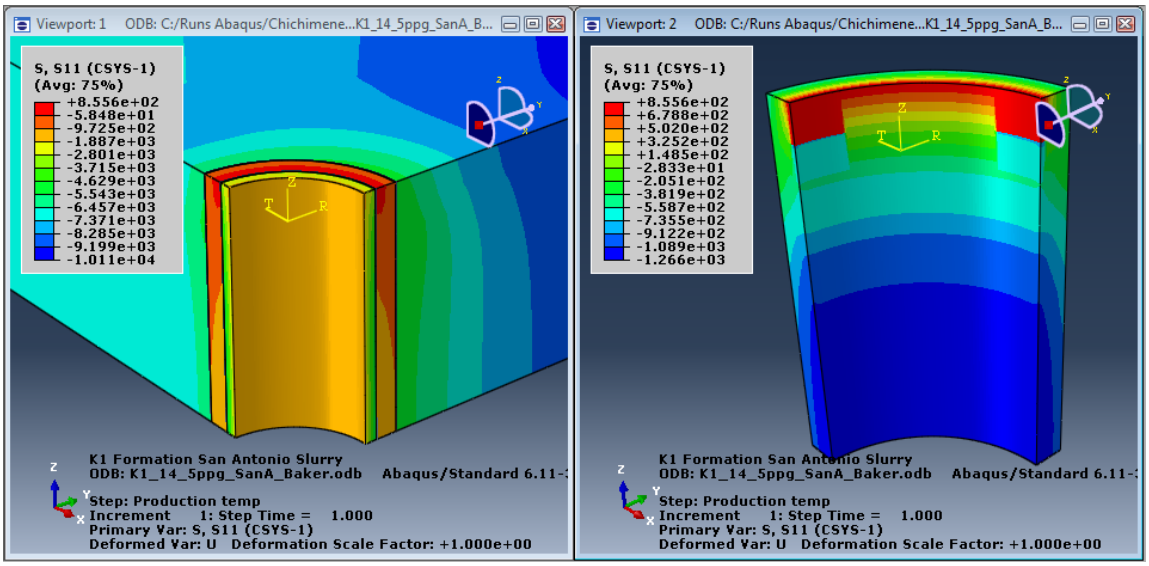

Fig. E-11—Radial stresses after well production at K1 formation of Chichimene wells using FEA. Left: casing, cement and formation. Right: cement. The maximum tensile radial stress was 855 psi at top of the cement sheath, and San Antonio cement partially debonds from casing, because the expected debonding strength was 560 psi.

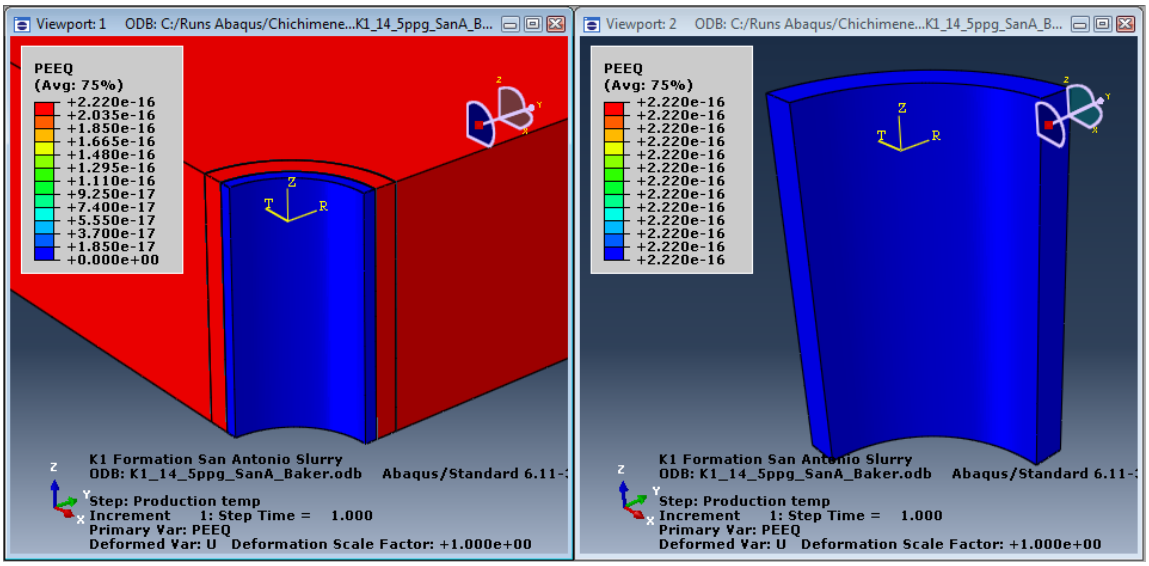

Fig. E-12—Equivalent plastic deformation (PEEQ) during well production at K1 formation of Chichimene wells using FEA. It is evident that there was not plastic deformation of San Antonio cement or formation.

FEA at K2 Formation of Chichimene Wells with 14.5-ppg San Antonio Cement of Baker Company

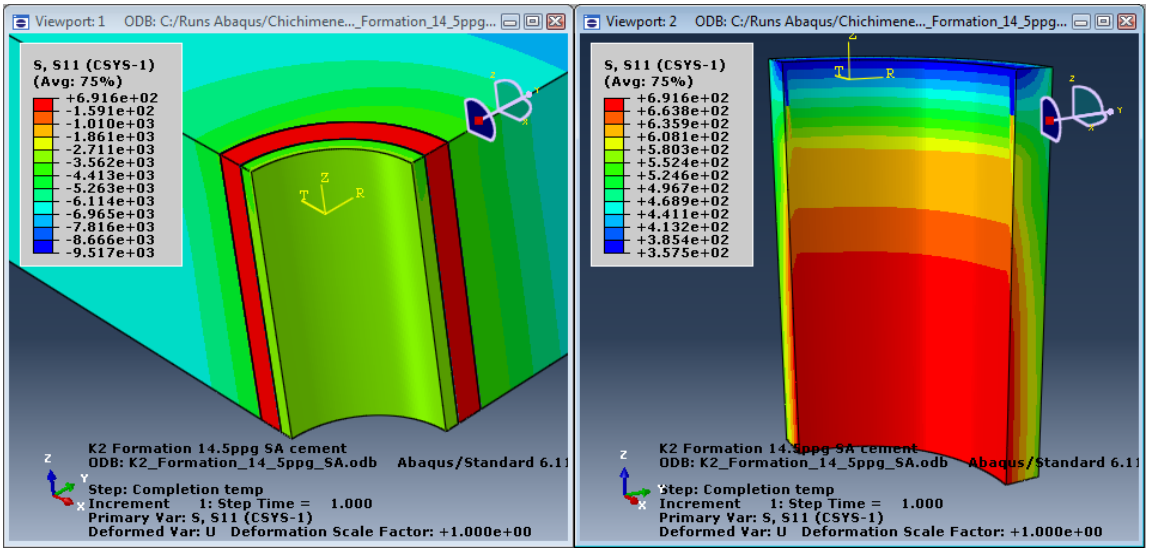

Fig. E-13—Radial stresses after well completion at K2 formation of Chichimene wells using FEA. Left: casing, cement and formation. Right: cement. High chances of cement debonding of casing, because tensile radial stresses of San Antonio cement had a value of 692 psi and estimated debonding strength of cement was 560 psi.

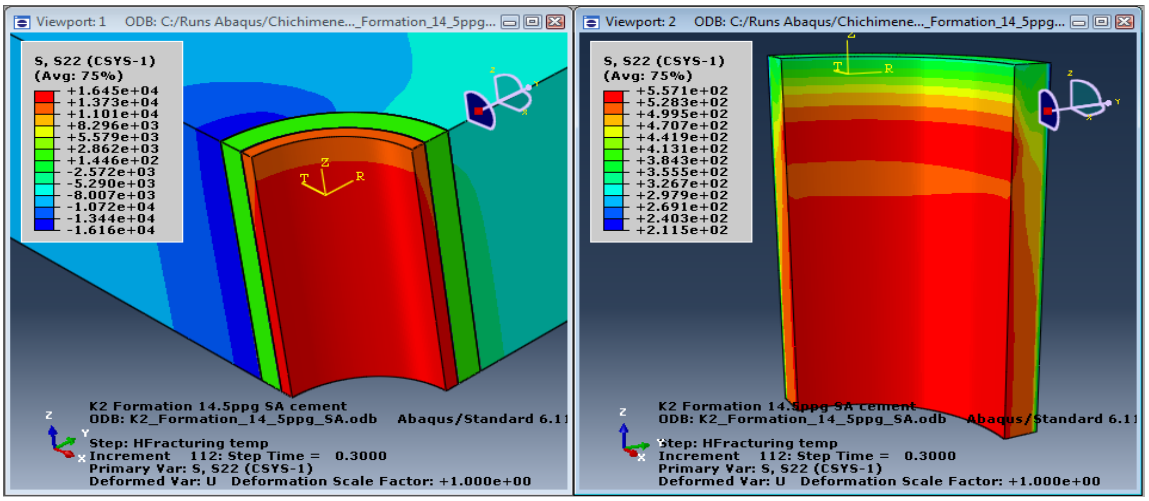

Fig. E-14—Tangential stresses after hydraulic fracturing at K2 formation of Chichimene well using FEA. Left: casing, cement and formation. Right: cement. San Antonio cement design did not have radial cracks, because its maximum tangential stress was 557 psi, and this cement had a tensile strength of 675 psi.

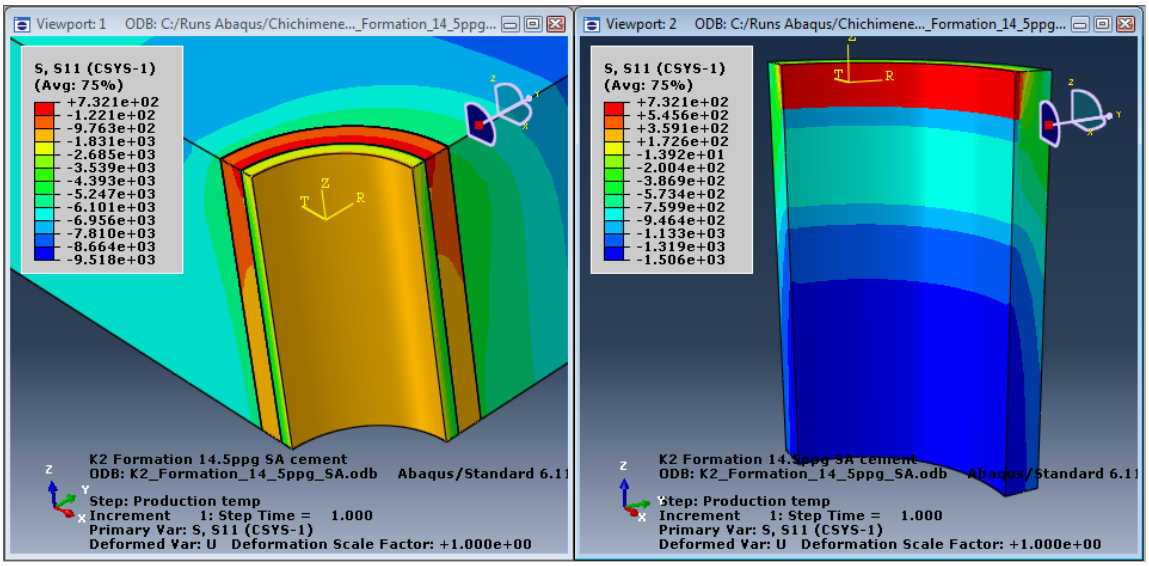

Fig. E-15—Radial stresses after well production at K2 formation of Chichimene wells using FEA. Left: casing, cement and formation. Right: cement. The maximum tensile radial stress of set cement was 732 psi at top of the cement sheath, and San Antonio cement partially debonded from casing, because the expected debonding strength was 560 psi.

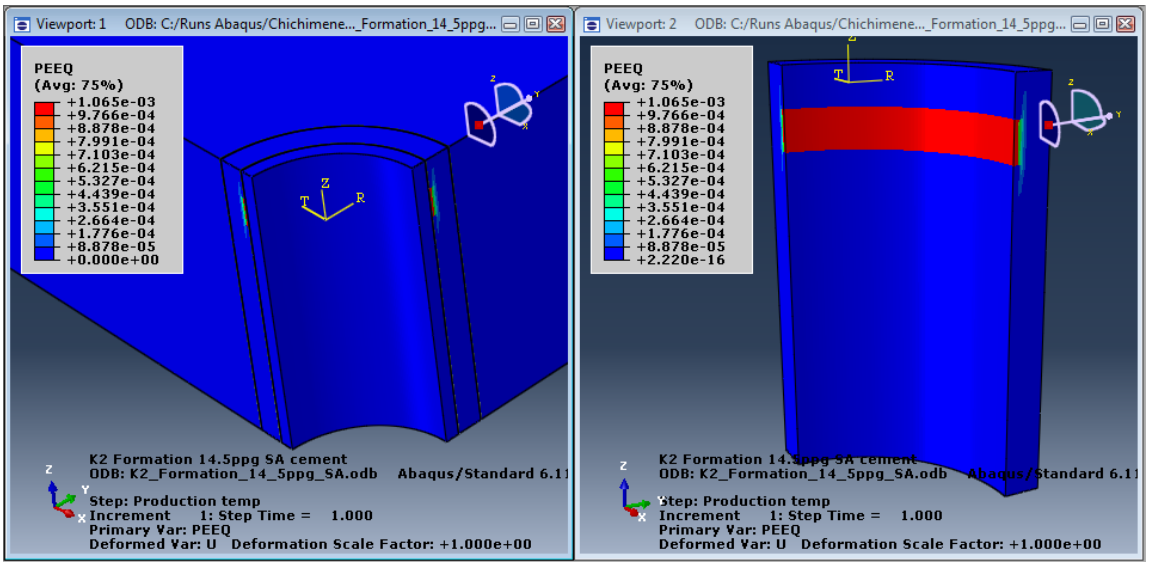

Fig. E-16—Equivalent plastic deformation (PEEQ) during well production at K2 formation of Chichimene wells using FEA. It is evident that there was plastic deformation of San Antonio cement at the top of the interval.

FEA at Mirador Formation of Cupiagua Wells with 14-5-ppg Cupiagua and 14.5-ppg Yopal Cements

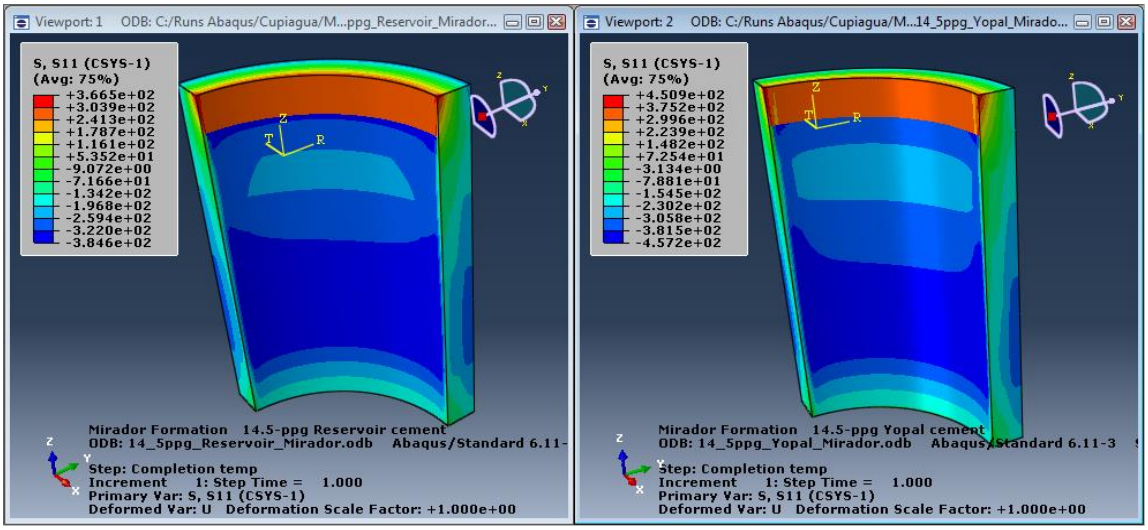

Fig. E-17— Radial stresses after well completion at Mirador formation of Cupiagua wells with two set cements using FEA. Left: Cupiagua cement. Right: Yopal cement. Radial stresses did not reach its debonding strength at Cupiagua cement (495 psi), but they reached its debonding strength at Yopal cement (445 psi) that could originate partial cement debonding.

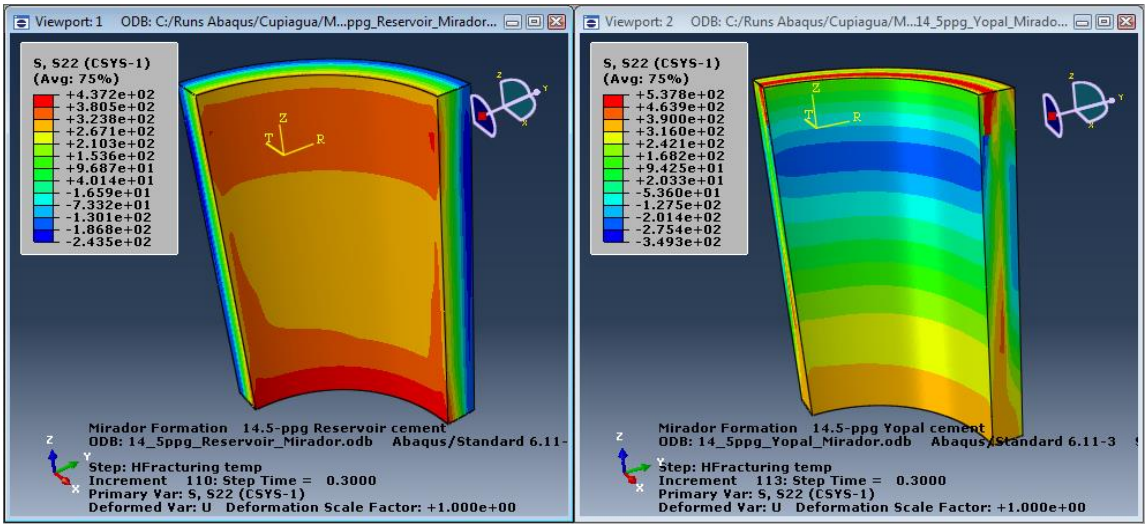

Fig. E-18— Tangential stresses after hydraulic fracturing at Mirador formation of Cupiagua wells with two set cements using FEA. Left: Cupiagua cement. Right: Yopal cement. Tangential stresses did not reach the tensile strength of Cupiagua cement (597 psi), but they reached its tensile strength at Yopal cement (536 psi) that could initiate radial cracks.

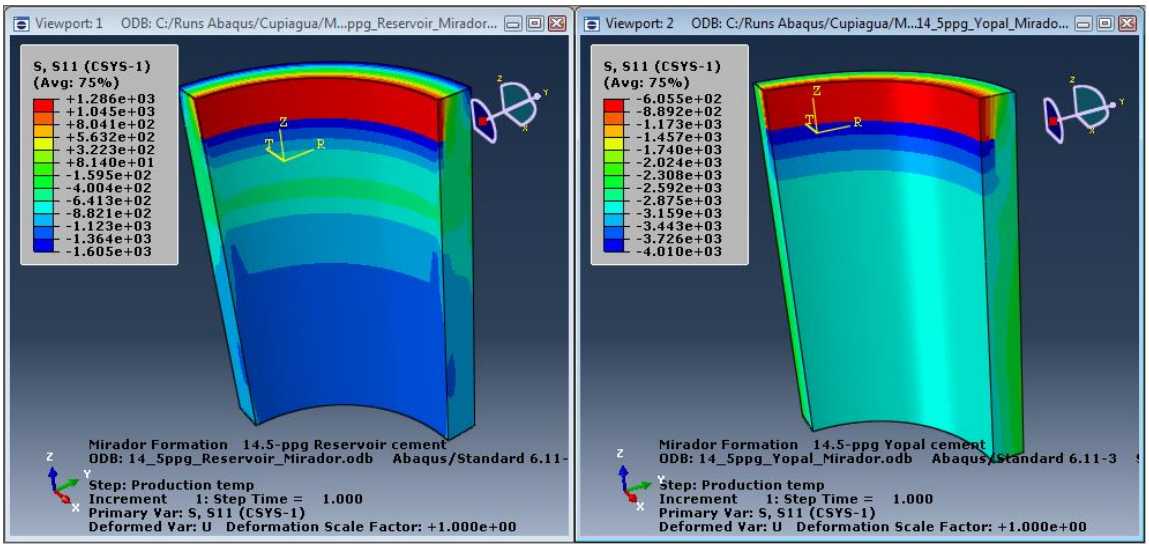

Fig. E-19— Radial stresses during well production at Mirador formation of Cupiagua wells with two set cements using FEA. Left: Cupiagua cement. Right: Yopal cement. Radial stresses reached its debonding strength at Cupiagua cement (495 psi) that could originate partial cement/casing debonding. Radial stresses of Yopal cement were compressive, and there were not chances of cement debonding.

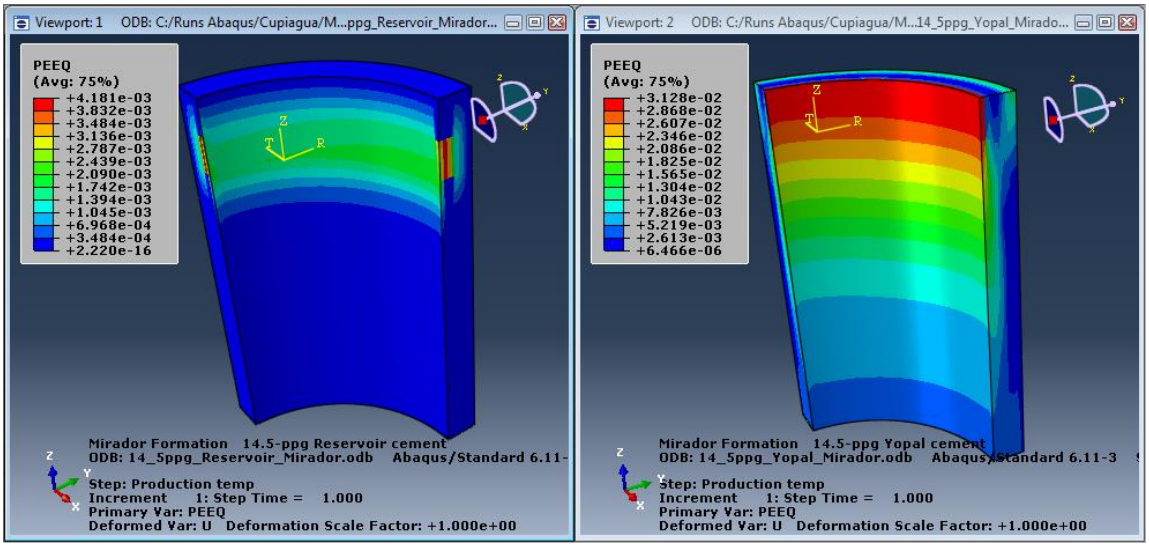

Fig. E-20— Equivalent plastic deformation during well production at Mirador formation of Cupiagua wells with two set cements using FEA. Left: Cupiagua cement. Right: Yopal cement. It was evident some cement plastic deformation, especially in the casing/cement interface. Plastic deformation of Cupiagua cement was lower than Yopal cement.

FEA at Cuervos Formation of Cupiagua Wells with 14-5-ppg Cupiagua and 14.5-ppg Yopal Cements

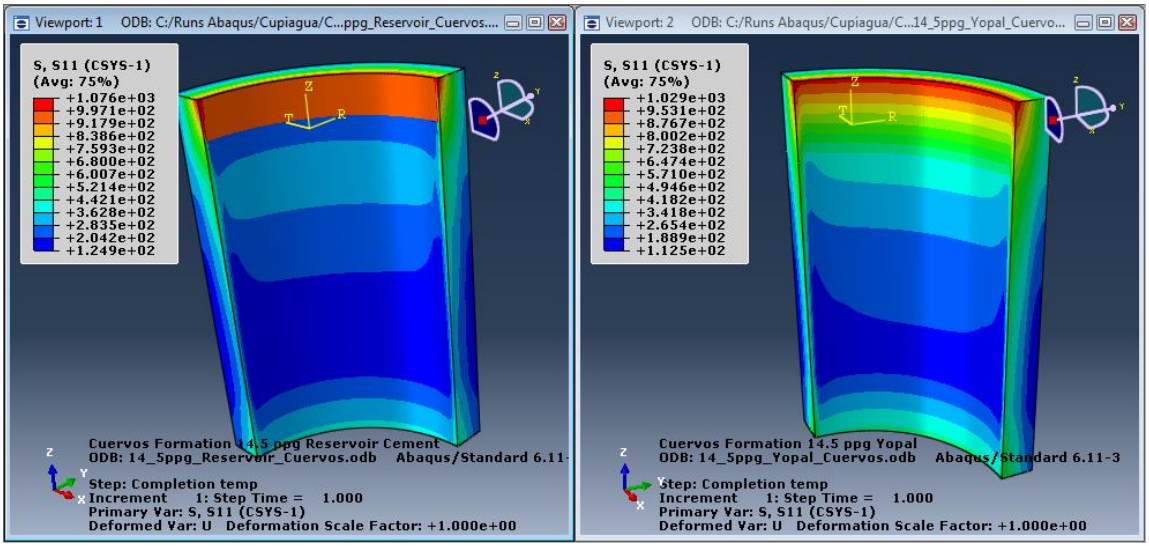

Fig. E-21—Radial stresses after well completion at Cuervos formation of Cupiagua well using FEA. Left: Cupiagua cement. Right: Yopal cement. It is unmistakable that there was cement partial debonding from casing because tensile radial stresses above the debonding strength of both cements.

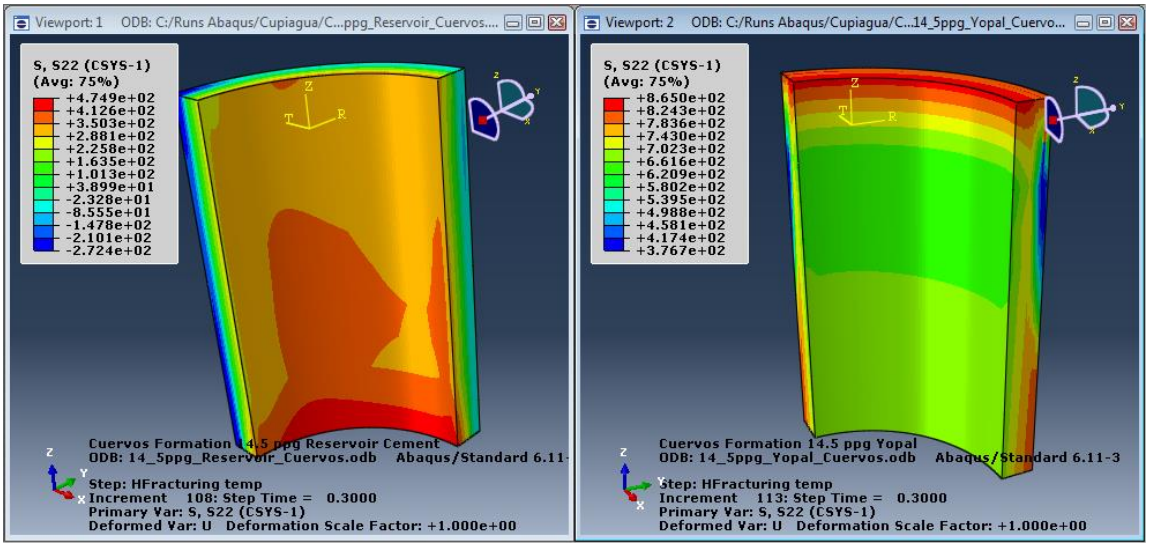

Fig. E-22— Tangential stresses after hydraulic fracturing at Cuervos formation of Cupiagua wells with two set cements using FEA. Left: Cupiagua cement. Right: Yopal cement. Tangential stresses did not reach the tensile strength of Cupiagua cement (597 psi), but they reached its tensile strength at Yopal cement (536 psi) that could create radial cracks.

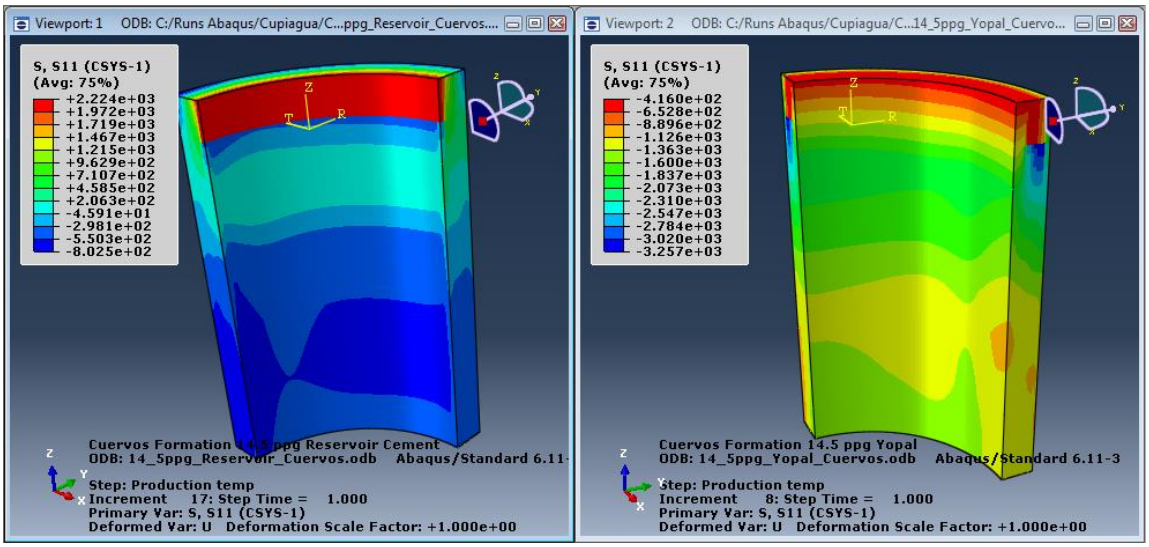

Fig. E-23—Radial stresses after well production at Cuervos formation of Cupiagua field using FEA. Left: Cupiagua cement. Right: Yopal cement. Radial stresses reached its debonding strength at Cupiagua cement (495 psi) that could originate partial cement/casing debonding. Radial stresses of Yopal cement were compressive, and there were not chances of cement debonding with bottom-hole production pressure of 1,000 psi.

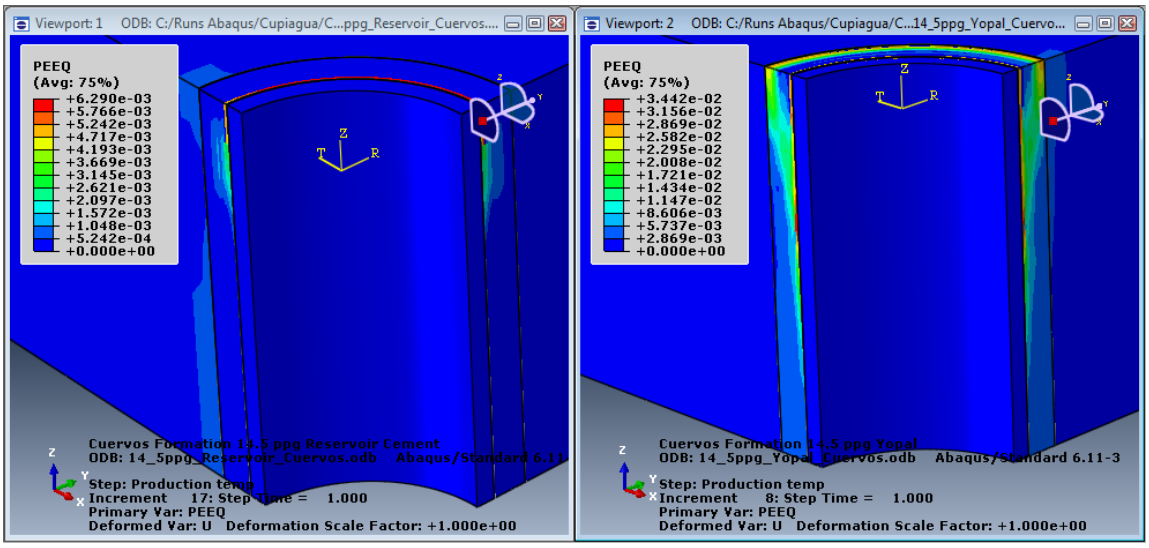

Fig. E-24—Equivalent plastic deformation during well production at Cuervos formation of Cupiagua wells with two set cements using FEA. Left: Cupiagua cement. Right: Yopal cement. It is evident some cement plastic deformation, especially in the casing/cement interface. Plastic deformation of Cupiagua cement was lower than Yopal cement. There was some plastic deformation of Cuervos formation with Cupiagua cement originated after hydraulic fracturing job and it persisted during well production.

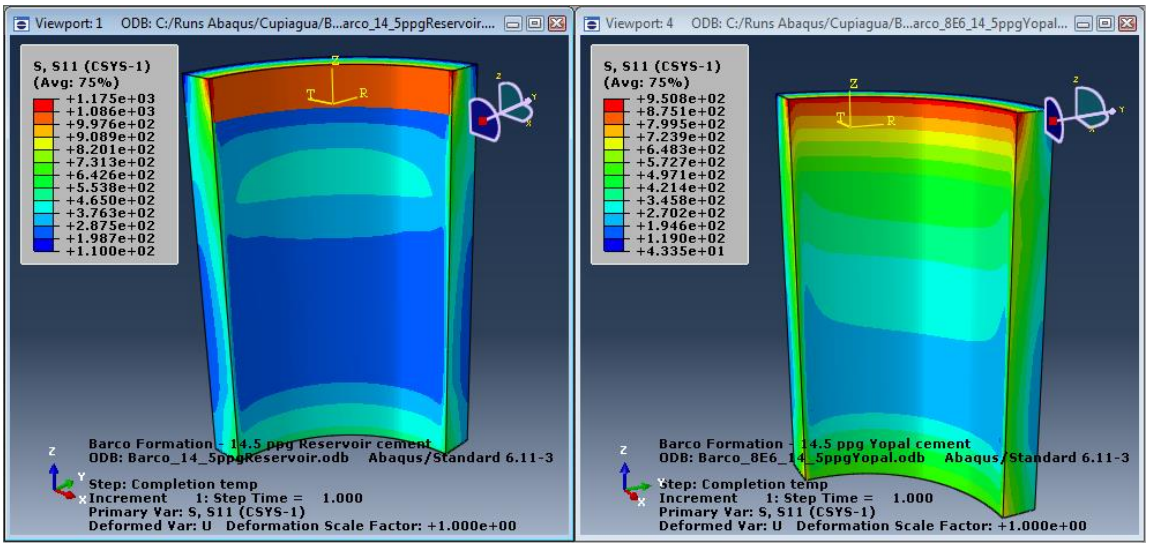

Fig. E-25— Radial stresses after well completion at Barco formation of Cupiagua well using FEA. Left: Cupiagua cement. Right: Yopal cement. It was unmistakable that there was cement partial debonding from casing because tensile radial stresses above the debonding strength of both cements.

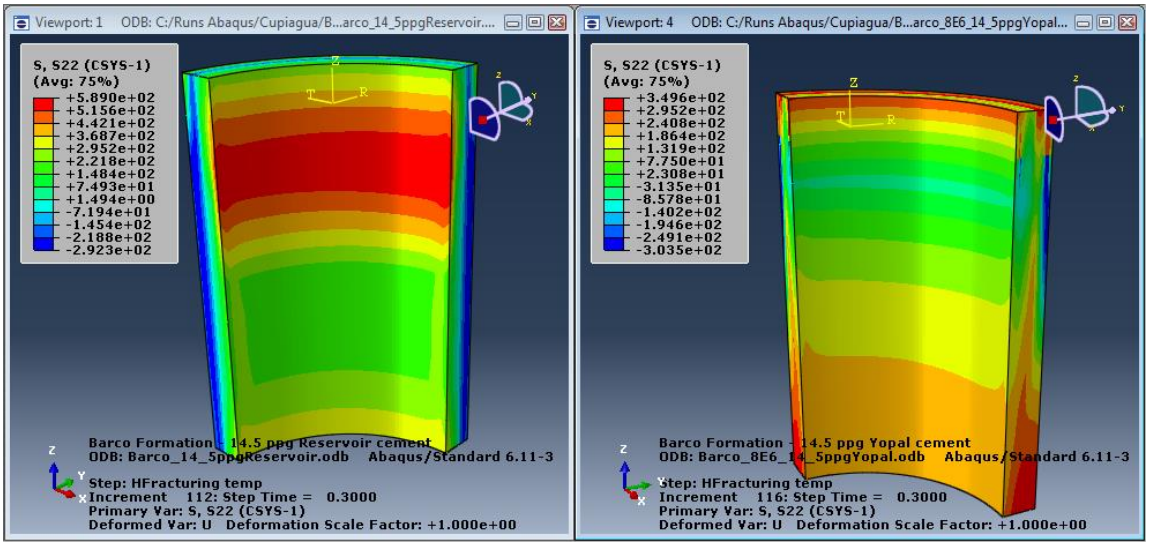

Fig. E-26— Tangential stresses after hydraulic fracturing at Barco formation of Cupiagua wells with two set cements using FEA. Left: Cupiagua cement. Right: Yopal cement. Tangential stresses did not reach the tensile strength of Cupiagua cement (597 psi), and Yopal cement (536 psi) that could create radial cracks. However, tangential stresses of Cupiagua cement were higher than Yopal cement.

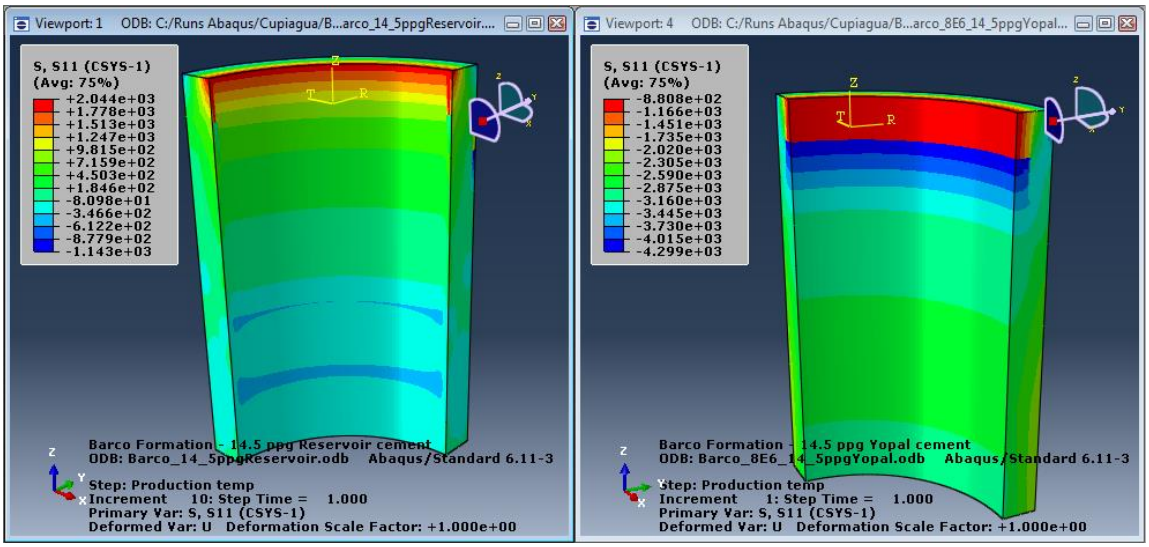

Fig. E-27— Radial stresses after well production at Barco formation of Cupiagua field using FEA. Left: Cupiagua cement. Right: Yopal cement. Radial stresses reached its debonding strength at Cupiagua cement (495 psi) that could originate partial cement/casing debonding. Radial stresses of Yopal cement were compressive, and there were not chances of cement debonding with bottom-hole production pressure of 1,000 psi.

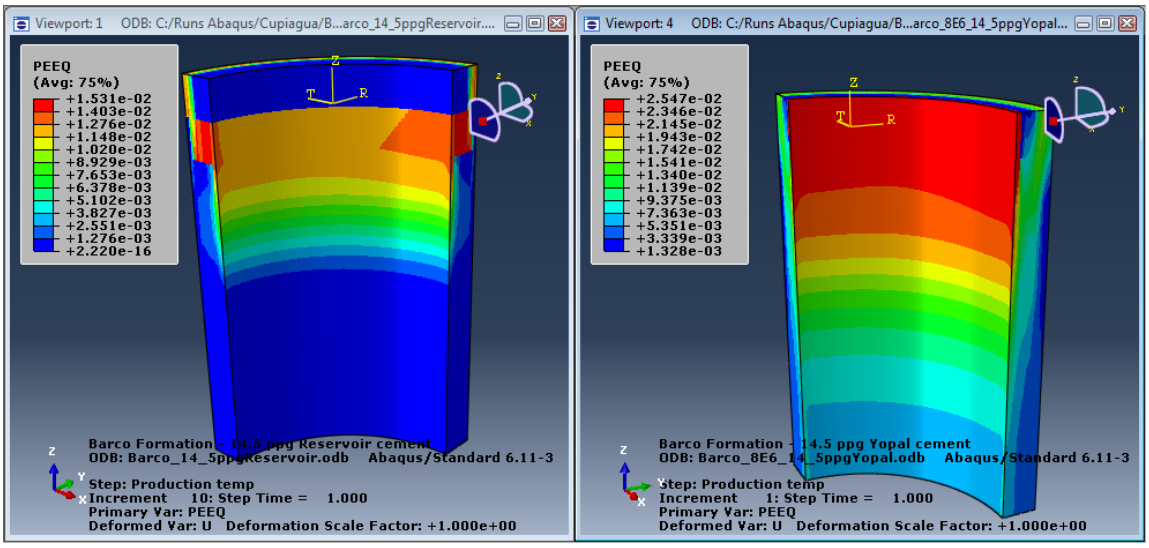

Fig. E-28— Equivalent plastic deformation during well production at Barco formation of Cupiagua wells with two set cements using FEA. Left: Cupiagua cement. Right: Yopal cement. Plastic deformation of Cupiagua cement was lower than Yopal cement.